Mathematical Modelling and Analysis of Industrial Manufacturing of Liquid Crystal Displays

Joseph Robert Leonard Cousins

Department of Mathematics and Statistics

University of Strathclyde

Glasgow, Scotland, UK

This thesis is submitted to the University of Strathclyde for the degree of Doctor of Philosophy in the Faculty of Science.

2021

Declaration of Authenticity and Author's Rights

This thesis is the result of the author's original research. It has been composed by the author and has not been previously submitted for examination which has led to the award of a degree.

The copyright of this thesis belongs to the author under the terms of the United Kingdom Copyright Acts as qualified by University of Strathclyde Regulation 3.50. Due acknowledgement must always be made of the use of any material contained in, or derived from, this thesis.

Chapter 2, Chapter 3, and Chapter 4 describe work that has been published in the research articles [36], [34], and [35], respectively. The results contained in each of these research articles are the author's original research in collaboration with the article's co-authors, namely Professor Stephen Wilson, Professor Nigel Mottram, Dr David Wilkes, and Dr Leo Weegels.

Signed:

Dated:

Acknowledgements

Firstly, I would like to acknowledge the financial support of the United Kingdom Engineering and Physical Sciences Research Council (EPSRC), the University of Strathclyde and Merck KGaA. Secondly, and most importantly, I would like to thank my supervisors, Professor Nigel Mottram and Professor Stephen Wilson. Thank you, Nigel, for always having an open door and seemingly endless knowledge of liquid crystals. Thank you, Stephen, for helping me become a better writer and, in general, a better scientist. I am also grateful for the significant work undertaken by Dr Brian Duffy. Despite not being an official supervisor of the project, I will always consider you to be one. I would also like to thank all of the people involved in the collaboration with Merck KGaA, namely Dr Leo Weegels, Dr David Wilkes and Dr David Allwright, for their support and, especially, for providing me with the opportunity to present my research in Japan. Additionally, thank you to Dr Lindsey Corson for her contributions towards Chapter 6 of this thesis.

To my Mum, Dad and sister, thank you for your endless support and kindness. To my friends, I can not thank you all enough. There are too many of you to name, but a special thanks should go to my office mates Craig, Russell and Feargus and most importantly, my best friend, Hugo.

And finally, thank you, Caoimhe. Thank you for everything.

Abstract

This thesis considers the mathematical modelling and analysis of the widely used One Drop Filling (ODF) method for the industrial manufacturing of liquid crystal displays. In the first part of the thesis, we consider three problems relating to the fluid dynamics of nematic liquid crystals (nematics) in the ODF method. In particular, we formulate and analyse a simple model for the squeezed coalescence of several nematic droplets, a squeeze-film model for a single nematic droplet, and a model for pressure-driven channel flow of nematic. Our results give significant insight into nematic flow effects in the ODF method and indicate that these effects could play an essential role in forming unwanted optical effects, known as ODF mura. In the second part of the thesis, we consider a static ridge of nematic resting on an ideal solid substrate surrounded by passive fluid. The analysis of this system gives insight into the initial stage of the ODF method and more general situations involving nematic free surfaces and three-phase contact lines. Specifically, we derive the governing equations for a static ridge, which include nematic Young and Young–Laplace equations, and then use these governing equations to study two related problems. Firstly, we consider the situation in which the ridge is thin and has pinned contact lines. Secondly, we use the nematic Young equations to determine the continuous and discontinuous transitions between the equilibrium states of complete wetting, partial wetting, and complete dewetting that can occur.

Contents

Chapter 1

Introduction

1.1 Liquid crystals

The three fundamental phases of matter are present in every aspect of life. *Solids* retain their shape, *liquids* (such as water at room temperature) retain their volume and flow freely, and *gases* (such as air at room temperature) expand to fill any available volume. In general, materials at constant pressure will change between the fundamental phases when an increase in ambient temperature raises (or lowers) the temperature of the material past certain critical values [88]. At these critical temperatures, phase transitions occur and the material changes phase. For example, in normal atmospheric conditions as temperature is increased, at the critical temperature 0° C, called the melting point, solid water (ice) undergoes a melting transition and turns into liquid water [88].

The three fundamental phases of matter are sufficient to describe most materials; however, certain materials in appropriate conditions can exist in *mesophases*, which are not one of the three fundamental phases of matter. One such group of materials, which are named after the mesophases they can form, are *liquid*

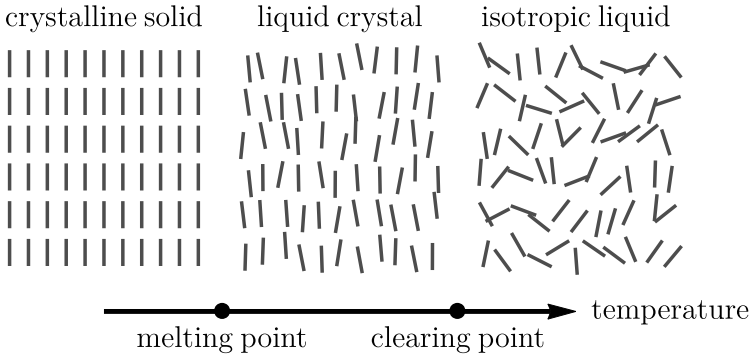

Figure 1.1: A schematic diagram of the constituent molecules (shown by grey rods) and phase transitions of a liquid crystal material with increasing temperature. The melting point and clearing point are also shown.

crystals [49].

At low temperatures (below the melting point), a liquid crystal material exists as a crystalline solid. Within the crystalline solid, long typically rod-like or disc-like constituent molecules display a preference for orientational and positional ordering with respect to their neighbouring molecules. As the temperature is increased above the melting point, the crystalline solid melts into a liquid crystal phase and the constituent molecules lose some order and begin to move more freely, whilst they maintain their preference for orientational molecular order. The liquid crystal phase is therefore an anisotropic liquid (i.e. a liquid possessing behaviour dependent on direction) with constituent molecules that align so that they display orientational molecular order. The mathematical description of this orientational molecular order will be discussed in detail in Section 1.5.

As the temperature is increased further, a different critical temperature, known as the clearing point, is reached. Above the clearing point, the liquid crystal constituent molecules lose their orientational molecular order, and molecules move and orient themselves freely as an isotropic liquid. A schematic diagram of the constituent molecule behaviour and phase transitions of a liquid crystal material with increasing temperature are shown in Figure 1.1.

Liquid crystal materials that display a liquid crystal mesophase due to temperature variation, like the scenario described above, are known as thermotropic liquid crystals [49, 201]. Some liquid crystal materials display a liquid crystal mesophase due to variation of their concentration in a solvent. These concentration-dependent liquid crystal materials are known as lyotropic liquid crystals [49, 201]. Liquid crystal materials can have varying shapes of the constituent molecules, for example, calamatic liquid crystals have rod-like molecules and discotic liquid crystals have disc-like molecules.

There are a number of different liquid crystal phases. The nematic liquid crystal phase contains no positional order and the constituent molecules locally align along a common direction, often called an anisotropic axis [49, 201]. When there is only a single anisotropic axis, nematic liquid crystals are referred to as uniaxial nematic liquid crystals. The cholesteric liquid crystal phase is observed in liquid crystal materials that have chiral constituent molecules (where there is asymmetry between the constituent molecules and the mirror image of constituent molecules) which encourages the formation of helical twist structures [49, 201]. Smectic liquid crystal phases contain some positional ordering which creates layers that contain orientational order. There are a number of smectic liquid crystal phases that are classified by their behaviour within the layered structure. For example, in smectic A phases, the liquid crystal molecules orient themselves parallel with respect to the layer normal, and in smectic C phases, the liquid crystal molecules are tilted with respect to the layer normal [201]. The various differences between liquid crystal phases can lead to them showing many different patterns and birefringence when viewed under a microscope, as shown in the photographs in Figure 1.2 [223].

In this thesis, we will be interested in calamatic uniaxial nematic liquid crystals, which we henceforth term *nematics*, as these are the most commonly used

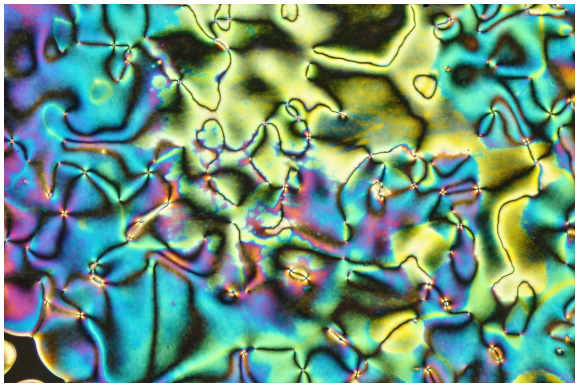

(a) The nematic phase

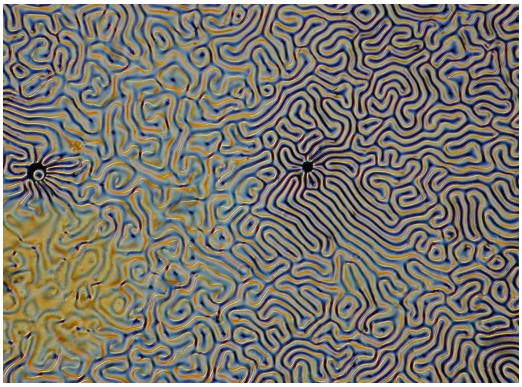

(b) The cholesteric phase

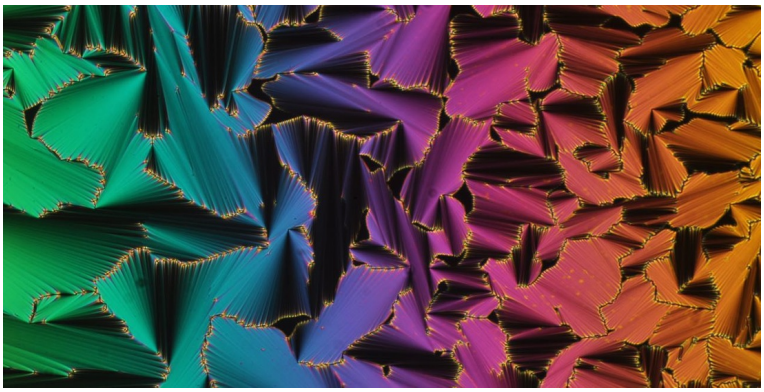

(c) The smectic A phase

Figure 1.2: Photographs of (a) the nematic phase, (b) the chloesteric phase, and (c) the smectic A phase viewed through a microscope. Photographs taken with permission from Vance Williams' blog *http://lcmicroscopy.weebly.com/lc-photogallery.html* [223].

liquid crystals in the liquid crystal display (LCD) industry [114]. From now on we will focus entirely on developing and using mathematical models for nematics. We will not discuss the mathematical descriptions of any other liquid crystal phase, but for a detailed consideration of these materials see de Gennes and Prost [49] or Stewart [201].

1.2 The discovery of liquid crystals

There is a long history of developments in chemistry and physics that proceed the modern-day use of nematics in LCDs. The first generally accepted discovery and description of a liquid crystal phase was by the Austrian botanist Friedrich Reinitzer in 1888 [176, 177]. Whilst Reinitzer was investigating cholesterol, he heated samples of cholesteryl benzoate (which is a solid at a room temperature) and observed a melting transition, at the melting point 145.5° C, at which point the solid cholesteryl benzoate melted into a cloudy liquid. To his surprise, upon further heating of his sample, he observed a second melting point at 178.5° C (which is recognised to be the aforementioned clearing point) at which point the cloudy liquid cholesteryl benzoate transitioned into a clear liquid [176, 177].

Excited by this discovery, Reinitzer sent samples of cholesteryl benzoate to the German crystallographer Otto Lehmann who had already observed similar transitions in his own material samples [32,110]. Part of Lehmann's current work was the design and creation of a heated microscope for observing the crystallisation of his material samples [32,110]. After observing Reintzer's samples with his heated microscope and continuing his investigations, Lehmann described Reintzer's samples as "flowing crystals" [126]. This was a remarkable observation of a new phase of matter; a liquid with crystalline properties. Around the same time, Lehmann was sent samples by Gattermann and Ritschke [81] who had developed the first

synthesised nematic material, *p*-azoxyanisole (PAA) [110]. In 1900, Lehmann's continued contributions to this developing field eventually lead him to adopt the term "liquid crystals" [110].

Further important developments occurred in 1907, when Vorländer experimentally determined that liquid crystal constituent molecules were typically rigid and linear [110,215]. In 1922, Georges Friedel developed the classification of liquid crystals into three distinct categories, nematics (derived from the Greek word for thread), smectics (derived from the Greek word for soap) and cholesteric (meaning cholesterol-like material) [32, 77]. Although the discovery of these liquid crystal materials and their categorisation had now come a long way in a short period, little was still known about their optoelectrical and viscoelastic properties, which now form the basis of an industry worth more than 150 billion dollars [140].

1.3 50 years of liquid crystal displays

The first optoelectrical effect in liquid crystals was found in 1918 by Björnstahl [16]. Björnstahl found that when an electric field was applied across a thin layer of PAA, the PAA molecules orientated themselves perpendicular to the direction of the applied field [110]. Similar optoelectric effects were obtained by Friedel in 1922 [110] and Zwetkoff in 1935 [103]; however, much of the interest in liquid crystals began to fade as Europe was overcome by the First and Second World Wars [110]. The potential technological application of optoelectric effects in nematics remained largely unexplored for the next 50 years.

Further reasons for the lack of development of a liquid crystal based display were firstly due to the success of the cathode ray tube television [80], and secondly, that at the time liquid crystal materials were highly unstable, with melting points much higher than room temperature [103]. It wasn't until 1963 that desire for

a flat panel display for use in aircraft turned attention back to liquid crystals. The light scattering experiments of Björnstahl and Zwetkoff were rediscovered by Richard Williams of the Radio Corporation of America (RCA) Laboratories in Princeton [222]. The work of Williams was then extended by Heilmeier and Zanoni [93] who produced the first patent of a practical LCD named a dynamic scattering LCD (DS-LCD) [92].

1.3.1 The dynamic scattering liquid crystal display (DS-LCD)

The DS-LCD operates using a negative dielectric anisotropy nematic (meaning that the nematic molecules align perpendicular to imposed electric fields [201]) doped with conductive particles, placed in a thin gap between two electrically conductive transparent substrates and crossed polarisers [108], as shown in Figure 1.3. The conductive particles allow an electrical current to pass through the nematic between the two substrates. In the off-state, the nematic aligns perpendicular to the substrates and any incident light is blocked by crossed polarisers which are positioned above and below the upper and lower substrates, respectively, as shown in Figure 1.3(a). In the on-state, a voltage is applied between the two substrates, creating an electric field and an electrical current (due to the conductive particles) between the two substrates. The electric field and electric current create two opposite torques on the nematic molecules [108]. Firstly, due to the negative dielectric anisotropy of the nematic, a torque from the electric field aligns the nematic molecules perpendicular to field (in-plane with the substrates), and secondly, a torque from the transport of current between the two substrates produces an opposing torque (out-of-plane with the substrates). At low field strengths these opposing torques produce the formation of striped structures called Williams domains, as shown in Figure 1.4 [222], but as the

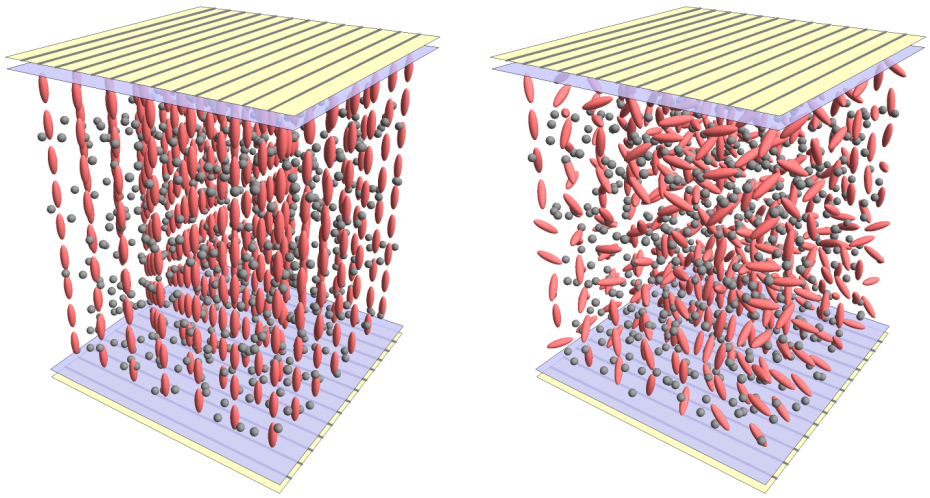

(a) DS-LCD off-state (b) DS-LCD on-state

Figure 1.3: A schematic diagram of the mechanism of a DS-LCD in the (a) off-state and (b) on-state. The nematic (red ellipsoids) doped with conductive particles (dark grey spheres) is contained between two electrically conductive transparent substrates (blue layers) and two crossed polarisers (yellow striped layers).

field strength is increased further, the large opposing torques produce turbulent motion of the nematic molecules, which scatters the incident light from the first polariser, randomly changing the direction and polarisation of the light [86]. This dynamic scattering of the incident light by the doped nematic allows some light to pass through the upper polariser [108], creating the on-state, as shown in Figure 1.3(b). The applied voltage may then be controlled, allowing switching between the on- and off-state, creating the basis of the display.

The invention of the DS-LCD inspired the first prototype LCD products, such as pocket calculators and digital wrist watches, however, these displays faced serious problems. Due to the requirement of conductive particles in the DS-LCD, electrochemical decomposition could cause build up on the electrodes on the substrates and the displays required large operating voltages [108]. Ultimately, these problems meant that DS-LCDs were not capable of replacing the cathode

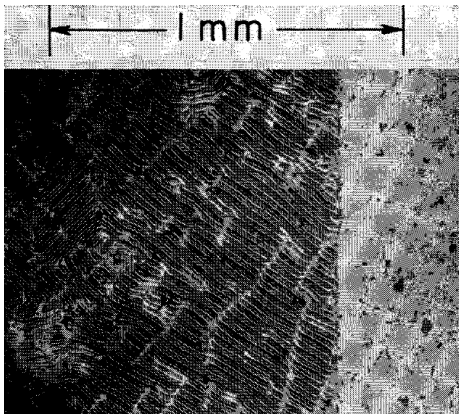

Figure 1.4: Williams domains observed in PAA. An electric field is applied on the left-hand side in the dark regions, and no electric field is applied in the right-hand side in the light region. Williams domains are evident in the small striped structures on the left-hand side in the dark regions. Figure taken from [222] with Copyright permission from The American Association for the Advancement of Science and Copyright Clearance Center.

ray tube for use in a large displays. With the large number of problems associated with DS-LCDs, a new mechanism for a liquid crystal based display was required.

1.3.2 The twisted nematic display (TN-LCD)

It was not until 1969, after the formation of the Roche liquid crystal research group in Switzerland, that Wolfgang Helfrich decided that investigating a display that used an imposed twist, which had previously been observed by a French crystallographer Mauguin in 1911 [143], was worth further investigation [103]. Mauguin had found that incident light on a twisted nematic state caused a change in the polarisation of the transmitted light. Helfrich and his colleague Martin Schadt, realised that by unwinding this imposed twist with an applied electric field they could control the polarisation of light incident on the nematic layer [103] which could be the basis of a new type of LCD.

In 1970, Helfrich and Schadt created reproducible unwinding and winding of

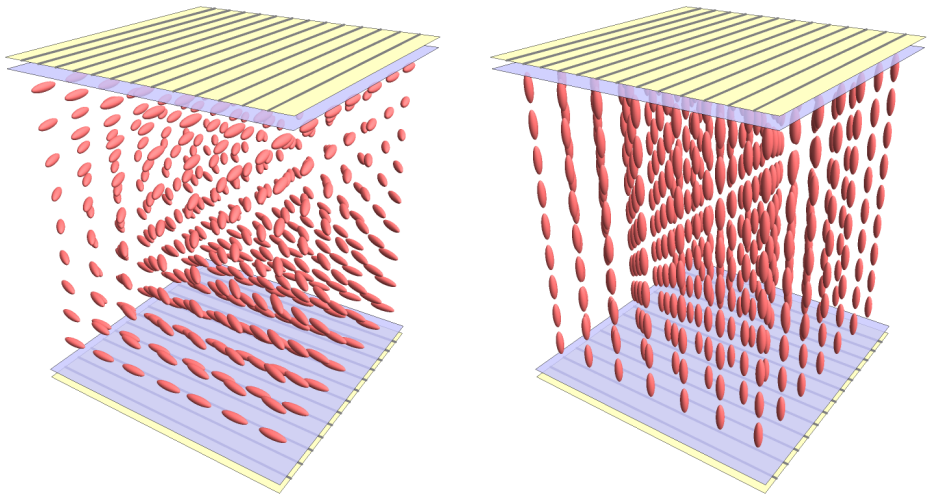

(a) TN-LCD off-state (b) TN-LCD on-state

Figure 1.5: A schematic diagram of the mechanism of a twisted nematic TN-LCD in the (a) off-state and (b) on-state. The nematic (red ellipsoids) is contained between two electrically conductive transparent substrates (blue layers) and two crossed polarisers (yellow striped layers).

an imposed twist and could now reliably switch the nematic between a twisted state and an untwisted state [103]. What was even more surprising about this discovery was the low operating voltages required for the switching of this nematic state. The invention was quickly patented and published within the year, and the twisted nematic display (TN-LCD) was ready to be commercialised [94, 191].

The TN-LCD, unlike the DS-LCD, operates using a positive dielectric anisotropy nematic (meaning that the molecules align parallel to imposed electric fields [201]) which is placed in a thin gap between two electrically conductive transparent substrates and crossed polarisers, as shown in Figure 1.5. In the off-state, the nematic contains an imposed twist, which is achieved by specific treatment of the lower and upper substrates (the specific treatment of the substrates, called *anchoring* will be discussed in Chapter 1.7.3), as shown in Figure 1.5(a). The imposed twist acts as a wave guide for the incident linear polarised

light and the polarisation is rotated 90° so that when it reaches the upper polariser the light is emitted. In the on-state, an electric field is applied between the substrates, and due to the positive dielectric anisotropy of the nematic, a torque from the electric field aligns the nematic molecules perpendicular to the substrates, as shown in Figure 1.5(b). With the nematic molecules perpendicular to the substrates the imposed twist is no longer present, and the polarisation of the incident light is no longer rotated and is therefore blocked by the upper polariser.

It often goes unmentioned that in 1970, Frank Leslie of the University of Strathclyde described the mathematical theory for a similar mechanism which unwound an imposed twist within a thin nematic layer using a magnetic field [129]. Leslie calculated the magnetomechanical threshold required to cause the nematic to untwist in a magnetic field and the analogous result for electric fields could easily be extracted from his work. This theoretical paper may have been the basis on which Helfrich and Schadt gained their inspiration to create the twisted nematic display, albeit using electric fields rather than magnetic fields [103, 108]. Five months after the patent was filed by Roche, the American company Ferguson submitted a similar TN-LCD patent [73] and a legal battle between Roche and Ferguson began. The conflict was eventually settled when Roche bought Ferguson's patent.

Within the next few years some practical issues arose for the TN-LCD, including a lack of stable and room temperature nematic materials which were crucial for creating a room temperature display. However, most significant of all problems was a lack of funding at Roche. At the time, Roche made the majority of its money through its cathode ray tube patents, and the company directors viewed the TN-LCD as unwanted competition [103].

Eventually, inspired by the success of the TN-LCD in Japan, Roche began to

focus on developing room temperature nematic materials to bring a commercial TN-LCD into reality. The creation of the nematic materials called cyanobiphenyls by George Gray and others at the University of Hull [85, 173] allowed the development of new nematic mixtures, which combined a number of nematic materials and chemical additives to achieve room temperature stable nematic mixtures [173]. Roche had now become primarily a chemical company, and focused its efforts developing these mixtures and entered licensing agreements with many Japanese companies, such as Seiko, Sharp and Hitachi [103]. This long and productive relationship brought about the first TN-LCD wrist watches, portable games consoles, and pocket calculators. The nematic material patents developed by Roche over this period were eventually purchased by Merck KGaA, who now continue the research, development and production of liquid crystal mixtures.

The TN-LCD was successfully used in small portable displays, but they could not replace the cathode ray tube for use in large displays, until their combination with the thin-film-transistor (TFT). The TFT, developed by Paul Weimer in 1962 [220], operates using thin semiconductor deposits which use electronic signals to allow the control of individual portions of a display, called pixels. In 1974, Brody et al. [22] combined a TFT and a TN-LCD to create a method for constructing a large TN-LCD. These so-called TFT-LCDs were finally able to replace the cathode ray tube for use in large displays, and LCDs took control of the display market.

Since the development of the TFT-LCD, advancements in engineering and chemical design of nematic materials has allowed the introduction of many new modes of LCDs, including the super-twisted nematic display (STN-LCD) [174], in-plane switching display (IPS-LCD) [99], and the vertically aligned nematic display (VAN-LCD) [228].

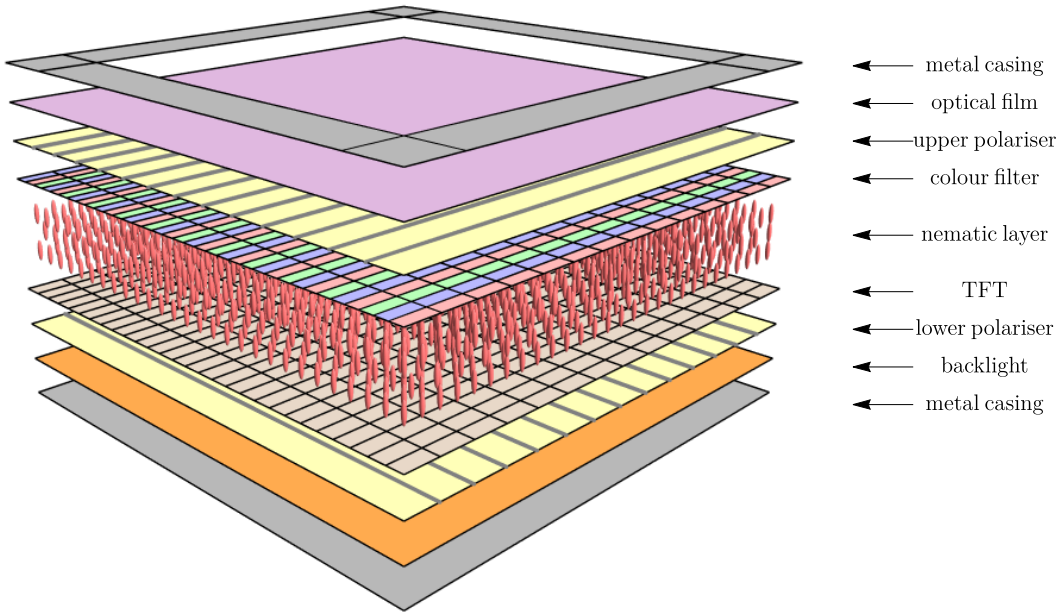

Figure 1.6: A schematic diagram of the layered structure of a modern LCD. From bottom-to-top the layers consist of the lower surrounding metal casing (shown by the grey layer), the backlight (shown by the bright orange layer), the lower polariser (shown by the yellow striped lower layer), the glass-mounted TFT (shown by the brown layer with a black imposed grid), the nematic layer (shown by the red ellipsoids), the colour filter (shown by the red, blue and green layer), the upper polariser (shown by the yellow striped lower layer), the optical film (shown by the purple layer), and finally, the upper surrounding metal casing (shown by the open grey layer) [225].

1.4 A modern liquid crystal display

A modern commercialised LCD requires the combination of several layered components [225], as shown in Figure 1.6. In particular, within the outer metal casing, the LCD is illuminated from the bottom by a mono-coloured backlight. The backlight typically uses a mono-coloured cathode fluorescent lamp or many individual light emitting diodes [19] to transmit light through the polariser and the glass-mounted TFT into the nematic layer.

The TFT is used to electronically control the many pixel regions that make up the display. In cutting-edge modern, so-called 8K resolution, LCDs, there can be

as many as 33 million individual pixels in a single display. These displays can now be over 60 inches in size (diagonal measurement of the display) and each pixel must be controlled by electronic signals through the TFT [113,202]. When a pixel is in the off-state, there is no change in the polarisation of the incident light on the nematic layer, and as such, the light is blocked by the second polariser, which is orientated 90° to the first. When a pixel is in the on-state, the polarisation of the incident light is changed by the orientation of the nematic molecules in the nematic layer.

The orientation of the nematic molecules in the on-state and off-state is different depending on the type (often called the *mode* of the LCD) of the display. The most common commercially available LCD modes, i.e. STN-LCD, IPS-LCD or VAN-LCD, all use imposed twists or rotations of the nematic molecules to act as a wave guide to change the polarisation of the incident light. As the light passes through the pixels in the on-state, it then passes through a colour filter which blocks certain colours from the mono-chromed light source to produce the desired colour of the final output. Finally, the output passes through an optical film which improves the quality of the final output [20].

Many LCD modes still exist on the market place because each mode provides unique advantages [65, 111]. For example, in computer monitors, the STN-LCD mode can be favoured by users who play computer games for fast refresh rates and response times; however, VAN-LCDs can be favoured for watching film and television as they provide greater colour depth and viewing angles [65]. Whilst LCDs in general still dominate the display market, the emergence of organic light emitting diode (OLED) displays [138] now provide a direct competition for LCDs. OLEDs operate through the combination of excited electrons and holes (the absence of an electron) within an organic polymer layer sandwiched between an anode and a cathode. When the electrons and holes combine, they form

excited states that relax by emission of a photon of a particular wavelength. The controlled reproduction of this effect forms the basis of the OLED display [138]. OLED displays are the current high-end display of choice, due to their improved black state, colour depth and viewing angles; however, LCDs are still preferred for their low manufacturing costs and longevity [29].

1.4.1 The alignment layer

In order to impose specific twists or tilts of the nematic molecules in the nematic layer which control the polarisation of emitted light, the glass-mounted TFT and colour filter, referred to henceforth as the *substrates*, are coated with thin alignment layers, whose purpose, as previously mentioned, is to ensure that the nematic molecules have the required orientation at the substrates for the final display. The precision to which the required orientation of the nematic molecules at the substrates must be maintained is often extremely high. For instance, in VAN-LCDs, in which the required nematic orientation is close to 90°, deviations in the orientation as small as 1° can lead to unacceptably large changes of an order of magnitude in the LCD contrast ratio [6]. The alignment layers are therefore crucial components of any LCD. In particular, they are, in large part, responsible for determining its optical characteristics [104].

There are a number of methods for fabricating alignment layers. A widely-used method for creating a preferred orientation at the substrates is the polymer stabilised (PS) method. This method involves adding an ultraviolet curable monomer to the nematic and then applying a voltage difference across the nematic layer while exposing it to UV light in order to achieve the desired orientation at the polymer layers which form on both substrates due to phase separation [90,221,228]. This method is now so widely used in the display industry that displays are often named after it, for example, the polymer stabilised VAN-LCD

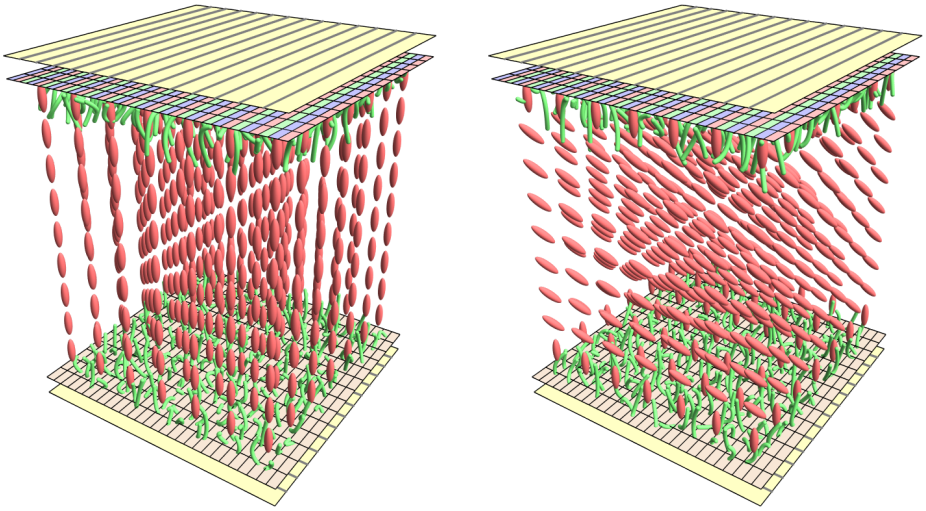

(a) PS-VA off-state (b) PS-VA on-state

Figure 1.7: A schematic diagram of the mechanism of a PS-VA in the (a) off-state and (b) on-state. The nematic (red ellipsoids) is stabilised by a polymer (green tubes) and is contained between the TFT (brown crossed layer), the colour filter two electrodes (red, blue, and green layer), and two crossed polarisers (yellow striped layer).

is often called just PS-VA. The PS-VA mode LCD is shown in Figure 1.7.

Another method for creating a preferred orientation at the substrates involves coating the substrates with a layer of polyimide, and then mechanically rubbing these layers to create nano-grooves in their surfaces with which the nematic tends to align [104]. Other displays use photo-activated alignment in which the substrates are coated in a polymer layer whose surface orientational properties are changed when they are exposed to polarised light [84]. All of the methods for creating an alignment layer rely on some form of adhesion between the molecules of the alignment layer and those of the nematic, which leads to an energetically preferred nematic orientation at the substrates. Depending on the alignment material used, the physical mechanism for this adhesion can be either mechanical or electrostatic [104].

1.4.2 Liquid crystal display manufacturing

The industrial manufacture of modern LCDs involves a number of different processes, a key one of which involves filling nematic between the substrates. There are two basic methods for doing this, namely capillary filling and One Drop Filling (ODF). The first step in both of these methods is to coat the two substrates in thin alignment layers to correctly orient the nematic molecules at the substrates.

In capillary filling, the substrates are positioned parallel to each other with a typical gap size of around 5 μm [106]. The nematic is then introduced into this gap from one side of the display and allowed to fill the space between the substrates by capillary action, often aided by an applied pressure difference (an enhancement sometimes referred to as "vacuum filling"). Even with an applied pressure gradient, the nematic flow is still slow, and as such, capillary filling was a bottleneck in the manufacturing process, leading to manufacturing times of the order of a day [71, 106].

In ODF, the nematic is dispensed onto the lower substrate in the form of droplets, as shown in Figure 1.8. These droplets are allowed to equilibriate and then the upper substrate is lowered towards the droplet-laden lower substrate, squeezing the droplets together to form the nematic layer.

Experimental images of the transmission of light through a two-droplet ODF test setup is shown in Figure 1.9. The ODF test set-up contains two converging substrates with polarisers at perpendicular directions (crossed polarisers) positioned on each substrate (shown by the green arrows in Figure 1.9). The exact gap between the converging substrates is unknown in each photograph; however, the orientation of nematic molecules can be inferred from the regions of low light transmission (black) and regions of high light transmission (white). While the nematic molecules are aligned parallel to either polariser or aligned parallel to direction of the transmitted light, no light is transmitted (black regions) through

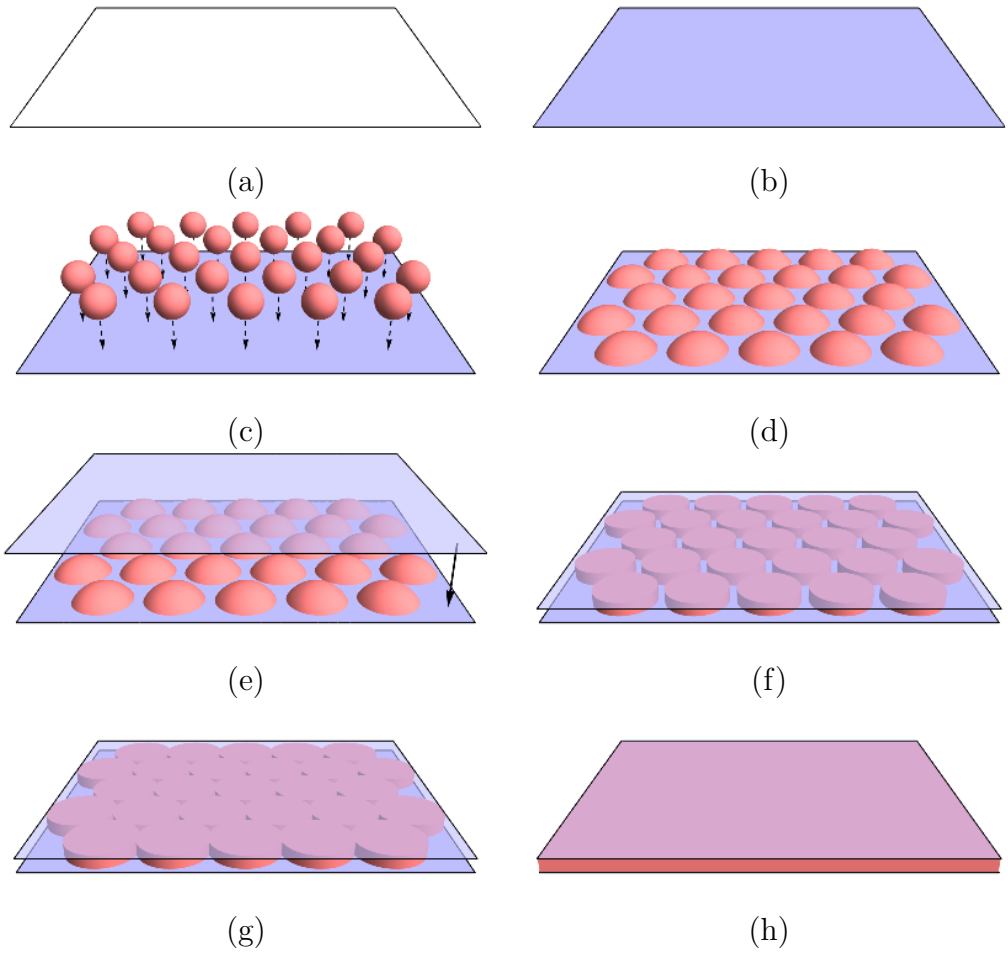

Figure 1.8: A schematic diagram of the stages of the ODF method. The substrates are ((a) and (b)) coated in alignment material (shown in light blue), ((c) and (d)) nematic droplets (shown in red) are dispensed and allowed to equilibriate on the lower substrate, and ((e)–(h)) the upper substrate is lowered onto the nematic droplets squeezing them from above to form a thin continuous layer of nematic.

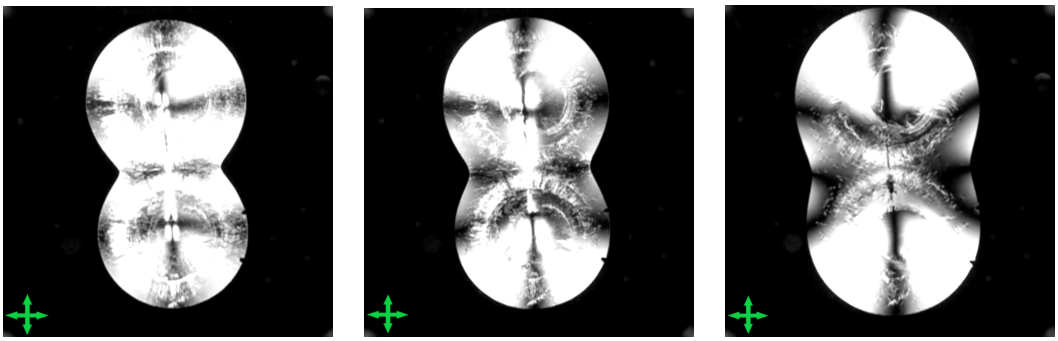

Figure 1.9: Experimental photographs of the transmission of light through a two-droplet ODF test setup between crossed polarisers (with polariser direction indicated by the green arrows). Left to right shows the increase of time and regions of white show complete transmission through the drops and regions of black show no transmission. [Photographs provided by Merck KGaA]

the ODF test setup. If the director is aligned 45° from both polarisers and perpendicular to the direction of the transmitted light, there is a maximum (white regions) amount of transmission through the nematic layer. In situations between these extremes, there is partial transmission of light through the nematic layer (grey regions). In Figure 1.9, a black cross within the center of each droplet represents that the orientation of nematic molecules is radial from the center of each droplet. As the gap between the substrates decreases, these black crosses move into the combined centre of the droplets. In Chapter 2, we will make comparisons between the experimental photographs shown in Figure 1.9 and numerical investigations of a two-droplet ODF setup.

The introduction of the ODF method significantly improved manufacturing speeds so that manufacturing times were reduced from of the order of a day to of the order of an hour [71, 106], and are now even shorter than this. However, since ODF is significantly faster than capillary filling, it involves significantly higher nematic flow speeds, which may cause transient flow-driven distortion of the nematic molecules at the substrates from their required orientation. This

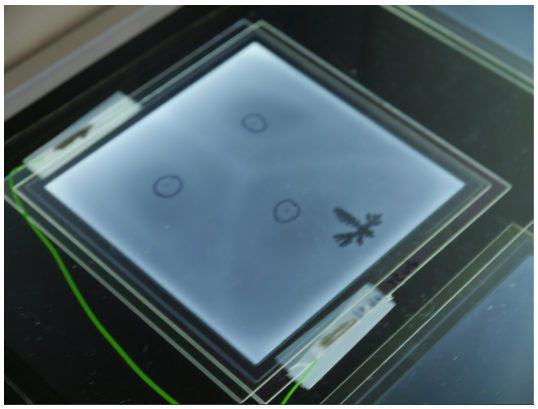

Figure 1.10: ODF mura formed in a three droplet ODF test cell. The hand-drawn circles indicate the positions where the three droplets were deposited on the bottom substrate. Note that the black shape to the right of the lowest hand-drawn circle is a defect in the test cell not related to the ODF mura. [Photograph provided by Merck KGaA]

may then lead to permanent or semi-permanent flow-driven misalignment of the orientation of the molecules in the alignment layers, which may in turn degrade the optical properties of the final display. In particular, flow-driven misalignment of the orientation of the molecules in the alignment layers may be the cause of unwanted optical effects known as "ODF mura" [36, 125, 167].

1.4.3 The ODF mura

Figure 1.10 shows an example of ODF mura formed in a three droplet ODF test cell. In particular, Figure 1.10 shows nonuniformity within the test cell in the form of three linear regions of relatively high light transmission equidistant between the original locations of each droplet (indicated with the hand-drawn circles in Figure 1.10) creating an inverted "Y-shape" and a radial non-uniformity away from the centre of the cell. For many LCD modes the ODF mura may recover over time, but for the PS-VA mode [119], any deformation to the orientation of the molecules in the alignment layers is "locked in" after ultraviolet light curing of the alignment

layer. In this thesis we will be particularly interested in mathematical modelling of nematic flow in LCD manufacturing, and understanding how nematic flow can lead to the formation of the ODF mura.

1.4.4 Typical parameter values in the ODF method

In Chapters 2 to 4 we will consider mathematical models for various aspects of the fluid dynamics in the ODF method. In each of these chapters we will use typical parameter values from the ODF method to motivate the various asymptotic regimes we consider and to produce plots of key results. The key geometrical parameters in the ODF method are; the initial radii of the nematic droplets, denoted by $\mathcal{R}$, the initial height of the nematic droplets, denoted by $\mathcal{H}$, the final gap between the substrates, denoted by $\mathcal{H}_{\mathrm{f}}$, the downward speed of the top substrate, denoted by s_{p}, and half the separation distance of each droplet, denoted by L. These key geometrical parameters are included in a sketch of the ODF method for a three droplet set-up in Figure 1.11. Based on private communications with Merck KGaA we assign typical values for these key geometrical parameters in Table 1.1. We will refer back to these values later in Chapters 2 to 4.

1.5 Mathematical models for nematics

There are many approaches used for mathematical modelling of nematic materials, ranging from atomistic and molecular models [25, 224, 230] to continuum models [49, 134, 200, 201, 212]. The first established mathematical model used to describe nematics was by Bose [18, 26] in 1907. The Bose model used a Maxwell–Boltzmann statistical description of nematic materials which is sometimes called "swarm theory" [26].

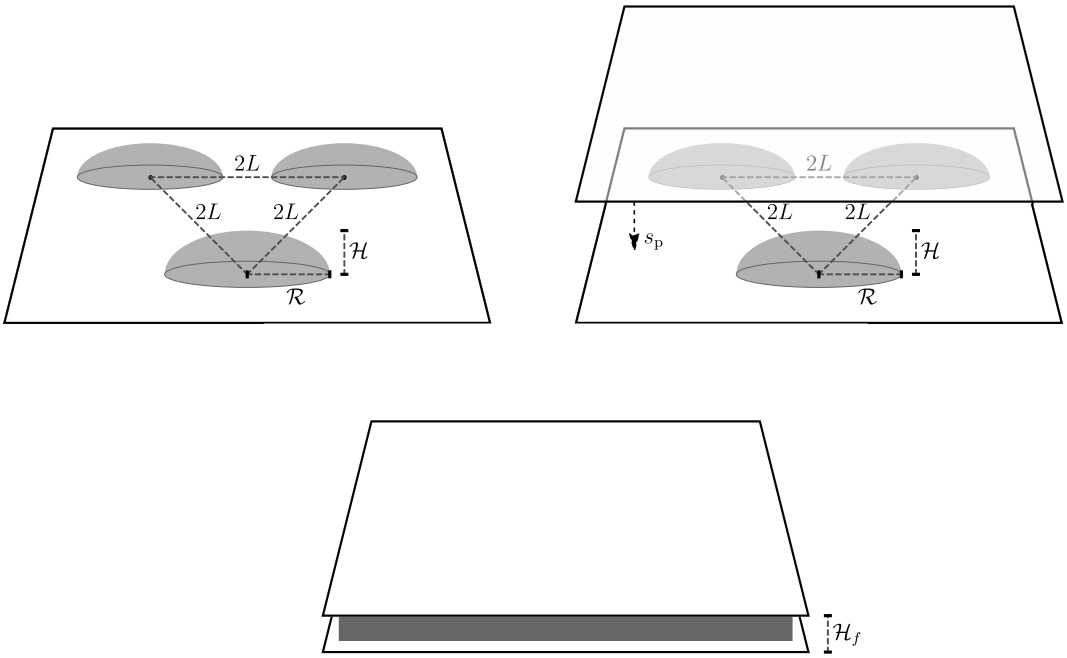

Figure 1.11: Schematic diagram indicating the geometrical parameter values in the ODF method. The initial radii of the nematic droplets $\mathcal{R}$, the initial height of the nematic droplets $\mathcal{H}$, the final gap between the substrates $\mathcal{H}_\mathrm{f}$, the downward speed of the top substrate s_p, and half the separation distance of each droplet L are shown.

Symbol	Value
$\mathcal{R}$	10^{-4}–10^{-2} m
$\mathcal{H}$	10^{-6}–10^{-4} m
$\mathcal{H}_\mathrm{f}$	10^{-6} m
s_p	10^{-3} m s^{-1}
L	10^{-3}–10^{-2} m
V	10^{-14}–10^{-8} m^3

Table 1.1: Typical values for the geometrical parameters in the ODF method; the initial radii of the nematic droplets $\mathcal{R}$, the initial height of the nematic droplets $\mathcal{H}$, the final gap between the substrates $\mathcal{H}_\mathrm{f}$, the downward speed of the top substrate s_p, and half the separation distance of each droplet L.

Swarm theory remained the leading theory for nematics up until the development of a static continuum theory by Oseen [160, 161] in 1925 and Zocher [235] in 1927. At the time, it was well known that the constituent molecules of nematics tend to align so that the long axis of the molecules share a common local preferred direction that is referred to as the anisotropic axis [201]. The theories developed by Oseen and Zocher used a unit vector, called the *director*, to describe the average local preferred direction of the constituent nematic molecules. The director formulation allows for a phenomenological theory which can account for anisotropic elasticity, body forces and surface effects. This static continuum theory developed by Oseen and Zocher is still widely used for nematics almost a hundred years later [201].

The static continuum description of nematics was eventually developed further by Frank [75] in 1958 and the resultant theory, now called Oseen–Frank theory, has been applied to many problems involving nematics [26, 201]. One of the many successes of the Oseen–Frank theory was its capability to explain the Freederickz transition, which was first observed by Freedericksz and Zolina [76] in 1933. The Freederickz transition is an effect observed when a magnetic field is imposed on a sample of nematic between two bounding substrates, which produces a magnetisation in the sample capable of changing the orientation (or director) of the nematic. At low magnetic field strengths, there is no observed change in the orientation of the nematic sample and the nematic aligns itself in accordance with the alignment of the bounding substrates. The orientation of the nematic remains unchanged as the magnetic field strength is increased until a critical magnetic field strength (called a Freederickz threshold) is reached, and the nematic director then attempts to align with the magnetic field. We note that in 1933, Zocher [236] successfully used his theory to explain the Freedericksz transition, however, without the detailed model provided by Frank in 1958 his results were only in qualitative agreement [26]. The model used by Zocher was identi-

Figure 1.12: Jerald Ericksen (right) and Frank Leslie (left) photographed in Glasgow, sometime in the mid-1970s [8]. Figure taken from [8] with Copyright permission from The American Association for the Advancement of Science and Copyright Clearance Center.

cal to a useful approximation of the Oseen–Frank model called the one-constant approximation which we will discuss in Section 1.7.1.

After the success of the static Oseen–Frank continuum theory, there was much effort to develop a dynamic continuum theory of nematics which would describe their viscoelastic properties. In 1961, Ericksen [67] formulated the balance laws for the conservation of linear and angular momentum for nematics. In 1966, Leslie [127, 128] formulated constitutive equations for these balance laws and the resultant dynamic theory was named Ericksen–Leslie theory. A photograph of Jerald Ericksen and Frank Leslie together is shown in Figure 1.12. Ericksen–Leslie theory uses the conservation of linear and angular momentum to describe coupling of the director, the nematic fluid velocity and the nematic fluid pressure [201]. Early validation of the Ericksen–Leslie equations was carried out by Atkin [7] in 1970, who considered nematic flow between coaxial cylinders. The scaling laws obtained by Atkin matched experimental observations of nematic flow between coaxial cylinders made by Fisher and Frederickson [74] in 1969. The Ericksen–Leslie theory has since been applied to numerous problems involving flow, electric

fields, magnetic fields, and free surfaces [201]. After describing the mathematical detail of Ericksen–Leslie theory in Section 1.8, we shall discuss relevant literature using Ericksen–Leslie theory for this thesis in Section 1.9.

One particular shortcoming of the Oseen–Frank static theory and the Ericksen–Leslie dynamic theory, is their difficulty describing so-called defects or disclinations that occur in samples of nematics. A continuum model accounting for these defects was established by Ericksen [69] in 1991. The most general static continuum theory for nematics, which describes both the director and defects, is called Q-tensor theory or Landau–de Gennes theory [49]. Q-tensor theory considers the coupled behaviour of the director and a new variable called the scalar order parameter, which describes the tendency for the nematic molecules to align with the director. A detailed review of the development of this continuum model can be found in [212] and a mathematical review of the detail in [152]. An often used dynamic version of Q-tensor theory is called Berris–Edwards theory [13].

For more details on the history and development of mathematical models of nematics, see the review by Carlsson and Leslie [26]. For the systems we shall consider in this thesis, for which variations occur on the micron length scale and the millisecond time scale, it is appropriate to use the director continuum model, namely the Oseen–Frank static model and the Ericksen–Leslie dynamic model. We will now overview the key concepts of both of these models which will be used in Chapter 2 onwards.

1.6 The director and scalar order parameter

Nematics align so that the long axis of each constituent molecule within a local region shares a common preferred direction, referred to as the anisotropic axis [201]. This common preferred direction is named the *director*, and is denoted by a unit

vector $\boldsymbol{n} = \boldsymbol{n}(x, y, z, t)$, where the director may be a function of space (x, y, and z) and time (t). For achiral nematics it is common to assume that $\boldsymbol{n}$ and $-\boldsymbol{n}$ are indistinguishable, i.e. the group of constituent molecules are symmetrical along their anisotropic axis. In this thesis we shall only consider a so-called uniaxial description of nematics materials, where a single director, which is associated with the common local preferred direction of the long axis of constituent molecules, is used. A more general theory, or a so-called biaxial description of nematics, takes into account a second director (usually denoted by $\boldsymbol{m}$) associated with the common local preferred direction of the short axis of constituent molecules, for more details see Leslie et al. [131].

For simplicity, in this thesis we will often adopt the use of index notation for vector variables so that the director components and the position vector components are denoted by n_i and x_i, respectively, where the index $i = 1$ corresponds to components in the x-direction, $i = 2$ corresponds to components in the y-direction, and $i = 3$ corresponds to components in the z-direction. As is standard in index notation, repeated indices will imply summation from 1 to 3 over that index, so that, for example, $J_{ii} = J_{11} + J_{22} + J_{33}$, and differentiation with respect to x, y or z is represented by the shorthand $G_{,i} = \partial G/\partial x_i$ with $i = 1$, $i = 2$ or $i = 3$.

As the director is a unit vector, its components must satisfy the constraint

$$n_i\, n_i = 1. \tag{1.1}$$

The director components are often written in terms of two angles called the tilt

director angle $\theta = \theta(x, y, z, t)$ and the twist director angle $\phi = \phi(x, y, z, t)$ so that

$$n_1 = \cos\theta \cos\phi, \tag{1.2}$$

$$n_2 = \cos\theta \sin\phi, \tag{1.3}$$

$$n_3 = \sin\theta. \tag{1.4}$$

The degree to which nematic molecules in a region Ω of nematic align with the director can be measured by the so-called order parameter $S = S(x, y, z, t)$. The order parameter is defined by a statistical average, namely

$$S = \frac{1}{2} < 3\cos^2\theta_m - 1 > = \frac{1}{2}\int \left(3\cos^2\theta_m - 1\right) f(\theta_m)\, \mathrm{d}\Omega, \tag{1.5}$$

where θ_m is the molecular angle measured between the long axis of each constituent molecule and the director and $f(\theta_m)$ is the angular probability density function for the molecules in Ω [49, 152]. If the orientation of each of the constituent molecules is completely random, as in the isotropic phase, then the order parameter is zero. If the orientation of each of the constituent molecules is identical to the director, then the order parameter is unity. An order parameter of unity corresponds to the degree of order observed in a crystalline solid. In the nematic phase the order parameter is typical between zero and unity, however, it is possible that the scalar order parameter can be negative for certain orientations [49, 152].

Within samples of nematic materials so-called defects or disclinations [75] can occur that are associated with an order parameter of $S = 0$ (for the uniaxial nematics considered in this thesis). At these defects, a disordering transition occurs and a director description of the nematic is not valid. Defects are classified by the behaviour of the director field surrounding the defect. In particular, the defect is named by the number of clockwise rotations of the director field com-

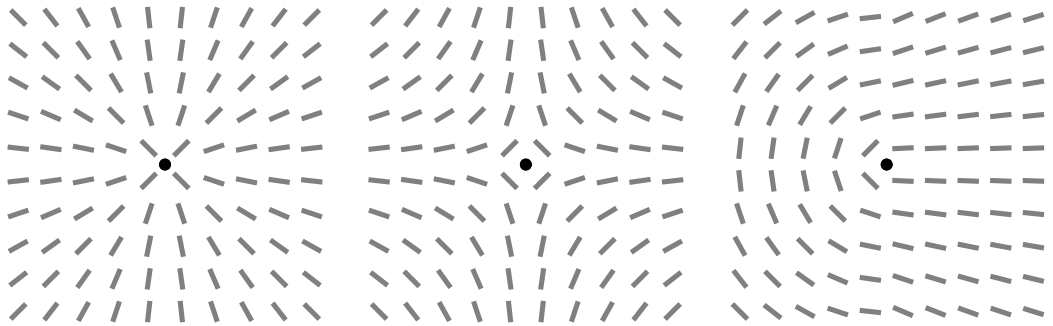

(a) +1-defect (b) −1-defect (c)+1/2-defect

Figure 1.13: The director field surrounding a (a) +1-defect, a (b) −1-defect, and a (c) +1-defect. The defect location is shown by the black solid circle and the director field is shown by grey rods.

pleted in a clockwise closed circuit around the defect. A clockwise circuit around a defect with $2\pi s$ rotations of the director field is named an $+s$-defect [49], where $2s$ is an integer. For example, the director field around a +1-defect completes a full clockwise rotation, the director field around a −1-defect completes a full anti-clockwise rotation, and the director field around a +1/2-defect completes a half clockwise rotation, as shown in Figure 1.13.

Henceforth, unless stated otherwise, we will not consider variations in the scalar order parameter and we shall pursue a uniaxial director description of nematic materials. For an introduction to the static Q-tensor theory, which also considers the order parameter, the reader is referred to Mottram and Newton [152]. For further mathematical descriptions of liquid crystals with non-rod-like constituent molecules, including bent-core or plank-like constituent molecules, see Sonnet and Virga [198].

1.7 The nematic free energy

Consider a region Ω of nematic enclosed by a surface Γ. The free energy E of the enclosed region of nematic can be defined by a combination of energy contributions, namely

$$E = \int \left(\omega_{\text{bulk}} + \omega_{\text{external}}\right) \, \mathrm{d}\Omega + \int \omega_{\text{surface}} \, \mathrm{d}\Gamma, \tag{1.6}$$

where ω_{bulk} is the bulk elastic energy density associated with elastic distortion of the nematic, ω_{external} is the energy density associated with any externally imposed body forces, and ω_{surface} is the interface energy density between the nematic and the enclosing surface. We will now discuss the forms taken for each of these energy contributions in this thesis.

1.7.1 The Oseen–Frank bulk elastic energy density

Following the approach used by Frank in 1958 [75], the bulk elastic energy density associated with elastic distortions of the nematic is assumed to depend on the director $\boldsymbol{n}$ and gradients of the director $\boldsymbol{\nabla n}$, and hence is of the form

$$\omega_{\text{bulk}} = \omega_{\text{bulk}} \left(\boldsymbol{n}, \boldsymbol{\nabla n}\right). \tag{1.7}$$

Using an equilibrium zero energy state $\boldsymbol{n} = \boldsymbol{n}_0 = (0, 0, 1)$, the bulk elastic energy density ω_{bulk} can be expanded as a quadratic function of six fundamental distortions a_i about the zero energy state, which yields

$$\omega_{\text{bulk}} = k_i a_i + \frac{1}{2} k_{ij} a_i a_j \quad \text{for} \quad i, j = 1, ..., 6, \tag{1.8}$$

where $a_1 = \partial n_1/\partial x$ and $a_6 = \partial n_2/\partial y$ are splay distortions, the $a_2 = \partial n_1/\partial y$ and $a_4 = \partial n_2/\partial x$ are twist distortions, $a_3 = \partial n_1/\partial z$ and $a_5 = \partial n_2/\partial z$ are bend distortions, and k_i and k_{ij} are the curvature elastic constants [201]. By considering frame indifference of (1.8), under both rotations and reflections, and the invariance of the nematic phase, namely that $\omega_{\text{bulk}}(\boldsymbol{n}, \boldsymbol{\nabla n}) = \omega_{\text{bulk}}(-\boldsymbol{n}, -\boldsymbol{\nabla n})$, the majority of the curvature elastic constants can be shown to be zero [201]. The non-zero curvature elastic constants are k_{11}, k_{22}, k_{33} and k_{24}, which are known as the Frank elastic constants, and are typically denoted

$$K_1 = k_{11}, \quad K_2 = k_{22}, \quad K_3 = k_{33}, \quad \text{and} \quad K_4 = k_{24}. \tag{1.9}$$

Using (1.8), the Frank elastic constants (1.9), and the six fundamental distortions a_i, the bulk elastic energy density associated with elastic distortions, called the Oseen–Frank elastic energy density, is given by

$$\begin{aligned}\omega_{\text{bulk}} = \frac{1}{2}(K_1 - K_2 - K_4)n_{i,i}n_{j,j} + \frac{1}{2}K_2 n_{i,j}n_{i,j} + \frac{1}{2}K_4 n_{i,j}n_{j,i} \\ + \frac{1}{2}(K_3 - K_2)n_j n_{i,j}n_k n_{i,k},\end{aligned} \tag{1.10}$$

or, alternatively, in vector form

$$\begin{aligned}\omega_{\text{bulk}} = \frac{1}{2}K_1(\nabla \cdot \boldsymbol{n})^2 + \frac{1}{2}K_2(\boldsymbol{n} \cdot \nabla \times \boldsymbol{n})^2 + \frac{1}{2}K_3(\boldsymbol{n} \times \nabla \times \boldsymbol{n})^2 \\ + \frac{1}{2}(K_2 + K_4)\nabla \cdot ((\boldsymbol{n} \cdot \nabla)\boldsymbol{n} - (\nabla \cdot \boldsymbol{n})),\end{aligned} \tag{1.11}$$

where $\nabla = (\partial/\partial x, \partial/\partial y, \partial/\partial z)$ [201].

Each of the Frank elastic constants is named after the elastic deformation they are associated with. In particular, K_1 is the splay elastic constant, K_2 is the twist elastic constant and K_3 is the bend elastic constant [49, 201], as shown in Figure 1.14. The combination $K_2 + K_4$ in (1.11), called the saddle-splay constant

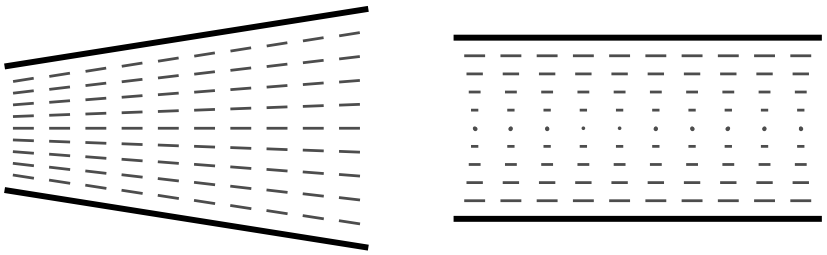

(a) K_1 splay elastic distortions (b) K_2 twist elastic distortions

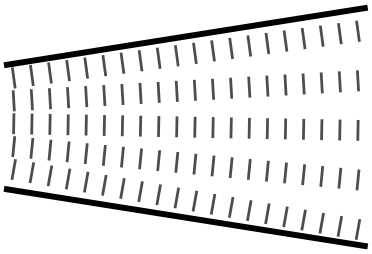

(c) K_3 bend elastic distortions

Figure 1.14: Schematic diagram of (a) K_1 splay elastic distortions, (b) K_2 twist elastic distortions, and (c) K_3 bend elastic distortions.

is often omitted from the bulk elastic energy density as it can be transformed into a surface term using the divergence theorem [201]. The Frank elastic constants must obey the *Ericksen inequalities* [68], given by

$$K_1 \geq 0, \quad K_2 \geq 0, \quad K_2 \geq 0, \quad K_2 \geq |K_4|, \quad K_1 \geq \tfrac{1}{2}\,(K_2 + K_4) \geq 0. \qquad (1.12)$$

The Frank elastic constants for the nematic 4-Cyano-4'-pentylbiphenyl (5CB) at 26° C are $K_1 = 6.2 \times 10^{-12}\,\mathrm{N}$, $K_2 = 3.9 \times 10^{-12}\,\mathrm{N}$ and $K_3 = 8.2 \times 10^{-12}\,\mathrm{N}$ [63], i.e. typically around $10^{-11}\,\mathrm{N}$.

A common simplification, which we will make use of in Chapters 2, 3, and 6 is the so-called "one-constant approximation" for the Oseen–Frank bulk elastic energy density ω_{bulk}. To produce a mathematically tractable system of equations it is common to assume that the splay, twist and bend elastic constants are

equal, so that $K = K_1 = K_2 = K_3$ and that $K_4 = 0$. While this one-constant approximation is certainly a simplification of the material properties of a typical nematic, in practice the ratios of elastic constants are rarely greater than two and the behaviour is not expected to change qualitatively when this approximation is used [63]. Using the one-constant approximation the Oseen–Frank elastic energy density (1.10), is given by

$$\omega_{\text{bulk}} = \frac{K}{2} n_{i,j} n_{i,j}, \tag{1.13}$$

and (1.11) is given by

$$\omega_{\text{bulk}} = \frac{K}{2}\Big[(\nabla \cdot \boldsymbol{n})^2 + (\nabla \times \boldsymbol{n})^2 + \boldsymbol{\nabla} \cdot ((\boldsymbol{n} \cdot \nabla)\boldsymbol{n} - (\nabla \cdot \boldsymbol{n})\boldsymbol{n})\Big]. \tag{1.14}$$

1.7.2 Externally imposed body forces

With the exception of a brief mention of gravitational force in Chapters 5 and 6, we will not consider any externally imposed body forces such as magnetic forces or electric forces. So henceforth, unless stated otherwise, we set $\omega_{\text{external}} \equiv 0$. We briefly mention the relevant energy density for an electric field as the application of electric fields on nematic layers is the basis of how LCDs operate. For an electric field with components E_k, the energy density associated with any external body forces is given by $\omega_{\text{external}} = \omega_{\text{elec}}$ [201], where

$$\omega_{\text{elec}} = -\frac{1}{2}\epsilon_0 \epsilon_{\text{a}} n_i n_j E_i E_j. \tag{1.15}$$

In (1.15), ϵ_0 is the permittivity of free space and ϵ_{a} is the so-called dielectric anisotropy of the nematic. In a positive dielectric nematic $\epsilon_{\text{a}} > 0$, like those used in the TN-LCD, the polarisation of the nematic constituent molecules cause it to align parallel to imposed electric fields. In a negative dielectric nematic

$\epsilon_a < 0$, like those used in the DS-LCD, the polarisation of the nematic constituent molecules cause it to align perpendicular to imposed electric fields. For a detailed discussion of body forces and the inclusion static and dynamic continuum model for nematics see Stewart [201].

In situations with no externally imposed body forces, the bulk equilibrium equations, which are obtained from the minimisation of (1.6), lead to the well known Euler–Lagrange equations for the Oseen–Frank bulk elastic energy density ω_{bulk}, which are given by

$$\lambda n_i = \frac{\partial \omega_{\text{bulk}}}{\partial n_i} - \frac{\partial}{\partial x_j}\left(\frac{\partial \omega_{\text{bulk}}}{\partial n_{i,j}}\right), \tag{1.16}$$

where λ is a Lagrange multiplier which arises from the constraint (1.1).

1.7.3 The Rapini–Papoular interface energy density

Throughout this thesis we will be particularly interested in situations which involve an interface between the nematic and a solid substrate, as occurs in the ODF method. Additionally, in Chapters 5 to 7, we will also be particularly interested in situations which involve an interface between the nematic and a surrounding atmosphere of passive gas, namely, situations involving a nematic free surface. In both of these situations we will use the Rapini–Papoular interface energy density [151,201], which was first proposed by Rapini and Papoular in 1969 [172], and is commonly called *weak anchoring*. The Rapini–Papoular interface energy density [172] determines the energetic preference of the nematic molecular alignment forces on the interfaces to align the director.

In the present work, we will consider two types of weak anchoring, *homeotropic weak anchoring*, where there is an energetic preference for the director to align normally to the interface, and *planar weak anchoring*, where there is an energetic

preference for the director to align tangentially to the interface. The strength of the energetic preference for a particular alignment of the director on an interface is measured by a parameter called the *anchoring strength*. In the limit in which the anchoring strength becomes infinitely large, the energetic preference for homeotropic or planar alignment fixes the director on the interface to align exactly normal or tangential, respectively. This situation is often called strong anchoring or, perhaps more accurately, *infinite anchoring*. When the anchoring strength is zero there is no energetic preference for homeotropic or planar alignment on the interface, and the director on the interface is determined by bulk forces. This situation is called *zero anchoring*.

As planar weak anchoring is defined as an energetic preference for the director to align tangentially to the interface, the preferred direction in the plane of the interface must also be discussed. Situations for which there is no energetic preference for a preferred direction in the plane of the interface are called *planar degenerate weak anchoring* and situations for which there is an energetic preference for a particular preferred direction in the plane of the interface are called *rubbed planar weak anchoring* (where the name *rubbed* originates from the experimental method used to create planar weak anchoring in a particular direction).

Of particular importance for systems with two interfaces are situations that involve opposing anchoring preferences on the two interfaces, e.g. when homeotropic director alignment is preferred on one interface and planar director alignment is preferred on the other interface or vice versa. This situation is called *antagonistic anchoring*, while *non-antagonistic anchoring* refers to the opposite situation in which the same director alignment is preferred on both interfaces. Even situations with non-antagonistic anchoring can involve competing anchoring forces, since the preferred director alignments are measured *relative* to the interfaces which are, in general, not parallel.

Specifically, as mentioned above, we use the Rapini–Papoular interface energy density [172], which is given by

$$\omega_{\text{surface}} = \sigma + \frac{C}{4}\left(1 - 2(\boldsymbol{\nu}\cdot\boldsymbol{n})^2\right), \tag{1.17}$$

where $\boldsymbol{\nu}$, C and σ are the outward unit normal, anchoring strength and isotropic interfacial tension of the interface, respectively. If $C > 0$ then a normal director, i.e. homeotropic alignment, is preferred on the interface, whereas if $C < 0$ then a tangential director, i.e. planar alignment, is preferred. The anchoring strength has units of $\mathrm{N\,m^{-1}}$ (i.e. $\mathrm{J\,m^{-2}}$), and its value depends on both the nematic and the material the nematic is in contact with (i.e. the solid substrate or the passive gas) [226]. Experimental techniques for the measurement of anchoring strengths for interfaces between a solid and a nematic are well established and hence representative values are readily available [157, 226, 227]; however, measurements for interfaces between a gas and a nematic are more difficult and hence representative values are less readily available [197]. Specifically, the anchoring strength of a planar or homeotropic nematic–substrate interface has been measured for a variety of nematic materials and substrate coatings in the range of $C = 10^{-6}$–$10^{-3}\,\mathrm{Nm^{-1}}$ [157, 197, 227], whereas, to the best of the author's knowledge, the only experimental measurements of the anchoring strength of the gas–nematic interface are $C > 10^{-5}\,\mathrm{Nm^{-1}}$ for the interface between air and the nematic mixture ZLI 2860 [196] and $C > 4\times10^{-4}\,\mathrm{Nm^{-1}}$ for the interface between air and the nematic p-methoxy-benzylidene-p-n-butyl aniline (MBBA) [30]. The anchoring strength of the nematic–substrate interface and the gas–nematic interface can therefore be of comparable magnitude.

Using ω_{bulk} given by (1.11), $\omega_{\text{external}} = 0$ and ω_{surface} given by (1.17), the

minimisation of (1.6) leads to the standard weak anchoring condition

$$\frac{\partial \omega_{\text{bulk}}}{\partial n_{i,j}} + \frac{\partial \omega_{\text{surface}}}{\partial n_i} = \lambda_{\text{s}} n_i \quad \text{on} \quad \Gamma, \tag{1.18}$$

where λ_{s} is a Lagrange multiplier which again arises from the constraint (1.1). Zero anchoring is implemented by setting $C = 0$ in (1.17) and (1.18) and infinite anchoring is implemented by replacing (1.18) with a Dirichlet condition on the director. While the anchoring energy ω_{surface} describes the preference of the director for the preferred orientation, it does not capture the dynamical processes which take place on an interface. In Section 1.8.2 we will discuss a dynamic anchoring condition called a dissipative weak anchoring condition which incorporates surface viscosity in to the weak anchoring condition (1.18).

1.7.4 The Jenkins–Barratt–Barbero–Barberi critical thickness

Of particular importance to parts of the work described in this thesis is a pioneering but often overlooked theoretical contribution published in 1974 by Jenkins and Barratt [102], who investigated a static layer of nematic of uniform thickness bounded between two parallel substrates with antagonistic anchoring. They showed that when the bulk elastic energy density for the nematic layer takes the Frank–Oseen form, there is a critical thickness of the layer below which a uniform director field (oriented according to the preferred alignment on the substrate with the strongest anchoring) is energetically preferred, and above which a distorted director field is energetically preferred. Subsequently, in 1983, Barbero and Barberi [9] (see also Hochbaum and Labes [98]) independently obtained the corresponding result for a situation with weak antagonistic anchoring on both substrates.

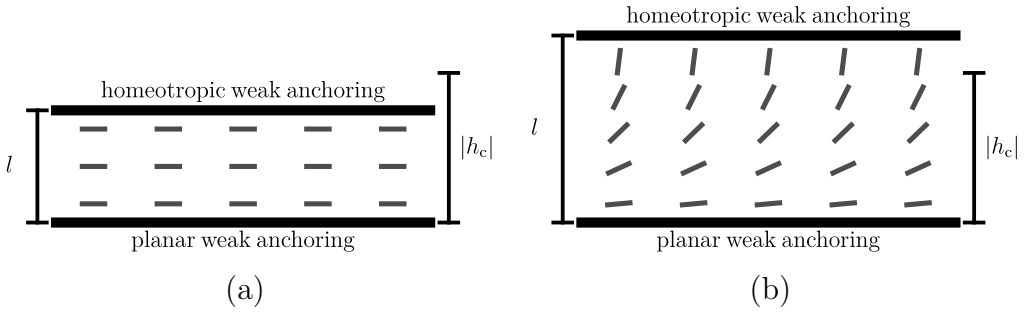

Figure 1.15: Schematic diagram a static layer of nematic of uniform thickness l between two parallel substrates with antagonistic anchoring when (a) $|h_c| \leq l$ and when (b) $|h_c| > l$.

The critical thickness of the layer is often referred to as the Barbero–Barberi critical thickness [9], but, for the reasons outlined above, we shall refer to it as the Jenkins–Barratt–Barbero–Barberi critical thickness [9, 102]. The Jenkins–Barratt–Barbero–Barberi critical thickness [9, 102], is denoted h_c and defined by

$$h_c = K\left(\frac{1}{C_H} + \frac{1}{C_P}\right), \tag{1.19}$$

where C_H and C_P are the anchoring strengths of the interface with homeotropic anchoring and planar anchoring, respectively. Specifically, when the film thickness, which we denote l, is lesser than the critical thickness $|h_c|$ a uniform director field is energetically preferred and when l is greater than $|h_c|$ a distorted director field is energetically preferred, as shown in Figure 1.15.

The critical thickness is of particular importance for the static ridge of nematic considered in Chapters 5 to 7 because the height of the ridge is, by definition, zero at the contact lines, but may exceed the critical thickness elsewhere. Understanding the behaviour of the director in any regions of the ridge in which the height of the ridge is greater than this critical thickness and hence a distorted director field is energetically favourable, and regions of the ridge in which the height of the ridge is less than the critical thickness and a uniform director field

is energetically favourable, is a key aspect of understanding the behaviour of the ridge.

1.8 The Ericksen–Leslie dynamic description of nematics

The dynamic theory used in this thesis is the aforementioned Ericksen–Leslie theory. For a nematic with fluid velocity $\boldsymbol{u} = \boldsymbol{u}(x, y, z, t)$ with components u_i, pressure $p = p(x, y, z, t)$, and director $\boldsymbol{n} = \boldsymbol{n}(x, y, z, t)$ with components n_i, the Ericksen–Leslie equations [66, 127, 201] with no externally imposed body forces, are the conservation of linear momentum and conservation of angular momentum, given by

$$\rho \dot{u}_i = -\frac{\partial}{\partial x_i}(p + \omega_{\text{bulk}}) + \tilde{g}_j n_{i,j} + \frac{\partial \tilde{t}_{ij}}{\partial x_j}, \tag{1.20}$$

$$\lambda n_i = \tilde{g}_i + \frac{\partial \omega_{\text{bulk}}}{\partial n_i} - \frac{\partial}{\partial x_j}\left(\frac{\partial \omega_{\text{bulk}}}{\partial n_{i,j}}\right), \tag{1.21}$$

respectively, with the unit director and incompressibility constraints given by,

$$n_i n_i = 1, \quad \text{and} \quad u_{i,i} = 0. \tag{1.22}$$

The terms appearing in (1.20) and (1.21) are; the density of the nematic ρ, the components of the nematic viscous anisotropic stress tensor $\tilde{t}_{ij}$, and the components of the vector $\tilde{g}_i$ which are related to the nematic viscous anisotropic stress tensor. The material time derivative of a quantity is indicated by the over dot. In particular, the material time derivative of the fluid velocity components $\dot{u}_i$ which

appears in (1.20), is defined by

$$\dot{u}_i = \frac{\partial u_i}{\partial t} + u_j u_{i,j}. \tag{1.23}$$

Motivated by experimental observations of nematic flows, Leslie [127] assumed that the nematic viscous anisotropic stress tensor components $\tilde{t}_{ij}$ are a linear function of both the rate of strain tensor e_{ij} [201], which is defined by

$$e_{ij} = \frac{1}{2}\left(u_{i,j} + u_{j,i}\right), \tag{1.24}$$

and the co-rotational time flux of the director N_i, which is defined by

$$N_i = \dot{n}_i - \frac{1}{2} n_j \left(u_{i,j} - u_{j,i}\right). \tag{1.25}$$

The components of nematic viscous anisotropic stress tensor t_{ij} can therefore be expressed in the form

$$\tilde{t}_{ij} = \mathcal{A}_{ij} + \mathcal{B}_{ijk} N_k + \mathcal{C}_{ijkp} e_{kp}, \tag{1.26}$$

where $\mathcal{A}_{ij}$, $\mathcal{B}_{ijk}$, and $\mathcal{C}_{ijkp}$ are functions of the director components n_i [201]. Using the symmetry of the nematic, incompressibility and symmetry of the rate of strain tensor ($e_{ii} = 0$ and $e_{ij} = e_{ji}$, respectively), and the unit director constraint which implies $n_i N_i = 0$, the components of nematic anisotropic stress tensor $\tilde{t}_{ij}$ reduce to

$$\begin{aligned} \tilde{t}_{ij} = {} & \alpha_1 n_k e_{kp} n_p n_i n_j + \alpha_2 N_i n_j + \alpha_3 n_i N_j \\ & + \alpha_4 e_{ij} + \alpha_5 n_i e_{ik} n_k + \alpha_6 n_i e_{jk} n_k, \end{aligned} \tag{1.27}$$

where the α_l with $l = 1, ..., 6$ are the Leslie viscosities.

The components of the vector $\tilde{g}_i$, appearing in (1.20) and (1.21) are defined by

$$\tilde{g}_i = -\gamma_1 N_i - \gamma_2 e_{ip} n_p, \tag{1.28}$$

where γ_1 is the rotational viscosity and γ_2 is the torsional viscosity [201]. The rotational and torsional viscosities can be related to the Leslie viscosities α_l by

$$\gamma_1 = \alpha_3 - \alpha_2, \tag{1.29}$$

$$\gamma_2 = \alpha_6 - \alpha_5 = \alpha_2 + \alpha_3, \tag{1.30}$$

where the two equivalent definitions for γ_2 are obtained from the *Parodi relation* $\alpha_6 - \alpha_5 = \alpha_2 + \alpha_3$ [40, 164].

We note that the Ericksen–Leslie conservation of linear momentum equation (1.20) reduces to the familiar Navier–Stokes conservation of linear momentum equation for an isotropic liquid upon the substitution of the isotropic viscous stress tensor $\tilde{t}_{ij} = 2\mu e_{ij}$, where μ is the isotropic viscosity [1], $\alpha_2 = \alpha_3 = 0$ (and hence $\tilde{g}_i = 0$), and $K_1 = K_2 = K_3 = K_4 = 0$ (and hence $\omega_{\text{bulk}} = 0$), which is given by

$$\rho \dot{u}_i = -p_{,i} + 2\mu e_{ij,j}. \tag{1.31}$$

From a direct comparison of (1.31) and, (1.20) and (1.27), the equivalent of the isotropic viscosity μ for nematics is $\alpha_4/2$.

1.8.1 Nematic bulk viscosities

The Leslie viscosities α_l are rarely measured directly in experiments, other than $\alpha_4/2$ [201]. However, there are certain linear combinations of the Leslie viscosities

that have intuitive physical interpretations that allow them to measured directly in experiments. These linear combinations of Leslie viscosities were first proposed by Miesowicz in 1946 [148, 149], before the aforementioned Leslie viscosities had been defined. The Miesowicz viscosities are denoted by η_1, η_2, η_3, and η_{12} and are defined in terms of Leslie viscosities as

$$\eta_1 = \frac{1}{2}\left(\alpha_2 + 2\alpha_3 + \alpha_4 + \alpha_5\right), \tag{1.32}$$

$$\eta_2 = \frac{1}{2}\left(-\alpha_2 + \alpha_4 + \alpha_5\right), \tag{1.33}$$

$$\eta_3 = \frac{1}{2}\alpha_4, \tag{1.34}$$

$$\eta_{12} = \alpha_1. \tag{1.35}$$

We note that γ_1, η_1, η_2, and η_3 are all positive for nematic materials, and that typically $\eta_2 > \eta_3 > \eta_1 \geq 0$ [63]. The torsional viscosity γ_2 and Miesowicz viscosity η_{12} can be negative or positive. In fact, the Miesowicz viscosity η_{12} is typically smaller in magnitude than the other Miesowicz viscosities and some authors use the assumption that $\eta_{12} \simeq 0$ to simplify governing equations, see for example Rickert et al. [188]. The Miesowicz viscosities for the nematic 5CB at 26° are $\eta_1 = 0.0204\,\mathrm{Pa\,s}$, $\eta_2 = 0.1052\,\mathrm{Pa\,s}$, $\eta_3 = 0.0326\,\mathrm{Pa\,s}$, and $\eta_{12} = -0.0060\,\mathrm{Pa\,s}$, and the rotational and torsional viscosity are $\gamma_1 = 0.0777\,\mathrm{Pa\,s}$ and $\gamma_2 = -0.0848\,\mathrm{Pa\,s}$, respectively [63], i.e. the viscosities are typically around 10^{-2}–$10^{-1}\,\mathrm{Pa\,s}$.

The Miesowicz viscosities can be physically interpreted by considering simple shear flow of nematic with velocity components $u_1 = kz$ and $u_2 = u_3 = 0$ (or $\boldsymbol{u} = (kz, 0, 0)$), where k is some positive constant, so that the only non-zero velocity gradient component is $u_{1,3} = \partial u_1/\partial z = k$ which is in the $\hat{\boldsymbol{z}}$ direction. When $\boldsymbol{n}$ is aligned parallel to $\boldsymbol{u}$ the relevant viscosity is η_1, when $\boldsymbol{n}$ is aligned parallel to the velocity gradient ($\hat{\boldsymbol{z}}$ direction) the relevant viscosity is η_2, and when $\boldsymbol{n}$ is orthogonal to $\boldsymbol{u}$ and the velocity gradient the relevant viscosity is

η_3 [201], as shown in Figure 1.16. We note that the Miesowicz viscosity η_{12} does not correspond to an intuitive physical measurement in the same way as η_1, η_2 and η_3 [201], however, it is important when $\boldsymbol{n}$ is not parallel to $\boldsymbol{u}$ or the velocity gradient. The viscosity η_3 is identical to the isotropic viscosity μ, namely $\eta_3 = \mu = \alpha_4/2$ [201].

The rotational viscosity γ_1 is also shown in Figure 1.16(d). This viscosity is associated with rotation of the director and is responsible for many important effects observed in nematics. For example, γ_1 is linked to the relaxation time in display switching problems and measures the strength of backflow, a process by which rotations of the director by externally imposed body forces produce a flow in the direction of the director rotation [201]. The torsional viscosity γ_2 describes coupling between shear gradients and the rotation of the director. For the details of experimentally measuring these five independent nematic viscosities see Gähwiller [79].

1.8.2 Nematic surface viscosity

In Chapter 4, we will investigate transient flow-driven distortion of the nematic molecules on the substrates of a channel which requires the use of a so-called dissipative weak anchoring condition. As previously mentioned, a weak anchoring condition describes the energetic preference for certain alignments of the director at a surface, however, it does not capture the dynamical processes which take place close to the surface. To include these dynamic effects we include surface dissipation which models the dissipation of energy on the surfaces. We assume that the only surface dissipation of energy occurs due to the rotation of the director because we assume molecules on the surface can not translate. The surface dissipation is therefore proportional to $\gamma_{\mathrm{S}} \left(\partial \boldsymbol{n}/\partial t\right)^2$, where $\gamma_{\mathrm{S}} \left(\geq 0\right)$ is the surface rotational viscosity. The surface rotational viscosity γ_{S} has units

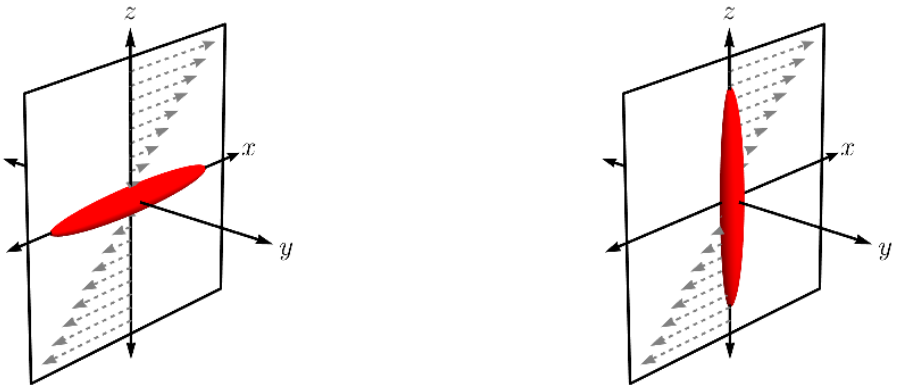

(a) η_1 (b) η_2

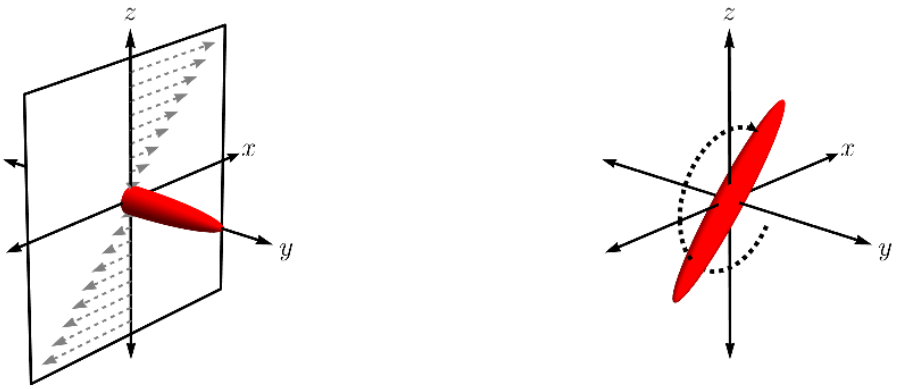

(c) η_3 γ_1 (d)

Figure 1.16: Schematic diagram of the measurement of Miesowicz viscosities (a) η_1, (b) η_2 and (c) η_3, and the (d) rotational viscosity γ_1.

of Pa m s, and its values are typically found experimentally to lie in the range $\gamma_S = 10^{-8}$–10^{-6} Pa m s [51, 162, 163]. We use the term *dissipative weak anchoring* for the combined effects of weak anchoring discussed in Section 1.7.3 and surface dissipation.

A dissipative weak anchoring condition was first proposed by Pikin et al. [166], and has since been used to study problems related to display switching [45, 83, 109, 180, 199], relaxation of director profiles [10, 50–52], and backflow [64, 145]. Surprisingly little research has thus far been conducted on the influence of dissipative weak anchoring on nematic flows. Two contributions of note are Kléman and Pikin [116], who formulated a dissipative weak anchoring condition in the context of Couette flow but only considered steady solutions, and Biscari [15], who investigated surface viscosity in the context of flow in the vicinity of a curved surface. However, to the best of the author's knowledge, no research has thus far been carried out on the influence of dissipative weak anchoring on the problem treated in Chapter 4, namely channel flow. There have been many previous works on nematic channel flow without surface viscosity which we will discuss in the next Section.

1.9 Previous work on nematic flows

The Ericksen–Leslie equations have been used for a variety of fluid dynamical problems including biological and industrial flows. An adapted version of the Ericksen–Leslie equations has been used for applications in living biological fluids [214, 217, 218], such as suspensions of bacteria [91], which are termed "active nematics". Industrial flows of nematics are relevant for many applications, including applications for particle transport [14, 27, 124], medical devices or processing flows [82, 124, 194], and because of their importance LCD manufactur-

ing. Some work of note which considers nematic flow in LCD manufacturing are Ericksen–Leslie models for capillary filling considered by Mi and Yang [147], and subsequently, by Dhar and Chakraborty [59] with the inclusion of an applied electric field, and blade coating flows of nematics considered by Quintans Carou et al. [168–171]. To the best of the author's knowledge, there has been no model of the ODF method using the Ericksen-Leslie theory, which will be the main focus of Chapters 2 to 4 of this thesis. In fact, as there is little published mathematical modelling of the ODF method at all we consider a simple model in Chapter 2, before considering the ODF method using the Ericksen-Leslie theory in Chapter 3 and in Chapter 4.

1.9.1 Flow-alignment in shear flow

Of particular interest in this thesis is the behaviour of a nematic in a shear flow, which was first considered by Leslie [127, 130]. In a simple shear flow, and when the director $\boldsymbol{n}$ is static and uniformly orientated, i.e. when θ = constant and ϕ = constant, substitution of a uniform shear flow of the form $\boldsymbol{u} = (kz, 0, 0)$ in the Ericksen–Leslie equations (1.20) and (1.21), leads to two possible solutions for the director angles [201]. A *log-rolling* solution, for which the director aligns perpendicular to the plane of shear, with the director angles given by

$$\theta = 0 \quad \text{and} \quad \phi = (2q+1)\frac{\pi}{2}, \tag{1.36}$$

and a *flow-alignment* solution, for which the director remains in the plane of shear, with the director angles given by

$$\theta = q\pi \pm \theta_{\mathrm{L}} \quad \text{and} \quad \phi = 0, \tag{1.37}$$

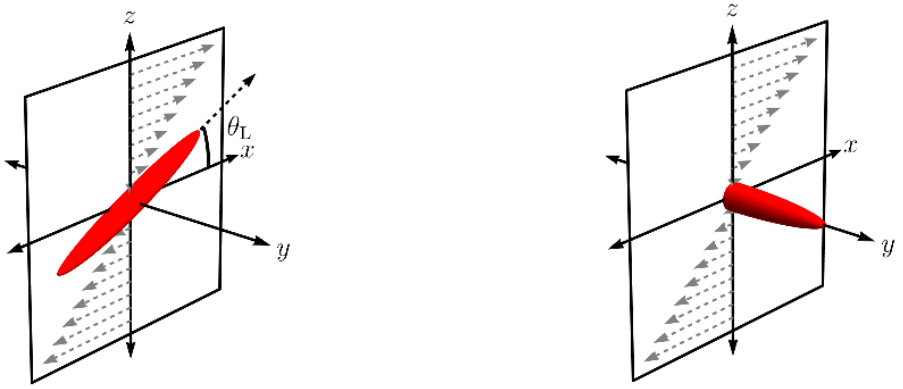

(a) (b)

Figure 1.17: Schematic diagram of (a) flow-alignment and (b) log-rolling solutions.

where q is an integer and θ_{L} ($0 \leq \theta_{\mathrm{L}} \leq \pi/2$) is the Leslie angle (sometimes called the flow-alignment angle) [201]. The Leslie angle can be defined in terms either the Leslie viscosities, or the rotational and torsional viscosities, by

$$\theta_{\mathrm{L}} = \tan^{-1}\sqrt{\frac{\alpha_3}{\alpha_2}} = \frac{1}{2}\cos^{-1}\sqrt{-\frac{\gamma_1}{\gamma_2}}. \tag{1.38}$$

The log-rolling solution and flow-alignment solutions are shown in Figure 1.17. The log-rolling and flow-alignment solutions have been observed by Piersanski and Guyon [165] and Gähwiller [78] for the nematic benzylidene-p-n-butyl aniline (MBBA), although only the flow-aligning solution remains stable for large shear rates (as k is increased) [165, 201].

For nematics with $\alpha_3/\alpha_2 \geq 0$ the flow-aligning solution is stable and hence these nematics are called "flow-aligning nematics". For nematics with $\alpha_3/\alpha_2 < 0$ the log-rolling solution is stable and hence these nematics are called "non-flow-aligning nematics". For example, for MBBA $\alpha_3/\alpha_2 \simeq 0.01$ [117, 201], and

hence, the flow-aligning solution is stable. Wahl and Fisher [216] experimentally measured the Leslie angle of MBBA to be $\theta_{\mathrm{L}} = 8^\circ \pm 0.5^\circ$, in agreement with the prediction obtained from (1.38) and the Leslie viscosities of MBBA $\alpha_2 = -0.1104$ and $\alpha_3 = -0.0011$ [78], namely $\theta_{\mathrm{L}} = 6^\circ$.

For nematic materials that are commonly used in industrial manufacturing of LCDs, typically $\sqrt{\alpha_3/\alpha_2} \geq 0$ and θ_{L} is small. For example, $\sqrt{\alpha_3/\alpha_2} \simeq 0.210$ and $\theta_{\mathrm{L}} \simeq 12^\circ$ for 5CB [201], $\sqrt{\alpha_3/\alpha_2} \simeq 0.143$ and $\theta_{\mathrm{L}} \simeq 8^\circ$ for 4-Cyano-4'-heptylbihenyl (7CB) [101], and $\sqrt{\alpha_3/\alpha_2} \simeq 0.001$ and $\theta_{\mathrm{L}} \simeq 0.06^\circ$ for 4-Cyano-4'-octyloxybiphenyl (8OCB) [31]. In fact, as most modern industrial manufacturing of LCDs use mixtures of nematics, for example, the mixture E7, which contains 51% 5CB, 25% 7CB, 16% 8OCB and 8% of other similar biphenyl compounds [211], and so typically $\alpha_3/\alpha_2 \geq 0$ and θ_{L} is small. We will therefore only consider flow aligning nematics in this thesis. We will also exploit the smallness of θ_{L} in Chapter 4 to pursue asymptotic solutions for the director angle.

The behaviour of flow-aligning nematics has been investigated for situations where the director is initially either in or out of the plane of shear flow, by Derfel [57] and Derfel and Radomska [58], respectively. For non-flow-aligning nematics, the Leslie angle does not exist and the director can exhibit complex unsteady behaviour known as tumbling where the director continually rotates [201,203,238]. Shear flows of non-flow-aligning nematics have been considered by Han and Rey [89] and Burghardt and Fuller [24].

In situations involving a flow-aligning nematic and a spatial variation in shear gradient, for example in classic situations in fluid dynamics such as Poiseuille flow or Jeffery–Hamel flow, there can be a change in the sign of the shear rate [1]. For a flow-aligning nematic, a stability analysis shows that in a region of positive shear rate ($\partial u/\partial z > 0$) or negative shear rate ($\partial u/\partial z < 0$) the director remains in the (x, z) plane and the director angle rotates towards the "positive" Leslie

angle $\theta = q\pi + \theta_{\mathrm{L}}$ or the "negative" Leslie angle $\theta = q\pi - \theta_{\mathrm{L}}$, respectively [165, 201, 238]. In Poiseuille flow of nematics, a reorientational boundary layer where by the director rotates between the positive and negative Leslie angle occurs in the central region where the shear rate changes sign [5,11,37,169,170,194,201]. Similar reorientational boundary layers have been obtained by Rey and Denn [185] for Jeffery–Hamel flow, by Rey [179] for flow between concentric disks, and by Krekhov et al. [118] and de Andrade Lima and Rey [46] for oscillatory flows.

In situations that include shear flow and solid boundaries, a director reorientational boundary layer can occur between the between the uniformly orientated bulk and the orientation dictated by the solid boundary [128, 154, 201]. The stability and multiplicity of solutions for Coeutte flow between solid boundaries has been considered extensively by Currie [39, 41–43] and McIntosh et al. [146], and more recently by Rickert et al. [188].

There has been much interest in channel flow of nematics. In particular, Quintans Carou et al. [168–170] considered steady flow of a nematic in a slowly-varying channel in the special case of infinite planar anchoring. Specifically, they used a combination of asymptotic and numerical methods to analyse the problem in the limit of small Leslie angle. More recently, Sengupta et al. [194] observed flow transitions in channel with homeotropic anchoring on the channel substrates. These flow transitions have been subsequently investigated theoretically with Ericksen–Leslie theory by Anderson et al. [5] and Crespo et al. [37] for weak homeotropic anchoring, and numerically using hybrid lattice Boltzmann simulations by Batista et al. [11] for weak homeotropic, planar and hybrid (i.e. homeotropic at one boundary and planar at the other boundary) anchoring.

Many other models have been used to describe the dynamic behaviour of nematic flows [186]. Statistical molecular models, such as Doi theory [62], have been used to investigate pressure-driven channel flow by Fend and Leal [72] and

Lattice-Boltzamn simulations have been used to investigate nematic flows by Denniston et al. [55,56]. A combination of Doi theory and Ericksen–Leslie theory has also been considered by Rey and Tsuji [187]. Confined flows of nematics have also been considered with models that include the nematic order parameter, including Berris–Edwards theory by Mondal et al. [150] and molecular theory by Hernández-Ortiz et al. [97].

1.10 Wetting and dewetting phenomena

Of particular interest in LCD manufacturing and in many emerging nematic technologies, such as adaptive lenses [3, 112], microelectronic components [82, 237], and diffraction gratings [17, 23], is understanding the so-called *wetting and dewetting phenomena* for nematics. Theoretical study of these systems often uses classical isotropic theories of wetting and dewetting for isotropic droplets and films [48] which fail to account for the anisotropic nature of nematics [197, Chapter 8].

Simply stated, *wetting* and *dewetting* are the phenomena in which a liquid advances and retreats, respectively, over a substrate [48]. When a finite volume of liquid advances or retreats over a flat horizontal substrate, it will eventually reach an equilibrium state. This equilibrium state is known as the *complete wetting* state (sometimes also called the full or perfect wetting state [48]) when the liquid completely coats the substrate; the *complete dewetting* state when the substrate completely repels the liquid; and the *partial wetting* state when the liquid partially coats the substrate. For use in Section 1.10.1 and later in Chapter 7, we denote the equilibrium state of complete dewetting by $\mathbb{D}$, the equilibrium state of partial wetting by $\mathbb{P}$, and the equilibrium state of complete wetting by $\mathbb{W}$. Transitions between these equilibrium states can occur due to changes in

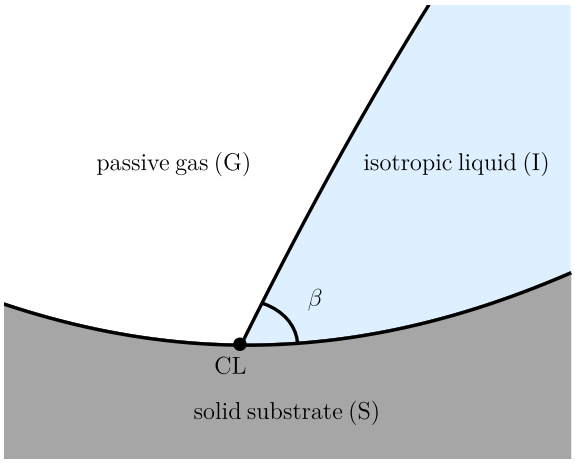

Figure 1.18: Schematic diagram of a three-phase contact line CL. The contact angle β is also indicated.

the liquid or substrate material properties caused by, for example, changes in temperature that cause the liquid to advance or retreat over the substrate and/or change its contact angle. The classification of each equilibrium state and the transitions that can occur between them is well-known for an isotropic system [48].

1.10.1 Wetting and dewetting phenomena for isotropic liquids

In the partial wetting state a static system comprising of an isotropic (I) liquid resting on an ideal (i.e. flat, rigid, perfectly smooth, and chemically homogeneous) solid substrate (S) in an atmosphere of passive gas (G), contains a three-phase contact line CL where all three phases meet, as shown in Figure 1.18. The interfacial energy densities of the three interfaces (which are constant for isotropic fluids) are related to the contact angle β, by the so-called Young equation [47,48]. The classical isotropic Young equation is given by

$$\sigma_{\mathrm{GS}} - \sigma_{\mathrm{IS}} - \sigma_{\mathrm{GI}} \cos\beta = 0, \tag{1.39}$$

where σ_{GS}, σ_{IS}, and σ_{GI} are the isotropic interfacial tensions of the gas–solid, liquid–solid and gas–liquid interfaces [47,48], respectively. The classical isotropic Young equation (1.39) is commonly written in terms of a single parameter, namely the (non-dimensional) isotropic spreading parameter S_{I} [47,48], which is defined by

$$S_{\mathrm{I}} = \frac{\sigma_{\mathrm{GS}} - \sigma_{\mathrm{NS}}}{\sigma_{\mathrm{GN}}} - 1. \tag{1.40}$$

The Young equation (1.39) is given, in terms of S_{I}, by

$$S_{\mathrm{I}} + 1 = \cos\beta. \tag{1.41}$$

Specifically, (1.41) shows that the partial wetting ($\mathbb{P}$) state exists only when $-2 \leq S_{\mathrm{I}} \leq 0$ and that the contact angle is then given by $\beta = \cos^{-1}(S_{\mathrm{I}} + 1)$.

As mentioned above, the equilibrium state can also be one of complete dewetting ($\mathbb{D}$) for which equation (1.41) is not relevant. Although there is no angle formed between the gas–liquid and liquid–solid interfaces in these states, and therefore there are no contact angles, we take the values $\beta = \pi$ and $\beta = 0$ to correspond to the complete dewetting and wetting states, respectively.

The classification of these equilibrium states can be obtained by analytically solving the classical isotropic Young–Laplace equation and expressing the lowest energy state in terms of the isotropic spreading parameter S_{I} [48, 153]. In particular, the lowest energy state is the $\mathbb{D}$ state for $S_{\mathrm{I}} < -2$, the $\mathbb{P}$ state for $-2 \leq S_{\mathrm{I}} \leq 0$, and the $\mathbb{W}$ state for $S_{\mathrm{I}} > 0$, as shown in Figure 1.19. The contact angle β of the lowest energy states of an isotropic system are plotted as a function of the isotropic spreading parameter S_{I} in Figure 1.20.

We define the values of S_{I} at which there is a change in the number of possible equilibrium states as *transition points*. At these points, a transition may occur

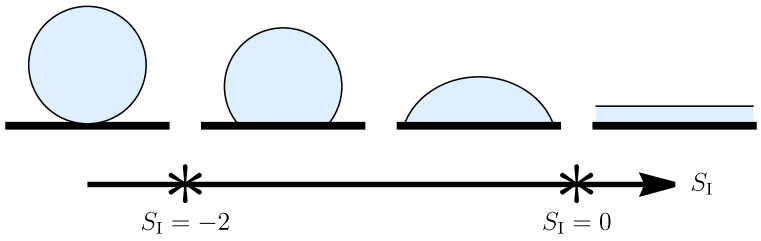

Figure 1.19: Schematic diagram of the lowest energy states as a function of the isotropic spreading parameter S_{I} for an isotropic system. The transition points at $S_{\mathrm{I}} = -2$ and $S_{\mathrm{I}} = 0$ are also shown by stars ($*$).

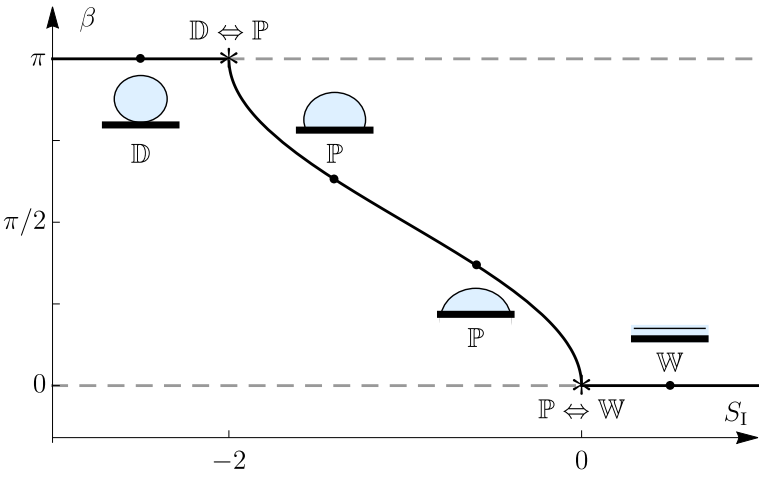

Figure 1.20: The contact angle β (solid black line) of the lowest energy states of an isotropic system are plotted as a function of the isotropic spreading parameter S_{I}. The transition points are denoted by stars ($*$) and the higher energy states are shown by dashed grey lines. Schematic diagrams of the lowest energy states for various values of S_{I} (solid black dots) are also shown.

as S_{I} increases or decreases if the previously lowest energy state ceases to exist or a new lowest energy state comes into existence. At the transition points $S_{\mathrm{I}} = -2$ and $S_{\mathrm{I}} = 0$, there is a change in the number of possible equilibrium states which leads to continuous transitions to a new lowest energy state as S_{I} increases or decreases through $S_{\mathrm{I}} = -2$ and $S_{\mathrm{I}} = 0$. For consistency with the notation used to describe transitions between equilibrium states for a static ridge of nematic in Chapter 7, we denote a continuous transition between two equilibrium states for both increasing and decreasing S_{I} with a double arrow ($\Leftrightarrow$). At $S_{\mathrm{I}} = -2$, there is a continuous transition from complete dewetting to partial wetting or vice versa, which is denoted as a $\mathbb{D} \Leftrightarrow \mathbb{P}$ transition. Similarly, at $S_{\mathrm{I}} = 0$, there is a continuous transition from complete wetting to partial wetting or vice versa, which is denoted as a $\mathbb{P} \Leftrightarrow \mathbb{W}$ transition.

We also note that the behaviour of the contact angle for this isotropic system is non-hysteretic. The well-known phenomenon of isotropic contact-angle hysteresis occurs only in isotropic systems with *non-ideal* substrates [48], and therefore does not occur for the isotropic system considered above.

The wetting and dewetting phenomena of isotropic liquids described above has been of scientific interest for centuries, and is now of increasing technological importance [70]. For systems in which creating a uniform liquid film (i.e. complete wetting) is required wetting is essential, and dewetting is undesirable [48]. However, in other situations, dewetting can be desirable, and in recent years there has been considerable research in the area of tailored dewetting of liquid films to produce patterned films [21, 82, 237]. In isotropic liquids, dewetting can be initiated in a variety of ways, such as amplification of thermal fluctuations on the liquid free surface, nucleation at impurities, chemical treatment of the substrate, and non-uniform evaporation [54]. The thermal, mechanical and chemical stability of isotropic liquid films is therefore an area of considerable research effort,

and understanding and controlling the onset of dewetting is crucial for creating and maintaining both uniform and patterned films. The possibility of dewetting leading to droplets and ridges means that it can be harnessed to organise a film into well-defined micro- or nanometre-size structures that can be controllably positioned on the substrate [82]. Harnessing spontaneous self-organisation in this way can replace time-consuming and expensive processes such as subtractive lithography, in which materials are arranged by delicate multi-step processes [95].

1.10.2 Wetting and dewetting phenomena for nematics

Wetting and dewetting phenomena for nematics can be more complicated than they are for isotropic liquids. In particular, for interfaces involving the nematic, the interfacial energy densities are no longer constant, and as discussed in Section 1.7.3, their energy densities depend on the nematic molecular alignment forces on the interfaces, and so, the classical isotropic Young equation is not sufficient to describe the wetting and dewetting behaviour in these situations [229].

Much of the recent theoretical interest in nematic wetting and dewetting phenomena has focused on spontaneous dewetting transitions, or so-called spinodal dewetting and nucleation events, that occur for thin nematic films. Spinodal dewetting occurs for thin films of many materials, and was first observed for thin polystyrene films by Reiter [178] in 1992, and subsequently observed in thin films of nematic materials by Herminghaus et al. [96] in 1998. A reflection micrograph showing spontaneous rupture of a thin film of nematic due to nucleation and spinodal dewetting is shown in Figure 1.21 [96]. In Figure 1.21, the formation of large holes in the free surface show the onset of nucleation events and the smaller-scale undulations in the free surface show the onset of spinodal dewetting.

Vandenbrouck et al. [209] and Demirel et al. [54] have since found that spinodal dewetting of nematic films occurs when the film thickness is sufficiently small

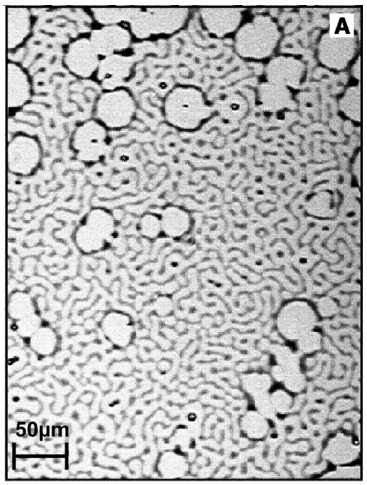

Figure 1.21: Spontaneous rupture of a thin film of the nematic tris(trimethylsiloxy)silane-ethoxycyanobiphenyl ($5AB_4$) of initial thickness 40 nm captured using a reflection micrograph. Figure taken from [96] with Copyright permission from The American Association for the Advancement of Science and Copyright Clearance Center.

(on the order of $40 - 100\,\text{Å}$ depending on the material [54]). Vandenbrouck et al. [209] proposed that spinodal dewetting occurs for nematic thin films due to a competition between van der Waals forces between the substrate and free surface of the thin film and nematic elastic forces. However, they ignored the impact of anchoring forces between the substrate and free surface which have since been shown to play an important role by van der Wielen et al. [207]. Consideration of anchoring forces is especially important when the anchoring between a free surface and the substrate is antagonistic (i.e. one is planar and one is homeotropic). We note that typically homeotropic anchoring is preferred on nematic free surfaces [196, 229], so antagonistic anchoring can be achieved by treating the substrate to prefer planar anchoring. In fact, spontaneous rupture of thin nematic films depends on many factors, including temperature [208], the presence of liquid crystal phase transitions [208], and the substrate shape [60]. Spinodal dewetting has also been observed for thin films of smectic liquid crystals [213].

Theoretical study of these spontaneous dewetting transitions of thin nematic films and spreading of nematic droplets has been carried out using a variety of models from Ericksen–Leslie continuum theory [120, 122, 135, 136], statistical mechanics [4, 190, 210], and mean-field theory [233, 234]. In particular, Lin et al. [135] considered the stability of a thin nematic film with infinite antagonistic anchoring between a planar preferred substrate and a homeotropic preferred free surface with Ericksen–Leslie theory. The authors found that elasticity stabilises the thin film with infinite anchoring conditions, however, in a later publication [136], they found that elasticity can act as a destabilising mechanism when combined with weak anchoring effects.

Lam et al. [120, 121] have subsequently extensively studied nucleation events and spinodal dewetting using Ericksen–Leslie continuum theory and sophisticated numerical tools. These authors derived a thin film evolution equation which depends on an effective disjoining pressure which captures the effects of weak anchoring, elasticity and van der Waals forces. The effective disjoining pressure as a function of the film thickness is used to summarise the possible regimes of thin film rupture. The authors model is in excellent qualitative agreement with experimentally observed rupture of thin nematic films by Herminghaus et al. [96], Vandenbrouck [209], and Schlagowski et al. [192]. Lam et al. have since applied their approach to study spreading of nematic droplets on patterned substrates [122]. Ziherl et al. [233, 234] discussed spinodal dewetting in relation to a "pseudo-Casimir" force, for which thermal fluctuations of nematic molecules can create a destabilising or stabilising elastic forces depending on the film thickness.

There has also been much interest in the wetting and dewetting phenomena for nematics outwith spontaneous rupture of nematic thin films. Molecular dynamics approaches have been used by Vanzo et al. [210] to consider the spreading and contact angles of nematic droplets, and by Rull and Romero-Enrique [190] and

Allen [4] to consider the dynamics of a nematic-vapour interface. Blow and Telo da Gama [17] and Rojas Gomez et al. [189] studied nematic electro-wetting on grooved surfaces, and Zou et al. [237] studied self-organisation of disctotic liquid crystal ridges. Luo et al. [137] studied the evaporation of an aqueous dispersion of graphene oxide, which is a lyotropic liquid crystal, and found that nematic order strongly effects evaporation and can prevent the well-known coffee-ring effect (see Deegan et al. [53]). More recently, van der Kooij et al. [206] demonstrated the control of liquid crystal polymer network free surface using incident light.

Much of the ongoing research on the wetting and dewetting phenomena for nematics includes the study of systems with a nematic–substrate–gas three-phase contact line. Nematic three-phase contact lines are particularly interesting because the preferred director orientations on the gas-–nematic and the nematic-–substrate interfaces are, in general, different. Even when the anchoring is non-antagonistic (i.e. either planar or homeotropic anchoring preferred on both interfaces), since the preferred director orientation of both interfaces is measured relative to that interface, and the two interfaces meet at the non-zero contact angles, the orientations are, in general, not the same. It is therefore unclear exactly how the director will orient in the vicinity and at the three-phase contact line. Theoretical study of wetting and dewetting phenomena for nematics that include contact lines often avoid the consideration of anchoring at the contact lines, by, for example, imposing infinite anchoring on the nematic–substrate interface which overrides the weak anchoring on the gas–nematic interface at the contact line (see, for example, Lam et al. [120, 122]), or assuming the existence of a thin precursor film on the substrate to remove the contact line entirely (see, for example, Lin et al. [136]). While there have been relatively few studies of nematic contact lines, Rey [183, 184] considered two rather specific two-dimensional scenarios, namely infinite planar anchoring and equal weak planar anchoring on the two interfaces. Although neither infinite anchoring nor equal weak anchoring is likely to occur

in practice, his studies of these somewhat idealised situations highlight the possibility that anchoring breaking, i.e. the process by which the preferred orientation of the nematic molecules on one of the interfaces is overridden by that on the other, occurs in the vicinity of the contact line. Rey [183, 184] also discusses the possibility of the formation of a defect, or disclination line in his two-dimensional scenarios, located at the contact line. In Chapters 5 to 7 we consider a theoretical model for a static ridge of nematic resting on an ideal solid substrate (S) in an atmosphere of passive gas (G), which allows significant insights into many of the systems discussed above which involve a nematic–substrate–gas three-phase contact line.

1.11 Organisation of the thesis

This thesis considers the mathematical modelling and analysis of two main problems relating to the ODF method. Firstly, in Chapters 2 to 4, we consider three problems relating to the fluid dynamics of nematics in the ODF method. Specifically, we investigate the possibility that flow effects are responsible for forming the ODF mura. Secondly, in Chapters 5 to 7, we consider a static ridge of nematic resting on an ideal solid substrate surrounded by passive fluid, which gives insight into the initial stage of the ODF method and more general situations involving nematic free surfaces and three-phase contact lines. A brief summary of the work undertaken in this thesis was published in *Mathematics Today* as part of the 2019 TakeAIM competition run by the Institute of Mathematics and its Applications (IMA) [33].

In Chapter 2, we formulate and analyse a simple model for the squeezed coalescence of several nematic droplets. This model predicts the radial boundary speed of droplets in the ODF method, which shows a striking qualitative similarity

to the ODF mura shown in Figure 1.10. The material in the first half of this chapter was presented at the 25th International Display Workshop (IDW) in Nagoya, Japan, and was subsequently published in the *Proceedings of the 25th International Display Workshops (IDW 2018)* [36]. The second half of Chapter 2 uses the conservation of volume model for the evolution of the droplet boundaries in two limiting regimes of Ericksen–Leslie theory, namely a flow dominated regime and an elasticity regime. We subsequently make qualitative comparisons between experimental photographs of the ODF method and numerical calculations of the transmission of light through the droplets. The work detailed in this chapter was presented orally at the Merck CASE Conference in 2018 in New Forest, the 25th IDW in 2018 in Nagoya, Japan, the British Applied Mathematics Colloquium (BAMC): Minisymposium on Toy Models in 2019 in Bath, and the British Liquid Crystal Society (BLCS) Meeting in 2019 in Leeds, and was presented in poster form at Droplets 2019 in Durham and the TakeAIM Award Ceremony in 2019 in London.

In Chapter 3, motivated by the need for a better fundamental understanding of the reorientation of the molecules due to the flow of the nematic during the ODF method, we formulate and analyse a squeeze-film model for a single nematic droplet in the ODF method. Specifically, we consider a nematic squeeze film in the asymptotic regime in which the drop is thin, inertial effects are weak, and elasticity effects are strong for four cases of infinite anchoring at the downward moving top substrate and the stationary bottom substrate, and for two different scenarios for the motion of the top substrate (namely, prescribed speed and prescribed force). The results presented in this chapter were published in *Physics of Fluids* [34]. Early versions of the results detailed in this chapter were orally presented at the BLCS: Young Researchers Meeting in 2017 in Durham, the Merck CASE Conference in 2017 in New Forest, and the Alan Tayler day in 2017 in Oxford. A more up-to-date version of the results were later orally presented at

the BAMC in 2018 in St Andrews, the UK Fluids conference 2019 in Cambridge, and at the Bath-Oxford-Strathclyde Network Meeting on Anisotropic Materials in 2019 in Glasgow.

In Chapter 4, we formulate and analyse a model for pressure-driven channel flow of nematic using a dissipative weak anchoring condition on the substrates to investigate the transient flow-driven distortion of the nematic molecules on the substrates from their required orientation in the ODF method. We obtain quasisteady asymptotic solutions for the director angle and the velocity in the limit of small Leslie angle, and find that solutions depend on two key non-dimensional parameters, a ratio of viscous and elastic effects, called the Ericksen number, and a ratio of anchoring and elasticity, called the anchoring strength parameter. The results presented in this chapter were published in *Physical Review E* [35] and have been presented orally at the Scottish Fluid Mechanics Meeting in 2018 in Aberdeen and the Merck Liquid Crystal Minisymposium in 2018 in Darmstadt, Germany.

In Chapter 5, the governing equations for a static ridge of nematic resting on an ideal solid substrate surrounded by passive fluid are derived. Specifically, we use constrained energy minimisation for the Oseen–Frank bulk elastic energy density and the Rapini–Papoular interface energy density to obtain the governing equations for the system, which include nematic Young and Young–Laplace equations. The results presented in this chapter are currently being prepared for submission to *Proceedings of the Royal Society A*.

In Chapter 6, we apply the governing equations derived Chapter 5 to the situation in which the ridge is thin and has pinned contact lines. We obtain an anchoring-strength solution parameter plane, which summarises the director solution behaviour in terms of the Jenkins–Barratt–Barbero–Barberi critical thickness. The free surface of the ridge is also numerically investigated. The results

presented in Chapter 6 are currently being compared with ongoing experimental work at Nottingham Trent University, and will subsequently be submitted to *Soft Matter*.

Motivated by the results of Chapter 6, which indicates that anchoring breaking occurs in the vicinity of nematic three-phase contact lines, in Chapter 7, we analyse the nematic Young equations derived in Chapter 5 with the assumption that anchoring breaking occurs in the vicinity of nematic three-phase contact lines. In particular, we use the nematic Young equations to determine the continuous and discontinuous transitions between the equilibrium states of complete wetting, partial wetting, and complete dewetting that can occur. The results detailed in Chapter 7 will be included in the manuscript to be submitted to *Proceedings of the Royal Society A*.

The work on nematic ridges presented in Chapters 5 to 7 has been orally presented at the Durham-Oxford-Strathclyde network on Anisotropic Materials in 2020 and 2021 (meetings held online), the 73rd Annual Meeting of the American Physical Society Division of Fluid Dynamics in 2020 in Chicago, US (meeting held online), the British Society of Rheology Mid Winter Meeting in 2021 (meeting held online), Droplets 2021 in Darmstadt, Germany (meeting held online), the BAMC in 2021 in Glasgow (meeting held online), as part of a research seminar at the New Jersey Insitute of Technology in 2021 (seminar held online), the Society of Industrial and Applied Mathematics (SIAM) Conference on Material Science in 2021 (meeting held online), and the UK Fluids Conference 2021 in Southampton (meeting held online).

Finally, in Chapter 8, we will present some concluding points and discuss the possible future extensions of the work described in this thesis.

Chapter 2

A simple model for the squeezed coalescence of nematic droplets

In this chapter we will present a simple model for the coalescence of nematic droplets between converging substrates, which we term "squeezed coalescence" to provide insight into the ODF method (discussed in Section 1.4.2). In particular, in Section 2.1 we describe a simple model for the evolution of the droplet boundary during squeezed coalescence, which predicts the radial boundary speed of the droplets. This simple model uses only the conservation of mass to describe the evolution of the droplet boundaries, and therefore neglects the effects of surface tension, elasticity, anchoring, and contact line dynamics. In the present work we consider the nematic to be an incompressible fluid, and therefore conservation of mass is equivalent to conservation of volume. Despite the simplicity of this model, in Section 2.2 a plot of the speed of droplet boundary as it passes over each point on the substrate is shown to have striking similarity with photographs of the ODF mura, shown in Figure 1.10. This similarity leads us to hypothesise that the formation of ODF mura is associated with stresses on the alignment layer caused by the advancing droplet boundary.

In Section 2.3, the behaviour of the director within an isolated droplet and two coalescing droplets is considered in both a flow-dominated regime and in an elasticity-dominated regime. In the flow-dominated regime, the dominant torque on the director derives from director-flow coupling and in the elasticity-dominated regime, the dominant torque on the director derives from elasticity. Finally, in Section 2.4, the director behaviour calculated in Section 2.3 is used to calculate the transmission of light through two squeezed coalescing droplets in the flow-dominated regime and in the elasticity-dominated regime. We then make comparisons between the transmission of light calculated in both regimes with the experimental photographs of the transmission of light through a two-droplet ODF test setup shown in Figure 1.9. We find similarities between the experimental photographs and the transmission of light calculated in the flow-dominated regime, indicating that the simple model described in this chapter is remarkably successfully at describing both the droplet boundary evolution and the director behaviour in squeezed coalescence.

2.1 A simple model for the evolution of droplet boundaries

During the squeezed coalescence of droplets in the ODF method, the droplet boundaries evolve according to a number of physical processes. In particular, the droplet boundaries expand as the gap between the substrates reduces due to conservation of volume, and the droplet boundaries evolve to minimise regions of high curvature due to surface tension. It is clear from the experimental photographs shown in Figure 1.9 that the droplet boundaries expand as the gap between the substrates is reduced. However, we note that as the droplet boundaries expand, sharp corners formed where the droplets meet are visible in all three photographs,

indicating that surface tension effects, which would tend to remove these regions of high curvature, are acting on a much slower timescale than the expansion of the droplet boundaries. Motivated by this qualitative experimental evidence, we proceed with a simple model in which we assume that the evolution of the droplet boundaries only occurs due to the conservation of volume. Specifically, this assumption requires that the timescale of coalescence due to surface tension effects is much longer than the time taken for the converging substrates to meet. The validity of this assumption is discussed further in Section 2.5, where we compare a naive estimate of the timescale of coalescence due to surface tension effects and the time taken for the converging substrates to meet.

Motivated by the qualitative experimental evidence discussed above, we now proceed by using a simple model that uses only the conservation of volume to describe the squeezed coalescence in the ODF method. Specifically, we model each droplet in the ODF method as a cylinder of fluid (with a constant volume V), being squeezed by two converging substrates which are both parallel to the xy-plane and have decreasing gap $H(t)$ between them, which therefore increases the cross-sectional area and the radius $R(t)$ of the droplets, as shown in Figure 2.1 for a three-droplet setup. We assume that the top substrate moves with a constant downward speed, s_p, starting at some initial height, $\mathcal{H}$, at $t = 0$, so that the position of the top substrate is given by

$$H(t) = \mathcal{H} - s_\mathrm{p} t \tag{2.1}$$

for $0 \leq t < t_\mathrm{max}$, where $t_\mathrm{max} = \mathcal{H}/s_\mathrm{p}$. For typical ranges of parameters used in the ODF method, as stated in Table 1.1, the initial gap between the substrates is $\mathcal{H} = 10^{-6}$–$10^{-4}\,\mathrm{m}$, and downward speed of the top substrate is $s_\mathrm{p} = 10^{-3}\,\mathrm{m\,s^{-1}}$, and so $t_\mathrm{max} = 10^{-3}$–$10^{-1}\,\mathrm{s}$ [36]. Note that, in theory, as $t \to t_\mathrm{max}$ the gap between the substrates approaches zero and the radius of the droplets $R(t)$ and radial

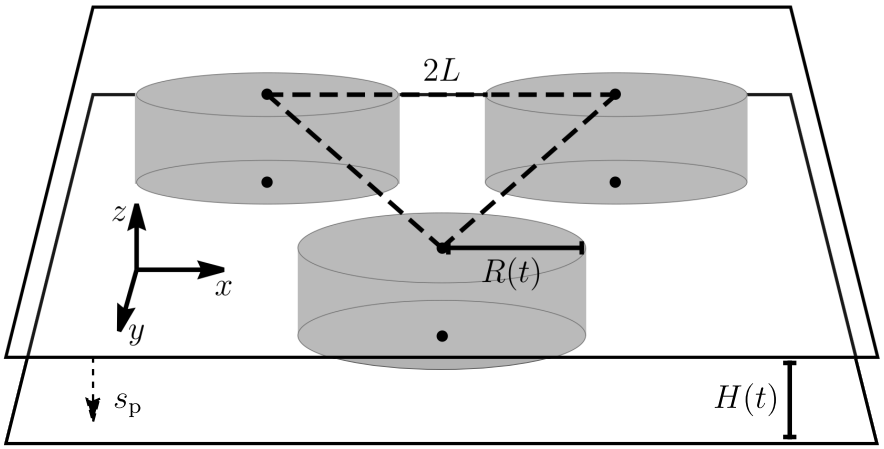

Figure 2.1: Schematic diagram of three cylindrical droplets (dark grey) in the ODF method. The gap between the substrates $H(t)$, the droplet radius $R(t)$, the separation distance of each droplet $2L$, the downward speed of the top substrate s_p, and the Cartesian coordinates (x, y, z), are shown.

speed of the boundary of the droplet approaches infinity. In practice, of course, the squeezing is stopped at some time before t_{max} to create a cell with a prescribed non-zero gap between the substrates.

In principle, any arrangement of droplets can be considered, but for direct comparison to the ODF mura shown in Figure 1.10 we shall consider the three-droplet setup shown in Figure 2.1. In particular, each droplet has initial radii $R(0) = \mathcal{R}$, where $0 < \mathcal{R} < L$, and volume $V = \pi \mathcal{R}^2 \mathcal{H}$ and is positioned at the vertex of an equilateral triangle with side length $2L$, where L is half the separation distance of each droplet, as shown in Figure 2.2(a).

Initially, the droplets are not touching and each droplet evolves as an isolated droplet. In particular, each droplet has constant volume $V = \pi \mathcal{R}^2 \mathcal{H} = \pi R(t)^2 H(t)$, and therefore $R(t) = (V/\pi H(t))^{1/2}$. The radial speed of the boundary of a single isolated droplet can be found by differentiating $R(t)$ with respect

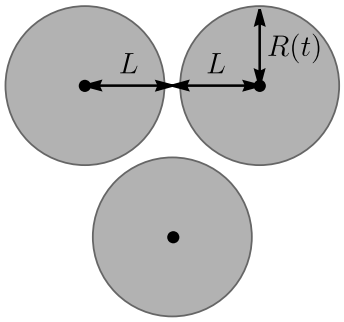

(a) initial phase
$(0 \leq t \leq t_{\mathrm{c}})$

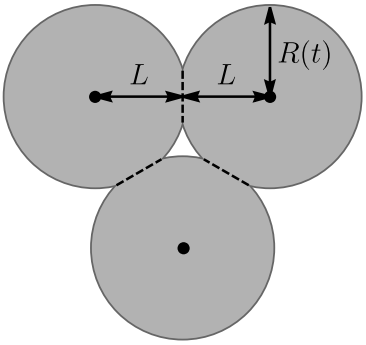

(b) partially coalesced phase
$(t_{\mathrm{c}} < t \leq t_{\mathrm{f}})$

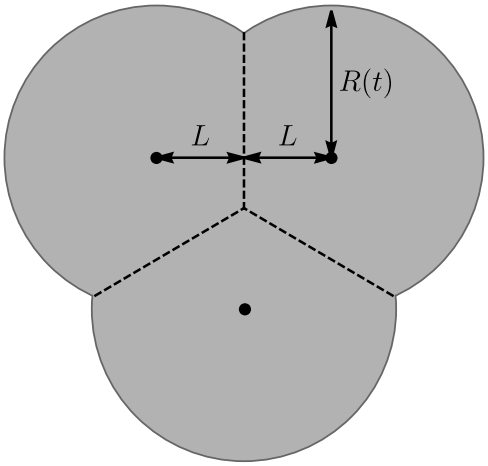

(c) fully coalesced phase
$(t_{\mathrm{f}} < t < t_{\mathrm{max}})$

Figure 2.2: The three stages of coalescence of three identical droplets; (a) the initial stage $(0 \leq t \leq t_{\mathrm{c}})$, (b) the partially coalesced stage $(t_{\mathrm{c}} < t \leq t_{\mathrm{f}})$, and (c) the fully coalesced stage $(t_{\mathrm{f}} < t < t_{\mathrm{max}})$.

to time to yield

$$R'(t) = -\frac{H'(t)R(t)}{2H(t)} = \sqrt{\frac{s_{\mathrm{p}}^2 V}{4\pi}}\left(\mathcal{H} - s_{\mathrm{p}}t\right)^{-3/2}. \tag{2.2}$$

As the gap between the substrates $H(t)$ continues to decrease, the three droplets will meet and begin to coalesce at some time before $t = t_{\max}$. In particular, for the present arrangement of three droplets, the droplets will meet when $R(t_{\mathrm{c}}) = L$ at the time $t = t_{\mathrm{c}}$, which is given by

$$t_{\mathrm{c}} = t_{\max} - \frac{V}{\pi s_{\mathrm{p}} L^2}, \tag{2.3}$$

and then enter a partially coalesced phase where a region of the substrate in the centre of the three droplet configuration is not covered by the droplets, as shown in Figure 2.2(b). If the three droplet configuration is surrounded by air then the region of the substrate in the centre of the configuration would form an air bubble. In the ODF method, which is carried out in vacuum, no air bubbles are formed [106] which we therefore assume in the present analysis. Using simple geometric considerations of the geometry shown in Figure 2.2(b), an implicit equation for the droplet radius $R(t)$ during the partially coalesced phase can be determined analytically, namely

$$\frac{V}{H(t)} = \left[\pi - 2\cos^{-1}\left(\frac{L}{R(t)}\right)\right] R(t)^2 + 2L\sqrt{R(t)^2 - L^2}. \tag{2.4}$$

Eventually, at a later time $t = t_{\mathrm{f}}$ (where $t_{\mathrm{c}} < t_{\mathrm{f}} < t_{\max}$) when $R(t_{\mathrm{f}}) = 2L/\sqrt{3}$, where t_{f} can be obtained using (2.4) and $R(t_{\mathrm{f}}) = 2L/\sqrt{3}$, to be

$$t_{\mathrm{f}} = t_{\max} - \frac{9\sqrt{3}V}{\left(8\pi\sqrt{3} + 18\right) s_{\mathrm{p}} L^2}, \tag{2.5}$$

the central gap between the droplets closes up entirely and the droplets enter the fully coalesced phase shown in Figure 2.2(c). Similarly, using simple geometric considerations of the geometry shown in Figure 2.2(C), an implicit equation for the droplet radius $R(t)$ during the fully coalesced phase can again be determined analytically, namely

$$\frac{V}{H(t)} = \left[\pi + P(t) - 2\cos^{-1}\left(\frac{L}{R(t)}\right)\right] R(t)^2 + 2L\sqrt{R(t)^2 - L^2} - \frac{2}{\sqrt{3}} R(t) L \sin P(t), \tag{2.6}$$

where

$$P(t) = \cos^{-1}\left(\sqrt{3}L + \frac{\sqrt{R(t)^2 - L^2}}{2R(t)}\right). \tag{2.7}$$

As in the initial phase, in the partially and fully coalesced phases the radial speed of the boundary of the droplets $R'(t)$ can be obtained by differentiation of (2.4) and (2.6), respectively. We can also determine the radial speed of the corners formed between the droplets $d'(t)$ in the partially and fully coalesced phases shown in Figure 2.2 (b) and (c), namely

$$d'(t) = \frac{R(t)\, R'(t)}{\sqrt{R(t)^2 - L^2}}, \tag{2.8}$$

and hence $d'(t) > R'(t)$ for $t_c < t < t_{\max}$. The radial speed of the boundary of the droplets $R'(t)$ radial speed of the corners between droplets $d'(t)$ is plotted as a function of time t in Figure 2.3 for particular ODF parameter values provided to us by Merck KGaA, stated in Table 2.1. (We note that these particular ODF values stated in Table 2.1 fall within the typical ranges for the parameters shown in Table 1.1.) Figure 2.3 shows that in all three coalescence phases $R'(t)$ increases as the gap between the substrates decreases and that, as shown by (2.8), the

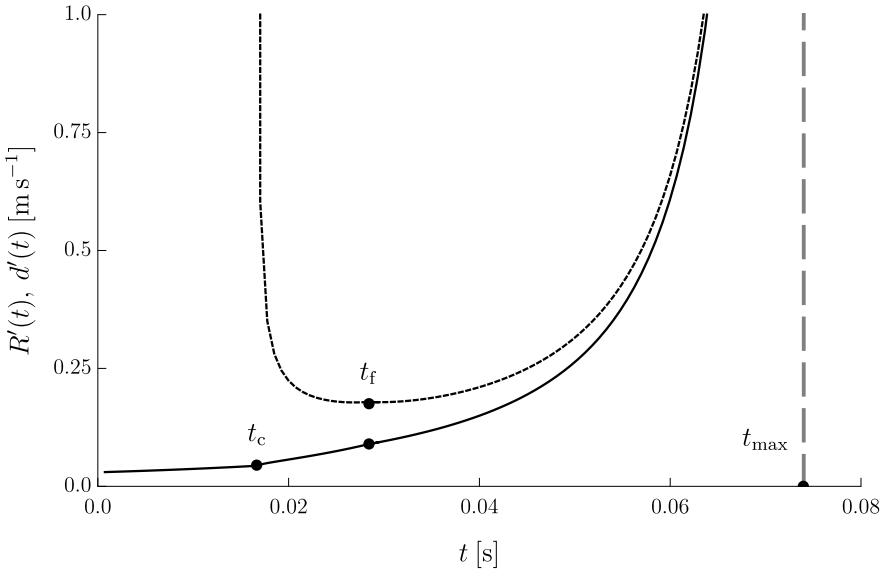

Figure 2.3: Radial speed of the boundary of the droplets $R'(t)$ (solid) and radial speed of the corners between droplets $d'(t)$ (dashed), as functions of time t for three identical droplets with $H(t) = \mathcal{H} - s_\mathrm{p} t$ and the ODF parameter values shown in Table 2.1. The solid dots show the times $t_\mathrm{c} = 1.669 \times 10^{-2}\,\mathrm{s}$, $t_\mathrm{f} = 2.840 \times 10^{-2}\,\mathrm{s}$, and $t_\mathrm{max} = 7.400 \times 10^{-2}\,\mathrm{s}$.

radial speed of the corners between droplets is greater than the radial speed of the boundary of the droplets for $t_\mathrm{c} \leq t < t_\mathrm{max}$.

2.2 A simple model for deformation to the director structure

Given the location of the ODF mura shown in Figure 1.10, and the fact that the present model predicts that the corner speed $d'(t)$ is larger than the radial speed of the droplet boundary $R'(t)$, we hypothesise that the formation of ODF mura is associated with stresses on the alignment layer caused by the advancing droplet boundary. We therefore use the value of $R'(t)$ predicted by our model to estimate the deformation to the director structure caused by the spreading

	Value
V	4.501×10^{-9} m^3
$\mathcal{H}$	7.400×10^{-5} m
s_p	1.000×10^{-3} m s^{-1}
L	5.000×10^{-3} m
t_max	7.400×10^{-2} s

Table 2.1: ODF parameter values provided to us by Merck KGaA; the volume of each droplet V, the initial height of the top substrate $\mathcal{H}$, the downward speed of the top substrate s_p, half the separation distance of each droplet L, and the maximum time t_max [36].

droplets. Specifically, the deformation to the director structure at any point is assumed to be proportional to the radial speed of the droplet boundary as it passes over that point. Therefore, areas with larger values of $R'(t)$ then correspond to areas where the spreading droplet front causes a high shear or torque on the alignment layer which could lead to the formation of ODF mura. The radial speed of the droplet boundary $R'(t)$ is shown in Figure 2.4 for the ODF parameter values stated in Table 2.1, where lighter regions in the plot indicate regions of larger values of $R'(t)$ and more deformation to the director structure, and darker regions indicate regions of smaller values of $R'(t)$ and less deformation to the director structure. In particular, Figure 2.3 shows increasing $R'(t)$, and therefore, increasing deformation to the director structure towards the outer edges. The theoretical prediction of the radial speed of the droplet boundary $R'(t)$ shown in Figure 2.4 shows a striking similarity to the ODF mura shown in Figure 1.10. In particular, both Figure 1.10 and Figure 2.4 show three lighter linear regions of non-uniformity between the origins of each droplet creating an inverted "Y-shape" in the centre of the cell and lighter regions towards the edges of the substrate, suggesting a link between areas of high $R'(t)$ and the positions of the ODF mura.

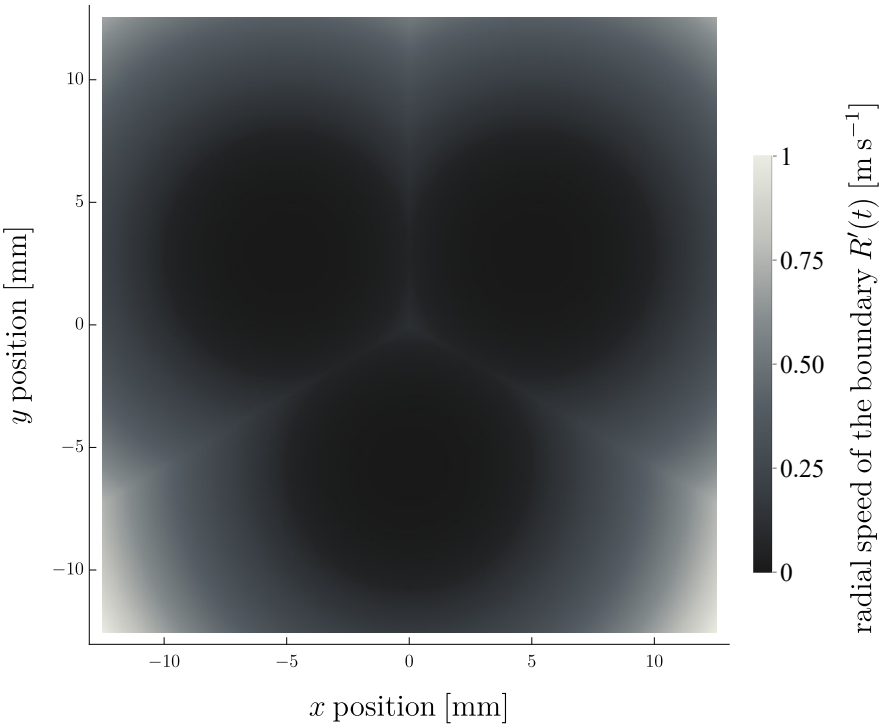

Figure 2.4: The radial speed of the droplet boundary $R'(t)$ with $H(t) = \mathcal{H} - s_{\mathrm{p}}t$ for the ODF parameter values shown in Table 2.1. Lighter regions in the plot indicate regions of larger values of $R'(t)$ and more deformation to the director structure, and darker regions indicate regions of smaller values of $R'(t)$ and less deformation to the director structure, as indicated by the plot key.

2.3 Fluid velocity and director field within squeezed coalescing nematic droplets

We now proceed by using the simple model considered above for the expanding droplet boundary, in two limiting cases for the behaviour of the nematic within the droplet. In particular, we consider the in-plane fluid velocity $\boldsymbol{u}_{=}$ and in-plane director $\boldsymbol{n}_{=}$ components in the plane of the substrates (i.e. the xy-plane) numerically with the finite element analysis, solver and multiphysics simulation software COMSOL Multiphysics [156]. The in-plane fluid velocity $\boldsymbol{u}_{=}$ and in-plane director $\boldsymbol{n}_{=}$ components are given by

$$\boldsymbol{n}_{=} = (\cos\phi, \sin\phi, 0), \tag{2.9}$$

$$\boldsymbol{u}_{=} = (u, v, 0), \tag{2.10}$$

respectively, where $\phi = \phi(x, y, t)$, $u = u(x, y, t)$, and $v = v(x, y, t)$. We will not explicitly consider the out-of-plane components of the fluid velocity $\boldsymbol{u}_{\perp}$ and director $\boldsymbol{n}_{\perp}$ that are parallel to the substrate normal, i.e. the z-axis. Whilst this is certainly an approximation, and requires further more robust analysis in the future, the present analysis it is remarkably successful in comparison to experiments.

We consider the in-plane fluid velocity $\boldsymbol{u}_{=}$ and in-plane director $\boldsymbol{n}_{=}$ components in two scenarios, namely a squeezed isolated droplet and two squeezed coalescing droplets separated by a distance $2L$, to allow comparison with the experimental photographs of the transmission of light through a two-droplet ODF test setup shown in Figure 1.9. The squeezed isolated droplet and the two squeezed coalescing droplets expand due to the decreasing gap between the substrates $H(t) = \mathcal{H} - s_{\mathrm{p}}t$, and the droplet boundaries are again modelled using the simple model for the evolution of the droplet boundaries given in Section 2.1. The

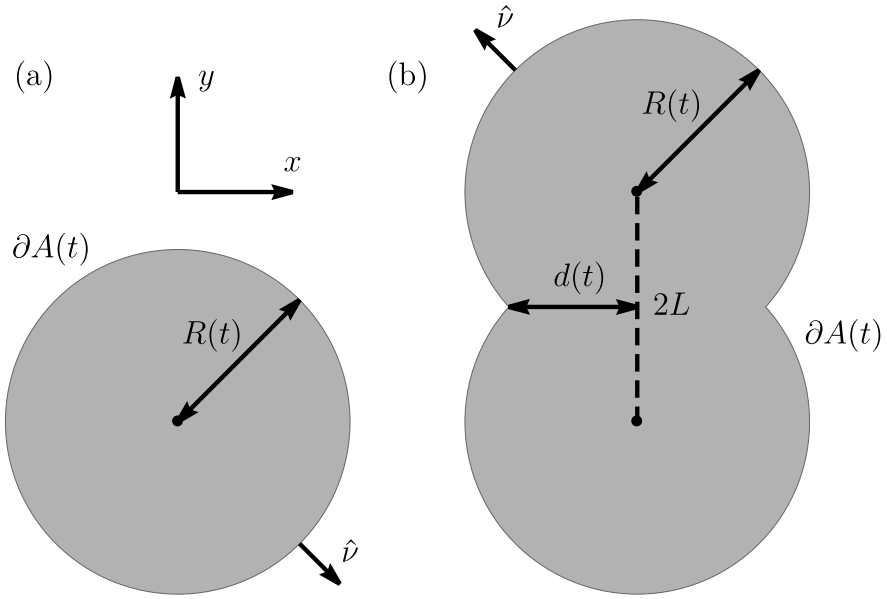

Figure 2.5: The (a) squeezed isolated droplet and (b) two squeezed coalescing droplets with boundary $\partial A(t)$, radius $R(t)$, and outward surface normal $\hat{\boldsymbol{\nu}}$. In part (b) the fixed separation of the droplets centres $2L$ and half the distance between the corners formed between the droplets $d(t)$ is shown. The Cartesian coordinates (x, y) are also indicated.

squeezed isolated droplet and the two squeezed coalescing droplets have droplet boundary $\partial A(t)$, radius $R(t)$, outward surface normal $\hat{\boldsymbol{\nu}} = \hat{\boldsymbol{\nu}}(x, y, t)$, and volume $V = \pi R(t)^2 H(t)$, as shown in Figures 2.5(a) and (b), respectively. For later use, the region of nematic within the droplet boundary $\partial A(t)$ is denoted $A(t)$. Without loss of generality, in the isolated droplet scenario, the droplet centre is positioned at $(0, 0)$. In the two coalescing droplets scenario, one droplet centre is positioned at $(0, L)$ and the second droplet centre is positioned at $(0, -L)$, so that in the coalescing phase, the centre of the two combined droplets, i.e. the centre of mass, is at $(0, 0)$ and the corners formed between the droplets are at $(d(t), 0)$ and $(-d(t), 0)$, where $d(t) = \sqrt{R(t)^2 - L^2}$.

For the isolated droplet, the droplet boundary $\partial A(t)$ and radius $R(t)$ evolve as described in the initial phase in Section 2.1. For the two coalescing droplets,

as the gap between the substrates decreases the droplets boundaries expand and make contact at time $t = t_c$ and enter a coalescing phase, for which the droplet boundaries obey the implicit equation for $R(t)$ given by

$$\frac{V}{H(t)} = \left[\pi - \cos^{-1}\left(\frac{L}{R(t)}\right)\right] R(t)^2 + L\sqrt{R(t)^2 - L^2}. \tag{2.11}$$

Unlike the arrangement of three droplets, for two droplets there are only two phases, namely the initial phase and the coalescing phase where the droplets obey (2.11) for $t_c \leq t < t_{\max}$. In order to avoid numerical issues for the two coalescing droplets incurred by having sharp corners in the numerical mesh at the corners formed between the droplets, the corners are rounded in COMSOL Multiphysics using quadratic Bézier curves [155]. Specifically, two quadratic Bézier curves are implemented in COMSOL Multiphysics using the control points $(\pm d(t) \pm \delta_d, L - (R(t)^2 - (d(t) + \delta_d)^2)^{1/2})$, $(\pm d(t), 0)$, and $(\pm d(t) \pm \delta_d, -L + (R(t)^2 - (d(t) + \delta_d)^2)^{1/2})$ and the weight of the control points 1, ϵ_c, and 1, respectively. The parameter δ_d can be varied to adjust the position of the control points whilst ensuring all control points remain on the droplet boundaries. The weight ϵ_c can be varied to alter the radius of curvature of the corners formed between the droplets, namely increasing ϵ_c decreases the radius of curvature and decreasing ϵ_c increases the radius of curvature. In all the numerical results presented below $\delta_d = 10^{-3}$ and $\epsilon_c = 2$ unless stated otherwise.

We will also consider two regimes of the in-plane director behaviour within the boundary $\partial A(t)$ for the isolated droplet and the two coalescing droplets. Firstly, we will consider a regime in which the dominant torque on the director derives from director-flow coupling for which the in-plane director will completely align with the in-plane fluid velocity vector and the out-of-plane director will align with the flow alignment angle, and, secondly, we will consider a regime in which the dominant torque on the director derives from elasticity for which the in-

plane director angle will obey Laplace's equation. The more general regime in which flow and elasticity are coupled requires defining the full two-dimensional Ericksen-Leslie equations within the droplet boundaries $\partial A(t)$ has not yet been considered. We note that an axisymmetric asymptotic approach for a single squeezed nematic droplet in a more general regime in which flow and elasticity are coupled is analysed in Chapter 3.

2.3.1 Flow-dominated regime

In the flow-dominated regime we assume that the in-plane director $\boldsymbol{n}_{=}$ aligns with the in-plane fluid velocity vector $\boldsymbol{u}_{=}$, i.e.

$$\boldsymbol{n}_{=} = \left(\frac{u}{|\boldsymbol{u}_{=}|}, \frac{v}{|\boldsymbol{u}_{=}|}, 0 \right), \tag{2.12}$$

which in terms of the in-plane director angle $\phi = \phi(x, y, t)$, is given by

$$\phi = \tan^{-1}\left(\frac{v}{u}\right). \tag{2.13}$$

Although we do explicitly consider the out-of-plane director $\boldsymbol{n}_{\perp}$, in the flow-dominated regime we assume that $\boldsymbol{n}_{\perp}$ is flow aligned at the Leslie angle $\theta = \pm\theta_{\mathrm{L}}$, and hence the fluid viscosity can be estimated as $\eta_{\mathrm{L}} = g(\theta_{\mathrm{L}})$, where $g(\theta)$ is a viscosity function, which will be introduced in Chapter 3 and Chapter 4. In particular, using $\eta_{\mathrm{L}} = g(\theta)$, η_{L} is given by

$$\eta_{\mathrm{L}} = \eta_1 \cos^2\theta_{\mathrm{L}} + \eta_2 \sin^2\theta_{\mathrm{L}} + \eta_{12} \sin^2\theta_{\mathrm{L}} \cos^2\theta_{\mathrm{L}}. \tag{2.14}$$

Alternatively, (2.14) can be expressed by using the definition of the Leslie angle (1.38) and rearranging, as

$$\eta_{\mathrm{L}} = \frac{1}{2}\left[\eta_1\left(1-\frac{\gamma_1}{\gamma_2}\right)+\eta_2\left(1+\frac{\gamma_1}{\gamma_2}\right)+\frac{\eta_{12}}{2}\left(1-\left(\frac{\gamma_1}{\gamma_2}\right)^2\right)\right]. \tag{2.15}$$

For the viscosities of the nematic 5CB, $\theta_{\mathrm{L}} \simeq \pm 12^\circ$ and $\eta_{\mathrm{L}} = 0.0237\,\mathrm{Pa\,s}$.

To find the in-plane fluid velocity $\boldsymbol{u}_{=}$, and hence the in-plane director $\boldsymbol{n}_{=}$ we use the Hele–Shaw approximation for the fluid flow within the droplet boundary $\partial A(t)$ shown in Figures 2.5(a) or 2.5(b), for an isolated droplet and two coalescing droplets, respectively. The flow of coalescing isotropic droplets in a Hele-Shaw cell has been studied by Crowdy and Kang [38] and Shelley et al. [195], in which the authors include the effects of surface tension (which we neglect) and use conformal mapping techniques to solve for the flow and evolving droplet boundaries. In the present model, we do not solve for the droplet boundary and instead we prescribe the droplet boundary using our model for squeezed droplet coalescence in Section 2.1.

The governing equations for flow in a Hele–Shaw cell within the boundary $\partial A(t)$ are given by the conservation of momentum, the conservation of mass, and the boundary condition on the fluid pressure $p = p(x, y, t)$, namely

$$\boldsymbol{u}_{=} = -\frac{H(t)^2}{12\eta_{\mathrm{L}}}\nabla p \quad \text{in} \quad A(t), \tag{2.16}$$

$$\boldsymbol{\nabla}\cdot\boldsymbol{u}_{=} = -\frac{H'(t)}{H(t)} \quad \text{in} \quad A(t), \tag{2.17}$$

$$p = p_{\mathrm{vac}} \quad \text{on} \quad \partial A(t), \tag{2.18}$$

where p_{vac} is the pressure outside the droplets. As the ODF method is carried out in vacuum, a vacuum pressure of around $p_{\mathrm{vac}} = 1\,\mathrm{Pa}$ [204] is appropriate. Combining the conservation of momentum (2.16) and the conservation of mass

(2.17) yields Poisson's equation for the fluid pressure p, namely

$$\nabla^2 p = \frac{12\eta_{\mathrm{L}} H'(t)}{H(t)^3} \quad \text{in} \quad A(t), \tag{2.19}$$

with the boundary condition (2.18). For an isolated droplet Poisson's equation for the fluid pressure (2.19) with the boundary condition (2.18) is solved analytically in Section 2.3.1.1 and for two coalescing droplets numerically using COMSOL Multiphysics in Section 2.3.1.2.

2.3.1.1 An isolated squeesed droplet

We now consider the solution of (2.19) with the boundary condition (2.18) for an isolated droplet. The boundary $\partial A(t)$ is simply the circle with centre (0,0) and increasing radius $R(t)$, where $R(t)$ can be calculated from $V = \pi R(t)^2 H(t)$ with $H(t) = \mathcal{H} - S_p t$. By means of direct integration of (2.19) the fluid pressure and in-plane velocity can be obtained, namely

$$p = \frac{3\eta_{\mathrm{L}} H'(t)}{H(t)^3} \left(x^2 + y^2 - R(t)^2\right) + p_a, \tag{2.20}$$

$$\boldsymbol{u}_{=} = \left(-\frac{xH'(t)}{2H(t)}, -\frac{yH'(t)}{2H(t)}, 0\right). \tag{2.21}$$

As the in-plane velocity is radial, the in-plane director is also radial, namely

$$\boldsymbol{n}_{=} = \left(\frac{x}{\sqrt{x^2+y^2}}, \frac{y}{\sqrt{x^2+y^2}}, 0\right). \tag{2.22}$$

We shall now consider the Hele–Shaw flow within two coalescing droplets numerically.

2.3.1.2 Two squeezed coalescing droplets

As previously stated, using (2.11) we can define the droplet boundary $\partial A(t)$ implicitly for two coalescing droplets for $t_c \leq t < t_{\max}$. Using COMSOL Multiphysics, Poisson's equation for the fluid pressure (2.19) and the boundary condition (2.18) are solved numerically in $A(t)$. The fluid pressure p, in-plane fluid speed $|\boldsymbol{u}_{=}|$, and in-plane director $\boldsymbol{n}_{=}$, given by (2.12), are plotted in Figure 2.6 for the times (a) $t = 0.02\,\mathrm{s}$ (when $H = 54\,\mu\mathrm{m}$), (b) $t = 0.04\,\mathrm{s}$ (when $H = 34\,\mu\mathrm{m}$), and (c) $t = 0.06\,\mathrm{s}$ (when $H = 14\,\mu\mathrm{m}$). Figure 2.6 shows that the fluid pressure p initially attains a local maxima at the centre of each droplet and as t increases, and hence $H(t)$ decreases, the maximum in the pressure moves towards the centre of the two combined droplets. Figure 2.6 also shows that the in-plane fluid speed $|\boldsymbol{u}_{=}|$ is initially low throughout the droplets and as t increases, and hence $H(t)$ decreases, $|\boldsymbol{u}_{=}|$ increases, especially in the corners between the two droplets. The increased fluid speed in the corners between the two droplets was predicted in Section 2.1, where the corner speed $d'(t)$ was shown to be larger than the radial speed of the boundary of the droplets $R'(t)$. We note that there is a mismatch between the numerical results for $|\boldsymbol{u}_{=}|$ on $\partial A(t)$ and the simple model for the evolution of the droplet boundaries which we will discuss shortly. Figure 2.6 also shows that the in-plane director field $\boldsymbol{n}_{=}$ points radially outwards from the positions where a maximum in the fluid pressure occurs, and hence, as t increases and the two maxima in the fluid pressure approach the combined center between the two droplets, the director approaches a radial distribution, as seen for an isolated droplet.

The in-plane fluid speed $|\boldsymbol{u}_{=}|$ on $\partial A(t)$ is similar to the radial speed of the boundary of the droplets $R'(t)$ predicted by the simple model for the expanding droplet boundary, except at the corners formed between the droplets where there is a significant mismatch between $|\boldsymbol{u}_{=}|$ at $(\pm d(t),0)$ and the radial speed

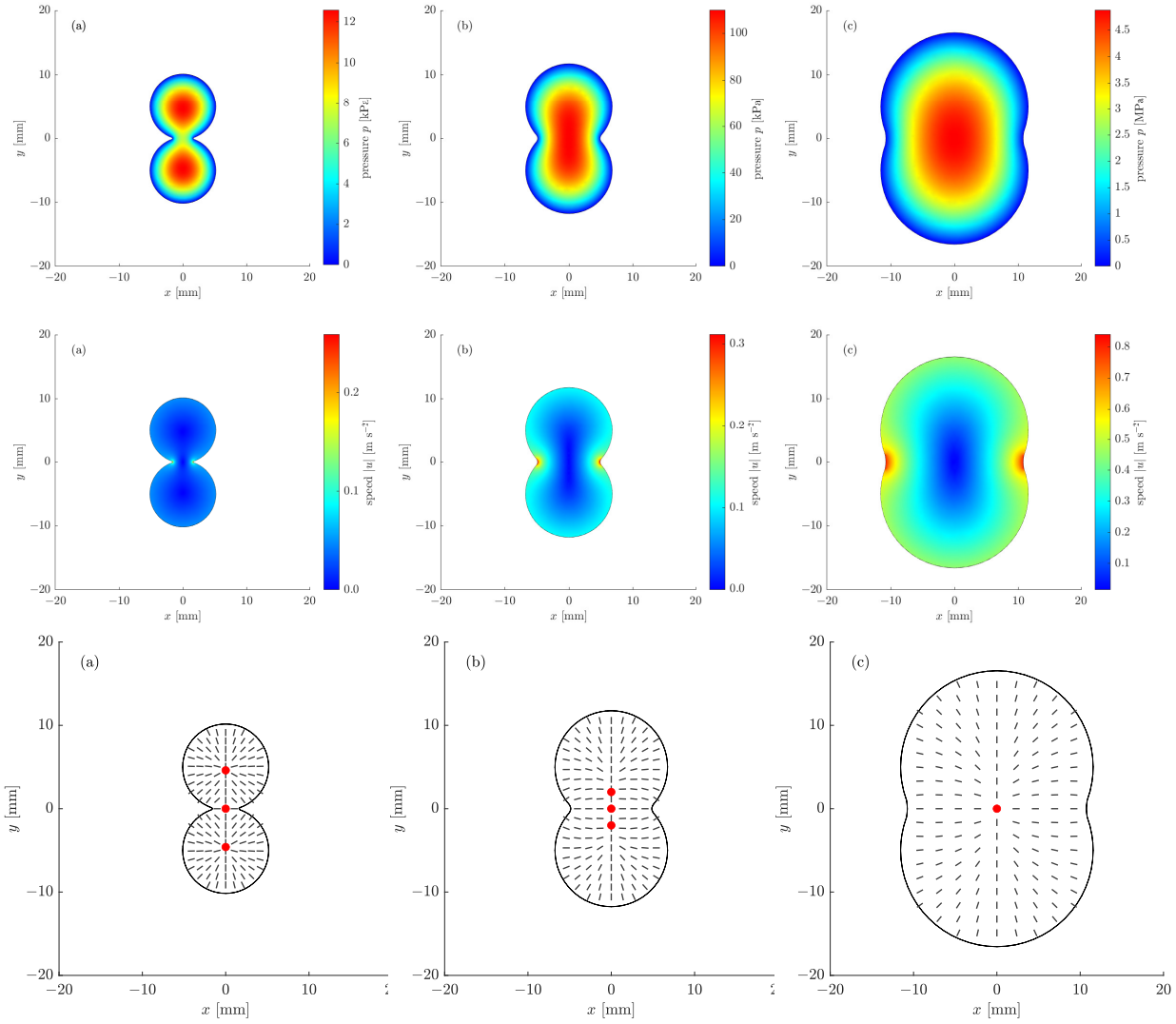

Figure 2.6: The fluid pressure p, in-plane fluid speed $|\boldsymbol{u}_{=}|$ and in-plane director field $\boldsymbol{n}_{=}$ in two coalescing droplets at (a) $t = 0.02\,\mathrm{s}$ (when $H = 54\,\mu\mathrm{m}$), (b) $t = 0.04\,\mathrm{s}$ (when $H = 34\,\mu\mathrm{m}$), and (c) $t = 0.06\,\mathrm{s}$ (when $H = 14\,\mu\mathrm{m}$) with $H(t) = \mathcal{H} - s_{\mathrm{p}}t$, the parameter values shown in Table 2.1, $\eta_{\mathrm{L}} = 0.0237\,\mathrm{Pa\,s}$ and $p_{\mathrm{vac}} = 1\,\mathrm{Pa}$. The position of the maxima in the fluid pressure is marked on the in-plane director field by a red dot.

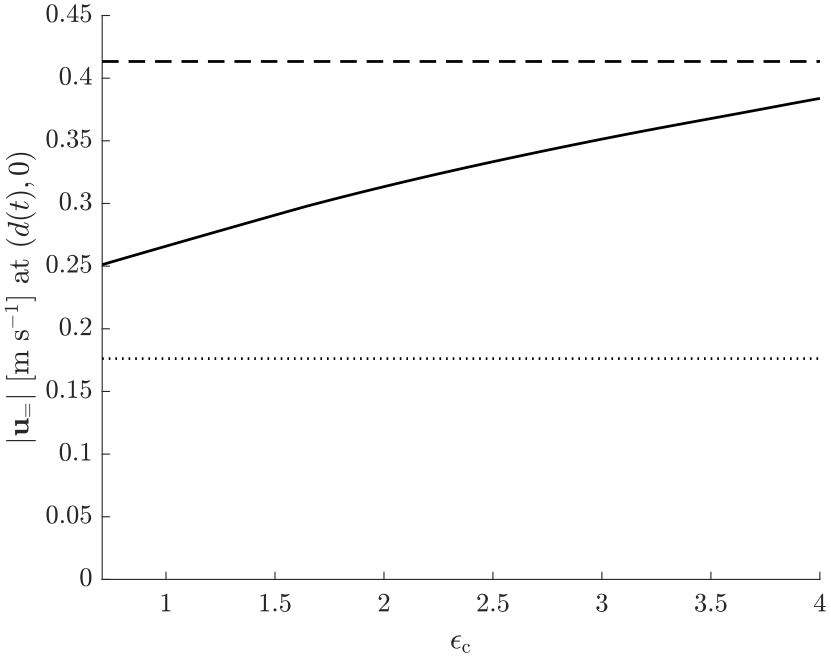

Figure 2.7: The in-plane fluid speed $|\boldsymbol{u}_=|$ at $(d(t), 0)$ as a function of ϵ_c for two coalescing droplets at $t = 0.04\,\mathrm{s}$ (when $H = 34\,\mu\mathrm{m}$) with $H(t) = \mathcal{H} - s_p t$, the parameter values shown in Table 2.1, $\eta_L = 0.0237\,\mathrm{Pa\,s}$ and $p_{vac} = 1\,\mathrm{Pa}$. The in-plane fluid speed $|\boldsymbol{u}_=|$ at $(d(t), 0)$ for a sharp corner without a quadratic Bézier curve (dashed) and the radial speed of the corner between the droplets $\dot{d}(t)$ (dotted) as predicted by the simple model for the expanding droplet boundary are also shown.

of the corners between droplets $d'(t)$. In particular, in Figure 2.6(b) at the point $(R(t), L)$, which is on $\partial A(t)$ but not at the corners, $|\boldsymbol{u}_=| = 0.114\,\mathrm{m\,s^{-1}}$ and $R'(t) = 0.119\,\mathrm{m\,s^{-1}}$ i.e. an error of 4.4%. Whereas in Figure 2.6(b) at the corner point $(d(t), 0)$, $|\boldsymbol{u}_=| = 0.314\,\mathrm{m\,s^{-1}}$ and $d'(t) = 0.176\,\mathrm{m\,s^{-1}}$ i.e. an error of 78.4%. We investigate this mismatch at the corner by varying the weight of the control points of the quadratic Bézier curve ϵ_c, namely varying the curvature of the corners formed between the droplets, which is implemented in COMSOL Multiphysics at the corners formed between the droplets. The in-plane fluid speed $|\boldsymbol{u}_=|$ at $(d(t), 0)$ as a function ϵ_c is plotted in Figure 2.7. Figure 2.7 shows that as ϵ_c is increased and the radius of curvature of the corners formed between the

droplets decreases, the in-plane fluid speed $|\boldsymbol{u}_{=}|$ at $(d(t), 0)$ approaches $|\boldsymbol{u}_{=}|$ at $(d(t), 0)$ calculated for a sharp corner without a quadratic Bézier curve (shown by the dashed line). As ϵ_{c} is decreased and the radius of curvature of the corners formed between the droplets increases, $|\boldsymbol{u}_{=}|$ at $(d(t), 0)$ decreases but remains significantly larger than the radial speed of the corner between the droplets $\dot{d}(t)$ (shown by the dashed line in Figure 2.7). We note that it is not sufficient to decrease ϵ_{c} to match $|\boldsymbol{u}_{=}|$ at $(d(t), 0)$ and $\dot{d}(t)$, as smaller values of ϵ_{c} correspond to increasing the radius of curvature of the corners formed between the droplets, which therefore leads to a geometry that is significantly different to the simple model for the expanding droplet boundary. We therefore note that despite the qualitative success of the present simple model, numerical results for the fluid speed and fluid pressure at the corners formed between the droplets should be used with caution to make quantitative predictions about the fluid speed and fluid pressure at the corners formed between droplets in squeezed coalescence. In any future considerations of the present work, surface tension should be included and coupled with, the conservation of volume and the Hele–Shaw equations.

2.3.2 Elasticity-dominated regime

We now consider a regime in which the dominant torque on the director derives from elasticity within two coalescing droplets. In this regime the in-plane director inside the two coalescing droplets will obey Laplace's equation for the director angle ϕ [201], namely

$$\frac{\partial^2 \phi}{\partial x^2} + \frac{\partial^2 \phi}{\partial y^2} = 0. \tag{2.23}$$

We apply homeotropic infinite anchoring (i.e. a Dirichlet condition) on the droplet boundary of the two coalescing droplets which is implemented using a Dirichlet

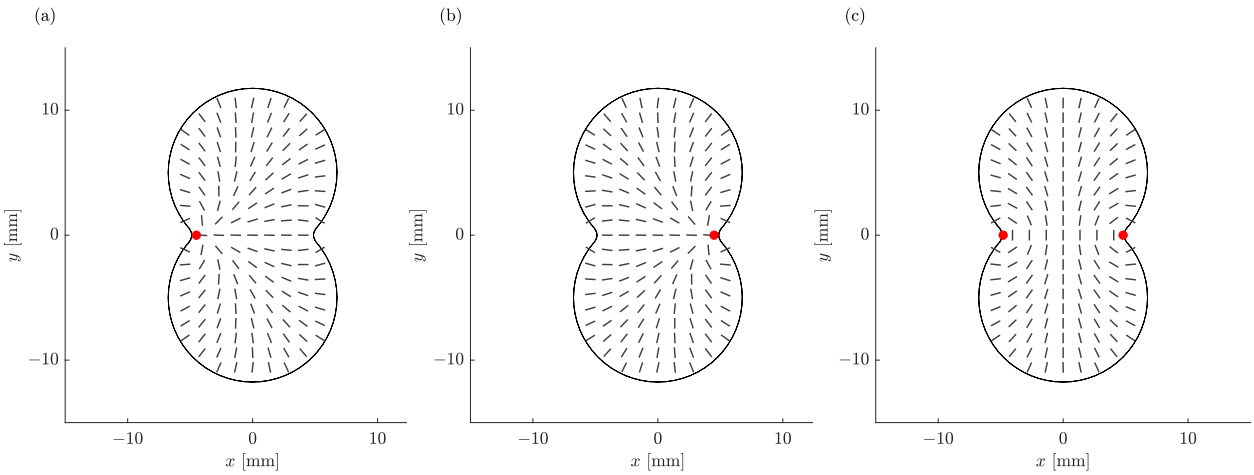

Figure 2.8: The in-plane director field $\boldsymbol{n}_{=}$ through two coalescing droplets in the elasticity-dominated regime for the three possible solutions,, (a) a defect at the left-hand corner between the droplets, (b) a defect at right-hand corner between the droplets, and (c) defects at both corners between the droplets, at $t = 0.04\,\mathrm{s}$ (when $H = 34\,\mu\mathrm{m}$). The position of the defects is indicated by the red dot.

condition on ϕ, given by

$$\hat{\boldsymbol{\nu}} \cdot \boldsymbol{n}_{=} = 1 \quad \text{on} \quad \partial A(t), \tag{2.24}$$

where $\hat{\boldsymbol{\nu}}$ is calculated from $\partial A(t)$ and is shown in Figure 2.5. As discussed in Section 1.7.3, homeotropic anchoring is typical on the interface between a nematic and air (or vacuum). Laplace's equation for the director angle (2.23) and the boundary condition (2.24) are solved in COMSOL Multiphysics and yield three possible solutions for the director. The three possible in-plane director solutions $\boldsymbol{n}_{=}$ are plotted in Figure 2.8 at $t = 0.04\,\mathrm{s}$ (when $H = 34\,\mu\mathrm{m}$). Figure 2.8 shows three different in-plane director solutions in the elasticity-dominated regime, namely solutions with a defect at the left-hand corner between the droplets, a defect at the right-hand corner between the droplets, and defects at both corners between the droplets.

2.4 Transmission of light through two coalescing droplets

We now consider the transmission of light through two squeezed coalescing droplets between cross polarisers to allow comparison between the in-plane director solutions described by the present model and the experimental setup discussed in Section 1.4.2 and shown in Figure 1.9. We approximate the transmission of light $T = T(x, y, t)$ through a layer of nematic with in-plane director angle ϕ with a polariser positioned on the bottom substrate and the top substrate aligned with the x-axis and y-axis, respectively, as

$$T = T_0 \sin^2(2\phi), \tag{2.25}$$

where T_0 is the transmission when the in-plane director is aligned 45° from both polarisers [12]. As discussed in Section 1.4.2, while the in-plane director is aligned parallel to either polariser, i.e. when $\phi = 0$ or $\phi = \pi/2$, there is no transmission of light and $T = 0$. If the in-plane director is aligned 45° from both polarisers, i.e. when $\phi = 3\pi/4$ or $\phi = \pi/4$, there is complete transmission of light and $T = T_0$. In situations between these extremes there is partial transmission of light and $0 < T < T_0$. The scaled transmission of light T/T_0 through two coalescing droplets in the flow-dominated regime and in the elasticity-dominated regime is shown in Figure 2.9 at (a) $t = 0.02\,\mathrm{s}$ (when $H = 54\,\mu\mathrm{m}$), (b) $t = 0.04\,\mathrm{s}$ (when $H = 34\,\mu\mathrm{m}$), and (c) $t = 0.06\,\mathrm{s}$ (when $H = 14\,\mu\mathrm{m}$). Figure 2.9(a)–(c) shows the evolution of the scaled transmission in the flow-dominated regime where initially there is a +1-defect at the centre of each droplet and there is also a −1-defect in the centre of the two combined droplets (the −1-defect and +1-defect are discussed Section 1.6). As the top substrate is lowered, the defects move towards the centre of the two combined droplets, as shown in Figure 2.9(c), leaving one

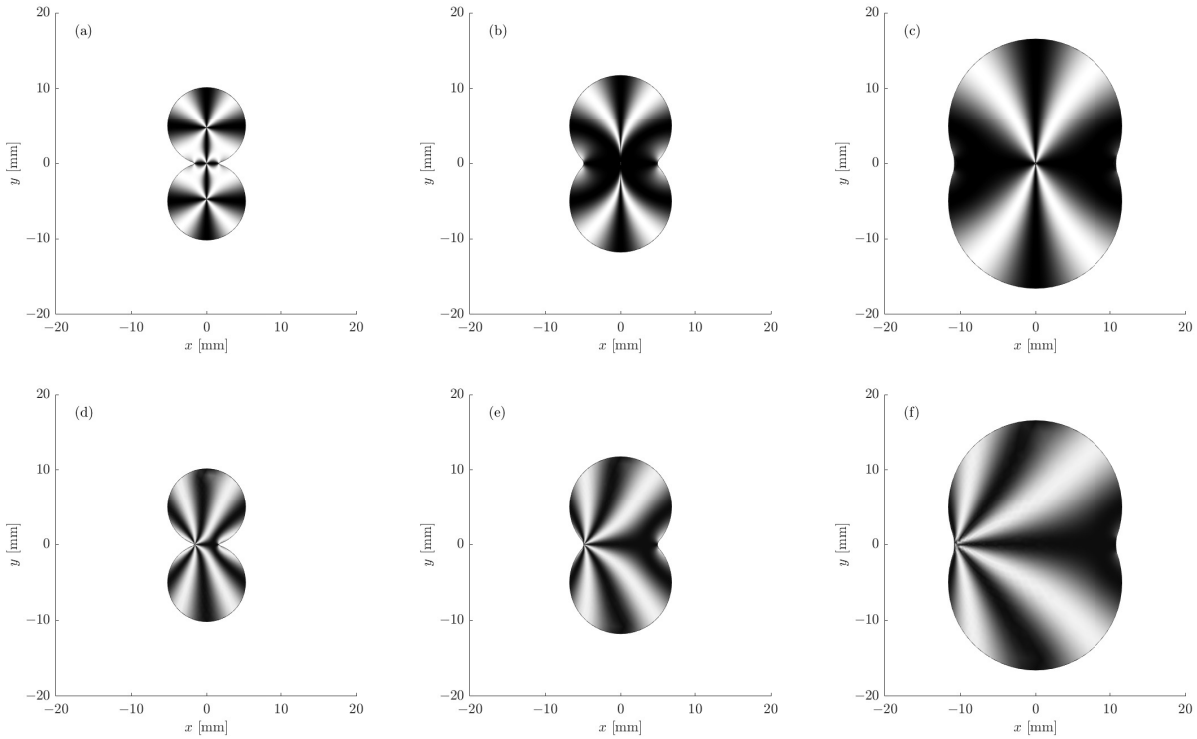

Figure 2.9: Scaled transmission of light T/T_0 through two squeezed coalescing droplets in the (a)–(c) flow-dominated regime and in the (d)–(f) elasticity-dominated regime at $t = 0.02\,\mathrm{s}$ (when $H = 54\,\mu\mathrm{m}$) in (a) and (d), $t = 0.04\,\mathrm{s}$ (when $H = 34\,\mu\mathrm{m}$) in (b) and (e), and $t = 0.06\,\mathrm{s}$ (when $H = 14\,\mu\mathrm{m}$) in (c) and (f) with $H(t) = \mathcal{H} - s_\mathrm{p} t$. Regions of white show complete transmission $T = 1$ and regions of black show no transmission $T = 0$.

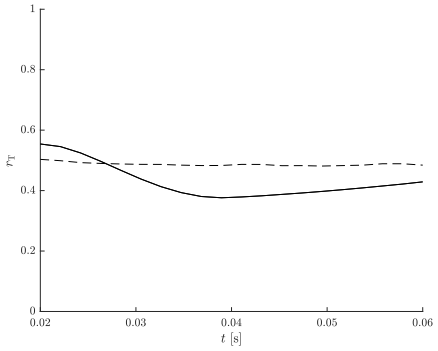

Figure 2.10: The ratio r_{T} for flow-dominated regime (solid line) and for the elasticity-dominated regime (dashed line) as a function of time t.

remaining +1-defect in the centre of the two combined droplets. Figure 2.9(d)–(f) shows the evolution of the scaled transmission for the elasticity-dominated regime for the solution where one defect remains in the left-hand corner between the coalescing droplets.

As the top substrate is lowered, there is a change in the transmission in both the flow-dominated regime (Figure 2.9(a)–(c)) and in the elasticity-dominated regime (Figure 2.9(d)–(f)). The change in the transmission can be quantified by the ratio r_{T} of the total transmission of light and the transmission when the in-plane director is aligned 45° from both polarisers throughout the two squeezed coalescing droplets, i.e.

$$r_{\mathrm{T}} = \frac{\int T/T_0 \, \mathrm{d}A(t)}{\int \mathrm{d}A(t)}. \tag{2.26}$$

Figure 2.10 shows changes in in the ratio r_{T} for flow-dominated regime (solid line) and for the elasticity-dominated regime (dashed line) as time increases. In particular, r_{T} shows small variation in the elasticity-dominated regime, whereas r_{T} clearly varies in the flow-dominated regime.

The transmission of light T for the elasticity-dominated regime is shown in

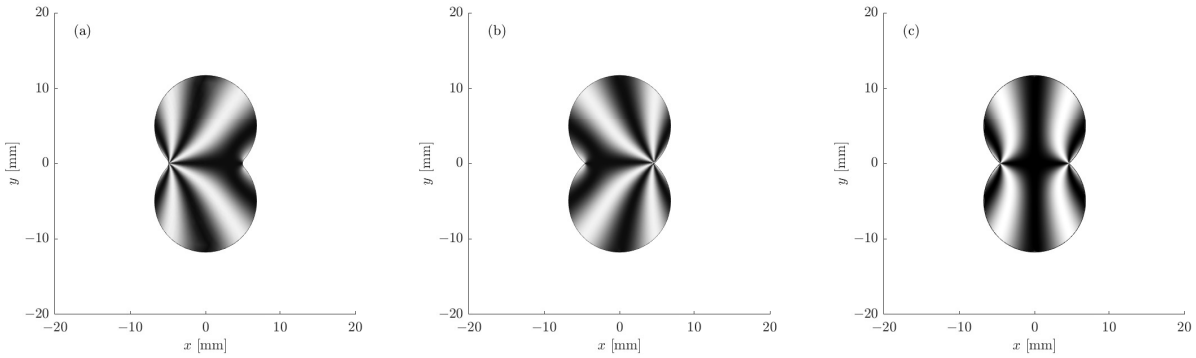

Figure 2.11: Transmission of light T through two coalescing droplets in the elasticity-dominated regime for the three possible solutions, (a) a defect at the left-hand corner between the droplets, (b) a defect at right-hand corner between the droplets, and (c) defects at both corners between the droplets, at $t = 0.04\,\mathrm{s}$ (when $H = 34\,\mu\mathrm{m}$). Regions of white show full transmission $T = 1$ and regions of black show no transmission $T = 0$.

Figure 2.11 at $t = 0.04\,\mathrm{s}$ (when $H = 34\,\mu\mathrm{m}$) for the three different numerical solutions obtained from (2.23) and (2.24). We also find that the two other in-plane director solutions, namely the defect on right-hand corner between the droplets and the defects on both the corners between the droplets in the elasticity-dominated regime, also show little change in transmission as the top substrate is lowered.

Comparing the transmission shown in Figure 2.9 and the experimental photographs of the transmission of light through a two-droplet ODF test setup shown in Figure 1.9, we see a striking resemblance between the photographs of transmission in the two-droplet ODF test setup and the flow-dominated regime. This, at least qualitatively, indicates that these experimental images of a two-droplet ODF test setup show the director behaving in a flow-dominated regime like Figure 2.9(a)–(c), and that the strong radial flow present in the ODF test setup is holding the defects in place at the centre of the droplets. Furthermore, we can say that the experimental photographs are significantly different to behaviour

seen in elasticity-dominated regime, where the defects are located on the droplet boundaries, as shown in Figure 2.9(d)–(f).

2.5 Conclusions

This chapter presented a simple model for the squeezed coalescence of nematic droplets between converging substrates. This simple model assumed that the timescale for coalescence due to surface tension is much longer than the timescale of coalescence due to squeezing. Therefore, the droplet boundaries evolve due to the conservation of volume, neglecting the effects of surface tension, elasticity, anchoring, and contact line dynamics. In practice, we should be able to justify this assumption by calculating the timescale of coalescence due to surface tension and showing that it is much longer than the time taken for the converging substrates to meet. A naive estimate of the timescale of coalescence due to surface tension in the ODF method can be made using the well-known timescale for the coalescence of two identical neighbouring droplets with radius $\bar{R}$ on a single stationary substrate, namely $\tau_{\mathrm{c}} = \sqrt{\rho \bar{R}^3/\sigma}$ [107, 231], where ρ is droplet density and σ is the droplet surface tension. For typical parameters values for the ODF method (as stated in Table 1.1) and material parameters for the nematic 5CB, for which $\rho = 1020\,\mathrm{kg\,m^{-3}}$ [63] and $\sigma = 4.000 \times 10^{-2}\,\mathrm{N\,m^{-1}}$ [61], coalescence of two identical neighbouring droplets occurs on the timescale $\tau_{\mathrm{c}} \simeq 10^{-4}$–$10^{-1}\,\mathrm{s}$ [107, 231], which is on the same order as the time taken for the converging substrates to meet is 10^{-3}–$10^{-1}\,\mathrm{s}$. This naive estimate of the timescale may indicate that surface tension effects could play an important role in the evolution of the droplet boundaries in the ODF method. However, this is not in agreement with the experimental photographs shown in Figure 1.9. In particular, Figure 1.9 shows that sharp corners formed where the droplets meet are visible in all three photographs, indicating that surface tension effects, which would tend to remove these regions

of high curvature, are acting on a much slower timescale than the expansion of the droplet boundaries. Clearly further work is required to determine the role played by surface tension effects in the ODF method.

In Section 2.1 we have assumed that each droplet can be modelled as a cylinder of constant volume so that as the gap between the substrates decreases, the evolution of the droplet boundary can be obtained using geometrical methods. This model allows us to obtain implicit expressions for the droplet boundary, which can be differentiated with respect to time to yield the radial speed of the droplet boundary $R'(t)$ for any arrangement of droplets. In Section 2.1 we considered an arrangement of three droplets positioned on the vertices of an equilateral triangle to allow direct comparison with the ODF mura shown in Figure 1.10. We hypothesised that the formation of the ODF mura is associated with stresses on the alignment layer caused by the advancing droplet boundary, and therefore assumed that the value of $R'(t)$ is proportional to the deformation to the director structure at any point on the substrate. Areas on the substrate for which $R'(t)$ is highest will therefore correspond to areas on the substrate for which the largest deformation to the director structure occurs. The deformation to the director structure, shown in Figure 2.4, shows a striking similarity to the ODF mura, shown in Figure 1.10. This similarity indicates that there may be a link between the formation of the ODF mura and the radial speed of the droplet boundaries in the ODF method.

The present simple model can therefore be used to suggest methods to reduce $R'(t)$, and hence, potentially to reduce the ODF mura. An obvious approach to reduce $R'(t)$ is to reduce the speed at which the top substrate is lowered, i.e. reduce $H'(t)$. Another possible method would be to dispense the total volume of nematic required for the ODF method into more droplets with a lower volume. The radial speed of the boundary of the droplets $R'(t)$ for a one droplet, two

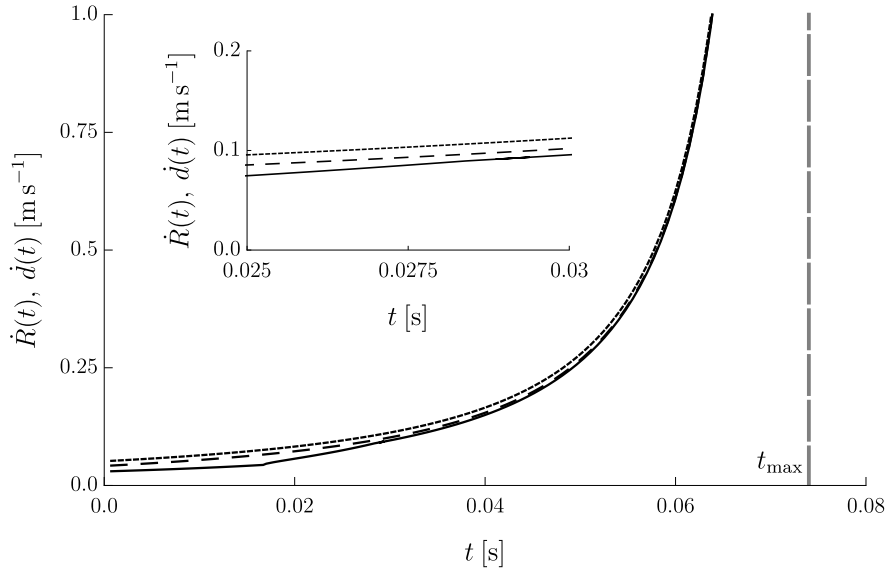

Figure 2.12: Radial speed of the boundary of the droplets $R'(t)$ for a one droplet (dotted line), two droplet (dashed line) and three droplet (solid line) arrangement of equal volume, as functions of time t with $H(t) = \mathcal{H} - s_{\mathrm{p}}t$ and the ODF parameter values shown in Table 2.1. Each arrangement of droplets has total volume $V = 1.350 \times 10^{-9}\,\mathrm{m}^3$.

droplet and three droplet arrangement of equal volume is shown in Figure 2.12. Figure 2.12 shows that the radial speed of the boundary of the droplets for a fixed volume decreases as the number of droplets increases. In reality, both of these methods to reduce $R'(t)$ are likely to increase manufacturing times as reducing the speed at which the top substrate is lowered will increase the time taken to fill the nematic layer and increasing the number of droplets dispensed increase the time taken to dispense the droplets. Manufacturers, who are often interested in decreasing manufacturing times to increase potential profits, may not want to pursue these options.

We have also considered the fluid velocity and director structure within the nematic droplets in two extreme regimes. Firstly, a flow-dominated regime in which the in-plane director aligns with the fluid velocity vector was considered, and secondly, an elasticity-dominated regime in which the in-plane director obeys

the Laplace equation (2.23) was considered. We have obtained the transmission of light through a two droplet setup in both of these regimes to allow us to make direct comparisons with experimental photographs of the transmission of light in a two-droplet ODF test setup shown in Figure 1.9. In the flow-dominated regime, we find a +1-defect in the centre of each droplet and a −1-defect in the centre of the two combined droplets. As the top substrate is lowered, the defects move towards the centre of the two combined droplets and combine. In the elasticity-dominated regime, there are three possible solutions for the in-plane director, namely a defect on the left-hand corner formed between droplets, a defect on the right-hand corner formed between droplets, and defects on both of the corners formed between droplets. In the elasticity-dominated regime, as the top substrate is lowered, the defects show little change. Upon comparison with the experimental photographs shown in Figure 1.9, we see a striking resemblance between the experimental photographs and the transmission of light in the flow-dominated regime.

The qualitative agreement of the ODF mura (shown in Figure 1.10) and the deformation to the director structure (shown in Figure 2.4), and the experimental photographs of transmission of light in a two-droplet ODF test setup (shown in Figure 1.9) and the transmission of light in the flow-dominated regime (shown in Figure 2.9(a)–(c)) indicate that the simple model considered in this chapter is remarkably successful. Further effort should be made in future studies to consider a regime in which flow, elasticity, and surface tension all play a role in the squeezed coalescence, however, this is beyond the scope of this thesis. We will now proceed in Chapter 3 by considering the full Ericksen–Leslie modelling of the director and fluid velocity within a single squeezed nematic droplet and then in Chapter 4 taking a closer examination of how significant transient flow-driven distortion of the nematic molecules at the substrates may lead to the formation of the ODF mura.

Chapter 3

Squeezing a nematic droplet with strong elasticity effects

We now focus on the behaviour of the director orientation and flow within a single nematic droplet in the ODF method. The flow of the nematic during the ODF method after the top plate has made contact with a single drop is similar to the classical squeeze-film problem in Newtonian fluid dynamics [100]. In this chapter we therefore consider a nematic squeeze-film problem, in which director orientation and flow are coupled, using the Ericksen–Leslie equations in place of the Navier–Stokes equations used to describe the Newtonian problem.

In Section 3.1, we formulate a squeeze-film model for the ODF method in which we assume an idealised form of the shape of the nematic drop, for four specific director anchoring cases at the substrate that are commonly used in LCDs, and for two scenarios for the motion of the top plate. After non-dimensionalising the governing equations and boundary conditions, in Section 3.2 we consider the asymptotic regime in which elasticity effects are much stronger than viscous ones, and solve the resulting system of equations and boundary conditions in order to better understand the effects of director–flow coupling. In particular, we obtain

analytical expressions for the director, velocity and pressure, as well as the force on the top plate (when the speed of the top plate is prescribed in Section 3.3) and the speed of the top plate (when the force on the top plate is prescribed in Section 3.4).

3.1 Model formulation

In order to model the squeezing and spreading of a nematic drop which occurs during the ODF method we use the same simplified model for the geometry of the droplet as considered in Chapter 2. In particular, we assume that at some time $t < 0$ the top substrate and the drop make contact, and that by time $t = 0$ any transient initial effects arising from starting the squeezing process can be ignored. For $t \geq 0$ we assume that the drop of nematic is cylindrical in shape, lies between the moving top substrate at $z = H(t)$ and the fixed bottom substrate at $z = 0$, and has radius $R(t)$ and height equal to the height of the top substrate $H(t)$, as shown in Figure 3.1. The substrates are assumed to have a fixed area, denoted by A_{S}, where we assume that throughout squeezing $A_{\mathrm{S}} > \pi R(t)^2$. The constant volume of the drop of nematic V is given in terms of its radius $R(t)$ and height $H(t)$ by

$$V = \pi R(t)^2 H(t). \tag{3.1}$$

Similarly to Chapter 2, by conservation of volume, the outer boundary of the nematic, $r = R(t)$, moves outward radially as the top substrate moves towards the bottom substrate. We consider two different ambient pressures; the internal ambient pressure between the top substrate and the bottom substrate, denoted by p_{I}, and the external ambient pressure above the top substrate, denoted by p_{E}. As discussed in Section 1.4.2, typically, manufacturing processes are carried out

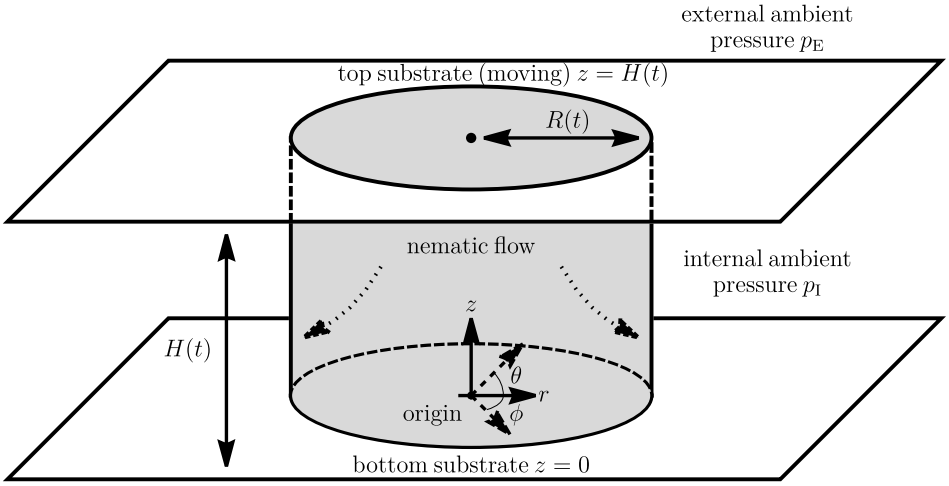

Figure 3.1: A schematic diagram of a nematic squeeze-film problem consisting of a cylindrical drop of radius $R(t)$ of nematic (grey) between a moving top substrate at $z = H(t)$ and a fixed bottom substrate at $z = 0$. The motion of the top substrate induces a flow of the nematic as indicated. The internal ambient pressure p_{I}, external ambient pressure p_{E}, the director angle θ, and the axisymmetric coordinates used to describe the problem are also indicated.

in a vacuum to avoid the formation of air bubbles [106], so in what follows we often set $p_{\mathrm{I}} = p_{\mathrm{E}} = 0$.

To model the squeezing and spreading of the nematic drop we use the Ericksen–Leslie equations [49, 66, 127, 201] to describe the dynamics of the director orientation, velocity and pressure, which were detailed in Section 1.8. At both the substrates we impose the standard no-slip and no-penetration conditions for the velocity. In addition, we assume that the director is at a fixed angle to the substrate surface normal with an infinite anchoring condition [201]. Although the analysis presented below is valid for any fixed angles of the director at the substrates, we will focus on four specific cases of infinite anchoring that are commonly used in LCDs, namely planar, homeotropic, hybrid aligned nematic (HAN), and π-cell anchoring [228]. All of these anchoring cases involve various combinations of the director being aligned parallel or perpendicular to the boundaries. In ad-

dition to the four anchoring cases, two different scenarios for the motion of the top substrate will be studied. The first scenario corresponds to the current ODF method in which the top substrate is moved downwards at a prescribed constant speed, and is hereafter referred to as the "prescribed speed" scenario. The second scenario corresponds to the situation in which the top substrate moves downwards under a prescribed force (such as, for example, its own weight), and is hereafter referred to as the "prescribed force" scenario.

3.1.1 The Ericksen–Leslie equations

We assume that both the director field and the velocity remain axisymmetric so that all dependent variables are independent of the twist angle, ϕ, shown in Figure 3.1. The director is assumed to lie in the r–z-plane, and can therefore be described by the radial-tilt angle θ between the director and the radial direction, also shown in Figure 3.1. We therefore write the director, pressure and velocity in the form

$$\boldsymbol{n} = \cos\left(\theta(r,z,t)\right)\hat{\mathbf{e}}_r + \sin\left(\theta(r,z,t)\right)\hat{\mathbf{e}}_z, \tag{3.2}$$

$$\mathbf{u} = u\left(r,z,t\right)\hat{\mathbf{e}}_r + w\left(r,z,t\right)\hat{\mathbf{e}}_z, \tag{3.3}$$

$$p = p(r,z,t), \tag{3.4}$$

where u is the component of velocity in the radial direction $\hat{\mathbf{e}}_r$ and w is the component of velocity in the vertical direction $\hat{\mathbf{e}}_z$. The Ericksen–Leslie equations, introduced in Section 1.8, for the director, velocity and pressure in the form of (3.2)–(3.4), respectively, are obtained from (1.20) and (1.21) in axisymmetric

form, and are given by

$$0 = \frac{1}{r}\frac{\partial (ru)}{\partial r} + \frac{\partial w}{\partial z}, \tag{3.5}$$

$$\rho \dot{u} + \frac{\partial p}{\partial r} = \frac{\partial}{\partial r}\left(\frac{\partial \mathcal{D}}{\partial u_r}\right) + \frac{\partial}{\partial z}\left(\frac{\partial \mathcal{D}}{\partial u_z}\right) - \theta_r \frac{\partial \mathcal{D}}{\partial \dot{\theta}}, \tag{3.6}$$

$$\rho \dot{w} + \frac{\partial p}{\partial z} = \frac{\partial}{\partial r}\left(\frac{\partial \mathcal{D}}{\partial w_r}\right) + \frac{\partial}{\partial z}\left(\frac{\partial \mathcal{D}}{\partial w_z}\right) - \theta_z \frac{\partial \mathcal{D}}{\partial \dot{\theta}}, \tag{3.7}$$

$$0 = \frac{\partial}{\partial r}\left(\frac{\partial \omega_F}{\partial \theta_r}\right) + \frac{\partial}{\partial z}\left(\frac{\partial \omega_F}{\partial \theta_z}\right) - \frac{\partial \omega_F}{\partial \theta} - \frac{\partial \mathcal{D}}{\partial \dot{\theta}}, \tag{3.8}$$

where the subscripts r and z in θ_r, θ_z, u_r, u_z, w_r and w_z represent partial derivatives with respect to that variable, a superposed dot denotes the material time derivative, and ρ is the constant fluid density. To produce a mathematically tractable system of equations we use the one-constant approximation of the Oseen–Frank bulk elastic energy density (1.14), which is given in axisymmetric form by

$$\omega_F = \frac{K}{2}\left[\left(\frac{\partial \theta}{\partial z}\right)^2 + \left(\frac{\partial \theta}{\partial r}\right)^2 + \frac{\cos^2\theta}{r^2}\right]. \tag{3.9}$$

The dissipation function $\mathcal{D}$ is obtained from a reformulation of the nematic viscous anisotropic stress tensor that can be found in Stewart [201]. We use the form for the dissipation function proposed by Leslie [127] given by

$$\begin{aligned}\mathcal{D} =& \frac{1}{2}\Big[\alpha_1 \left(n_i e_{ij} n_j\right)^2 + 2\gamma_2 N_i e_{ij} n_j + \alpha_4 e_{ij} e_{ij} \\ &+ \left(\alpha_5 + \alpha_6\right) n_i e_{ij} e_{jk} n_k + \gamma_1 N_i N_i\Big],\end{aligned} \tag{3.10}$$

where the components of the rate of strain tensor e_{ij}, the co-rotational time flux of the director $\boldsymbol{N}$, the components of the vorticity tensor W_{ij}, the rotational viscosity $\gamma_1 = \alpha_3 - \alpha_2$, the torsional viscosity $\gamma_2 = \alpha_3 + \alpha_2$, and the Leslie

viscosities α_l are defined in Section 1.8. Using (3.2) and (3.3) leads to

$$\begin{aligned}\mathcal{D} = \frac{1}{2}\Bigg[&\alpha_1\left(u_r\cos^2\theta + \frac{1}{2}(u_z+w_r)\sin 2\theta + w_z\sin^2\theta\right)^2 \\ &+ 2\gamma_2\left(\frac{1}{2}(w_z-u_r)\sin 2\theta + \frac{1}{2}(u_z+w_r)\cos 2\theta\right)\left(\dot\theta + \frac{1}{2}(u_z-w_r)\right) \\ &+ \alpha_4\left(u_r^2 + \frac{u^2}{r^2} + \frac{1}{2}\left(u_z+w_r\right)^2 + w_z^2\right) \\ &+ \left(\alpha_5+\alpha_6\right)\left(u_r^2\cos^2\theta + \frac{1}{4}(u_z+w_r)^2 + w_z^2\sin^2\theta\right) \\ &+ \gamma_1\left(\dot\theta + \frac{1}{2}(u_z-w_r)\right)^2\Bigg]. \end{aligned} \tag{3.11}$$

3.1.2 Non-dimensionalisation

In order to determine the important parameter groups, and to enable progress in considering important asymptotic regimes, the equations are now non-dimensionalised according to

$$\begin{aligned}
t &= \frac{\mathcal{R}}{\mathcal{U}}\hat t, & r &= \mathcal{R}\hat r, & z &= \mathcal{H}\hat z, & & \\
V &= \mathcal{R}^2\mathcal{H}\hat V, & R(t) &= \mathcal{R}\hat R(t), & H(t) &= \mathcal{H}\hat h(t), & A &= \mathcal{R}^2\hat A, \\
\theta &= \hat\theta, & u &= \mathcal{U}\hat u, & w &= \frac{\mathcal{U}\mathcal{H}}{\mathcal{R}}\hat w, & p &= \frac{\mu\mathcal{U}\mathcal{R}}{\mathcal{H}^2}\hat p, \\
\gamma_1 &= \mu\hat\gamma_1, & \gamma_2 &= \mu\hat\gamma_2, & \alpha_1 &= \mu\hat\alpha_1, & \alpha_2 &= \mu\hat\alpha_2, \\
\alpha_3 &= \mu\hat\alpha_3, & \alpha_4 &= \mu\hat\alpha_4, & \alpha_5 &= \mu\hat\alpha_5, & \alpha_6 &= \mu\hat\alpha_6, \\
\omega_F &= \frac{K}{\mathcal{H}^2}\hat\omega_F, & \mathcal{D} &= \frac{\mu\mathcal{U}^2}{\mathcal{H}^2}\hat{\mathcal{D}}, & F &= \frac{\mu\mathcal{U}\mathcal{R}^3}{\mathcal{H}^2}\hat F, & W_p &= \frac{\mu\mathcal{U}\mathcal{R}^3}{\mathcal{H}^2}\hat W_p
\end{aligned} \tag{3.12}$$

where the caret ($\hat{}$) denotes non-dimensional variables, F is the force on the top substrate, which will be introduced in Section 3.2.3, and W_p is the weight of the top substrate, which will be introduced in Section 3.4. Typical values of the radial scale $\mathcal{R}$, height scale $\mathcal{H}$ and radial velocity scale $\mathcal{U}$ are given in Section 3.1.5.

The viscosity used in the non-dimensionalisation (3.12) is the isotropic viscosity, namely $\mu = \alpha_4/2$ or $\mu = \eta_3$ [148, 201].

The non-dimensional aspect ratio δ, defined by the ratio of the height scale $\mathcal{H}$ and the radial scale $\mathcal{R}$, is

$$\delta = \frac{\mathcal{H}}{\mathcal{R}}. \tag{3.13}$$

In practice, the aspect ratio is typically small, corresponding to a thin film of nematic, for which the radial length scale is much larger than the height scale, and so a thin-film (i.e. small δ) approximation is appropriate. The reduced Reynolds number, defined by

$$\mathrm{Re} = \frac{\rho \mathcal{U} \mathcal{H}^2}{\mu \mathcal{R}}, \tag{3.14}$$

is a non-dimensional measure of the relative strength of inertial effects and viscous effects. The limit of zero Reynolds number ($\mathrm{Re} \to 0$) corresponds to a regime in which there are no inertial effects (i.e. Stokes flow), while the limit of infinite Reynolds number ($\mathrm{Re} \to \infty$) corresponds to a regime in which there are no viscous effects (i.e. inviscid flow). The Ericksen number, defined by

$$\mathrm{Er} = \frac{\mu \mathcal{U} \mathcal{H}}{K}, \tag{3.15}$$

is a non-dimensional measure of the relative strength of viscous effects and splay elastic effects. The limit of zero Ericksen number ($\mathrm{Er} \to 0$) corresponds to a regime in which there are no viscous effects, while the limit of infinite Ericksen number ($\mathrm{Er} \to \infty$) corresponds to a regime in which there are no elastic effects.

From (3.5)–(3.8) the non-dimensional equations that govern the director angle θ, the radial velocity component u, the vertical velocity component w, and the

pressure p are

$$0 = \frac{1}{r}\frac{\partial(ru)}{\partial r} + \frac{\partial w}{\partial z}, \tag{3.16}$$

$$\begin{aligned}
\mathrm{Re}\,\rho\dot{u} + p_r = \frac{\partial}{\partial r}\Bigg[&\hat{\alpha}_1\Big(\delta^2 u_r\cos^4\theta + \left(\delta u_z + \delta^3 w_r\right)\sin\theta\cos^3\theta + \delta^2 w_z\sin^2\theta\cos^2\theta\Big) \\
&- \frac{\hat{\gamma}_2}{2}\left(\delta^3 u_r\dot{\theta}\sin 2\theta + \frac{1}{2}\left(\delta^2 u_z - \delta^4 w_r\right)u_r\sin 2\theta\right) \\
&+ 2\delta u_r + \left(\hat{\alpha}_5 + \hat{\alpha}_6\right)\delta u_r\cos^2\theta\Bigg] \\
+ \frac{\partial}{\partial z}\Bigg[&\hat{\alpha}_1\Big(\delta u_r\sin\theta\cos^3\theta + \left(u_z + \delta^2 w_r\right)\sin^2\theta\cos^2\theta + \delta^2\hat{w}_z\sin^3\theta\cos\theta\Big) \\
&+ \frac{\gamma_2}{2}\left(\delta\dot{\theta}\cos 2\theta + \frac{1}{2}\left(u_z - \delta u_r\right)\cos 2\theta + \frac{1}{2}\left(\delta w_z - \delta u_r\right)\sin 2\theta\right. \\
&\qquad\left. + \frac{1}{2}\left(u_z + \delta^2 w_r\right)\cos 2\theta\right) \\
&+ \left(u_z + \delta^2 w_r\right) + \frac{\left(\hat{\alpha}_5 + \hat{\alpha}_6\right)}{4}\left(u_z + \delta^2 w_r\right) \\
&+ \frac{\hat{\gamma}_1}{2}\left(\delta\dot{\theta} + \frac{1}{2}(u_z - \delta^2 w_r)\right)\Bigg] \\
- \frac{\hat{\gamma}_2}{2}&\left((\delta^2 w_z - \delta^2 u_r)\theta_r\sin 2\theta + (\delta u_z + \delta^3 w_r)\theta_r\cos 2\theta\right) \\
+ \hat{\gamma}_1&\left(\delta^2\theta_r\dot{\theta} + \frac{1}{2}(\delta u_z - \delta^3 w_r)\theta_r\right),
\end{aligned} \tag{3.17}$$

$$\delta^2 \operatorname{Re} \rho \dot{w} + p_z = \frac{\partial}{\partial r}\Bigg[\hat{\alpha}_1\Bigg(\delta^3 u_r \sin\theta\cos^3\theta + \frac{1}{2}\left(\delta^2 u_z + \delta^4 w_r\right)\sin^2\theta\cos^2\theta + \delta^3 w_z \sin^3\theta\cos\theta\Bigg) - \frac{\hat{\gamma}_2}{4}\left(\left(\delta^3 w_z - \delta^3 u_r\right)\sin 2\theta + \left(\delta^2 u_z + \delta^4 w_r\right)\cos 2\theta\right) + \frac{\hat{\gamma}_2}{2}\left(\delta^3\dot{\theta}\cos 2\theta + \frac{1}{2}\left(\delta^2 u_z - \delta^4 w_r\right)\cos 2\theta\right) \frac{\hat{\alpha}_4}{2}\left(\delta^2 u_z + \delta^4 w_r\right) + \frac{\left(\hat{\alpha}_5 + \hat{\alpha}_6\right)}{4}\left(\delta^2 u_z + \delta^4 w_r\right) - \frac{\hat{\gamma}_1}{2}\left(\delta^3\dot{\theta} + \frac{1}{2}\left(\delta^2 u_z - \delta^4 w_r\right)\right)\Bigg] + \frac{\partial}{\partial z}\Bigg[\hat{\alpha}_1\left(\delta^2 u_r \sin^2\theta\cos^2\theta + \left(\delta u_z + \delta^3 w_r\right)\sin^3\theta\cos\theta + \delta^2 w_z \sin^4\theta\right) + \frac{\hat{\gamma}_2}{2}\left(\delta^2\dot{\theta}\sin 2\theta + \frac{1}{2}\left(\delta u_z - \delta^3 w_r\right)\sin 2\theta\right) + \hat{\alpha}_4\delta^2 w_z + \left(\hat{\alpha}_5 + \hat{\alpha}_6\right)\delta^2 w_z \sin^2\theta\Bigg] - \frac{\hat{\gamma}_2}{2}\left(\left(\delta^2 w_z - \delta^2 u_r\right)\theta_z \sin 2\theta + \left(\delta u_z + \delta^3 w_r\right)\theta_z \cos 2\theta\right) + \hat{\gamma}_1\left(\delta^2\dot{\theta}\theta_z + \frac{1}{2}\left(\delta u_z - \delta^3 w_r\right)\theta_z\right), \tag{3.18}$$

and

$$0 = \theta_{zz} - \frac{1}{2}\operatorname{Er} u_z\left(\gamma_1 + \gamma_2\cos 2\theta\right) + \delta\operatorname{Er}\left[-\gamma_2\frac{1}{2}(w_z - u_r)\sin 2\theta - \gamma_1\dot{\theta}\right] + \delta^2\left[\theta_{rr} - \frac{2\sin 2\theta}{r^2} - \frac{1}{2}\operatorname{Er} w_r\left(\gamma_1 + \gamma_2\cos 2\theta\right)\right], \tag{3.19}$$

where we have now dropped the caret ($\hat{}$) notation for simplicity since all quantities are now non-dimensional. We will later solve (3.16)–(3.19) using certain assumptions made about the size of the relative non-dimensional parameters δ, Re and Er and subject to appropriate boundary conditions on θ, u, w and p.

3.1.3 Rescaled radial and vertical coordinates

Before proceeding further, it is convenient to rescale the radial and vertical coordinates according to

$$\tilde{r} = \frac{r}{R(t)} = \sqrt{\frac{\pi}{V}} H(t)^{1/2} r \quad \text{and} \quad \tilde{z} = \frac{z}{H(t)}, \tag{3.20}$$

where $\tilde{r}$ is the rescaled radial coordinate and $\tilde{z}$ is the rescaled vertical coordinate, and where $\tilde{r}$ can be expressed in terms of the height of the top substrate $H(t)$ using (3.1). In terms of the rescaled vertical coordinate $\tilde{z}$, the top substrate and bottom substrate are fixed at $\tilde{z} = 1$ and $\tilde{z} = 0$, respectively. The change in the height of the top substrate $H(t)$ is included in the rescaled versions of the Ericksen–Leslie equations (3.16)–(3.19) via the appropriate rescaling of derivatives of r and z, namely $\partial/\partial r \to V^{-1/2}\pi^{1/2}H(t)^{1/2}\partial/\partial\tilde{r}$ and $\partial/\partial z \to H(t)^{-1}\partial/\partial\tilde{z}$, respectively.

Henceforth we will express all equations and boundary conditions in terms of the rescaled coordinates $\tilde{r}$ and $\tilde{z}$ given by (3.20). However, for clarity and to aid physical interpretation, we will plot results in terms of the original unscaled radial coordinate r and vertical coordinate z.

3.1.4 Boundary conditions

In order to solve (3.16)–(3.19), appropriate boundary conditions must be imposed on the variables θ, u, w and p. For the velocity components, u and w, we impose no-slip and no-penetration conditions on the solid boundaries at $\tilde{z} = 0$ and $\tilde{z} = 1$. The bottom substrate at $\tilde{z} = 0$ is stationary and the top substrate at $\tilde{z} = 1$ is moving with vertical velocity $H'(t) = \mathrm{d}H/\mathrm{d}t$, and so the appropriate boundary conditions are $u(\tilde{r}, 0, t) = 0$, $u(\tilde{r}, 1, t) = 0$, $w(\tilde{r}, 0, t) = 0$ and $w(\tilde{r}, 1, t) = H'(t)$. The pressure, p, is assumed to be fixed at the constant internal ambient pressure, p_{I}, at the outer edge of the nematic drop, so that $p(1, \tilde{z}, t) = p_{\mathrm{I}}$. We impose

regularity and axisymmetry at the centre of the drop by assuming that $\partial p/\partial \tilde{r} = 0$ at $\tilde{r} = 0$. In summary, the boundary conditions for velocity and pressure are

$$u = 0 \quad \text{on } \tilde{z} = 0, \tag{3.21}$$

$$w = 0 \quad \text{on } \tilde{z} = 0, \tag{3.22}$$

$$u = 0, \quad \text{on } \tilde{z} = 1, \tag{3.23}$$

$$w = H'(t) \quad \text{on } \tilde{z} = 1, \tag{3.24}$$

$$\frac{\partial p}{\partial \tilde{r}} = 0 \quad \text{on } \tilde{r} = 0, \tag{3.25}$$

$$p = p_{\mathrm{I}} \quad \text{on } \tilde{r} = 1. \tag{3.26}$$

As mentioned previously, we consider four specific anchoring cases that commonly occur in nematic devices, namely planar, homeotropic, hybrid aligned nematic (HAN), and π-cell anchoring. In the planar anchoring case the director is parallel to the boundary at both the bottom substrate and top substrate, so that $\theta(\tilde{r}, 0, t) = \theta(\tilde{r}, 1, t) = 0$, and in the homeotropic anchoring case the director is perpendicular to the boundary at both the bottom substrate and top substrate, so that $\theta(\tilde{r}, 0, t) = \theta(\tilde{r}, 1, t) = \pi/2$. In the HAN anchoring case the director is parallel to the bottom substrate and perpendicular to the top substrate, so that $\theta(\tilde{r}, 0, t) = 0$ and $\theta(\tilde{r}, 1, t) = \pi/2$, and in the π-cell anchoring case the director is parallel to the bottom substrate so that $\theta(\tilde{r}, 0, t) = 0$ and parallel to the top substrate so that $\theta(\tilde{r}, 1, t) = \pi$. The equilibrium director configurations in the limit of no flow for these anchoring cases, namely (3.52)–(3.55), will be calculated later and are sketched in Figure 3.2.

It is worth noting at this point that the axisymmetric form of the non-

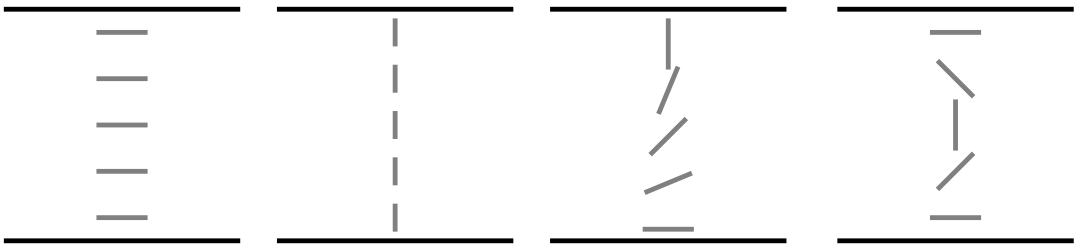

(a) planar (b) homeotropic (c) HAN (d) π-cell anchoring

Figure 3.2: Sketches of the equilibrium director configurations in the limit of no flow for the four specific anchoring cases considered: (a) planar, (b) homeotropic, (c) HAN, and (d) π-cell anchoring.

dimensional elastic energy given by (3.9) is

$$\omega_F = \frac{1}{2}\left[\frac{1}{H(t)^2}\left(\frac{\partial\theta}{\partial\tilde{z}}\right)^2 + \delta^2\frac{\pi}{V}H(t)\left(\left(\frac{\partial\theta}{\partial\tilde{r}}\right)^2 + \frac{\cos^2\theta}{\tilde{r}^2}\right)\right], \tag{3.27}$$

and therefore the elastic energy is undefined if $\theta \neq \pi/2$ at $\tilde{r} = 0$, a situation that occurs for the planar, HAN and π-cell anchoring cases. This type of singularity in the elastic energy is associated with a discontinuity in the director orientation and can lead to point or line defects. However, in subsequent sections we will find that since the aspect ratio is small (i.e. $\delta \ll 1$), the singular $\tilde{r}^{-2}$ term in (3.27) does not appear at leading order in δ. The results in the present work are therefore valid away from the centre of the drop at $\tilde{r} = 0$. In summary, the boundary conditions for the four anchoring cases are

$$\text{planar:} \quad \theta = 0 \quad \text{on} \quad \tilde{z} = 0, \quad \theta = 0 \quad \text{on} \quad \tilde{z} = 1, \tag{3.28}$$

$$\text{homeotropic:} \quad \theta = \pi/2 \quad \text{on} \quad \tilde{z} = 0, \ \theta = \pi/2 \quad \text{on} \quad \tilde{z} = 1, \tag{3.29}$$

$$\text{HAN:} \quad \theta = 0 \quad \text{on} \quad \tilde{z} = 0, \quad \theta = \pi/2 \quad \text{on} \quad \tilde{z} = 1, \tag{3.30}$$

$$\pi\text{-cell:} \quad \theta = 0 \quad \text{on} \quad \tilde{z} = 0, \quad \theta = \pi \quad \text{on} \quad \tilde{z} = 1. \tag{3.31}$$

Non-dimensional group	Definition	Typical value
δ	$\dfrac{\mathcal{H}}{\mathcal{R}}$	10^{-4}–1
Re	$\dfrac{\rho \mathcal{U} \mathcal{H}^2}{\mu \mathcal{R}} = \dfrac{\rho s_\mathrm{p} \mathcal{H}^2}{\mu}$	10^{-2}–10^{-4}
Er	$\dfrac{\mu \mathcal{U} \mathcal{H}}{K} = \dfrac{\mu s_\mathrm{p} \mathcal{R}}{K}$	10^{2}–10^{4}

Table 3.1: Typical values of the non-dimensional groups in the ODF method, calculated using the range of ODF parameters values listed in Table 1.1 and isotropic viscosity $\mu = 10^{-2}$ Pa s, one-constant elastic constant $K = 10^{-11}$ N, and density $\rho = 10^{3}$ kg m^{-3} [36, 63].

3.1.5 Typical values of non-dimensional groups

In this subsection we consider the asymptotic regimes for the sizes of the non-dimensional groups δ, Re and Er corresponding to those present in the ODF method for the ODF parameter values stated in Table 1.1 and an isotropic viscosity $\mu = 10^{-2}\,\mathrm{Pa\,s}$ one-constant elastic constant $K = 10^{-11}\,\mathrm{N}$, and density $\rho = 10^{3}\,\mathrm{kg\,m^{-3}}$ [63], as shown in Table 3.1. The radial velocity scale, $\mathcal{U}$, appearing in the reduced Reynolds number and Ericksen number is calculated using the conservation of mass equation, (3.16), to give $\mathcal{U} = s_\mathrm{p}\mathcal{R}/\mathcal{H}$. As Table 3.1 shows, the assumptions of small aspect ratio ($\delta \ll 1$) and small reduced Reynolds number (Re $\ll 1$) are well justified for the range of ODF parameter values shown in Table 1.1. The Ericksen number is typically much larger than unity during the ODF method, indicating that viscous effects are typically stronger than elasticity effects, and that a large Ericksen number approximation, Er $\gg 1$, is appropriate.

However, in this chapter we consider the possibility of using smaller drops of nematic and slower downward speed of the top substrate in order to access a possible future manufacturing regime. Specifically we consider the smallest

length-scales possible in the ODF method, namely a height of the drop $\mathcal{H} = 10^{-6}\,\mathrm{m}$, a radius of the drop $\mathcal{R} = 10^{-4}\,\mathrm{m}$, and a reduced downward speed of the top substrate of $s_{\mathrm{p}} = 10^{-6}\,\mathrm{m\,s^{-1}}$. These values may be relevant for a future manufacturing method that uses ink-jet printing of nematic droplets [2, 28]. All of the material parameters (namely the viscosity, elastic constant, and density of the nematic) remain the same as before and the aspect ratio is given by $\delta = 10^{-2}$, the reduced Reynolds number is given by $\mathrm{Re} = 10^{-7}$, and the Ericksen number is given by $\mathrm{Er} = 10^{-1}$, indicating that the assumptions of small aspect ratio ($\delta \ll 1$) and small reduced Reynolds number ($\mathrm{Re} \ll 1$) remain well justified, but now the value of the Ericksen number is smaller, indicating that a small Ericksen number approximation, $\mathrm{Er} \ll 1$, is now appropriate. In this chapter we will therefore consider the asymptotic regime in which $\delta \ll 1$, $\mathrm{Re} \ll 1$ and $\mathrm{Er} \ll 1$, which corresponds to a thin film of nematic in which inertial effects are weak and elasticity effects are strong compared to viscous effects. We note that the asymptotic regime in which $\delta \ll 1$, $\mathrm{Re} \ll 1$ and $\mathrm{Er} \gg 1$, which corresponds to a thin film of nematic in which inertial effects are weak and viscous effects are strong compared to elastic effects will be considered in Chapter 3, albeit in a different geometry and with different assumptions.

3.1.6 The thin-film approximation

With the assumptions that the aspect ratio and the Reynolds number are both small, $\delta \ll 1$ and $\mathrm{Re} \ll 1$, at leading order in δ the radial momentum equation, (3.17), rescaled using (3.20), becomes

$$\frac{\partial p}{\partial \tilde{r}} = \sqrt{\frac{V}{\pi}} H(t)^{-5/2} \frac{\partial}{\partial \tilde{z}} \Bigg[\Big(\frac{\alpha_1}{4} \sin^2 2\theta + \frac{\gamma_2}{2} \cos 2\theta + 1 + \frac{\alpha_5 + \alpha_6}{4} + \frac{\gamma_1}{4} \Big) \frac{\partial u}{\partial \tilde{z}} \Bigg]. \tag{3.32}$$

With the Parodi relation, given by (1.30), we can rewrite (3.32) in terms of the non-dimensional Miesowicz viscosities, given by (1.32)–(1.35), defined by

$$\eta_{12} = \alpha_1, \quad \eta_1 = \frac{1}{2}\left(\alpha_2 + 2\alpha_3 + 2 + \alpha_5\right), \quad \eta_2 = \frac{1}{2}\left(-\alpha_2 + 2 + \alpha_5\right), \tag{3.33}$$

as

$$\frac{\partial p}{\partial \tilde{r}} = \sqrt{\frac{V}{\pi}} H(t)^{-5/2} \frac{\partial}{\partial \tilde{z}} \left[\left(\eta_{12} \sin^2\theta \cos^2\theta + \eta_1 \cos^2\theta + \eta_2 \sin^2\theta \right) \frac{\partial u}{\partial \tilde{z}} \right]. \tag{3.34}$$

Similarly the vertical momentum equation, (3.18), rescaled using (3.20), becomes

$$\frac{\partial p}{\partial \tilde{z}} = 0. \tag{3.35}$$

Therefore, at leading order in δ the pressure is independent of the rescaled vertical coordinate $\tilde{z}$ and hence is given by

$$p = p(\tilde{r}, t). \tag{3.36}$$

In addition, the angular momentum equation, (3.19), again rescaled using (3.20), becomes

$$0 = \frac{1}{H(t)} \frac{\partial^2 \theta}{\partial \tilde{z}^2} - \frac{1}{2} \mathrm{Er} \left(\gamma_1 + \gamma_2 \cos 2\theta \right) \frac{\partial u}{\partial \tilde{z}}. \tag{3.37}$$

In summary, in what follows we will solve equations (3.34), (3.37) and (3.16) subject to the boundary conditions (3.21)–(3.26) together with the appropriate conditions from (3.28)–(3.31) for the particular problem under consideration for the dependent variables $\theta(\tilde{r}, \tilde{z}, t)$, $u(\tilde{r}, \tilde{z}, t)$, $w(\tilde{r}, \tilde{z}, t)$ and $p(\tilde{r}, t)$.

3.2 The Limit of Small Ericksen Number

In the limit of small Ericksen number $\mathrm{Er} \ll 1$ we seek an asymptotic solution to the problem in the form

$$\theta = \theta_0 + \mathrm{Er}\ \theta_1 + \mathrm{Er}^2\theta_2 + \mathcal{O}\left(\mathrm{Er}^3\right), \tag{3.38}$$

$$u = u_0 + \mathrm{Er}\ u_1 + \mathrm{Er}^2 u_2 + \mathcal{O}\left(\mathrm{Er}^3\right), \tag{3.39}$$

$$w = w_0 + \mathrm{Er}\ w_1 + \mathrm{Er}^2 w_2 + \mathcal{O}\left(\mathrm{Er}^3\right), \tag{3.40}$$

$$p = p_0 + \mathrm{Er}\ p_1 + \mathrm{Er}^2 p_2 + \mathcal{O}\left(\mathrm{Er}^3\right). \tag{3.41}$$

Substituting these asymptotic expansions into the governing equations, (3.16), (3.34) and (3.37), we are able to obtain the leading-order solutions that describe the dominant behaviour at small Ericksen number. By finding the higher-order corrections to these solutions we are then able to describe the perturbations to this leading-order behaviour. Using the expansions for the velocity components given by (3.39) and (3.40) and the rescaling (3.20), the conservation of mass equation, (3.16), takes the same form at each order in the Ericksen number, namely

$$\sqrt{\frac{\pi}{V}} H(t)^{3/2} \frac{1}{\tilde{r}} \frac{\partial\left(\tilde{r} u_i\right)}{\partial \tilde{r}} + \frac{\partial w_i}{\partial \tilde{z}} = 0 \tag{3.42}$$

for $i = 0, 1, 2, \ldots$. Using the expansions (3.38)–(3.41) and the rescaling (3.20) in (3.34) and (3.37), and considering the appropriate expressions at different orders in the Ericksen number, yields, at leading order,

$$\sqrt{\frac{\pi}{V}} H(t)^{5/2} \frac{\partial p_0}{\partial \tilde{r}} = \frac{\partial}{\partial \tilde{z}}\left[g(\theta_0)\frac{\partial u_0}{\partial \tilde{z}}\right], \tag{3.43}$$

$$\frac{\partial^2 \theta_0}{\partial \tilde{z}^2} = 0, \tag{3.44}$$

at first order,

$$\sqrt{\frac{\pi}{V}}H(t)^{5/2}\frac{\partial p_1}{\partial \tilde{r}} = \frac{\partial}{\partial \tilde{z}}\left[g'(\theta_0)\theta_1\frac{\partial u_0}{\partial \tilde{z}} + g(\theta_0)\frac{\partial u_1}{\partial \tilde{z}}\right], \tag{3.45}$$

$$\frac{1}{H(t)}\frac{\partial^2\theta_1}{\partial \tilde{z}^2} = m(\theta_0)\frac{\partial u_0}{\partial \tilde{z}}, \tag{3.46}$$

and at second order,

$$\sqrt{\frac{\pi}{V}}H(t)^{5/2}\frac{\partial p_2}{\partial \tilde{r}} = \frac{\partial}{\partial \tilde{z}}\left[g'(\theta_0)\theta_2\frac{\partial u_0}{\partial \tilde{z}} + \frac{1}{2}g''(\theta_0)\theta_1^2\frac{\partial u_0}{\partial \tilde{z}} + g'(\theta_0)\theta_1\frac{\partial u_1}{\partial \tilde{z}} + g(\theta_0)\frac{\partial u_2}{\partial \tilde{z}}\right], \tag{3.47}$$

$$\frac{1}{H(t)}\frac{\partial^2\theta_2}{\partial \tilde{z}^2} = m'(\theta_0)\theta_1\frac{\partial u_0}{\partial \tilde{z}} + m(\theta_0)\frac{\partial u_1}{\partial \tilde{z}}, \tag{3.48}$$

where

$$g(\theta) = \eta_{12}\sin^2\theta\cos^2\theta + \eta_1\cos^2\theta + \eta_2\sin^2\theta, \tag{3.49}$$

$$m(\theta) = \frac{1}{2}\left(\gamma_1 + \gamma_2\cos 2\theta\right). \tag{3.50}$$

Equation (3.44) and (3.46) show that, while the flow of the nematic does not affect the leading-order director angle θ_0, the leading-order radial flow u_0 may affect the first-order director angle θ_1. Indeed (3.46) has similarities to that describing the classical flow alignment problem in a nematic [201] and, as we will see later, has similar behaviour. Specifically, when the leading-order shear rate $\partial u_0/\partial \tilde{z}$ is large, the director will be forced to align, at least away from boundaries, at angles given by $m(\theta_0) = 0$. For a positive shear rate the relevant solution to $m(\theta_0) = 0$ is

$$\theta_0 = q\pi \pm \theta_{\mathrm{L}}, \tag{3.51}$$

where θ_{L} is the Leslie angle [201] discussed in Section 1.9. We remind the reader that the terms "positive" and "negative" Leslie angles refer to the sign of the shear

rate that is flow aligning the director rather than to the sign of the numerical value of the angle. Considering various different Leslie angles will be important in subsequent sections for understanding the behaviour of the first-order director angle θ_1 in each of the four anchoring cases.

3.2.1 General solution

The leading-order angular momentum equation, (3.44), can be immediately solved to yield the leading-order director angle $\theta_0 = \theta_0(\tilde{z})$ for each of the four anchoring cases given by (3.28)–(3.31), namely

$$\theta_0 = 0 \text{ for the planar anchoring case,} \tag{3.52}$$

$$\theta_0 = \frac{\pi}{2} \text{ for the homeotropic anchoring case,} \tag{3.53}$$

$$\theta_0 = \frac{\pi\tilde{z}}{2} \text{ for the HAN anchoring case,} \tag{3.54}$$

$$\theta_0 = \pi\tilde{z} \text{ for the } \pi\text{-cell anchoring case.} \tag{3.55}$$

These solutions are the equilibrium director configurations in the limit of no flow for the four anchoring cases previously sketched in Figure 3.2. Note that these solutions for θ_0 given in (3.54) and (3.55) are dependent on time via the rescaled vertical coordinate $\tilde{z}$. Integrating (3.43) twice with respect to $\tilde{z}$ and using the boundary conditions (3.21) and (3.23) then yields the solution for the leading-order radial velocity,

$$u_0(\tilde{r},\tilde{z},t) = \sqrt{\frac{\pi}{V}}H(t)^{5/2}\int_0^{\tilde{z}}\frac{1}{g\left(\theta_0\right)}\left(\frac{\partial p_0(\tilde{r},t)}{\partial\tilde{r}}\tilde{z}+B\right)\mathrm{d}\xi, \tag{3.56}$$

where the function $B = B(\tilde{r},t)$ is found from the boundary conditions to be

$$B = -\frac{\partial p_0(\tilde{r},t)}{\partial\tilde{r}}\int_0^1\frac{\tilde{z}}{g\left(\theta_0\right)}\mathrm{d}\tilde{z}\left(\int_0^1\frac{\mathrm{d}\tilde{z}}{g\left(\theta_0\right)}\right)^{-1}. \tag{3.57}$$

From (3.21), (3.56) and (3.57) we can then express the leading-order radial velocity as

$$u_0\left(\tilde{r},\tilde{z},t\right)=\sqrt{\frac{\pi}{V}}H(t)^{5/2}\frac{\partial p_0(\tilde{r},t)}{\partial r}\Pi_1(\tilde{z}), \tag{3.58}$$

where

$$\Pi_1(\tilde{z})=\int_0^{\tilde{z}}\frac{\xi}{g\left(\theta_0\right)}\mathrm{d}\xi-\int_0^{\tilde{z}}\frac{1}{g\left(\theta_0\right)}\mathrm{d}\xi\int_0^1\frac{\tilde{z}}{g\left(\theta_0\right)}\mathrm{d}\tilde{z}\left(\int_0^1\frac{1}{g\left(\theta_0\right)}\mathrm{d}\tilde{z}\right)^{-1}. \tag{3.59}$$

The first-order correction to the leading-order director angle, θ_1, is calculated by integrating the first-order angular momentum equation, (3.46), twice with respect to $\tilde{z}$, and using the solution for u_0 given by (3.58) and the boundary conditions $\theta_1=0$ on both $\tilde{z}=0$ and $\tilde{z}=1$, to give

$$\theta_1\left(\tilde{r},\tilde{z},t\right)=\sqrt{\frac{\pi}{V}}H(t)^{7/2}\frac{\partial p_0(\tilde{r},t)}{\partial\tilde{r}}\Pi_2(\tilde{z}), \tag{3.60}$$

where

$$\Pi_2(\tilde{z})=\int_0^{\tilde{z}}\int_0^{\xi}m\left(\theta_0\right)\frac{\mathrm{d}\Pi_1}{\mathrm{d}\zeta}\mathrm{d}\zeta\mathrm{d}\xi-\tilde{z}\int_0^1\int_0^{\zeta}m\left(\theta_0\right)\frac{\mathrm{d}\Pi_1}{\mathrm{d}\xi}\mathrm{d}\xi\mathrm{d}\zeta. \tag{3.61}$$

We can now calculate the first-order correction to the leading-order radial velocity, u_1, by integrating (3.45) with respect to z, using expressions for u_0 and θ_1 from (3.58) and (3.60) as well as the first-order boundary conditions $u_1=0$ on both $\tilde{z}=0$ and $\tilde{z}=1$, to obtain

$$u_1\left(\tilde{r},\tilde{z},t\right)=\sqrt{\frac{\pi}{V}}H(t)^{5/2}\frac{\partial p_1\left(\tilde{r},t\right)}{\partial\tilde{r}}\Pi_1(\tilde{z})+\frac{\pi}{V}H(t)^6\left(\frac{\partial p_0\left(\tilde{r},t\right)}{\partial\tilde{r}}\right)^2\Pi_3(\tilde{z}), \tag{3.62}$$

where

$$\Pi_3(\tilde{z}) = \int_0^{\tilde{z}} \frac{1}{g\left(\theta_0\right)} \mathrm{d}\xi \left(\int_0^1 \frac{1}{g\left(\theta_0\right)} \mathrm{d}\zeta \right)^{-1} \int_0^1 \frac{g'\left(\theta_0\right) \Pi_2 \frac{\mathrm{d}\Pi_1}{\mathrm{d}\zeta}}{g\left(\theta_0\right)} \mathrm{d}\zeta - \int_0^{\tilde{z}} \frac{g'\left(\theta_0\right) \Pi_2 \frac{\mathrm{d}\Pi_1}{\mathrm{d}\xi}}{g\left(\theta_0\right)} \mathrm{d}\xi. \tag{3.63}$$

To calculate the leading- and first-order vertical velocity components, w_0 and w_1, the solutions for u_0 and u_1, given by (3.58) and (3.62), and the conservation of mass equation, (3.42), with $i = 0, 1$, are used, yielding

$$w_0(\tilde{r}, \tilde{z}, t) = -\frac{\pi}{V} H(t)^4 \frac{1}{\tilde{r}} \frac{\partial}{\partial \tilde{r}} \left(\tilde{r} \frac{\partial p_0(\tilde{r}, t)}{\partial \tilde{r}} \right) \int_0^{\tilde{z}} \Pi_1(\xi) \mathrm{d}\xi, \tag{3.64}$$

$$w_1(\tilde{r}, \tilde{z}, t) = -\frac{\pi}{V} H(t)^4 \frac{1}{\tilde{r}} \frac{\partial}{\partial \tilde{r}} \left(\tilde{r} \frac{\partial p_1(\tilde{r}, t)}{\partial \tilde{r}} \right) \int_0^{\tilde{z}} \Pi_1(\xi) \mathrm{d}\xi - \left(\frac{\pi}{V} \right)^{3/2} H(t)^{15/2} \frac{1}{\tilde{r}} \frac{\partial}{\partial \tilde{r}} \left(\tilde{r} \left(\frac{\partial p_0(\tilde{r}, t)}{\partial \tilde{r}} \right)^2 \right) \int_0^{\tilde{z}} \Pi_3(\xi) \mathrm{d}\xi. \tag{3.65}$$

To calculate the leading-order pressure, p_0, we apply the boundary condition (3.24) to the leading-order vertical velocity, given by (3.64), and integrate with respect to $\tilde{r}$ and impose the condition on the pressure gradient, (3.25), which leads to

$$\frac{\partial p_0\left(\tilde{r}, t\right)}{\partial \tilde{r}} = -\frac{V H'(t) \tilde{r}}{2\pi H(t)^4} \left(\int_0^1 \Pi_1\left(\xi\right) \mathrm{d}\xi \right)^{-1}. \tag{3.66}$$

The leading-order pressure gradient, (3.66), can be substituted into (3.58), (3.60), (3.62), (3.64) and (3.65) to yield the full solutions for θ_1, u_0, u_1, w_0 and w_1, respectively. A further integration of (3.66) with respect to $\tilde{r}$ and application of the boundary condition on the pressure, (3.26), yields the solution for the leading-order pressure,

$$p_0\left(\tilde{r}, t\right) = p_{\mathrm{I}} + \frac{V H'(t)}{4\pi H(t)^4} \left(1 - \tilde{r}^2\right) \left(\int_0^1 \Pi_1\left(\xi\right) \mathrm{d}\xi \right)^{-1}. \tag{3.67}$$

The same approach is used to calculate the first-order pressure gradient and first-order pressure,

$$\frac{\partial p_1(\tilde{r},t)}{\partial r} = -\frac{V^{3/2}H'(t)^2}{4\pi^{3/2}H(t)^{9/2}}\tilde{r}^2\left(\int_0^1 \Pi_1(\xi)\mathrm{d}\xi\right)^{-3}\int_0^1 \Pi_3(\xi)\mathrm{d}\xi, \tag{3.68}$$

$$p_1(\tilde{r},t) = \frac{V^{3/2}H'(t)^2}{12\pi^{3/2}H(t)^{9/2}}\left(1-\tilde{r}^3\right)\left(\int_0^1 \Pi_1(\xi)\mathrm{d}\xi\right)^{-3}\int_0^1 \Pi_3(\xi)\mathrm{d}\xi. \tag{3.69}$$

In summary, in addition to the solutions for the leading-order director angle θ_0 for each anchoring case, given by (3.52)–(3.55), we find the leading-order radial velocity u_0, given by (3.58), the first-order director angle θ_1, given by (3.60), first-order radial velocity u_1, given by (3.62), leading-order vertical velocity w_0, given by (3.64), first-order vertical velocity w_1, given by (3.65), leading-order pressure p_0, given by (3.67), and first-order pressure p_1, given by (3.69). Equations (3.58), (3.60), (3.62), (3.64), (3.65), (3.67) and (3.69) describe the director angle, velocity and pressure at leading and first order for any fixed angles of the director at the substrates, however, in present work we will focus on the four anchoring cases given by (3.28)–(3.31). In fact, (3.58), (3.60), (3.62), (3.64), (3.65), (3.67) and (3.69) provide the solution at first-order for any leading-order director angle θ_0, including the more general situation where one or more of the substrates exhibit weak anchoring rather than infinite anchoring.

The leading-order pressure, given by (3.67), can be expressed as

$$p_0 = p_{\mathrm{I}} - \eta(\theta_0)\frac{3VH'(t)}{\pi H(t)^4}\left(1-\tilde{r}^2\right), \tag{3.70}$$

where

$$\eta(\theta_0) = -\left(12\int_0^1 \Pi_1(\xi)\,\mathrm{d}\xi\right)^{-1} \tag{3.71}$$

is an effective viscosity which depends on the leading-order director angle via the

Anchoring case	Effective viscosity $\eta(\theta_0)$
Planar	$\eta_1 = 0.6258$
Homeotropic	$\eta_2 = 3.2270$
HAN	1.6006
π-cell	0.9184

Table 3.2: Values of the effective viscosity $\eta(\theta_0)$ given by (3.71) for the four anchoring cases given by (3.28)–(3.31) using the material parameter values for the nematic 5CB [201].

expression for Π_1 given by (3.59). For future reference, values of the effective viscosity $\eta(\theta_0)$ for the four anchoring cases given by (3.28)–(3.31), are listed in Table 3.2 using parameter values for the standard nematic 5CB [201]. Table 3.2 shows that $\eta(\theta_0)$ is largest for the homeotropic anchoring case for which $\eta(\theta_0) = \eta_2$ and smallest for the planar anchoring case for which $\eta(\theta_0) = \eta_1$.

Note that substituting (3.70) into (3.58), (3.60) and (3.64) yields

$$\theta_1(\tilde{r}, \tilde{z}, t) = 6\sqrt{\frac{V}{\pi}}\frac{\eta(\theta_0)H'(t)}{H(t)^{1/2}}\Pi_2(\tilde{z})\,\tilde{r}, \tag{3.72}$$

$$u_0(\tilde{r}, \tilde{z}, t) = 6\sqrt{\frac{V}{\pi}}\frac{\eta(\theta_0)H'(t)}{H(t)^{3/2}}\Pi_1(\tilde{z})\,\tilde{r}, \tag{3.73}$$

$$w_0(\tilde{z}, t) = 12\eta(\theta_0)H'(t)\int_0^{\tilde{z}}\Pi_1(\xi)\mathrm{d}\xi, \tag{3.74}$$

and if we substitute $\eta(\theta_0) = \mu$ and $g(\theta_0) = \mu$ into (3.70), (3.73) and (3.74) we recover the classical solution to the Newtonian squeeze-film problem [100].

Equations (3.72)–(3.74) show that the first-order director angle and the leading-order radial velocity are proportional to $\tilde{r}$, while the leading-order vertical velocity is independent of $\tilde{r}$. Thus the magnitudes, but not the qualitative behaviour, of θ_1 and u_0, vary with $\tilde{r}$. Equations (3.67) and (3.72)–(3.74) also give the time

dependence of the solutions θ_1, u_0, w_0 and p_0, namely

$$\theta_1 \propto \frac{H'(t)}{H(t)^{1/2}}, \quad u_0 \propto \frac{H'(t)}{H(t)^{3/2}}, \quad w_0 \propto H'(t) \quad \text{and} \quad p_0 \propto \frac{H'(t)}{H(t)^4}. \tag{3.75}$$

While (3.58), (3.60), (3.62), (3.64), (3.65), (3.67) and (3.69) provide explicit expressions for the leading- and first-order solutions in the limit of small Ericksen number, these expressions depend on the calculation of the integrals Π_1, Π_2 and Π_3. These integrals cannot be analytically evaluated for general forms of the leading-order director angle θ_0. However, in two of the four anchoring cases we consider, namely the planar, (3.28), and homeotropic, (3.29), anchoring cases, $g(\theta_0)$ is constant and hence further analytic progress is possible. For the other two anchoring cases, namely the HAN, (3.30), and π-cell, (3.31), anchoring cases, $g(\theta_0)$ is not constant, and so the integrals and solutions must, in general, be evaluated numerically.

For the two cases in which θ_0 is constant, and so $\eta(\theta_0)$, $g(\theta_0)$, and $m(\theta_0)$ are constant and $\eta(\theta_0) = g(\theta_0)$, analytical expressions for the integrals Π_1, Π_2 and Π_3 can be readily obtained and used to calculate the leading- and first-order solutions, namely

$$\theta_1 = \frac{1}{2}\sqrt{\frac{V}{\pi}}\frac{m(\theta_0)H'(t)}{H(t)^{1/2}}\tilde{z}\,(1-2\tilde{z})\,(1-\tilde{z})\,\tilde{r}, \tag{3.76}$$

$$u_0 = -3\sqrt{\frac{V}{\pi}}\frac{H'(t)}{H(t)^{3/2}}\tilde{z}\,(1-\tilde{z})\,\tilde{r}, \tag{3.77}$$

$$u_1 = 0, \tag{3.78}$$

$$w_0 = H'(t)\tilde{z}^2\,(3-2\tilde{z})\,, \tag{3.79}$$

$$w_1 = 0, \tag{3.80}$$

$$p_0 = p_{\mathrm{I}} - \frac{3g(\theta_0)VH'(t)}{\pi H(t)^4}\left(1-\tilde{r}^2\right), \tag{3.81}$$

$$p_1 = 0. \tag{3.82}$$

In particular, in the planar case $\theta_0 = 0$, $\eta(\theta_0) = g(\theta_0) = \eta_1$ and $m(\theta_0) = \gamma_1 + \gamma_2$, while in the homeotropic case $\theta_0 = \pi/2$, $\eta(\theta_0) = g(\theta_0) = \eta_2$ and $m(\theta_0) = \gamma_1 - \gamma_2$. In both cases the first-order radial and vertical velocities, as well as the first-order pressure, are all identically zero since $\Pi_3 = 0$. Analytical expressions for the higher-order terms in these cases can also be readily obtained, but are omitted here for brevity.

3.2.2 Shear stress and couple stress on the substrates

As mentioned in Chapter 1, liquid crystal device performance can be affected by the misalignment of the molecules at the substrates [36, 125, 167]. The source of this misalignment is a current topic of research, but there is some evidence that this is an effect of the flow of the liquid crystal during the ODF method [36]. Flow of a nematic may affect the alignment layer at one or both of the substrates through, for example, a frictional force derived from the shear stress at the substrates or a director torque derived from the couple stress at the substrates. These stresses can be calculated from the director angle and velocity.

The leading-order shear stress, $g(\theta_0)\partial u_0/\partial \tilde{z}$, can be obtained from (3.52)–(3.55) and (3.58) yielding

$$g(\theta_0)\left.\frac{\partial u_0}{\partial \tilde{z}}\right|_{\tilde{z}=1} = 6\sqrt{\frac{V}{\pi}}\frac{\eta(\theta_0)H'(t)}{H(t)^{3/2}}\tilde{r}\left[1 - \frac{\displaystyle\int_0^1 \frac{\xi}{g(\theta_0)}\mathrm{d}\xi}{\displaystyle\int_0^1 \frac{1}{g(\theta_0)}\mathrm{d}\xi}\right], \tag{3.83}$$

$$g(\theta_0)\left.\frac{\partial u_0}{\partial \tilde{z}}\right|_{\tilde{z}=0} = -6\sqrt{\frac{V}{\pi}}\frac{\eta(\theta_0)H'(t)}{H(t)^{3/2}}\tilde{r}\frac{\displaystyle\int_0^1 \frac{\xi}{g(\theta_0)}\mathrm{d}\xi}{\displaystyle\int_0^1 \frac{1}{g(\theta_0)}\mathrm{d}\xi}, \tag{3.84}$$

at the top substrate and bottom substrate, respectively.

The torque on the director depends on the couple stress. From (3.52)–(3.55), the leading-order couple stress, $\partial\theta_0/\partial\tilde{z}$, is constant, and is equal to zero for the planar and homeotropic anchoring cases, $\pi/2$ for the HAN anchoring case, and π for the π-cell anchoring case. The first-order couple stress, $\mathrm{Er}\,\partial\theta_1/\partial\tilde{z}$, can be obtained from (3.52)–(3.55) and (3.60) yielding

$$\left.\frac{\partial\theta_1}{\partial\tilde{z}}\right|_{\tilde{z}=1} = 6\sqrt{\frac{V}{\pi}}\frac{\eta(\theta_0)H'(t)}{H(t)^{1/2}}\tilde{r}\left[\int_0^1 m(\theta_0)\frac{\mathrm{d}\Pi_1(\xi)}{\mathrm{d}\xi}\mathrm{d}\xi - \int_0^1\int_0^\xi m(\theta_0)\frac{\mathrm{d}\Pi_1(\zeta)}{\mathrm{d}\zeta}\mathrm{d}\zeta\mathrm{d}\xi\right], \tag{3.85}$$

$$\left.\frac{\partial\theta_1}{\partial\tilde{z}}\right|_{\tilde{z}=0} = -6\sqrt{\frac{V}{\pi}}\frac{\eta(\theta_0)H'(t)}{H(t)^{1/2}}\tilde{r}\int_0^1\int_0^\xi m(\theta_0)\frac{\mathrm{d}\Pi_1(\zeta)}{\mathrm{d}\zeta}\mathrm{d}\zeta\mathrm{d}\xi, \tag{3.86}$$

at the top substrate and the substrate, respectively. The leading-order shear stress and the leading- and first-order couple stresses, for the four anchoring cases, will be described below.

3.2.3 Forces on the substrates

In an experimental or industrial setting, two measurable quantities are the forces on the top substrate and on the bottom substrate. Indeed, measuring the force on the top substrate is one method used industrially to monitor the distance between substrates and hence to determine when the squeezing of the nematic should be stopped. The forces on the top substrate and on the bottom substrate can be calculated by integrating the stress tensor over the appropriate boundary. The dimensional forces on the top substrate and bottom substrate are defined by

$$[F]_{z=H(t)} = -\int_S \left[\hat{\mathbf{e}}_z\cdot\underline{\underline{\mathbf{t}}}\cdot\hat{\mathbf{e}}_z\right]_{z=H(t)}\mathrm{d}S \quad \text{and}$$
$$[F]_{z=0} = -\int_S \left[\hat{\mathbf{e}}_z\cdot\underline{\underline{\mathbf{t}}}\cdot\hat{\mathbf{e}}_z\right]_{z=0}\mathrm{d}S, \tag{3.87}$$

respectively, where the nematic anisotropic stress tensor $\underline{\underline{\mathbf{t}}}$ is expressed in component form as

$$t_{ij} = -p\delta_{ij} - \frac{\partial \omega_F}{\partial \left[\nabla \boldsymbol{n}\right]_{kj}} \left[\nabla \boldsymbol{n}\right]_{kj} + \alpha_1 n_k e_{kp} n_p n_i n_j + \alpha_2 N_i n_j + \alpha_3 n_i N_j + \alpha_4 e_{ij} + \alpha_5 n_j e_{ik} n_k + \alpha_6 n_i e_{jk} n_k. \tag{3.88}$$

In the present asymptotic limit of small Ericksen number, the leading-order term in the stress tensor is simply that due to the pressure, and the non-dimensional leading-order force F_0 evaluated on the top substrate and on the bottom substrate are then

$$\left[F_0\right]_{z=H(t)} = \int_S p_0 \mathrm{d}S \quad \text{and} \quad \left[F_0\right]_{z=0} = \int_S p_0 \mathrm{d}S, \tag{3.89}$$

respectively. Using the rescaling (3.20) and substituting the leading-order pressure, (3.67), into (3.89) and integrating over the entire top substrate or bottom substrate with respect to θ and $\tilde{r}$ yields

$$\left[F_0\right]_{\tilde{z}=1} = -\left[F_0\right]_{\tilde{z}=0} = A_{\mathrm{s}} p_{\mathrm{I}} - \frac{3\eta(\theta_0) V^2 H'(t)}{2\pi H(t)^5}. \tag{3.90}$$

The leading-order force on the top substrate $\left[F_0\right]_{\tilde{z}=1}$ is equal and opposite to the leading-order force on the bottom substrate $\left[F_0\right]_{\tilde{z}=0}$. Since the effective viscosity $\eta(\theta_0)$ appearing in (3.90) does not depend on time, the forces on the top substrate and on the bottom substrate increase like $H(t)^{-5}$. As $\eta(\theta_0)$ is largest for the homeotropic anchoring case (see Table 3.2), we find that this anchoring case is associated with the largest forces on the substrates, whilst the planar anchoring case is associated with the smallest forces on the substrates. In general, (3.90) shows that as the film is squeezed and the height of the top substrate $H(t)$ reduces, an increasing force is required to move the top substrate, and the difference in force required to move the top substrate for each anchoring case depends on the value of the effective viscosity $\eta(\theta_0)$ for each anchoring case.

The director, velocity and pressure, as well as the shear stresses, the couple stresses and the forces on the substrates, described above all depend on the manner in which the height of the top substrate $H(t)$ varies in time. As described previously, there are two important scenarios for the time-dependence of $H(t)$: the prescribed speed scenario and the prescribed force scenario. The ODF method, in which the motion of top substrate is controlled by a machine which squeezes the film of nematic until there is a prescribed gap between the substrates, corresponds to the first scenario. Typically the ODF method uses a constant downward speed of the top substrate, and so this special case is considered in Section 3.3 (although the analysis can be readily generalised to other cases). The widely-studied problem in which the top substrate moves downwards under a constant force due to its own weight is a particular case of the second scenario, and so this special case is considered in Section 3.4 (although, again, the analysis can be readily generalised to other cases).

3.3 Results for a prescribed speed

In the scenario of the top substrate moving with prescribed constant speed we set the dimensional height of the top substrate to be $H(t) = \mathcal{H} - s_{\mathrm{p}}t$. The initial dimensional height of the top substrate, $\mathcal{H}$, and the constant dimensional downward speed of the top substrate, s_{p}, can then be used to set the values used in the non-dimensionalisation given by (3.12) in Section 3.1.2 using $\mathcal{U} = s_{\mathrm{p}}\sqrt{V/(\pi\mathcal{H}^3)}$. The non-dimensionalised height of the top substrate is then simply

$$H(t) = 1 - t. \tag{3.91}$$

For the numerical solutions described in this section we will set $p_{\mathrm{I}} = 0$ and use the material parameter values for the nematic 5CB [201] unless stated otherwise.

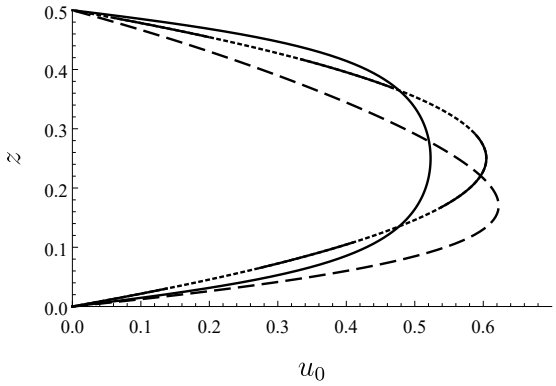

Figure 3.3: Leading-order radial velocity u_0, given by (3.58), plotted as a function of the vertical coordinate z for the four anchoring cases; planar (solid), homeotropic (dotted), HAN (dashed), and π-cell (dashed-dotted) at $r = R(t)/2$ and $t = 0.5$ using $p_{\mathrm{I}} = 0$ and the material parameter values for the nematic 5CB [201]. The results for the planar and homeotropic anchoring cases are identical, indicated by the solid and dotted curves being plotted intermittently.

3.3.1 Leading-order radial velocity

The leading-order radial velocity u_0, given by (3.58), is plotted in Figure 3.3 as a function of the original unscaled vertical coordinate z for the four anchoring cases at $r = R(t)/2$ and $t = 0.5$. As Figure 3.3 shows, the radial velocity is identical in the planar (solid line) and homeotropic (dotted line) anchoring cases, with both of these anchoring cases having a symmetric Poiseuille flow. As Figure 3.3 also shows, the leading-order radial velocity for the HAN anchoring case (dashed line) has a Poiseuille-like profile, with the flow skewed towards the lower viscosity region in the lower part of the squeeze film. For the π-cell anchoring case (dashed-dotted line), Figure 3.3 shows similar behaviour, with lower velocity in the higher viscosity region in the centre of the squeeze film and a higher velocity in the lower viscosity regions near the substrates. The location of the maximum radial velocity, denoted by $z = z^*$, can be found using (3.73) and the rescaling (3.20) to

be

$$z^* = H(t)\frac{\displaystyle\int_0^1 \frac{\xi}{g(\theta_0)}\mathrm{d}\xi}{\displaystyle\int_0^1 \frac{1}{g(\theta_0)}\mathrm{d}\xi}. \tag{3.92}$$

Clearly from (3.92) the location of the maximum velocity is a fraction $H(t)$, and so varies with time t like $H(t)$. In the planar, homeotropic and π-cell (but not the HAN) anchoring cases it is straight forward to show that $z^* = H(t)/2$ (i.e. the maximum velocity is always in the centre of the squeeze film).

For the HAN and π-cell anchoring cases, the higher velocity in the lower viscosity regions leads to changes in the shear stress at the substrates, as indicated by the gradient $\partial u_0/\partial z$ at $z = 0$ and $z = H(t)$ in Figure 3.3, when compared to the Poiseuille flow in the planar and homeotropic anchoring cases.

The evolution of the leading-order radial velocity u_0, given by (3.58), is plotted in Figure 3.4 as function of z at $r = R(t)/2$ for $t = 0$, $t = 0.2$, $t = 0.4$ and $t = 0.6$ for each of the four anchoring cases. For each of the four anchoring cases the radial velocity retains the same functional form shown in Figure 3.3 but increases in magnitude as time increases. As (3.75) shows, this increase in magnitude is proportional to $H'(t)/H(t)^{3/2}$.

3.3.2 Leading-order vertical velocity

The leading-order vertical velocity w_0, given by (3.64), is plotted in Figure 3.5 as a function of z for the four anchoring cases at $r = R(t)/2$ and $t = 0.5$. The behaviour of the leading-order vertical flow can be understood by considering the leading-order radial velocity shown in Figure 3.3. By conservation of mass, a reduction in the radial velocity must be matched by an increase in the vertical velocity. The leading-order radial velocity is identical for the planar and

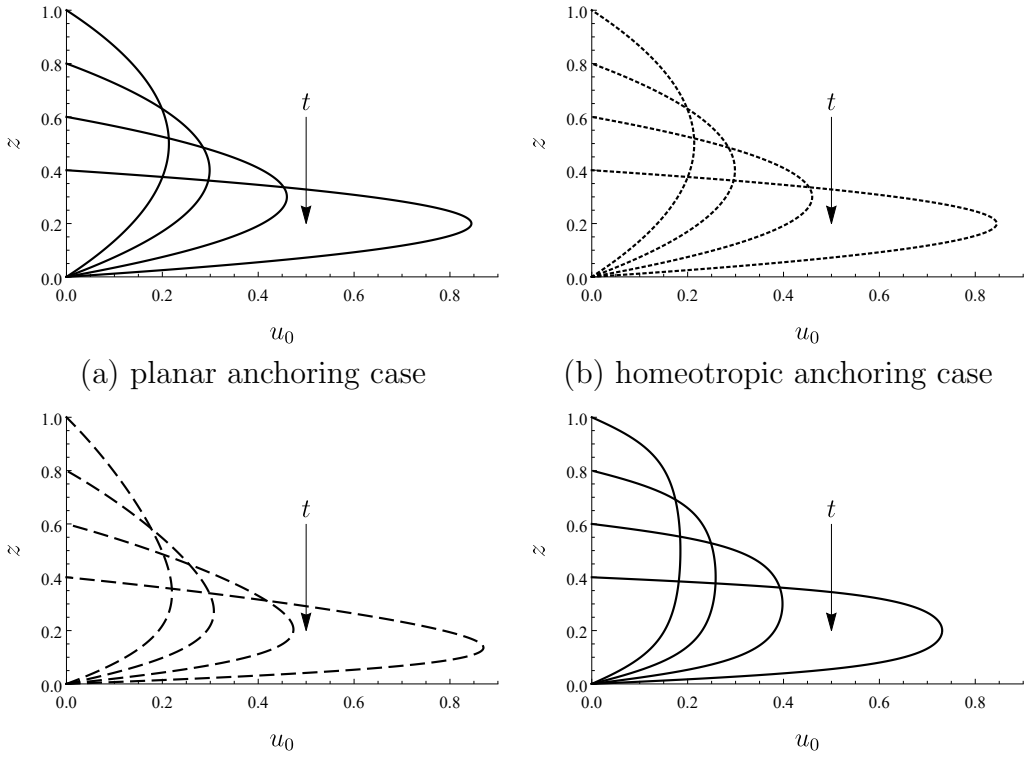

(a) planar anchoring case

(b) homeotropic anchoring case

(c) HAN anchoring case

(d) π-cell anchoring case

Figure 3.4: The evolution of the leading-order radial velocity u_0, given by equation (3.58), plotted as a function of vertical coordinate z for the four anchoring cases; (a) planar (solid), (b) homeotropic (dotted), (c) HAN (dashed), and (d) π-cell (dashed-dotted) at $r = R(t)/2$ for $t = 0$, $t = 0.2$, $t = 0.4$ and $t = 0.6$ using $p_{\mathrm{I}} = 0$ and the material parameter values for the nematic 5CB [201].

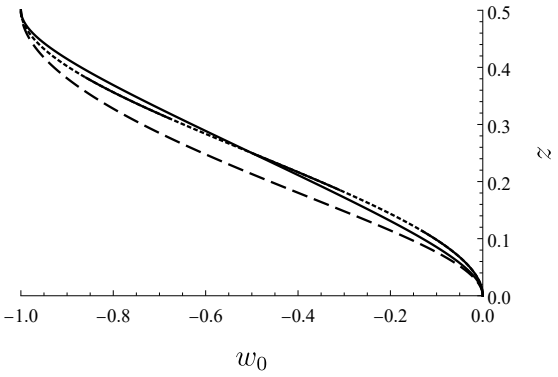

Figure 3.5: Leading-order vertical velocity w_0, given by (3.64), plotted as a function of vertical coordinate z for the four anchoring cases; planar (solid), homeotropic (dotted), HAN (dashed), and π-cell (dashed-dotted) at $r = R(t)/2$ and $t = 0.5$ using $p_{\mathrm{I}} = 0$ and the material parameter values for the nematic 5CB [201]. The results for the planar and homeotropic anchoring case are identical, indicated by the solid and dotted curves being plotted intermittently.

homeotropic anchoring cases, this leads to the leading-order vertical velocity also being identical, as shown in (3.79). As Figure 3.5 shows, for the HAN anchoring case, the leading-order vertical velocity is larger in magnitude at all values of z than any of the other three anchoring cases. This is due to the leading-order radial velocity being skewed toward the lower part of the squeeze film, leading to a larger vertical flux into this lower viscosity region and thus a larger downward vertical velocity. In the π-cell anchoring case, there is a smaller vertical velocity in the upper half ($H(t)/2 < z < H(t)$) of the squeeze film and a larger velocity in the lower half ($0 < z < H(t)/2$) than in the planar and homeotropic anchoring cases. As shown in Figure 3.3, there is larger radial velocity near the top substrate in the π-cell anchoring case than in the planar and homeotropic anchoring cases resulting in smaller vertical flow in the π-cell anchoring case than in the planar and homeotropic anchoring cases. The vertical velocity near the bottom substrate is larger in the π-cell anchoring case than in the planar and homeotropic anchoring cases, as the radial velocity in the middle of the squeeze film is smaller, as shown in Figure 3.3, in the π-cell anchoring case than that of the planar and

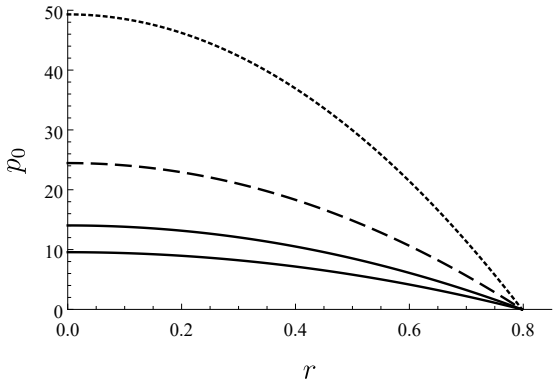

Figure 3.6: Leading-order pressure p_0, given by (3.67), plotted as a function of radial coordinate r for the four anchoring cases; planar (solid), homeotropic (dotted), HAN (dashed), and π-cell (dashed-dotted) at $t = 0.5$ using $p_{\mathrm{I}} = 0$ and the material parameter values for the nematic 5CB [201].

homeotropic anchoring cases. Plots of the evolution of the leading-order vertical velocity w_0, given by (3.64), are omitted since, as (3.75) and (3.91) show, the leading-order vertical velocity does not depend on time in the prescribed speed scenario.

3.3.3 Leading-order pressure

The leading-order pressure p_0, given by (3.67), is plotted in Figure 3.6 as a function of r for the four anchoring cases at $t = 0.5$. The results given in Table 3.2 show that the homeotropic anchoring case has the largest effective viscosity and hence the highest pressure, whilst the planar anchoring case has the smallest effective viscosity and hence the lowest pressure, in agreement with Figure 3.6. The pressures in the HAN and the π-cell anchoring cases lie between those in the planar and homeotropic anchoring cases, with the pressure in the HAN case being larger due to it having a larger effective viscosity.

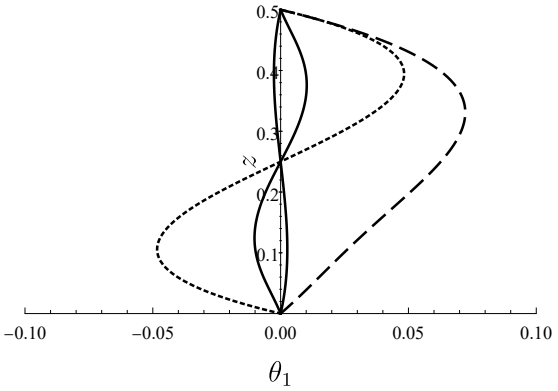

Figure 3.7: First-order director angle θ_1, given by (3.60), plotted as a function of vertical coordinate z for the four anchoring cases; planar (solid), homeotropic (dotted), HAN (dashed), and π-cell (dashed-dotted) at $r = R(t)/2$ and $t = 0.5$ using $p_{\mathrm{I}} = 0$ and the material parameter values for the nematic 5CB [201].

3.3.4 First-order director angle

As we have seen, since the Ericksen number is small, the director angle is dominated by elastic effects and flow has no effect on the leading-order director angle. However, at higher orders the flow has an effect on the director angle. The first-order director angle θ_1, given by (3.60), is plotted in Figure 3.7 as a function of z for the four anchoring cases at $r = R(t)/2$ and $t = 0.5$. As Figure 3.7 shows, the planar and homeotropic anchoring cases exhibit a flow-aligning correction to the leading-order director angle in response to the leading-order radial velocity shown in Figure 3.3. For the planar anchoring case (solid line), as a consequence of the leading-order Poiseuille flow profile, the leading-order solution $\theta_0 = 0$ is increased towards the positive Leslie angle θ_{L} in the lower half ($0 < z < H(t)/2$) of the squeeze film and decreased towards the negative Leslie angle $-\theta_{\mathrm{L}}$ in the upper half ($H(t)/2 < z < H(t)$) of the squeeze film. The homeotropic anchoring case (dotted line) has a similar behaviour, the leading-order solution $\theta_0 = \pi/2$ is decreased towards the positive Leslie angle θ_{L} in the lower half of the squeeze film and increased towards the closest negative Leslie angle $\pi - \theta_{\mathrm{L}}$ in the upper

half of the squeeze film. (Recall that the terms "positive" and "negative" Leslie angles refer to the sign of the shear rate that is flow aligning the director rather than to the sign of the numerical value of the angle.) The perturbation in the homeotropic anchoring case is larger than that in the planar anchoring case since the closest Leslie angle for the nematic 5CB is $\theta_{\mathrm{L}} \approx 0.208$, which is closer to 0 than to $\pi/2$, so that the torque applied to the director, and hence the perturbation to the director angle, due to the flow is larger in the homeotropic anchoring case.

The behaviour in the HAN anchoring case (dashed line) is more complicated. Close to the top substrate, where the leading-order director is similar to the leading-order director for the homeotropic anchoring case, the behavior of the first-order director angle is similar to that in the homeotropic case (denoted by the dotted line in Figure 3.7), such that, in this region the flow acts to align the director towards the nearest negative Leslie angle $\pi - \theta_{\mathrm{L}} \approx 2.933$, resulting in a positive perturbation θ_1. Indeed, because the shear rate is negative over the majority of the squeeze film (see Figure 3.3), the torque in the majority of the cell will be positive, tending to increase the first-order director angle. However, close to the bottom substrate at $z = 0$, the torque applied to the director will attempt to align the director towards the positive Leslie angle $\theta_{\mathrm{L}} \approx 0.208$. Therefore, for leading-order director angles less than θ_{L}, this will lead to a positive first-order perturbation θ_1, whereas for leading-order director angles greater than θ_{L} this should lead to a negative first-order perturbation θ_1. However, the strength of the elasticity and the large positive torque in the rest of the squeeze film means that the net result is a positive perturbation θ_1 throughout the squeeze film.

For the π-cell anchoring case, in the upper half of the squeeze film the leading-order director angle is greater than $\pi/2$ and in the lower half of the squeeze film the leading-order director angle is less than $\pi/2$. Therefore, in the upper half

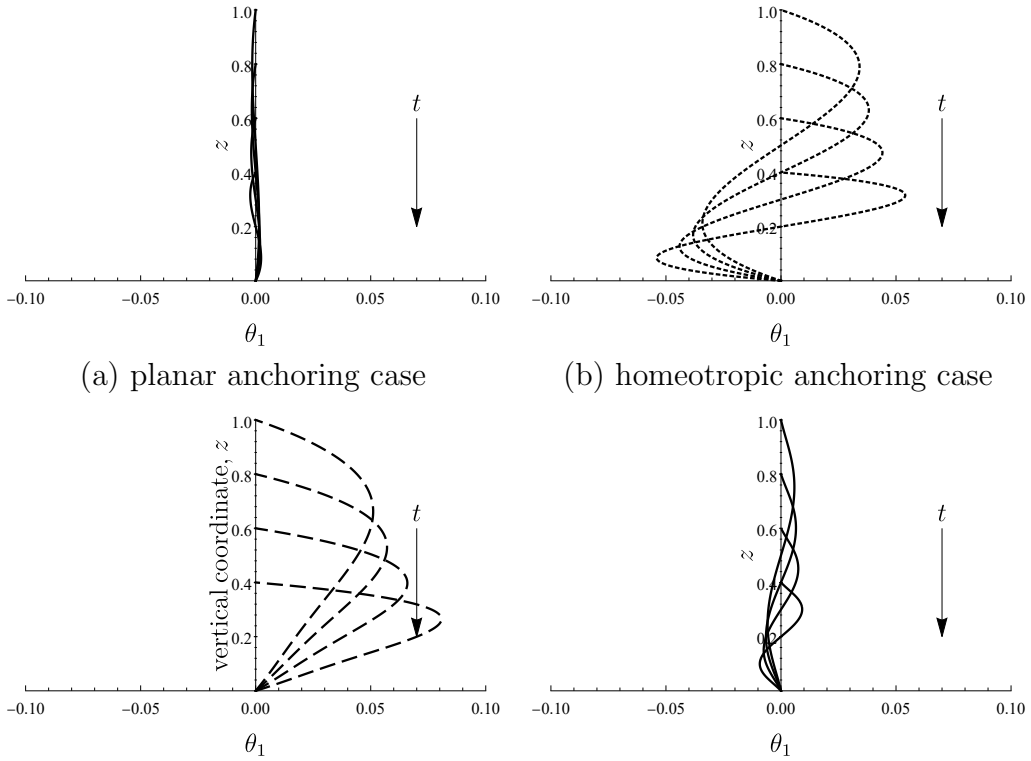

(a) planar anchoring case (b) homeotropic anchoring case

(c) HAN anchoring case (d) π-cell anchoring case

Figure 3.8: The evolution of the first-order director angle θ_1, given by (3.60), plotted as a function of vertical coordinate z for the four anchoring cases; (a) planar (solid), (b) homeotropic (dotted), (c) HAN (dashed), and (d) π-cell (dashed-dotted) at $r = R(t)/2$ for $t = 0$, $t = 0.2$, $t = 0.4$ and $t = 0.6$ using $p_{\mathrm{I}} = 0$ and the material parameter values for the nematic 5CB [201]. The arrow shows the direction of increasing time, t.

of the squeeze film the torque applied to the director will lead to a positive perturbation θ_1 towards the nearest negative Leslie angle $\pi - \theta_{\mathrm{L}}$, and in the lower half of the squeeze film the torque applied to the director will lead to a negative perturbation θ_1 towards the nearest positive Leslie angle θ_{L}.

The evolution of the first-order director angle θ_1, given by (3.60), is plotted in Figure 3.8 as function of z for the four anchoring cases at $r = R(t)/2$ for $t = 0$, $t = 0.2$, $t = 0.4$ and $t = 0.6$. As the squeezing occurs the shear rate increases, leading to an increase in the torque on the director, and thus the magnitude

of the first-order director angle $|\theta_1|$ increases as the shear gradient aligns the director closer towards the closest Leslie angle. As (3.75) shows, this increase in magnitude of θ_1 is proportional to $H'(t)/H(t)^{1/2}$.

In order to visualise the perturbations of the leading-order director due to flow, Figure 3.9 shows the leading-order director field $\boldsymbol{n}(\theta_0)$ and the director field up to first-order $\boldsymbol{n}(\theta_0 + \mathrm{Er}\theta_1)$. Note that in order to clearly show the first-order perturbation to the leading-order director field we have exaggerated the first-order perturbation by artificially increasing the Ericksen number to Er = 100 in Figure 3.9(b), Er = 10 in Figure 3.9(d) and Figure 3.9(f) and Er = 35 in Figure 3.9(h).

3.3.5 Shear stress and couple stress on the substrates

The leading-order shear stress $g(\theta_0)\partial u_0/\partial\tilde{z}$ at the top substrate $\tilde{z} = 1$ and the bottom substrate $\tilde{z} = 0$, given by (3.83) and (3.84), and the leading- and first-order couple stress $\partial\theta_0/\partial\tilde{z} + \mathrm{Er}\partial\theta_1/\partial\tilde{z}$ at $\tilde{z} = 1$ and $\tilde{z} = 0$, given by (3.85) and (3.86), are shown in Table 3.3 and Table 3.4, respectively, for the four anchoring cases, at $r = R(t)/2$ and $t = 0.5$, and using material parameter values for the nematic 5CB [201]. Table 3.3 shows that the leading-order shear stress is largest for the homeotropic anchoring case, which is due to the large value of $g(\theta_0)$ at both $\tilde{z} = 1$ and $\tilde{z} = 0$ in this case. The HAN anchoring case is the only case with an asymmetric solution for u_0, as shown in Figure 3.3, which gives rise to a corresponding asymmetry in the shear stress at $\tilde{z} = 1$ and $\tilde{z} = 0$. For the planar, homeotropic and π-cell anchoring cases the solution for θ_1 is antisymmetric about $\tilde{z} = 0.5$, as shown in Figure 3.7, which leads to equal first-order couple stresses at $\tilde{z} = 1$ and $\tilde{z} = 0$ in these cases. For the HAN anchoring case the solution for θ_1 is asymmetric, leading to different values of the couple stress at $\tilde{z} = 1$ and $\tilde{z} = 0$, as shown in Table 3.4. As (3.83)–(3.86) show, the magni-

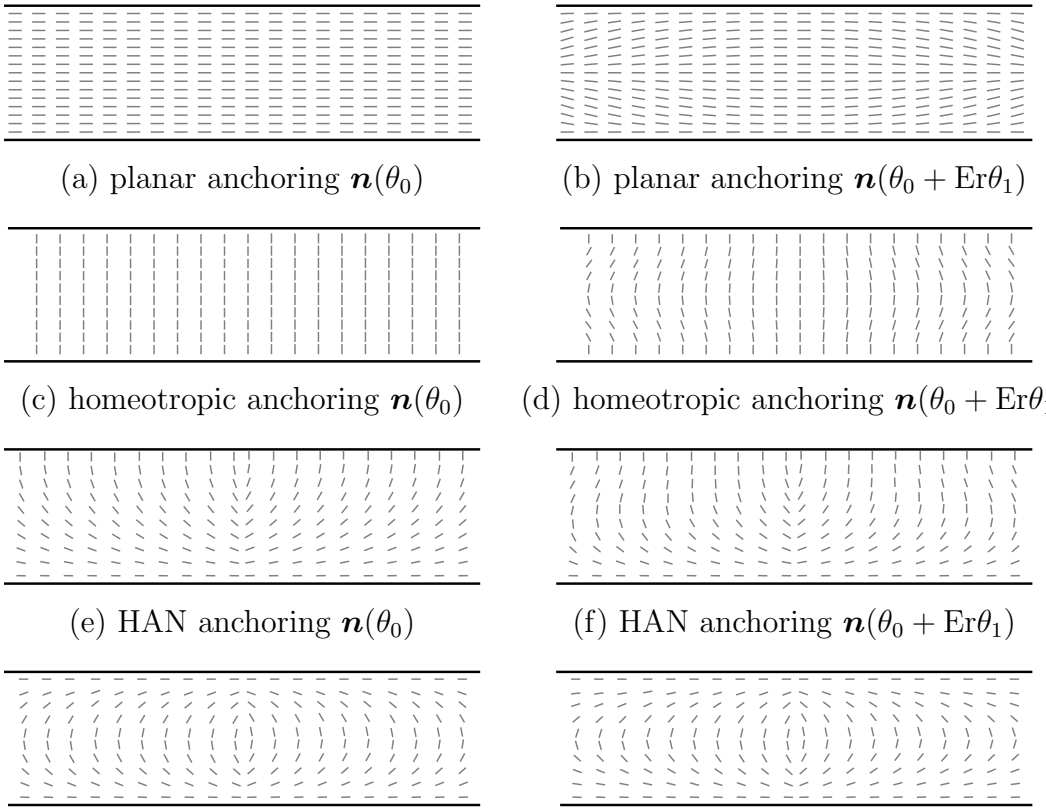

(a) planar anchoring $\boldsymbol{n}(\theta_0)$

(b) planar anchoring $\boldsymbol{n}(\theta_0 + \mathrm{Er}\theta_1)$

(c) homeotropic anchoring $\boldsymbol{n}(\theta_0)$

(d) homeotropic anchoring $\boldsymbol{n}(\theta_0 + \mathrm{Er}\theta_1)$

(e) HAN anchoring $\boldsymbol{n}(\theta_0)$

(f) HAN anchoring $\boldsymbol{n}(\theta_0 + \mathrm{Er}\theta_1)$

(g) π-cell anchoring $\boldsymbol{n}(\theta_0)$

(h) π-cell anchoring $\boldsymbol{n}(\theta_0 + \mathrm{Er}\theta_1)$

Figure 3.9: The leading-order director field $\boldsymbol{n}(\theta_0)$ ((a), (c), (e) and (g)) and the director field up to first-order $\boldsymbol{n}(\theta_0 + \mathrm{Er}\theta_1)$ ((b), (d), (f) and (h)) for the four anchoring cases; (a) and (b) planar, (c) and (d) homeotropic, (e) and (f) HAN and (g) and (h) π-cell at $t = 0.09$, where $\mathrm{Er} = 100$ in (b), $\mathrm{Er} = 10$ in (d) and (f) and $\mathrm{Er} = 35$ in (h), using $p_{\mathrm{I}} = 0$ and the material parameter values for the nematic 5CB [201]. Note that in order to clearly show the first-order perturbation to the leading-order director field we have exaggerated the first-order perturbation by artificially increasing the Ericksen number.

Anchoring case	Shear stress $g(\theta_0)\partial u_0/\partial\tilde{z}$	
	$\tilde{z}=1$	$\tilde{z}=0$
Planar	-1.1952	1.1952
Homeotropic	-6.1637	6.1637
HAN	-4.0358	2.0786
π-cell	-1.7543	1.7543

Table 3.3: Leading-order shear stress $g(\theta_0)\partial u_0/\partial\tilde{z}$ at the top substrate $\tilde{z}=1$ and the bottom substrate $\tilde{z}=0$, given by (3.83) and (3.84), evaluated for the four anchoring cases; planar, homeotropic, HAN, and π-cell, at $r=R(t)/2$ and $t=0.5$, using the material parameter values for the nematic 5CB [201].

Anchoring case	Couple stress $\partial\theta_0/\partial\tilde{z}+\mathrm{Er}\partial\theta_1/\partial\tilde{z}$	
	$\tilde{z}=1$	$\tilde{z}=0$
Planar	$0.0173\,\mathrm{Er}$	$0.0173\,\mathrm{Er}$
Homeotropic	$-0.3967\,\mathrm{Er}$	$-0.3967\,\mathrm{Er}$
HAN	$\pi/2-0.3855\,\mathrm{Er}$	$\pi/2+0.1076\,\mathrm{Er}$
π-cell	$\pi-0.0315\,\mathrm{Er}$	$\pi-0.0315\,\mathrm{Er}$

Table 3.4: Leading- and first-order couple stress $\partial\theta_0/\partial\tilde{z}+\mathrm{Er}\partial\theta_1/\partial\tilde{z}$ at $\tilde{z}=1$ and $\tilde{z}=0$, given by (3.85) and (3.86), evaluated for the four anchoring cases; planar, homeotropic, HAN, and π-cell, at $r=R(t)/2$ and $t=0.5$, using the material parameter values for the nematic 5CB [201].

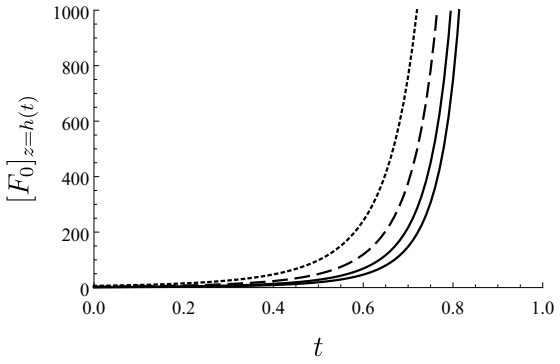

Figure 3.10: Leading-order force on the top substrate $[F_0]_{z=H(t)}$, given by (3.90), plotted as a function of time t for the four anchoring cases; planar (solid), homeotropic (dotted), HAN (dashed) and π-cell (dashed-dotted) using $p_{\mathrm{I}} = 0$ and the material parameter values for the nematic 5CB [201].

tude of the leading-order shear stress and the first-order couple stress increase as $H'(t)/H(t)^{3/2}\tilde{r}$ and $H'(t)/H(t)^{1/2}\tilde{r}$, respectively.

3.3.6 Leading-order force on the substrates

The leading-order force on the top substrate $[F_0]_{z=H(t)}$, given by (3.90), is plotted in Figure 3.10 as a function of time for the four anchoring cases. This is the force required to squeeze the nematic film at a constant prescribed speed. The leading-order force on the bottom substrate is equal and opposite to the leading-order force on the top substrate, i.e. $[F_0]_{z=0} = -[F_0]_{z=H(t)}$. As Figure 3.10 shows, an increasing magnitude of force must be applied to the top substrate to close the squeeze film at a constant prescribed speed. Indeed, as is immediately evident from (3.90), the force needed to maintain a constant prescribed speed increases as $H(t)^{-5} = (1-t)^{-5}$ for all anchoring cases, and so approaches infinity as t approaches the time $t = 1$ at which the top substrate meets the bottom substrate. It is also evident from Figure 3.10 that the anchoring case that produces the largest pressure requires the largest force to close the squeeze film, so that the

homeotropic anchoring case requires the largest force to close the squeeze film to a given height of the top substrate, and therefore requires the most work during manufacturing.

3.4 Results for a prescribed force

The second scenario studied is that in which the top substrate is free to move under a prescribed constant force due to its own dimensional weight. Although this is not the situation in the ODF method, it is the more commonly studied situation for a Newtonian fluid and is of scientific interest in its own right. The initial dimensional height of the top substrate, $\mathcal{H}$, and the constant dimensional weight of the top substrate, s_{p}, can then be used to set the values used in the non-dimensionalisation given by (3.12) in Section 3.1.2 using $\mathcal{U} = s_{\mathrm{p}}\mathcal{H}^2/\mu\mathcal{R}^3$. The non-dimensionalised initial height of the top substrate is then $H = 1$ at $t = 0$. Unlike the previous scenario, for $t > 0$ the height of the top substrate $H(t)$ is now unknown and must be determined by considering the balance of forces on the top substrate. In the limit of small Ericksen number we seek a solution for the height of the top substrate $H(t)$ as an asymptotic expansion in the form

$$H(t) = H_0(t) + \mathcal{O}(\mathrm{Er}). \tag{3.93}$$

The force on the top substrate, given by (3.90), can then be used to calculate the unknown leading-order height of the top substrate $H_0(t)$ by equating the sum of the weight of the top substrate and the force from a fixed constant external ambient pressure, p_{E}, with the leading-order force, namely $[F_0]_{z=H(t)} = W_p + A_{\mathrm{S}}p_{\mathrm{E}}$. Substituting the asymptotic expansion for the height of the top substrate (3.93)

into (3.90) at leading order in Er we obtain

$$W_p + A_{\mathrm{S}} p_{\mathrm{E}} = A_{\mathrm{S}} p_{\mathrm{I}} - \frac{3\eta(\theta_0)V^2}{2\pi H_0^5}\frac{\mathrm{d}H_0}{\mathrm{d}t}. \tag{3.94}$$

Rearranging, setting $\tilde{W}_p = W_p - A_{\mathrm{S}}(p_I - p_E)$ and integrating (3.94) with respect to t we obtain the solution from leading-order height of the top substrate,

$$H_0 = \frac{1}{(1+\zeta t)^{1/4}}, \quad \text{where} \quad \zeta = \frac{8\pi\tilde{W}_p}{3\eta(\theta_0)V^2} \tag{3.95}$$

and $\eta(\theta_0)$ is the effective viscosity defined in (3.71). As mentioned previously, typically the ODF method is carried out in vacuum where $p_{\mathrm{I}} = p_{\mathrm{E}} = 0$ so that $\tilde{W}_p = W_p$ and hence the leading-order height of the top substrate decreases in time, however, we note that for $A_{\mathrm{S}}(p_{\mathrm{I}} - p_{\mathrm{E}}) > W_p$ the leading-order height of the top substrate increases in time and for $A_{\mathrm{S}}(p_{\mathrm{I}} - p_{\mathrm{E}}) = W_p$ the leading-order height of the top substrate remains fixed at $H_0 = 1$. We note that upon substituting $\eta(\theta_0) = \mu$ the classical solution for height of the top substrate for a Newtonian fluid is recovered [100].

In this chapter we have only considered four infinite anchoring cases. However, note that the expression (3.95) is more general than this, and, in fact, represents the leading-order height of the top substrate $H_0(t)$ for *any* θ_0 that is the solution of (3.44) and *any* anchoring condition (for example, a weak anchoring condition [172]). The leading-order height of the top substrate H_0, given by (3.95), is plotted in Figure 3.11 as a function of time t for the four anchoring cases using $p_{\mathrm{I}} = p_{\mathrm{E}}$. Figure 3.11 shows that H_0 reduces fastest for the planar anchoring case. This result is as might have been expected, since the planar anchoring case has the smallest effective viscosity $\eta(\theta_0)$, and so requires the smallest force to close it at the same rate as the other anchoring cases. The results for each of the anchoring cases differ due to the values of the effective viscosity shown in

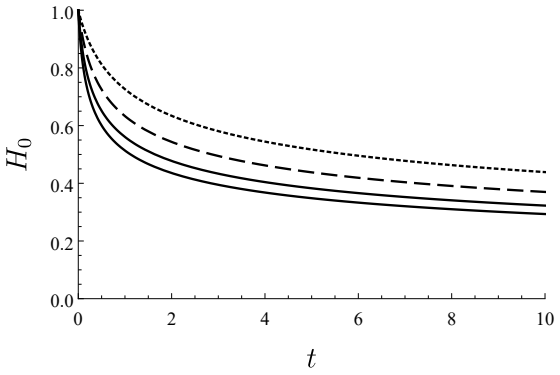

Figure 3.11: The leading-order height of the top substrate H_0 in the prescribed force scenario, given by (3.95), plotted as a function of time t for the four anchoring cases; planar (solid), homeotropic (dotted), HAN (dashed) and π-cell (dashed-dotted) using $p_{\mathrm{I}} = p_{\mathrm{E}}$, $W_p = 1$ and $V = 1$, and the material parameter values for the nematic 5CB [201].

Table 3.2. As is evident from (3.95), the smaller the effective viscosity, the faster H_0 decreases.

Using the leading-order height of the top substrate H_0, given by (3.95), the solutions for the first-order director angle θ_1, the leading-order radial velocity u_0, the leading-order vertical velocity w_0, and the leading-order pressure p_0 in the prescribed force scenario are

$$\theta_1(\tilde{r},\tilde{z},t) = -\frac{3}{2}\zeta\eta\left(\theta_0\right)\sqrt{\frac{V}{\pi}}\frac{\Pi_2(\tilde{z})\,\tilde{r}}{(1+\zeta t)^{9/8}}, \tag{3.96}$$

$$u_0(\tilde{r},\tilde{z},t) = -\frac{3}{2}\zeta\eta\left(\theta_0\right)\sqrt{\frac{V}{\pi}}\frac{\Pi_1(\tilde{z})\,\tilde{r}}{(1+\zeta t)^{7/8}}, \tag{3.97}$$

$$w_0(\tilde{z},t) = 3\zeta\eta\left(\theta_0\right)\sqrt{\frac{V}{\pi}}\frac{\int_0^{\tilde{z}}\Pi_1(\xi)\mathrm{d}\xi}{(1+\zeta t)^{5/4}}, \tag{3.98}$$

$$p_0(\tilde{r},t) = p_{\mathrm{I}} + \frac{3V\zeta\eta(\theta_0)}{4\pi}\frac{(1-\tilde{r}^2)}{(1+\zeta t)^{1/4}}. \tag{3.99}$$

As (3.96)–(3.99) show, the first-order director angle θ_1, the leading-order radial velocity u_0, the leading-order vertical velocity w_0, and the leading-order pressure

difference $p_0 - p_\mathrm{I}$, all tend toward zero in the limit $t \to \infty$.

The leading-order shear stress and the leading- and first-order couple stresses at the top substrate and the bottom substrate for the four anchoring cases can be calculated using (3.96) and (3.97). However, since their behaviour is qualitatively the same as that in the prescribed speed scenario, the details are omitted for brevity.

3.5 Conclusions

Motivated by the need for a better fundamental understanding of the reorientation of the molecules due to the flow of the liquid crystal during the industrial manufacture of liquid crystal devices, in the present work we formulated and analysed a squeeze-film model for the ODF method. Specifically, we considered a nematic squeeze film in the asymptotic regime in which the drop is thin, inertial effects are weak, and elasticity effects are strong (i.e. in which the aspect ratio $\delta \ll 1$, the reduced Reynolds number $\mathrm{Re} \ll 1$, and the Ericksen number $\mathrm{Er} \ll 1$ are all small) for four specific anchoring cases at the substrates (namely, planar, homeotropic, HAN, and π-cell infinite anchoring conditions) and for two different scenarios for the motion of the top substrate (namely, prescribed speed and prescribed force). Analytical expressions for the leading- and first-order director angles, θ_0 and θ_1, radial velocity, u_0 and u_1, vertical velocity, w_0 and w_1, and pressure, p_0 and p_1, were obtained and interpreted in terms of the effective viscosity $\eta(\theta_0)$, given by (3.71), and the relevant Leslie angles, θ_L, $-\theta_L$ and $\pi - \theta_L$, where θ_L is given by (3.51).

The results obtained in the present work help to improve our understanding of the ODF method. Specifically, as mentioned in Chapter 1, the misalignment of the molecules at the substrates due to the flow of the liquid crystal has been

proposed as a possible mechanism for the formation of mura. The present results capture the flow-driven reorientation of the molecules during squeezing via the first-order director angle θ_1. In particular, we found that the magnitude of θ_1 increases like $H'(t)/H(t)^{1/2}$ and that the behaviour of θ_1 depends on the anchoring case. Specifically, the magnitude of θ_1 is largest for the homeotropic and HAN anchoring cases, suggesting that these cases are potentially more susceptible to the formation of mura. As also mentioned in Chapter 1, damage to the molecular alignment at the substrates has also been proposed as a possible mechanism for the formation of mura. If this is the case, the molecular alignment at the substrates might be related to the shear stress and/or the couple stress. The leading-order couple stress is zero for the planar and homeotropic anchoring cases, $\pi/2$ for the HAN anchoring case, and π for the π-cell anchoring case. The leading-order shear stress and the first-order couple stress on the top substrate and the bottom substrate are given by (3.83)–(3.86). In particular, we found that the magnitudes of the leading-order shear stress and the first-order couple stress increase as $H'(t)/H(t)^{3/2}\tilde{r}$ and $H'(t)/H(t)^{1/2}\tilde{r}$, respectively, suggesting that the formation of mura will more likely when the downward speed of the top substrate, $H'(t)$, is large, the height of the top substrate, $H(t)$, is small, and at a large radius, $\tilde{r}$.

The force required to squeeze the nematic film at a constant prescribed speed is proportional to the effective viscosity, and so in the scenario in which the top substrate moves with constant prescribed speed, the homeotropic anchoring case requires the largest force and the planar condition the smallest force. Correspondingly, in the scenario in which the top substrate moves downwards under its own weight, the height of the top substrate reduces fastest for the planar anchoring case and slowest for the homeotropic anchoring case. Note that although we only considered four specific anchoring cases of infinite anchoring in the present work, the solutions for θ_0, θ_1, u_0, u_1, w_0, p_0 and p_1 also hold for other anchoring

conditions, including weak anchoring.

Finally, it should be pointed out that, while in the present work we have focused on the possible future manufacturing regime in which elasticity effects are stronger than viscous ones (i.e. in which the Ericksen number $\mathrm{Er} \ll 1$ is small), in Section 3.1.5 we showed that in the current manufacturing regime elasticity effects are typically weaker than viscous ones (i.e. the Ericksen number $\mathrm{Er} \gg 1$ is typically large), and so this asymptotic regime is also of considerable practical interest.

Chapter 4

Transient flow-driven distortion of a nematic in channel flow with dissipative weak planar anchoring

In this chapter we investigate another aspect of the ODF method. Specifically, we consider the possibility that significant transient flow-driven distortion of the nematic molecules at the substrates from their required orientation may occur during in the ODF method. We proceed by considering a rather different geometrical setup then those described in Chapters 2 and 3, namely pressure-driven flow of a nematic within a two-dimensional channel with fixed substrates, and we now focus on the behaviour of the nematic molecules close to the substrates. In particular, we will use a dissipative weak anchoring condition, which was introduced in Section 1.8.2, to investigate if transient flow-driven distortion of the nematic molecules on the substrates could play a role in the formation of the ODF mura. We proceed in Section 4.1 by formulating the governing equations and boundary conditions for pressure-driven flow of a nematic within a two-dimensional channel with fixed substrates and then consider asymptotic solutions in the limit of a

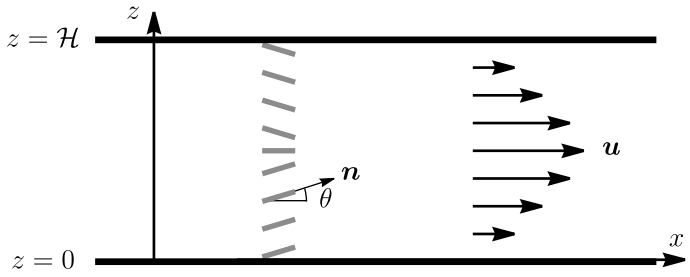

Figure 4.1: Unidirectional pressure-driven flow of a nematic within a two-dimensional channel with fixed substrates located at $z = 0$ and $z = \mathcal{H}$. The flow is driven by a prescribed constant pressure gradient in the x-direction, $G = -\mathrm{d}p/\mathrm{d}x\,(> 0)$, and is indicated by the black solid arrows. The director $\boldsymbol{n}$ with director angle θ is indicated by the grey lines. The Cartesian coordinates (x, z) are also indicated.

small Leslie angle in Sections 4.2 to 4.5.

4.1 Model formulation

4.1.1 Governing equations and boundary conditions

Consider unidirectional flow of a nematic with velocity in the x-direction within a two-dimensional channel with fixed substrates located at $z = 0$ and $z = \mathcal{H}$, as shown in Figure 4.1, where (x, z) are Cartesian coordinates and t denotes time. The flow is driven by a prescribed constant pressure gradient in the x-direction, denoted by $G = -\mathrm{d}p/\mathrm{d}x\,(> 0)$, where $p = p(x)$ is the fluid pressure, and we assume that the director remains in the (x, z)-plane. We therefore seek solutions for the director $\boldsymbol{n} = \boldsymbol{n}(z, t)$ and the velocity $\boldsymbol{u} = \boldsymbol{u}(z, t)$ in the channel in the forms

$$\boldsymbol{n} = (\cos(\theta(z,t)), 0, \sin(\theta(z,t))), \tag{4.1}$$

$$\boldsymbol{u} = (u(z,t), 0, 0), \tag{4.2}$$

where $\theta = \theta(z,t)$ is the angle between the director and x-axis, hereafter referred to as the director angle, as shown in Figure 4.1. For this situation, the Ericksen–Leslie equations [66, 127, 201], given by (1.20) and (1.21), for the director angle θ and the velocity u are given by

$$\gamma_1 \frac{\partial \theta}{\partial t} = f(\theta)\frac{\partial^2 \theta}{\partial z^2} + \frac{1}{2} f'(\theta)\left(\frac{\partial \theta}{\partial z}\right)^2 - m(\theta)\frac{\partial u}{\partial z}, \tag{4.3}$$

$$\rho \frac{\partial u}{\partial t} = G + \frac{\partial}{\partial z}\left(g(\theta)\frac{\partial u}{\partial z} + m(\theta)\frac{\partial \theta}{\partial t}\right), \tag{4.4}$$

where the constants ρ and γ_1 are the density and the bulk rotational viscosity, respectively. For a full derivation of the Ericksen–Leslie equations for rectilinear flow, see, for example, Appendix A of Crespo et al. [37]. The elasticity function $f(\theta)$ and viscosity functions $m(\theta)$ and $g(\theta)$ appearing in (4.3) and (4.4) are defined by

$$f(\theta) = K_1 \cos^2\theta + K_3 \sin^2\theta, \tag{4.5}$$

$$m(\theta) = \alpha_3 \cos^2\theta - \alpha_2 \sin^2\theta, \tag{4.6}$$

$$g(\theta) = \frac{1}{2}(\alpha_4 + \alpha_3 + \alpha_6)\cos^2\theta + \frac{1}{2}(\alpha_4 - \alpha_2 + \alpha_5)\sin^2\theta + \alpha_1 \sin^2\theta\cos^2\theta, \tag{4.7}$$

respectively, where the reader is reminded that the constants K_1 and K_3 are the splay and bend elastic constants, and $\alpha_1, \ldots, \alpha_6$ are the Leslie viscosities (of which $\alpha_4/2$ is the isotropic viscosity) which were introduced in Chapter 1. The elasticity function $f(\theta)$ is the effective elastic constant that the nematic exhibits in a simple shear flow with a fixed director angle θ. The viscosity function $m(\theta)$, which is also mentioned in Chapter 3, describes the director-dependent coupling between the rotation of the director, $\partial\theta/\partial t$, and the shear rate, $\partial u/\partial z$. The viscosity function $g(\theta)$, which is also mentioned in boths Chapters 2 and 3, is the effective viscosity that the nematic exhibits in a simple shear flow with a fixed director angle θ.

We take the boundary conditions for the director angle to be planar dissipative weak anchoring conditions (see, for example, [10,45,50–52,64,116,145,180]), given by

$$\gamma_{\rm S}\frac{\partial\theta}{\partial t} = +f(\theta)\frac{\partial\theta}{\partial z} - C\sin 2\theta \quad \text{at} \quad z = 0, \tag{4.8}$$

$$\gamma_{\rm S}\frac{\partial\theta}{\partial t} = -f(\theta)\frac{\partial\theta}{\partial z} - C\sin 2\theta \quad \text{at} \quad z = \mathcal{H}, \tag{4.9}$$

where the constants $\gamma_{\rm S}\,(\geq 0)$ is the surface viscosity and $C\,(\geq 0)$ is the anchoring strength, which were discussed in Section 1.8.2 and in Section 1.7.3, respectively. For anchoring conditions of this form the preferred director orientation on the substrates is $\theta \equiv p\pi$, where p is an integer. The present analysis is relevant to displays with planar anchoring for which the preferred director orientations on the substrates are parallel, such as in-plane switching display (IPS-LCD) [99]. While the present analysis is not directly relevant to displays with homeotropic anchoring, such as vertically aligned nematic display (VAN-LCD) [228], or to displays in which the director does not remain in the (x, z)-plane, such as twisted nematic display (TN-LCD) or super-twisted nematic display (STN-LCD) [175], we anticipate that many of the qualitative features of the present results will also occur in these displays.

For the velocity we impose standard no-slip boundary conditions given by

$$u = 0 \quad \text{at} \quad z = 0, \tag{4.10}$$

$$u = 0 \quad \text{at} \quad z = \mathcal{H}. \tag{4.11}$$

Appropriate initial conditions on θ and u will be described in Section 4.1.4.

4.1.2 Non-dimensionalisation

The governing equations (4.3) and (4.4) with (4.5), (4.6) and (4.7) subject to (4.8)–(4.11) are non-dimensionalised according to

$$\begin{gathered} t = \tau\hat{t}, \quad z = \mathcal{H}\hat{z}, \quad u = \frac{G\mathcal{H}^2}{\alpha_4}\hat{u}, \quad f = K_1\hat{f}, \quad m = \alpha_4\hat{m}, \quad g = \alpha_4\hat{g}, \\ K_3 = K_1\hat{K}_3, \quad \alpha_i = \alpha_4\hat{\alpha}_i \quad \text{for} \quad i = 1,\dots,6, \quad \gamma_i = \alpha_4\hat{\gamma}_i \quad \text{for} \quad i = 1,2, \end{gathered} \tag{4.12}$$

where τ is an appropriate timescale, which will be discussed in detail in Section 4.1.4, and non-dimensional variables are denoted by a superimposed hat ($\hat{}$). Note that the velocity is non-dimensionalised using the characteristic velocity of pressure-driven channel flow of a Newtonian fluid, which depends on G, h and α_4, the elastic function f and the bend elastic constant K_3 are non-dimensionalised with the splay elastic constant K_1, while the viscosity functions m and g, the Leslie viscosities α_i for $i = 1,\dots,6$, the bulk rotational viscosity γ_1, and the torsional viscosity γ_2 are all non-dimensionalised with α_4.

The non-dimensional Ericksen–Leslie equations (4.3) and (4.4) are given by

$$\frac{\gamma_1\mathcal{H}^2}{K_1\tau}\frac{\partial\theta}{\partial\hat{t}} = \hat{f}(\theta)\frac{\partial^2\theta}{\partial\hat{z}^2} + \frac{1}{2}\hat{f}'(\theta)\left(\frac{\partial\theta}{\partial\hat{z}}\right)^2 - \mathrm{Er}\,\hat{m}(\theta)\frac{\partial\hat{u}}{\partial\hat{z}}, \tag{4.13}$$

$$\mathrm{Re}\,\frac{\alpha_4}{G\mathcal{H}\tau}\frac{\partial\hat{u}}{\partial\hat{t}} = 1 + \frac{\partial}{\partial\hat{z}}\left(\hat{g}(\theta)\frac{\partial\hat{u}}{\partial\hat{z}} + \frac{\alpha_4}{G\mathcal{H}\tau}\,\hat{m}(\theta)\frac{\partial\theta}{\partial\hat{t}}\right), \tag{4.14}$$

where the non-dimensional elasticity and viscosity functions (4.5)–(4.7) are given by

$$\hat{f}(\theta) = \cos^2\theta + \hat{K}_3\sin^2\theta, \tag{4.15}$$

$$\hat{m}(\theta) = \hat{\alpha}_3\cos^2\theta - \hat{\alpha}_2\sin^2\theta, \tag{4.16}$$

$$\hat{g}(\theta) = \frac{1}{2}(1+\hat{\alpha}_3+\hat{\alpha}_6)\cos^2\theta + \frac{1}{2}(1-\hat{\alpha}_2+\hat{\alpha}_5)\sin^2\theta + \hat{\alpha}_1\sin^2\theta\cos^2\theta, \tag{4.17}$$

the non-dimensional dissipative weak anchoring conditions (4.8) and (4.9) are

$$\frac{\gamma_{\mathrm{S}}\mathcal{H}}{K_1\tau}\frac{\partial\theta}{\partial\hat{t}} = +\hat{f}(\theta)\frac{\partial\theta}{\partial\hat{z}} - \mathcal{C}\sin 2\theta \quad \text{at} \quad \hat{z}=0, \tag{4.18}$$

$$\frac{\gamma_{\mathrm{S}}\mathcal{H}}{K_1\tau}\frac{\partial\theta}{\partial\hat{t}} = -\hat{f}(\theta)\frac{\partial\theta}{\partial\hat{z}} - \mathcal{C}\sin 2\theta \quad \text{at} \quad \hat{z}=1, \tag{4.19}$$

and the non-dimensional no-slip conditions (4.10) and (4.11) are

$$\hat{u}=0 \quad \text{at} \quad \hat{z}=0, \tag{4.20}$$

$$\hat{u}=0 \quad \text{at} \quad \hat{z}=1. \tag{4.21}$$

Equations (4.13)–(4.21) involve three key non-dimensional groups, namely the Ericksen number Er defined by

$$\mathrm{Er} = \frac{G\mathcal{H}^3}{K_1}, \tag{4.22}$$

the Reynolds number Re defined by

$$\mathrm{Re} = \frac{\rho G\mathcal{H}^3}{\alpha_4^2}, \tag{4.23}$$

and the anchoring strength parameter $\mathcal{C}$ defined by

$$\mathcal{C} = \frac{C\mathcal{H}}{K_1}. \tag{4.24}$$

We note that the Ericksen number (4.22) and Reynolds number (4.23) have identical interpretations to those described in Chapter 3, namely (3.14) and (3.15), respectively. The anchoring strength parameter $\mathcal{C}$ is a non-dimensional measure of the relative strength of anchoring and splay elastic effects on the substrates. As described in Section 1.7.3, the limit of zero anchoring strength parameter ($\mathcal{C}\to 0$) corresponds to a regime in which there is zero anchoring on the substrates, while

the limit of infinite anchoring strength parameter ($\mathcal{C} \to \infty$) corresponds to a regime in which there is infinite anchoring on the substrates.

Solving the governing equations and boundary conditions (4.13)–(4.21) must, in general, be done numerically. However, we follow an approach similar to that of Quintans Carou et al. [169, 170] and use a combination of asymptotic and numerical methods to analyse the problem in the limit of small Leslie angle.

4.1.3 Flow alignment

As discussed at length in Section 1.4.1, for flow-aligning nematics considered in this thesis, i.e. for nematics whose viscosities satisfy $\hat{\alpha}_3/\hat{\alpha}_2 \geq 0$, in shear flow the director angle approaches $\theta = p\pi \pm \theta_{\mathrm{L}}$, where θ_{L} is given by (1.38) and p is an integer. When viscous effects dominate splay elastic effects within the channel (i.e. when $\mathrm{Er} \gg 1$), the director angle approaches the "positive" and "negative" Leslie angle in the bulk of the channel and reorientational boundary and/or internal layers may occur between the uniformly orientated bulk and/or the orientation dictated by the substrates [5, 11, 37, 169, 170, 194, 201].

We introduce a non-dimensional viscosity ratio denoted by $\epsilon\,(\geq 0)$ and defined by

$$\epsilon = \sqrt{\frac{\hat{\alpha}_3}{\hat{\alpha}_2}}, \tag{4.25}$$

so that the Leslie angle defined by (1.38) can be written in terms of ϵ as $\theta_{\mathrm{L}} = \tan^{-1}\epsilon$. The viscosity ratio ϵ can also be expressed in terms of the more commonly measured bulk rotational viscosity $\hat{\gamma}_1$ and torsional viscosity $\hat{\gamma}_2$ [201] as

$$\epsilon = \sqrt{\frac{\hat{\gamma}_1 + \hat{\gamma}_2}{\hat{\gamma}_2 - \hat{\gamma}_1}}. \tag{4.26}$$

As stated in Section 1.9.1, for nematic materials that are commonly used

in industrial manufacturing of LCDs, typically ϵ is small. For example, for the nematic materials discussed in Section 1.9.1, $\epsilon \simeq 0.210$ for 5CB [201], $\epsilon \simeq 0.143$ for 7CB [101], and $\epsilon \simeq 0.001$ for 8OCB [31]. In Section 4.2 we will exploit the smallness of ϵ to seek asymptotic solutions in the limit $\epsilon \to 0$.

For future reference, we note that the non-dimensional viscosity functions $\hat{m}(\theta)$ and $\hat{g}(\theta)$ given by (4.16) and (4.17) can be written without explicitly mentioning $\hat{\alpha}_3 = \epsilon^2 \hat{\alpha}_2$ as

$$\hat{m}(\theta) = \hat{\alpha}_2 \left(-\sin^2\theta + \epsilon^2 \cos^2\theta \right), \tag{4.27}$$

$$\hat{g}(\theta) = \frac{1}{2}\left(1 + \epsilon^2\hat{\alpha}_2 + \hat{\alpha}_6\right)\cos^2\theta + \frac{1}{2}\left(1 - \hat{\alpha}_2 + \hat{\alpha}_5\right)\sin^2\theta + \hat{\alpha}_1 \sin^2\theta \cos^2\theta. \tag{4.28}$$

4.1.4 Timescales

We now discuss four timescales occurring in (4.13)–(4.21), namely

$$\tau_1 = \frac{\gamma_1 \mathcal{H}^2}{K_1}, \qquad \tau_2 = \frac{\rho \mathcal{H}^2}{\alpha_4}, \qquad \tau_3 = \frac{\alpha_2}{G\mathcal{H}}, \qquad \tau_4 = \frac{\gamma_{\mathrm{S}} \mathcal{H}}{K_1}, \tag{4.29}$$

over which different physical effects occur.

Using the definitions (4.27) and (4.29) in (4.13), (4.14), (4.18) and (4.19) yields the governing equations

$$\frac{\tau_1}{\tau}\frac{\partial \theta}{\partial \hat{t}} = \hat{f}(\theta)\frac{\partial^2 \theta}{\partial \hat{z}^2} + \frac{1}{2}\hat{f}'(\theta)\left(\frac{\partial \theta}{\partial \hat{z}}\right)^2 - \hat{\alpha}_2 \mathrm{Er}\left(\epsilon^2 \cos^2\theta - \sin^2\theta\right)\frac{\partial \hat{u}}{\partial \hat{z}}, \tag{4.30}$$

$$\frac{\tau_2}{\tau}\frac{\partial \hat{u}}{\partial \hat{t}} = 1 + \frac{\partial}{\partial \hat{z}}\left[\hat{g}(\theta)\frac{\partial \hat{u}}{\partial \hat{z}} + \frac{\tau_3}{\tau}\left(\epsilon^2 \cos^2\theta - \sin^2\theta\right)\frac{\partial \theta}{\partial \hat{t}}\right], \tag{4.31}$$

and the dissipative weak anchoring conditions

$$\frac{\tau_4}{\tau}\frac{\partial\theta}{\partial\hat{t}} = +\hat{f}(\theta)\frac{\partial\theta}{\partial\hat{z}} - \mathcal{C}\sin 2\theta \quad \text{at} \quad \hat{z}=0, \tag{4.32}$$

$$\frac{\tau_4}{\tau}\frac{\partial\theta}{\partial\hat{t}} = -\hat{f}(\theta)\frac{\partial\theta}{\partial\hat{z}} - \mathcal{C}\sin 2\theta \quad \text{at} \quad \hat{z}=1. \tag{4.33}$$

The *bulk director rotation timescale* τ_1 appears in the angular momentum equation (4.30) and is the timescale of rotation of the director within the bulk of the channel induced by the splay elastic reorientation towards a uniform director. The *fluid inertia timescale* τ_2 appears in the linear momentum equation (4.31) and is the familiar inertial timescale for a Newtonian fluid. The *director-flow coupling timescale* τ_3 also appears in the linear momentum equation (4.31) and is the timescale on which changes in the velocity affect the director orientation and vice versa. The *substrate director rotation timescale* τ_4 appears in the dissipative weak anchoring conditions (4.32) and (4.33) and is the timescale of rotation of the director on the substrates of the channel driven by splay elastic effects. In contrast to the bulk rotation timescale τ_1, the substrate director rotation timescale τ_4 depends on the surface rotational viscosity γ_{S} rather than the bulk rotational viscosity γ_1. The timescales τ_1 and τ_4 depend on splay elastic reorientation, for a discussion of the timescales depending on twist elastic reorientation (i.e. those depending on K_2), the reader is referred to the work of Rey [180].

In order to obtain order-of-magnitude estimates of the timescales τ_1, τ_2, τ_3 and τ_4 in the ODF method we use estimated parameter values for a typical nematic mixture used in industrial manufacturing of LCDs, namely a nematic density $\rho = 10^3\ \mathrm{kg\,m^{-3}}$ [201], surface rotational viscosity $\gamma_{\mathrm{S}} = 10^{-8}$–$10^{-6}\ \mathrm{Pa\,s\,m}$ [51,162], Leslie viscosities $\alpha_2 = 10^{-2}\ \mathrm{Pa\,s}$ and $\alpha_4 = 10^{-1}\ \mathrm{Pa\,s}$ [31, 201], bulk rotational viscosity $\gamma_1 = 10^{-2}\ \mathrm{Pa\,s}$ [201], viscosity ratio $\epsilon = 10^{-1}$, splay elastic constant $K_1 = 10^{-11}\ \mathrm{N}$ [201], and a gap between the substrates of the $\mathcal{H} = \mathcal{H}_{\mathrm{f}} = 10^{-6}\,\mathrm{m}$

Timescale	Definition	Physical Meaning	Value
τ_1	$\dfrac{\gamma_1 \mathcal{H}^2}{K_1}$	bulk director rotation	10^{-3} s
τ_2	$\dfrac{\rho \mathcal{H}^2}{\alpha_4}$	fluid inertia	10^{-8} s
τ_3	$\dfrac{\alpha_2}{G\mathcal{H}}$	director-flow coupling	10^{-8} s
τ_4	$\dfrac{\gamma_{\mathrm{S}} \mathcal{H}}{K_1}$	substrate director rotation	10^{-3}–10^{-1} s

Table 4.1: Order-of-magnitude estimates of the timescales τ_1, τ_2, τ_3 and τ_4 in the ODF method using the estimated parameter values given in the text.

to represent the final gap between the substrates in the ODF method (as stated in Table 1.1). To estimate the timescale τ_3 we require an estimate of the pressure gradient G. The flow of the nematic in the ODF method is driven by the squeezing together of the substrates, and so the pressure gradient can be estimated by using the rescalings used in Chapter 3 in (3.1.2), namely $G = \alpha_4 \bar{L} s_{\mathrm{p}} / \mathcal{H}^3$, where $\bar{L}$ is the horizontal length scale of the flow and s_{p} is the speed of the downward moving top substrate [100]. The timescale of squeezing in the ODF method discussed in Chapter 2, denoted here by τ_{ODF}, is the timescale over which the substrates are squeezed together. We take the horizontal length scale $\bar{L}$ to be half the separation distance of each droplet L, namely $L = 10^{-2}$ m (see Table 1.1), the the speed of the downward moving top substrate to be $s_{\mathrm{p}} = 10^{-3}\ \mathrm{m\,s^{-1}}$ (see Table 1.1), which yields an estimate of the pressure gradient in the ODF method of $G = 10^{12}$ $\mathrm{Pa\,m^{-1}}$.

Table 4.1 shows order-of-magnitude estimates of the timescales τ_1, τ_2, τ_3 and τ_4 in the ODF method using the estimated parameter values given above. In particular, Table 4.1 shows that the fluid inertia timescale and director flow coupling timescale, τ_2 and τ_3, are much shorter than the two director rotation timescales, τ_1

and τ_4, and so these effects can safely be treated as instantaneous on the timescale of the ODF method, and henceforth we set $\tau_2 = 0$ and $\tau_3 = 0$. The two director rotation timescales are comparable when $\gamma_S = 10^{-8}$ Pa s m, suggesting that the regime in which $\tau = \tau_1 \simeq \tau_4$ is worthy of study, but since τ_1 is 100 times shorter than τ_4 when $\gamma_S = 10^{-6}$ Pa s m, we also set $\tau_1 = 0$. Since all of the timescales except the substrate director rotation timescale τ_4 have been set to zero, we can now, without loss of generality, set $\tau = \tau_4$, so that the governing equations (4.30) and (4.31) become

$$\hat{f}(\theta)\frac{\partial^2\theta}{\partial\hat{z}^2} + \frac{1}{2}\hat{f}'(\theta)\left(\frac{\partial\theta}{\partial\hat{z}}\right)^2 = \hat{\alpha}_2 \mathrm{Er}\left(\epsilon^2\cos^2\theta - \sin^2\theta\right)\frac{\partial\hat{u}}{\partial\hat{z}}, \tag{4.34}$$

$$0 = 1 + \frac{\partial}{\partial\hat{z}}\left(g(\theta)\frac{\partial\hat{u}}{\partial\hat{z}}\right), \tag{4.35}$$

subject to the dissipative weak anchoring conditions (4.18) and (4.19),

$$\frac{\partial\theta}{\partial\hat{t}} = +\hat{f}(\theta)\frac{\partial\theta}{\partial\hat{z}} - \mathcal{C}\sin 2\theta \quad \text{at} \quad \hat{z} = 0, \tag{4.36}$$

$$\frac{\partial\theta}{\partial\hat{t}} = -\hat{f}(\theta)\frac{\partial\theta}{\partial\hat{z}} - \mathcal{C}\sin 2\theta \quad \text{at} \quad \hat{z} = 1, \tag{4.37}$$

and the no-slip conditions (4.20) and (4.21), where the hat ($\hat{}$) notation on non-dimensional variables has been dropped for clarity.

Given that the time derivatives have been removed from the governing equations (4.34) and (4.35), leaving only time derivatives of the director angle in the dissipative weak anchoring conditions (4.36) and (4.37), we no longer require initial conditions on the director angle and the velocity (i.e. $\theta(z,0)$ and $u(z,0)$) within the bulk of the channel. Instead we only require initial conditions on the director angle on the substrates (i.e. $\theta(0,0)$ and $\theta(1,0)$). Specifically, we impose

initial conditions on the director angle on the substrates in the form

$$\theta = +\theta_{\mathrm{L}}\vartheta \quad \text{at} \quad z = 0 \quad \text{and} \quad t = 0, \tag{4.38}$$

$$\theta = -\theta_{\mathrm{L}}\vartheta \quad \text{at} \quad z = 1 \quad \text{and} \quad t = 0, \tag{4.39}$$

where $\vartheta\,(\geq 0)$ is the magnitude of the initial director angle on the substrates scaled with θ_{L}.

At this point it is useful to consider typical values of the important non-dimensional groups Er and $\mathcal{C}$ in the ODF method. Using the values discussed above for Table 4.1, the Ericksen number is found to be $\mathrm{Er} = 10^5$, indicating that the flow is usually dominated by viscous effects. However, this large value is slightly misleading because, as we will show in Section 4.2, the effective Ericksen number, denoted by $\bar{\mathrm{E}}\mathrm{r}$, takes the somewhat smaller value $\bar{\mathrm{E}}\mathrm{r} = 1.7 \times 10^2$ and so, for completeness, we will consider all values of $\bar{\mathrm{E}}\mathrm{r}$ in what follows. As mentioned in Section 1.7.3, anchoring strengths are typically found experimentally to lie in the range of $C = 10^{-5}$–10^{-3} $\mathrm{N\,m^{-1}}$ [157, 227], and so, using (4.24) and the values in Table 4.1, this corresponds to values of the anchoring strength parameter in the range $\mathcal{C} = 1$–10^2.

4.2 Asymptotic solutions in the limit of small Leslie angle

As described in Section 4.1.3, typically the viscosity ratio ϵ for commonly used nematics and mixtures of nematics is small, and so henceforth we obtain asymptotic solutions in the limit $\epsilon \to 0$. In particular, in this limit the Leslie angle $\theta_{\mathrm{L}} = \tan^{-1}\epsilon \sim \epsilon \ll 1$ is small.

In the limit $\epsilon \to 0$ we seek asymptotic solutions for θ and u in powers of ϵ in

the forms

$$\theta(z,t) = \theta_0(z,t) + \epsilon\theta_1(z,t) + \epsilon^2\theta_2(z,t) + O\left(\epsilon^3\right), \tag{4.40}$$

$$u(z,t) = u_0(z,t) + \epsilon u_1(z,t) + \epsilon^2 u_2(z,t) + O\left(\epsilon^3\right). \tag{4.41}$$

Substituting the expansions (4.40) and (4.41) into the angular momentum equation (4.34), the linear momentum equation (4.35), the dissipative weak anchoring conditions (4.36) and (4.37), the initial conditions (4.38) and (4.39), and the no-slip conditions (4.20) and (4.21), and defining an appropriately rescaled *effective Ericksen number* $\bar{\mathrm{Er}}$ [169, 170] (hereafter simply referred to as the Ericksen number) given by

$$\bar{\mathrm{Er}} = -\frac{\epsilon\alpha_2}{1+\alpha_6}\,\mathrm{Er}, \tag{4.42}$$

yields the leading-order equations

$$0 = \sin^2\theta_0 \frac{\partial u_0}{\partial z}, \tag{4.43}$$

$$0 = 1 + \frac{\partial}{\partial z}\left(g(\theta_0)\frac{\partial u_0}{\partial z}\right), \tag{4.44}$$

subject to the leading-order dissipative weak anchoring conditions

$$\frac{\partial\theta_0}{\partial t} = +f(\theta_0)\frac{\partial\theta_0}{\partial z} - 2\mathcal{C}\theta_0 \quad \text{at} \quad z = 0, \tag{4.45}$$

$$\frac{\partial\theta_0}{\partial t} = -f(\theta_0)\frac{\partial\theta_0}{\partial z} - 2\mathcal{C}\theta_0 \quad \text{at} \quad z = 1. \tag{4.46}$$

(Note that the definition of $\bar{\mathrm{Er}}$ given in (4.42) incorporates the $O(1)$ factor of $-\alpha_2/(1+\alpha_6)$ in order to simplify some of the subsequent expressions.)

The leading-order director angle is obtained by solving (4.43) and (4.44) subject to the (4.45) and (4.46) to yield the trivial solution $\theta_0 \equiv 0$, i.e. the leading-order director angle is planar throughout the channel, and so at leading order

the functions $f(\theta)$ and $g(\theta)$ appearing in (4.34)–(4.37) are given by $f(\theta) = 1$ and $g(\theta) = (1 + \alpha_6)/2$.

The leading-order velocity is determined by integrating (4.44) with $\theta_0 \equiv 0$ subject to the no-slip conditions (4.20) and (4.21) to obtain the classical Poiseuille flow profile

$$u_0 = \frac{z\,(1-z)}{1+\alpha_6}. \tag{4.47}$$

The first-order angular momentum equation is identically satisfied, and the first-order linear momentum equation has the trivial solution $u_1 \equiv 0$.

The first-order director angle then satisfies the second-order angular momentum equation

$$\frac{\partial^2 \theta_1}{\partial z^2} = \bar{\mathrm{E}}\mathrm{r}\,(2z-1)\left(1-\theta_1^2\right), \tag{4.48}$$

subject to the first-order dissipative weak anchoring conditions

$$\frac{\partial \theta_1}{\partial t} = +\frac{\partial \theta_1}{\partial z} - 2\mathcal{C}\theta_1 \quad \text{at} \quad z = 0, \tag{4.49}$$

$$\frac{\partial \theta_1}{\partial t} = -\frac{\partial \theta_1}{\partial z} - 2\mathcal{C}\theta_1 \quad \text{at} \quad z = 1, \tag{4.50}$$

and the first-order initial conditions

$$\theta_1 = +\vartheta \quad \text{at} \quad z = 0 \quad \text{and} \quad t = 0, \tag{4.51}$$

$$\theta_1 = -\vartheta \quad \text{at} \quad z = 1 \quad \text{and} \quad t = 0. \tag{4.52}$$

The second-order velocity satisfies the second-order linear momentum equation

$$0 = \frac{\partial}{\partial z}\left[\alpha_2 \frac{\partial u_0}{\partial z} + (2\alpha_1 - \alpha_2 + \alpha_5 - \alpha_6)\,\theta_1^2 \frac{\partial u_0}{\partial z} + (1+\alpha_6)\frac{\partial u_2}{\partial z}\right], \tag{4.53}$$

which can be integrated subject to the no-slip conditions (4.20) and (4.21) to

obtain

$$u_2 = \frac{2\alpha_1 - \alpha_2 + \alpha_5 - \alpha_6}{(1+\alpha_6)^2}\left[\int_0^z (2Z-1)\theta_1^2\,\mathrm{d}Z - z\int_0^1 (2z-1)\theta_1^2\,\mathrm{d}z\right] + \frac{\alpha_2}{(1+\alpha_6)^2}z(z-1). \tag{4.54}$$

In the remainder of this chapter we shall discuss the quasi-steady solutions for the first-order director angle θ_1 (hereafter simply referred to as "the director angle") of (4.48) (hereafter simply referred to as "the director angle equation") subject to the dissipative weak anchoring conditions (4.49) and (4.50), and the initial conditions (4.51) and (4.52). In particular, we will obtain asymptotic solutions in the limit of large Ericksen number $\bar{\mathrm{E}}\mathrm{r} \to \infty$ in Section 4.3 and in the limit of small Ericksen number $\bar{\mathrm{E}}\mathrm{r} \to 0$ in Section 4.4, as well as numerical solutions for general values of the Ericksen number in Section 4.5. Since we are particularly interested in the transient flow-driven distortion of the director from its required orientation on the substrates of the channel, we write $\Theta(t) = \theta_1(0,t)$ for the director angle at $z = 0$ (hereafter simply referred to as "the director angle on the substrates"), and note that since θ_1 is symmetric about $z = 1/2$, the director angle at $z = 1$ is given by $\theta_1(1,t) = -\Theta(t)$. As we shall show, in the limit $t \to \infty$ the director angle approaches a steady state solution which we denote by $\theta_1 = \theta_{1\mathrm{SS}}(z)$ and $\Theta = \Theta_{\mathrm{SS}}$, i.e. $\theta_1 \to \theta_{1\mathrm{SS}}$ and $\Theta \to \Theta_{\mathrm{SS}}$ as $t \to \infty$. Once the director angle θ_1 has been determined, the second-order velocity u_2 can be calculated using (4.54).

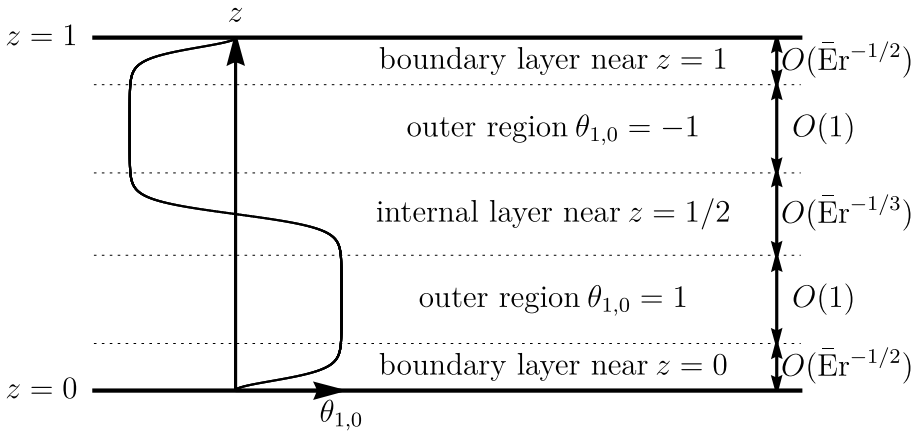

Figure 4.2: The structure of the leading-order director angle $\theta_{1,0}$ in the limit of large Ericksen number, $\bar{\mathrm{Er}} \to \infty$.

4.3 Asymptotic solution in the limit of large Ericksen number

In the limit of large Ericksen number $\bar{\mathrm{Er}} \to \infty$ the solution for the director angle θ_1 has narrow reorientational boundary layers near $z = 0$ and $z = 1$ and a narrow reorientational internal layer near $z = 1/2$ separated by two outer regions, as shown in Figure 4.2.

4.3.1 Outer solution

The outer solution valid in the outer regions away from the boundary and internal layers can be obtained by seeking an asymptotic solution for θ_1 in powers of $\bar{\mathrm{Er}}^{-1}$ when $\epsilon \ll \bar{\mathrm{Er}}^{-1} \ll 1$ in the form $\theta_1 = \theta_{1,0} + O(\bar{\mathrm{Er}}^{-1})$, where $\theta_{1,0}$ denotes the term that is first order in ϵ and leading order in $\bar{\mathrm{Er}}^{-1}$. Substituting this expansion into the director angle equation (4.48) yields the simple solution $\theta_{1,0} = \pm 1$, which corresponds to the director angle being equal to either the positive or the negative Leslie angle at leading order. The leading-order velocity u_0 given by

(4.47) satisfies $\partial u_0/\partial z > 0$ for $0 < z < 1/2$ and $\partial u_0/\partial z < 0$ for $1/2 < z < 1$, and so, as described in Section 1.4.1, the appropriate uniformly orientated leading-order outer solution is $\theta_{1,0} = 1$ for $0 < z < 1/2$ and $\theta_{1,0} = -1$ for $1/2 < z < 1$, as shown in Figure 4.2.

4.3.2 Inner solutions in the boundary layers

Inspection of (4.48) suggests that the boundary layer near $z = 0$ is of width $O\left(\bar{\mathrm{E}}\mathrm{r}^{-1/2}\right) \ll 1$ in which the director angle adjusts from its uniform value in the outer region to its value at the substrate, and so we introduce an appropriately rescaled inner coordinate Z defined by $z = \bar{\mathrm{E}}\mathrm{r}^{-1/2} Z$ to yield

$$\frac{\partial^2 \theta_1}{\partial Z^2} = \left(2\bar{\mathrm{E}}\mathrm{r}^{-1/2} Z - 1\right)\left(1 - {\theta_1}^2\right). \tag{4.55}$$

Seeking an asymptotic solution of (4.55) in the form $\theta_1 = \theta_{1,0} + O\left(\bar{\mathrm{E}}\mathrm{r}^{-1/2}\right)$ yields the leading-order equation

$$\frac{\partial^2 \theta_{1,0}}{\partial Z^2} = {\theta_{1,0}}^2 - 1. \tag{4.56}$$

The appropriate exact solution of (4.56) subject to the matching conditions $\theta_{1,0} \to 1$ and $\partial\theta_{1,0}/\partial Z \to 0$ as $Z \to \infty$ is

$$\theta_{1,0} = 3\tanh^2\left(\frac{Z}{\sqrt{2}} + \tanh^{-1}\sqrt{\frac{2+\Theta_0}{3}}\right) - 2, \tag{4.57}$$

where $\Theta_0(t) = \theta_{1,0}(0,t)$ is the leading-order director angle on the substrates. Note that setting $\Theta_0 \equiv 0$ in (4.57) recovers the steady solution obtained by Quintans Carou et al. [169,170] in the limit of infinite planar anchoring, $\mathcal{C} \to \infty$. However, in the present problem Θ_0 is, of course, not constant, and the singular ordinary differential equation for the evolution of Θ_0 can be obtained by substituting $\theta_{1,0}$

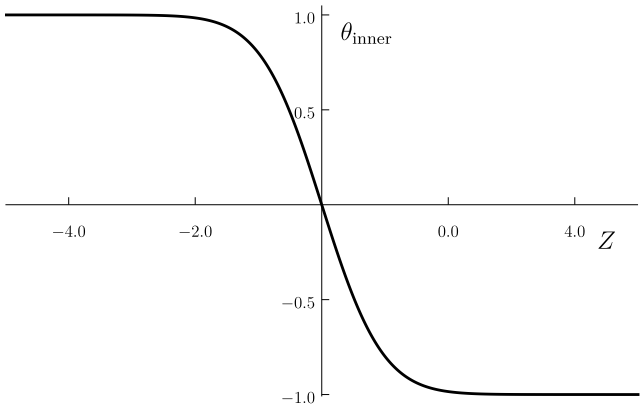

Figure 4.3: The leading-order director angle in the internal layer θ_{inner} obtained by solving (4.59) numerically using the matching conditions $\theta_{\text{inner}} \to -1$ as $Z \to \infty$ and $\theta_{\text{inner}} \to 1$ as $Z \to -\infty$ plotted as a function of the inner variable Z.

given by (4.57) into the dissipative weak anchoring condition (4.49) to yield

$$\bar{\text{Er}}^{-1/2}\frac{\mathrm{d}\Theta_0}{\mathrm{d}t} = \sqrt{\frac{2}{3}}\,(1-\Theta_0)\sqrt{2+\Theta_0} - 2k\Theta_0, \quad \text{where} \quad k = \frac{\mathcal{C}}{\bar{\text{Er}}^{1/2}}\,(\geq 0). \quad (4.58)$$

In Section 4.3.5 we will consider the solution to (4.58) subject to the initial condition $\Theta_0(0) = \vartheta$. The corresponding inner solution valid in the boundary layer near $z = 1$ follows immediately from the symmetry of θ_1 about $z = 1/2$ mentioned earlier.

4.3.3 Inner solution in the internal layer

Inspection of (4.48) also suggests that the internal layer near $z = 1/2$ is of width $O\left(\bar{\text{Er}}^{-1/3}\right) \ll 1$ (i.e. much wider than the boundary layers but still much narrower than the channel) in which the director angle adjusts between its uniform values in the outer regions, and so we introduce an appropriately rescaled inner coordinate Z defined by $z = 1/2 + \bar{\text{Er}}^{-1/3}Z$. Seeking an asymptotic solution in the form

$\theta_1 = \theta_{1,0} + O\left(\bar{\mathrm{Er}}^{-1/3}\right)$ yields the leading-order equation

$$\frac{\partial^2 \theta_{1,0}}{\partial Z^2} = 2Z(1 - {\theta_{1,0}}^2) \tag{4.59}$$

subject to the matching conditions $\theta_{1,0} \to -1$ as $Z \to \infty$ and $\theta_{1,0} \to 1$ as $Z \to -\infty$. Equation (4.59) cannot be solved analytically, but, since it contains no parameters, it only needs to be solved once numerically. This numerical solution is denoted by $\theta_{\mathrm{inner}}(Z) = \theta_{1,0}(Z)$ and is plotted as a function of Z in Figure 4.3.

4.3.4 Composite solution

Combining the inner and outer solutions for θ_1 yields the composite solution

$$\begin{aligned} \theta_1 = {} & 3\tanh^2\left(\sqrt{\frac{\bar{\mathrm{Er}}}{2}}\, z + \tanh^{-1}\sqrt{\frac{2+\Theta_0}{3}}\right) \\ & - 3\tanh^2\left(\sqrt{\frac{\bar{\mathrm{Er}}}{2}}\,(1-z) + \tanh^{-1}\sqrt{\frac{2-\Theta_0}{3}}\right) \\ & + \theta_{\mathrm{inner}}\left(\bar{\mathrm{Er}}^{1/3}\left(z - \frac{1}{2}\right)\right) + O\left(\bar{\mathrm{Er}}^{-1}\right), \end{aligned} \tag{4.60}$$

where Θ_0 satisfies (4.58) subject to the initial condition $\Theta_0(0) = \vartheta$.

4.3.5 The director angle on the substrates

As we have already seen, the leading-order director angle on the substrates Θ_0 satisfies the singular ordinary differential equation (4.58) subject to the initial condition $\Theta_0(0) = \vartheta$. Inspection of (4.58) reveals that Θ_0 rapidly evolves towards its constant steady state value of $\Theta_{0\mathrm{SS}}$ given by

$$\Theta_0 = \Theta_{0\mathrm{SS}} = \frac{2}{3}\left[k - |\chi|^{1/3}\cos\left(\frac{1}{3}\arg(\chi)\right)\right]^2 - 2 + O\left(\bar{\mathrm{Er}}^{-1}\right) \tag{4.61}$$

over a short timescale of $O\left(\bar{\mathrm{Er}}^{-1/2}\right) \ll 1$. Rescaling t appropriately according to $t = \bar{\mathrm{Er}}^{-1/2}\tilde{t}$ shows that this rapid evolution is described by the implicit solution

$$-\sqrt{\frac{2}{3}}\tilde{t} = a\log\left(\frac{\sqrt{2+\Theta_0}-v_1}{\sqrt{2+\vartheta}-v_1}\right) + b\log\left(\frac{\sqrt{2+\Theta_0}-v_2}{\sqrt{2+\vartheta}-v_2}\right) + c\log\left(\frac{\sqrt{2+\Theta_0}-v_3}{\sqrt{2+\vartheta}-v_3}\right), \tag{4.62}$$

where

$$a = \frac{2v_1}{(v_1-v_2)(v_1-v_3)}, \tag{4.63}$$

$$b = \frac{2v_2}{(v_2-v_1)(v_2-v_3)}, \tag{4.64}$$

$$c = \frac{2v_3}{(v_3-v_1)(v_3-v_2)}. \tag{4.65}$$

The constants v_1, v_2, and v_3 are the roots of the cubic polynomial

$$\mathcal{F}(v) = v^3 + \sqrt{6}kv^2 - 3v - 2\sqrt{6}k, \tag{4.66}$$

which can be written explicitly as

$$v_1 = -\sqrt{\frac{2}{3}}\left[k - |\chi|^{1/3}\cos\left(\frac{1}{3}\arg(\chi)\right)\right], \tag{4.67}$$

$$v_2 = -\sqrt{\frac{2}{3}}\left[k + |\chi|^{1/3}\cos\left(\frac{1}{3}\arg(\chi) - \frac{\pi}{3}\right)\right], \tag{4.68}$$

$$v_3 = -\sqrt{\frac{2}{3}}\left[k + |\chi|^{1/3}\cos\left(\frac{1}{3}\arg(\chi) + \frac{\pi}{3}\right)\right], \tag{4.69}$$

where $|\chi|$ and $\arg(\chi)$ are the modulus and argument, respectively, of the complex number χ, defined by

$$\chi = 18k - 8k^3 + 6i\sqrt{6 + 3k^2 + 16k^4}. \tag{4.70}$$

It is informative to consider three cases for the size of the parameter k (and hence for the relative size of the non-dimensional groups $\bar{\mathrm{E}}\mathrm{r}$ and $\mathcal{C}$) in which further analytical progress can be made. Specifically, we consider the cases $k \gg 1$ ($\mathcal{C} \gg \bar{\mathrm{E}}\mathrm{r}^{1/2} \gg 1$), $k \ll 1$ (either $\bar{\mathrm{E}}\mathrm{r}^{1/2} \gg \mathcal{C} \gg 1$ or $\bar{\mathrm{E}}\mathrm{r}^{1/2} \gg 1 \gg \mathcal{C}$), and $k = O(1)$ ($\bar{\mathrm{E}}\mathrm{r}^{1/2} = O(\mathcal{C}) \gg 1$).

4.3.5.1 The case $k \gg 1$

In the case $k \gg 1$ ($\mathcal{C} \gg \bar{\mathrm{E}}\mathrm{r}^{1/2} \gg 1$) the implicit solution (4.62) reduces to the simple explicit solution

$$\Theta_0 = \vartheta \mathrm{e}^{-2k\tilde{t}}, \quad \text{i.e.} \quad \Theta_0 = \vartheta \mathrm{e}^{-2\mathcal{C}t}, \tag{4.71}$$

which approaches its steady state value $\Theta_{0\mathrm{SS}} = 0$ as $t \to \infty$, i.e. the director on the substrates becomes planar as $t \to \infty$. This case represents a regime in which the anchoring is sufficiently strong that the effects of flow are negligible on the substrates, and the (non-dimensional) timescale of the evolution of the director on the substrates towards its steady state value, denoted by σ_{S}, is given by

$$\sigma_{\mathrm{S}} = \frac{1}{2\mathcal{C}} \ll 1. \tag{4.72}$$

4.3.5.2 The case $k \ll 1$

In the case $k \ll 1$ (either $\bar{\mathrm{E}}\mathrm{r}^{1/2} \gg \mathcal{C} \gg 1$ or $\bar{\mathrm{E}}\mathrm{r}^{1/2} \gg 1 \gg \mathcal{C}$) the implicit solution (4.62) reduces to the appropriate explicit solution

$$\Theta_0 = -2 + 3\tanh\left(\sqrt{\frac{1}{2}}\tilde{t} + \tanh^{-1}\sqrt{\frac{2+\vartheta}{3}}\right)^2, \tag{4.73}$$

which approaches its steady state value $\Theta_{0\mathrm{SS}} = 1$ as $t \to \infty$, i.e. the director angle on the substrates approaches the Leslie angle as $t \to \infty$, according to

$$\Theta_0 = 1 - 12\exp\left[-2\tanh\sqrt{\frac{2+\vartheta}{3}} - \sqrt{2}\bar{\mathrm{Er}}^{1/2}t\right] + O\left(\exp\left[-2\bar{\mathrm{Er}}^{1/2}t\right]\right). \quad (4.74)$$

This case represents a regime in which the flow is sufficiently strong that the effects of anchoring are negligible on the substrates, and the timescale σ_{S} is given by

$$\sigma_{\mathrm{S}} = \frac{1}{\sqrt{2}\bar{\mathrm{Er}}^{1/2}} \ll 1. \quad (4.75)$$

4.3.5.3 The case $k = O(1)$

In the case $k = O(1)$ ($\bar{\mathrm{Er}}^{1/2} = O(\mathcal{C}) \gg 1$) the implicit solution (4.62) approaches its steady state value $\Theta_{0\mathrm{SS}}$ ($0 < \Theta_{0\mathrm{SS}} < 1$) given by (4.61) as $t \to \infty$. Unfortunately (4.62) does not yield an explicit expression for the timescale σ_{S}. However, as we shall show in Section 4.5.2, σ_{S} is always less than both (4.72) and (4.75), and so (4.72) and (4.75) provide a upper bound on σ_{S} for all values of k. This case represents a regime in which the effects of anchoring and flow are comparable on the substrates, and hence the behaviour of the director on the substrates depends on a combination of these two effects.

4.4 Asymptotic solution in the limit of small Ericksen number

In the limit of small Ericksen number $\bar{\mathrm{Er}} \to 0$ we seek an asymptotic solution for θ_1 in powers of $\bar{\mathrm{Er}}$ when $\epsilon \ll \bar{\mathrm{Er}} \ll 1$ in the form $\theta_1 = \theta_{1,0} + \bar{\mathrm{Er}}\,\theta_{1,1} + O\left(\bar{\mathrm{Er}}^2\right)$, where $\theta_{1,0}$ denotes the term that is first order in ϵ and leading order in $\bar{\mathrm{Er}}$ and $\theta_{1,1}$ denotes the term that is first order in ϵ and first order in $\bar{\mathrm{Er}}$.

At leading order in $\bar{\mathrm{E}}\mathrm{r}$ the director angle equation (4.48) reduces to simply

$$\frac{\partial^2 \theta_{1,0}}{\partial z^2} = 0, \tag{4.76}$$

subject to the dissipative weak anchoring conditions (4.49) and (4.50)

$$\frac{\partial \theta_{1,0}}{\partial t} = +\frac{\partial \theta_{1,0}}{\partial z} - 2\mathcal{C}\theta_{1,0} \quad \text{at} \quad z = 0, \tag{4.77}$$

$$\frac{\partial \theta_{1,0}}{\partial t} = -\frac{\partial \theta_{1,0}}{\partial z} - 2\mathcal{C}\theta_{1,0} \quad \text{at} \quad z = 1, \tag{4.78}$$

and the initial conditions (4.51) and (4.52) $\theta_{1,0}(0,0) = +\vartheta$ and $\theta_{1,0}(1,0) = -\vartheta$. Integrating (4.76) twice with respect to z, using (4.77) and (4.78) and the initial conditions on $\theta_{1,0}$, yields the solution for $\theta_{1,0}$, namely

$$\theta_{1,0} = \vartheta(1 - 2z)\,\mathrm{e}^{-2(1+\mathcal{C})t}. \tag{4.79}$$

At first order in $\bar{\mathrm{E}}\mathrm{r}$ the director angle equation (4.48) reduces to

$$\frac{\partial^2 \theta_{1,1}}{\partial z^2} = (2z - 1)(1 - \theta_{1,0}^2), \tag{4.80}$$

subject to the dissipative weak anchoring conditions (4.49) and (4.50)

$$\frac{\partial \theta_{1,1}}{\partial t} = +\frac{\partial \theta_{1,1}}{\partial z} - 2\mathcal{C}\theta_{1,1} \quad \text{at} \quad z = 0, \tag{4.81}$$

$$\frac{\partial \theta_{1,1}}{\partial t} = -\frac{\partial \theta_{1,1}}{\partial z} - 2\mathcal{C}\theta_{1,1} \quad \text{at} \quad z = 1, \tag{4.82}$$

and the initial conditions (4.51) and (4.52) $\theta_{1,1}(0,0) = 0$ and $\theta_{1,1}(1,0) = 0$. Integrating (4.80) twice with respect to z, using (4.79), (4.81) and (4.82) and the

initial conditions on $\theta_{1,1}$, yields the solution for $\theta_{1,1}$, namely

$$\theta_{1,1} = \frac{2z-1}{60}\left[5\left(2z^2-2z-\frac{1}{1+\mathcal{C}}\right)+\frac{5+3\vartheta^2}{1+\mathcal{C}}\,\mathrm{e}^{-2(1+\mathcal{C})t}\right.$$
$$\left.+\,3\vartheta^2\left(4z^4-8z^3+6z^2-2z+\frac{1}{1+\mathcal{C}}\right)\mathrm{e}^{-4(1+\mathcal{C})t}\right]. \qquad (4.83)$$

Using (4.79) and (4.83) the asymptotic solution for θ_1 is therefore

$$\theta_1 = \vartheta(1-2z)\mathrm{e}^{-2(1+\mathcal{C})t}$$
$$+\frac{2z-1}{60}\left[5\left(2z^2-2z-\frac{1}{1+\mathcal{C}}\right)+\frac{5+3\vartheta^2}{1+\mathcal{C}}\,\mathrm{e}^{-2(1+\mathcal{C})t}\right.$$
$$\left.+3\vartheta^2\left(4z^4-8z^3+6z^2-2z+\frac{1}{1+\mathcal{C}}\right)\mathrm{e}^{-4(1+\mathcal{C})t}\right]\bar{\mathrm{E}}\mathrm{r}$$
$$+\,O\left(\bar{\mathrm{E}}\mathrm{r}^2\right), \qquad (4.84)$$

and hence the asymptotic solution for the director angle on the substrates Θ is

$$\Theta = \vartheta\,\mathrm{e}^{-2(1+\mathcal{C})t}+\frac{1}{60(1+\mathcal{C})}\left[5-(5+3\vartheta^2)\,\mathrm{e}^{-2(1+\mathcal{C})t}-3\vartheta^2\,\mathrm{e}^{-4(1+\mathcal{C})t}\right]\bar{\mathrm{E}}\mathrm{r}$$
$$+\,O\left(\bar{\mathrm{E}}\mathrm{r}^2\right). \qquad (4.85)$$

In particular, from (4.84) the steady state solution $\theta_{1\mathrm{SS}}$ is given by

$$\theta_{1\mathrm{SS}} = \frac{2z-1}{12}\left[2z^2-2z-\frac{1}{1+\mathcal{C}}\right]\bar{\mathrm{E}}\mathrm{r}+O\left(\bar{\mathrm{E}}\mathrm{r}^2\right), \qquad (4.86)$$

and from either (4.85) or (4.86) the steady state value Θ_{SS} is given by

$$\Theta_{\mathrm{SS}} = \frac{\bar{\mathrm{E}}\mathrm{r}}{12(1+\mathcal{C})}+O\left(\bar{\mathrm{E}}\mathrm{r}^2\right). \qquad (4.87)$$

In particular, the solution for the director angle given by (4.84) and (4.85) is dominated by splay elastic effects with viscous effects appearing at $O\left(\bar{\mathrm{E}}\mathrm{r}\right) \ll 1$.

In addition, from (4.85) the timescale σ_{S} is given by

$$\sigma_{\mathrm{S}} = \frac{1}{2(1+\mathcal{C})}. \tag{4.88}$$

Note that even in the special case $\mathcal{C} = 0$ in which case there is no anchoring force in (4.49) and (4.50), there is still an elastic restoring force due to the $\partial\theta_1/\partial z$ term, and hence the director angle on the substrates still rotates such that $\Theta \to \Theta_{\mathrm{SS}} = \bar{\mathrm{E}}\mathrm{r}/12 + O\left(\bar{\mathrm{E}}\mathrm{r}^2\right)$ as $t \to \infty$.

4.5 Solutions for general values of the Ericksen number

In this section we obtain numerical solutions of the director angle equation (4.48) subject to (4.49)–(4.52) for general values of the Ericksen number and, in particular, compare them with the quasi-steady asymptotic solutions in the limits of large and small $\bar{\mathrm{E}}\mathrm{r}$ described in Sections 4.3 and 4.4, respectively. The numerical approach we adopt uses the programming and numerical computing platform MATLAB [142]. In particular, we the MATLAB boundary value problem solver *bvp4c* with an implicit Euler method for approximating the time derivatives in (4.49) and (4.50). In all of our numerical calculations the simulation time is chosen to be six times longer than the appropriate timescale given by (4.72), (4.75) or (4.88) in order to allow sufficient time for convergence to the steady state solution. In all of the numerical calculations reported here use the value $\vartheta = 0.5$ for the initial value of the director angle on the substrates.

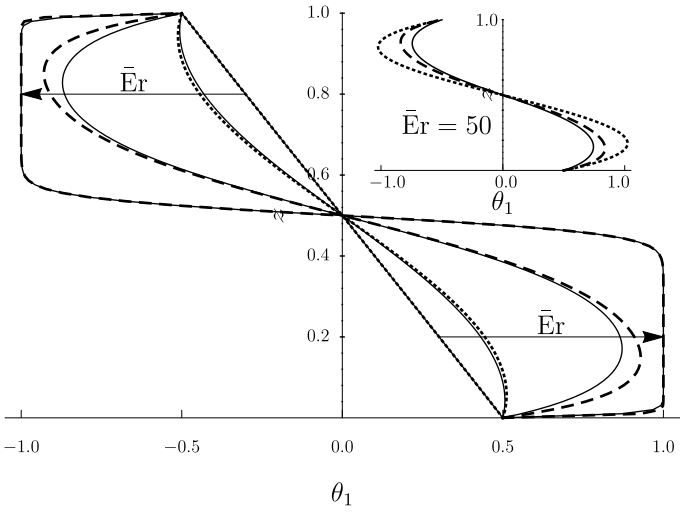

(a)

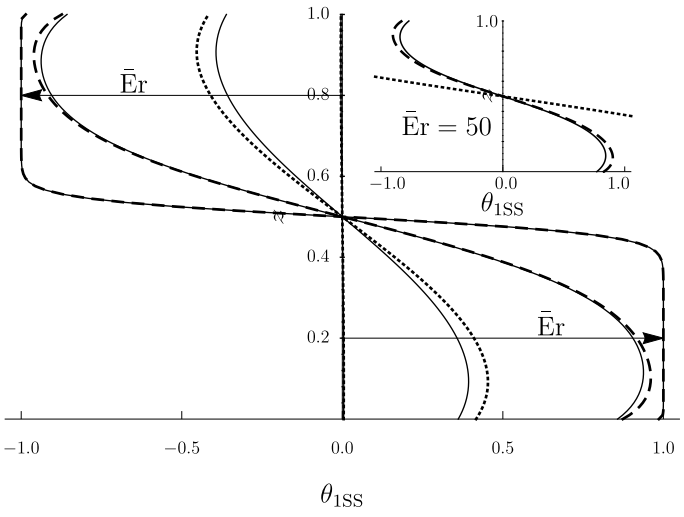

(b)

Figure 4.4: (a) The initial director angle $\theta_1(z,0)$ and (b) the steady state solution for the director angle $\theta_{1\mathrm{SS}}(z)$ plotted as functions of z for $\mathcal{C} = 1$ and $\vartheta = 0.5$ according to the numerical solution (solid lines) when $\bar{\mathrm{Er}} = 10^{-1}$, $\bar{\mathrm{Er}} = 10$, $\bar{\mathrm{Er}} = 10^2$ and $\bar{\mathrm{Er}} = 10^4$, the large $\bar{\mathrm{Er}}$ asymptotic solution (dashed lines) given by (4.60) when $\bar{\mathrm{Er}} = 10^2$ and $\bar{\mathrm{Er}} = 10^4$, and the small $\bar{\mathrm{Er}}$ asymptotic solution (dotted lines) given by (4.84) when $\bar{\mathrm{Er}} = 10^{-1}$ and $\bar{\mathrm{Er}} = 10$. In both (a) and (b) the insets show the corresponding results when $\bar{\mathrm{Er}} = 50$. The arrows show the direction of increasing $\bar{\mathrm{Er}}$.

4.5.1 The director angle

Figure 4.4(a) shows the initial director angle $\theta_1(z,0)$ and Figure 4.4(b) shows the steady state solution for the director angle $\theta_{1\mathrm{SS}}(z)$, both plotted as functions of z according to the numerical solution (solid lines) when $\bar{\mathrm{E}}\mathrm{r} = 10^{-1}$, $\bar{\mathrm{E}}\mathrm{r} = 10$, $\bar{\mathrm{E}}\mathrm{r} = 10^2$ and $\bar{\mathrm{E}}\mathrm{r} = 10^4$, the large $\bar{\mathrm{E}}\mathrm{r}$ asymptotic solution (dashed lines) given by (4.60) when $\bar{\mathrm{E}}\mathrm{r} = 10^2$ and $\bar{\mathrm{E}}\mathrm{r} = 10^4$, and the small $\bar{\mathrm{E}}\mathrm{r}$ asymptotic solution (dotted lines) given by (4.84) when $\bar{\mathrm{E}}\mathrm{r} = 10^{-1}$ and $\bar{\mathrm{E}}\mathrm{r} = 10$. The insets in Figure 4.4 show the corresponding results for an intermediate value of $\bar{\mathrm{E}}\mathrm{r}$, namely $\bar{\mathrm{E}}\mathrm{r} = 50$. In particular, Figure 4.4 shows how the leading-order velocity in the channel u_0 given by (4.47) affects both the initial director angle and the steady state director angle. Specifically, as described in Section 4.1.3, in the lower half of the channel the positive shear rate ($\partial u_0/\partial z > 0$) rotates the director angle towards the positive Leslie angle $\theta_1 = +1$, while in the upper half of the channel the negative shear rate ($\partial u_0/\partial z < 0$) rotates it towards the negative Leslie angle $\theta_1 = -1$. When $\bar{\mathrm{E}}\mathrm{r}$ is large (e.g. when $\bar{\mathrm{E}}\mathrm{r} = 10^4$), the behaviour of the director is dominated by viscous effects, with flow alignment at either the positive or the negative Leslie angle except for within the narrow reorientational boundary and internal layers at leading order in the limit of large $\bar{\mathrm{E}}\mathrm{r}$, as described in Section 4.3. When $\bar{\mathrm{E}}\mathrm{r}$ is small (e.g. when $\bar{\mathrm{E}}\mathrm{r} = 10^{-1}$), the behaviour of the director is dominated by splay elastic effects, with viscous effects appearing at first order in the limit of small $\bar{\mathrm{E}}\mathrm{r}$, as described in Section 4.4. Figure 4.4 also shows that as $\bar{\mathrm{E}}\mathrm{r}$ varies there is a continuous transition between the asymptotic behaviour for large $\bar{\mathrm{E}}\mathrm{r}$ and that for small $\bar{\mathrm{E}}\mathrm{r}$ and that, in fact, the two asymptotic solutions capture the behaviour of θ_1 rather well for all values of $\bar{\mathrm{E}}\mathrm{r}$. This continuous transition is rather different to the discontinuous transitions observed in channel flow of a nematic with homeotropic anchoring by Sengupta et al. [194], Anderson et al. [5], Crespo et al. [37], and Batista et al. [11].

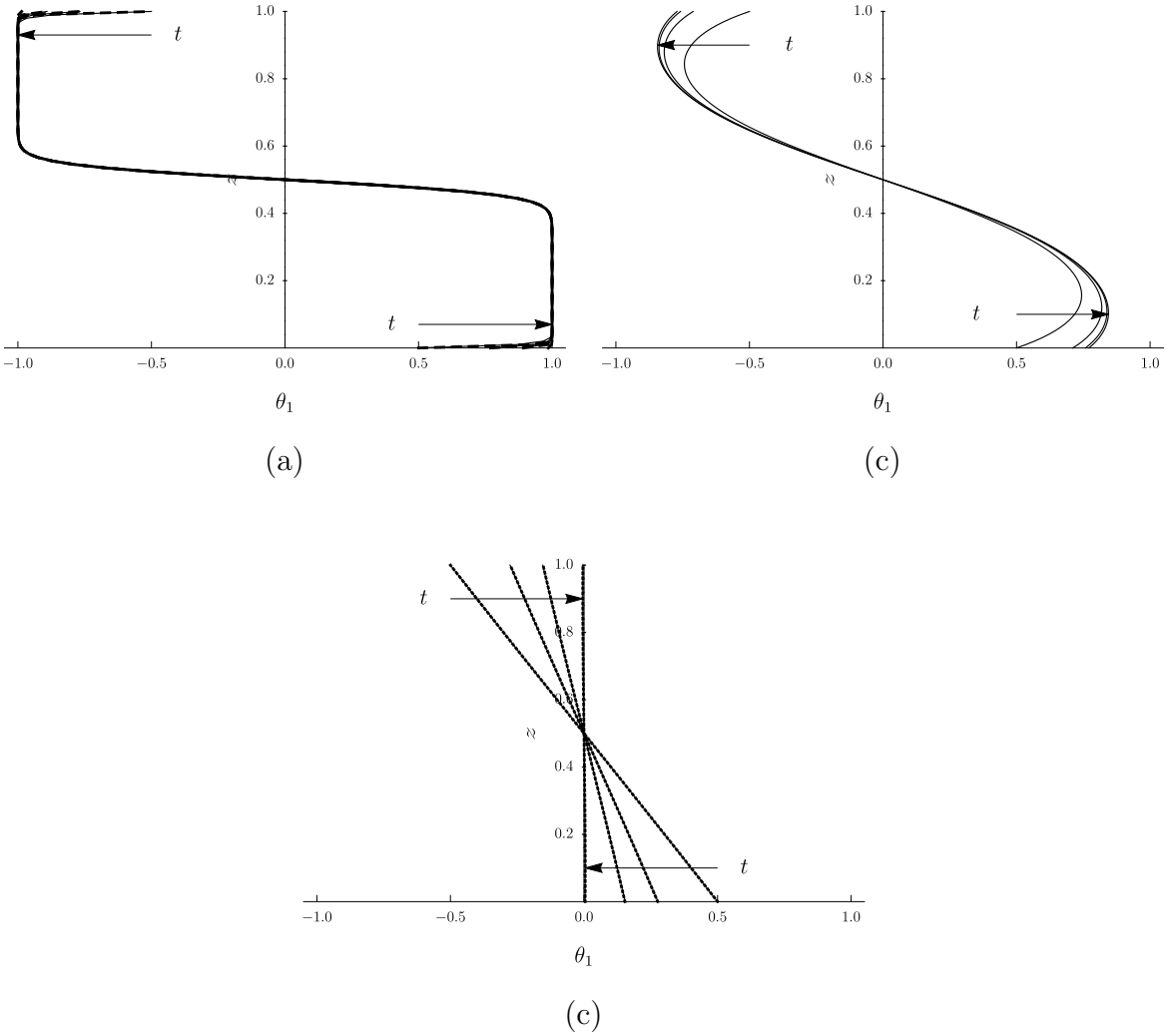

Figure 4.5: The director angle $\theta_1(z,t)$ plotted as a function of z for $\mathcal{C} = 1$ and $\vartheta = 0.5$ according to (a) the numerical solution (solid lines) and the (barely visible) large $\bar{\mathrm{E}}\mathrm{r}$ asymptotic solution (dashed lines) given by (4.60) when $\bar{\mathrm{E}}\mathrm{r} = 10^4$ for $t = 0.0$, $t = 0.006$, $t = 0.012$, and $t = 0.06$, (b) the numerical solution (solid lines) when $\mathrm{Er} = 50$ for $t = 0.0$, $t = 0.15$, $t = 0.3$ and $t = 3.0$, and (c) the numerical solution (solid lines) and the (barely visible) small $\bar{\mathrm{E}}\mathrm{r}$ asymptotic solution (dotted lines) given by (4.84) when $\bar{\mathrm{E}}\mathrm{r} = 10^{-1}$ for $t = 0.0$, $t = 0.15$, $t = 0.3$ and $t = 3.0$. The arrows show the direction of increasing t.

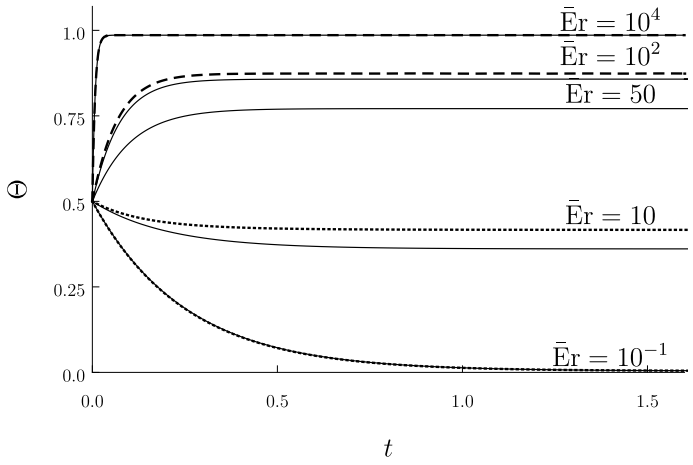

Figure 4.6: The director angle on the substrates Θ plotted as a function of time t for $\mathcal{C} = 1$ and $\vartheta = 0.5$ according to the numerical solution (solid lines) when $\bar{\mathrm{Er}} = 10^{-1}$, $\bar{\mathrm{Er}} = 10$, $\bar{\mathrm{Er}} = 50$, $\bar{\mathrm{Er}} = 10^2$ and $\bar{\mathrm{Er}} = 10^4$, the large $\bar{\mathrm{Er}}$ asymptotic solution (dashed lines) given by (4.62) when $\bar{\mathrm{Er}} = 10^2$ and $\bar{\mathrm{Er}} = 10^4$, and the small $\bar{\mathrm{Er}}$ asymptotic solution (dotted lines) given by (4.85) when $\bar{\mathrm{Er}} = 10^{-1}$, $\bar{\mathrm{Er}} = 10$.

Figure 4.5 shows the director angle $\theta_1(z,t)$ plotted as a function of z for various times t according to (a) the numerical solution (solid lines) and the large $\bar{\mathrm{Er}}$ asymptotic solution (dashed lines) when $\bar{\mathrm{Er}} = 10^4$, (b) the numerical solution (solid lines) when $\mathrm{Er} = 50$, and (c) the numerical solution (solid lines) and the small $\bar{\mathrm{Er}}$ asymptotic solution (dotted lines) when $\bar{\mathrm{Er}} = 10^{-1}$. In each part of Figure 4.5 the final time plotted is chosen so that the solution is close to its steady state solution $\theta_{1\mathrm{SS}}$ shown in Figure 4.4(b). In particular, Figure 4.5 illustrates that θ_1 always approaches its steady state solution $\theta_{1\mathrm{SS}}$ monotonically as $t \to \infty$.

Figure 4.6 shows the director angle on the substrates Θ plotted as a function of time t according to the numerical solution (solid lines) when $\bar{\mathrm{Er}} = 10^{-1}$, $\bar{\mathrm{Er}} = 10$, $\bar{\mathrm{Er}} = 50$, $\bar{\mathrm{Er}} = 10^2$ and $\bar{\mathrm{Er}} = 10^4$, the large $\bar{\mathrm{Er}}$ asymptotic solution (dashed lines) when $\bar{\mathrm{Er}} = 10^2$ and $\bar{\mathrm{Er}} = 10^4$, and the small $\bar{\mathrm{Er}}$ asymptotic solution (dotted lines) when $\bar{\mathrm{Er}} = 10^{-1}$, $\bar{\mathrm{Er}} = 10$. In particular, Figure 4.6 illustrates that Θ always approaches its steady state value Θ_{SS} monotonically from above when $\Theta_{\mathrm{SS}} < \vartheta$ and from below when $\Theta_{\mathrm{SS}} > \vartheta$ as $t \to \infty$, and that Θ_{SS} is a monotonically

increasing function of $\bar{\mathrm{E}}\mathrm{r}$.

Figures 4.5 and 4.6 also illustrate that the approach to the steady state solution gets monotonically faster as $\bar{\mathrm{E}}\mathrm{r}$ is increased. This behaviour will be analysed in more detail in Section 4.5.2.

Figure 4.7 shows the steady state value the director angle on the substrates Θ_{SS} plotted as a function of the Ericksen number $\bar{\mathrm{E}}\mathrm{r}$ according to the numerical solution (solid lines), the large $\bar{\mathrm{E}}\mathrm{r}$ asymptotic solution given by (4.61) (dashed lines), and the small $\bar{\mathrm{E}}\mathrm{r}$ asymptotic solution (dotted lines) given by (4.87) for various values of $\mathcal{C}$. In particular, Figure 4.7 illustrates that Θ_{SS} is a monotonically decreasing function of $\mathcal{C}$. Figure 4.7 also confirms that the numerical solutions for Θ_{SS} for large and small values of $\bar{\mathrm{E}}\mathrm{r}$ are in excellent agreement with the asymptotic solutions in the limits $\bar{\mathrm{E}}\mathrm{r} \to \infty$ and $\bar{\mathrm{E}}\mathrm{r} \to 0$ given in Sections 4.3 and 4.4, respectively. Moreover, as we have already seen, in the former limit the leading-order expression for the value of Θ_{SS} depends on $\bar{\mathrm{E}}\mathrm{r}$ and $\mathcal{C}$ only in the combination $k = \mathcal{C}/\bar{\mathrm{E}}\mathrm{r}^{1/2}$, and hence the curves for Θ_{SS} for large values of $\bar{\mathrm{E}}\mathrm{r}$ are simply appropriately horizontally stretched versions of each other, and as Figure 4.7 illustrates, the range of validity of this expression widens as $\mathcal{C}$ increases.

4.5.2 The timescale of substrate director rotation

In order to extract the timescale σ_{S} introduced in Section 4.3.5.1 from the numerical solutions we fitted the numerical solutions for Θ_{SS} with a function of t of the form

$$\log|\Theta_{\mathrm{SS}} - \Theta| = C - \frac{t}{\sigma_{\mathrm{S}}}, \tag{4.89}$$

where $C = C(\vartheta)$ is a function of the initial director angle on the substrates only. In particular, this procedure recovers the asymptotic expressions for σ_{S} derived in Sections 4.3.5 and 4.4, namely (4.72), (4.75) and (4.88).

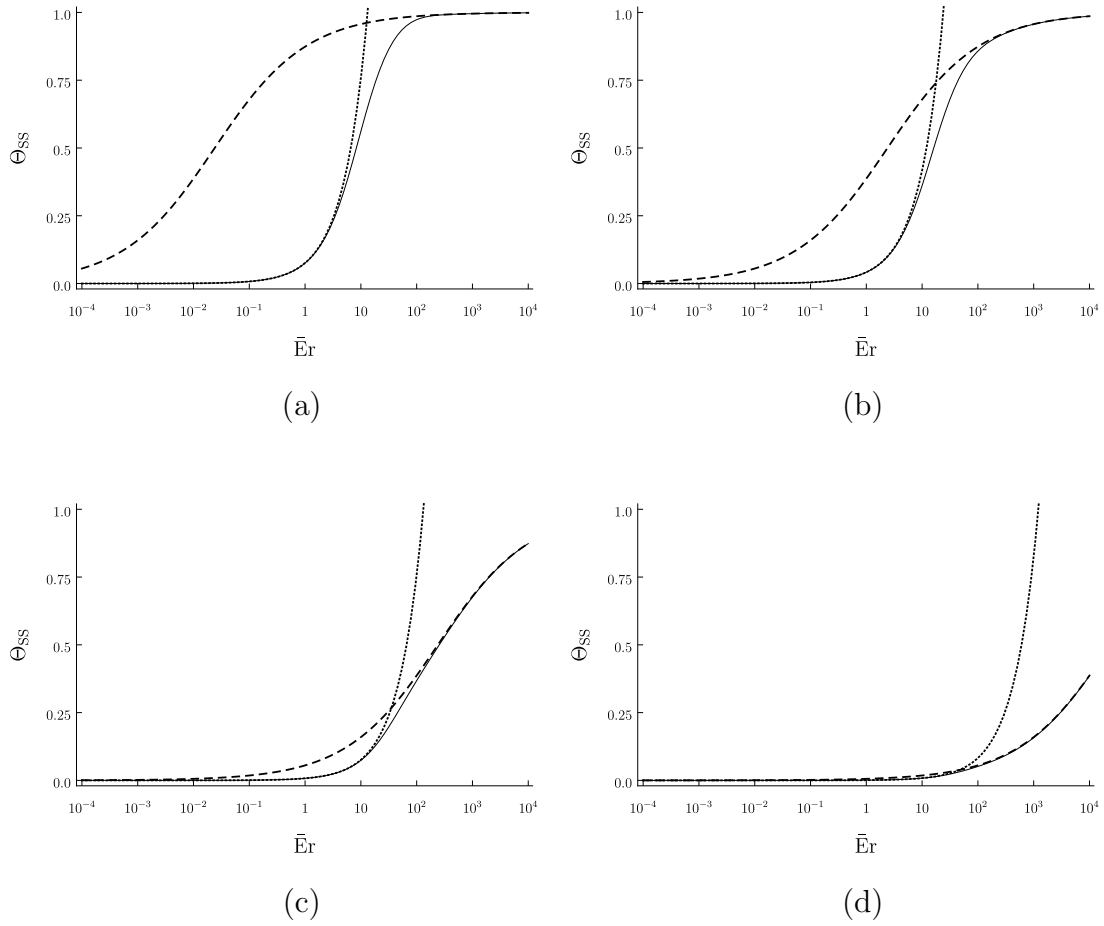

Figure 4.7: The steady state value of the director angle on the substrates Θ_{SS} plotted as a function of the Ericksen number $\bar{\mathrm{E}}\mathrm{r}$ according to the numerical solution (solid lines), the large $\bar{\mathrm{E}}\mathrm{r}$ asymptotic solution (dashed lines) given by (4.61), and the small $\bar{\mathrm{E}}\mathrm{r}$ asymptotic solution (dotted lines) given by (4.87) for (a) $\mathcal{C} = 10^{-1}$, (b) $\mathcal{C} = 1$, (c) $\mathcal{C} = 10$, and (d) $\mathcal{C} = 10^{2}$.

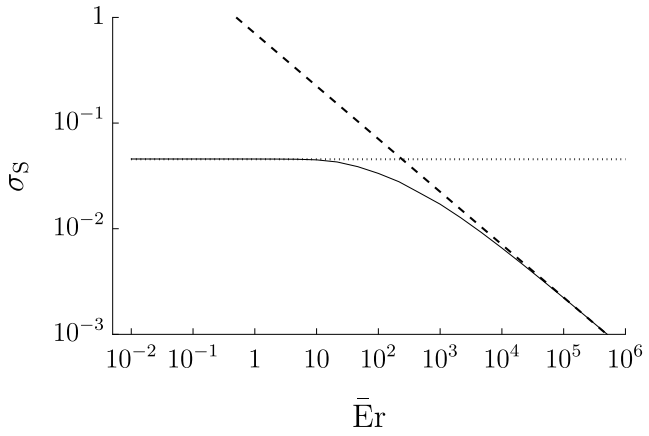

Figure 4.8: The timescale σ_S plotted as a function of the Ericksen number $\bar{\mathrm{E}}\mathrm{r}$ extracted from the numerical solution using (4.89) (solid line) and according to the large $\bar{\mathrm{E}}\mathrm{r}$ asymptotic solution when $k \ll 1$ (dashed line) given by (4.75) and the small $\bar{\mathrm{E}}\mathrm{r}$ asymptotic solution (dotted line) given by (4.88) for $\mathcal{C} = 10$ and $\vartheta = 0.5$.

Figure 4.8 shows σ_S plotted as a function of $\bar{\mathrm{E}}\mathrm{r}$ extracted from the numerical solution using (4.89) and according to the large $\bar{\mathrm{E}}\mathrm{r}$ asymptotic solution when $k \ll 1$ given by (4.75) and the small $\bar{\mathrm{E}}\mathrm{r}$ asymptotic solution given by (4.88). (Note that, for clarity, the timescale according to the large $\bar{\mathrm{E}}\mathrm{r}$ asymptotic solution when $k \gg 1$, namely $\sigma_S = 1/(2\mathcal{C})$, is omitted from Figure 4.8 as it is virtually indistinguishable from $\sigma_S = 1/(2(1+\mathcal{C}))$.) In particular, Figure 4.8 shows that σ_S is a monotonically decreasing function of $\bar{\mathrm{E}}\mathrm{r}$, and that as $\bar{\mathrm{E}}\mathrm{r}$ varies there is a continuous transition between $\sigma_S = 1/(\sqrt{2}\bar{\mathrm{E}}\mathrm{r}^{1/2}) = O\left(\bar{\mathrm{E}}\mathrm{r}^{-1/2}\right) \ll 1$ for large values of $\bar{\mathrm{E}}\mathrm{r}$ and $\sigma_S = 1/(2(1+\mathcal{C})) = O(1)$ for small values of $\bar{\mathrm{E}}\mathrm{r}$. Moreover, Figure 4.8 also shows, as mentioned in Section 4.3.5.3, that σ_S is always less than both (4.72) and (4.75), and so (4.72) and (4.75) provide a upper bound on σ_S for all values of $\bar{\mathrm{E}}\mathrm{r}$.

4.6 Conclusions

Motivated by the need for understanding the flow-driven distortion of nematic molecules on the substrates in the ODF method, we analysed pressure-driven flow of a nematic in a channel with dissipative weak planar anchoring on the substrates of the channel. We obtained quasi-steady asymptotic solutions for the director angle θ and the velocity u in the limit of small Leslie angle, in which case the key parameters are the Ericksen number $\bar{\mathrm{E}}\mathrm{r}$ and the anchoring strength parameter $\mathcal{C}$. In the limit of large Ericksen number $\bar{\mathrm{E}}\mathrm{r} \to \infty$ the solution for the director angle has narrow reorientational boundary layers of width $O\left(\bar{\mathrm{E}}\mathrm{r}^{-1/2}\right) \ll 1$ near $z = 0$ and $z = 1$ and a narrow reorientational internal layer of width $O\left(\bar{\mathrm{E}}\mathrm{r}^{-1/3}\right) \ll 1$ near $z = 1/2$ separated by two outer regions in which the director is aligned at the positive Leslie angle in the lower half of the channel and the negative Leslie angle in the upper half of the channel. On the other hand, in the limit of small Ericksen number $\bar{\mathrm{E}}\mathrm{r} \to 0$ the solution for the director angle given by (4.84) and (4.85) is dominated by splay elastic effects with viscous effects appearing at $O\left(\bar{\mathrm{E}}\mathrm{r}\right) \ll 1$. As $\bar{\mathrm{E}}\mathrm{r}$ varies there is a continuous transition between these asymptotic behaviours and, in fact, the two asymptotic solutions capture the behaviour rather well for all values of $\bar{\mathrm{E}}\mathrm{r}$. The steady state value of the director angle on the substrates Θ_{SS} and the timescale of the evolution towards this steady state value σ_{S} in the asymptotic limits of large and small $\bar{\mathrm{E}}\mathrm{r}$ are summarised in Table 4.2. In particular, the values of σ_{S} in Table 4.2 correspond to the dimensional substrate director rotation timescale $\sigma_{\mathrm{S}}\tau_4$ given by

$$\sigma_{\mathrm{S}}\tau_4 \sim \gamma_{\mathrm{S}} \times \begin{cases} \dfrac{1}{2C} & \text{for} \quad \bar{\mathrm{E}}\mathrm{r} \gg 1 \quad \text{and} \quad k \gg 1, \\ \sqrt{\dfrac{-(\alpha_4+\alpha_6)}{2(\alpha_2\alpha_3)^{1/2}G\mathcal{H}K_1}} & \text{for} \quad \bar{\mathrm{E}}\mathrm{r} \gg 1 \quad \text{and} \quad k \ll 1, \\ \dfrac{\mathcal{H}}{2(K_1 + C\mathcal{H})} & \text{for} \quad \bar{\mathrm{E}}\mathrm{r} \ll 1. \end{cases} \tag{4.90}$$

	$\bar{\mathrm{Er}} \to \infty$			$\bar{\mathrm{Er}} \to 0$
	$k \gg 1$	$k = O(1)$	$k \ll 1$	
Θ_{SS}	0	Equation (4.61)	1	$\dfrac{\bar{\mathrm{Er}}}{12(\mathcal{C}+1)} \ll 1$
σ_{S}	$\dfrac{1}{2\mathcal{C}} \ll 1$	$(\star)$	$\dfrac{1}{\sqrt{2}\bar{\mathrm{Er}}^{1/2}} \ll 1$	$\dfrac{1}{2(\mathcal{C}+1)}$

Table 4.2: The steady state value for the director angle on the substrates Θ_{SS} and the timescale σ_{S} in the asymptotic limit of large $\bar{\mathrm{Er}}$ in the cases $k \gg 1$, $k = O(1)$ and $k \ll 1$, where $k = \mathcal{C}/\bar{\mathrm{Er}}^{1/2}$, and in the asymptotic limit of small $\bar{\mathrm{Er}}$. The star $(\star)$ denotes that, while there is no explicit expression for σ_{S} in this case, the expressions for $k \gg 1$ and $k \ll 1$ provide a upper bound on σ_{S} for all values of k.

Using the estimated parameter values for the ODF method given Section 4.1.4 gives $\bar{\mathrm{Er}} = 1.7 \times 10^2$, $\mathcal{C} = 1$–10^2 and hence $k = 0.08$–8, suggesting that the regimes in which $\bar{\mathrm{Er}} \gg 1$ and $k \ll 1$ or $k = O(1)$ are probably the most relevant to the ODF method. Hence (4.90) yields a dimensional substrate director rotation timescale of $\sigma_{\mathrm{S}}\tau_4 \simeq 5 \times 10^{-3}$ s or less, which is substantially shorter than the dimensional timescale of the ODF method of $\tau_{\mathrm{ODF}} = 10^{-1}$ s, suggesting that there is sufficient time for significant transient flow-driven distortion of the nematic molecules on the substrates from their required orientation to occur, which could lead to the formation of ODF mura. An obvious conclusion is that this distortion could, in theory, be reduced by decreasing $\bar{\mathrm{Er}}$ and/or increasing $\mathcal{C}$ by, for example, reducing the speed at which the substrates are squeezed together and/or increasing the anchoring strength between the alignment layer and the nematic, however the extent to which either of these are realistic options in practice is not clear. It should, however, be noted that once the squeezing stops, and hence the flow of the nematic virtually ceases (so that $\bar{\mathrm{Er}}$ becomes very small), then (4.90) yields a dimensional substrate director rotation timescale of approximately $\sigma_{\mathrm{S}}\tau_4 \simeq 2.5 \times 10^{-2}$ s or less, which means that the flow-driven distortion of the

nematic molecules relaxes almost immediately. The remaining issue is, therefore, whether the significant transient flow-driven distortion of the nematic molecules described in the present work causes permanent or semi-permanent flow-driven misalignment of the orientation of the molecules in the alignment layers. Answering this question could lead to further understanding of ODF mura but requires more detailed modelling of the molecules in the alignment layer.

Finally, as mentioned in Section 4.1.1, the present analysis of dissipative weak planar anchoring is not directly relevant to displays with homeotropic anchoring, such as VAN displays, or to displays in which the director does not remain in the (x, z)-plane, such as TN or STN displays. However, in such displays flow alignment towards the (typically small) Leslie angle involves a much larger rotation of the director than that described in the present work, and so we suspect that such displays are even more susceptible to flow-driven misalignment of the director on the substrates during filling than those studied in this chapter.

Chapter 5

The governing equations for a static ridge of nematic

Motivated by a need for increased understanding of situations involving nematic droplets and films, such as the initial stage of the ODF method (shown in Figure 1.8)(d) and (e)), we now consider a two-dimensional static ridge of nematic resting on an ideal (i.e. flat, rigid, perfectly smooth, and chemically homogeneous) solid substrate surrounded by passive fluid. In addition to understanding the initial stages of the ODF method, there are many many emerging technologies that were discussed in Chapter 1 which involve nematic free surfaces and three-phase contact lines that may benefit from an increased understanding of this situation. For the subsequent theory and results to make comparisons with the most common experimental situation, we refer to the fluid surrounding the nematic to be an atmosphere of passive gas. However, the results detailed apply also to a ridge of nematic surrounded by a static isotropic liquid.

The theoretical description of a volume of nematic bounded by a gas–nematic and nematic–substrate interface has previously been considered by Jenkins and Barratt [102], who obtained general forms of the interfacial conditions and the

force per length on a contact line, and Rey [181, 182], who obtained the general forms of the nematic Young–Laplace equation and the nematic Young equations. In this chapter, we combine aspects of these two approaches to provide the first complete theoretical description for a static ridge of nematic, which includes the interfacial conditions, the bulk elastic equation, the nematic Young equations, and the relevant boundary conditions. We also provide full details of a straightforward and, therefore, readily accessible derivation of the governing equations, which in future work may be readily adapted to include electromagnetic forces, additional contact line effects, non-ideal substrates, or more detailed models for the nematic molecular order, such as Q-tensor theory [152].

We proceed by constructing the free energy of the system as a function of both the shape of the gas–nematic interface (i.e. the nematic free surface) and the director field, and then by minimising the free energy using the calculus of variations, we will derive the governing equations, including both nematic Young and nematic Young–Laplace equations. In order to determine the free energy of the system, we will use the well-established Oseen–Frank bulk elastic energy density W (which was discussed at length in Section 1.7.1), the gravitational potential energy, and the Rapini–Papoular [172] interface energy density ω (which was discussed at length in Section 1.7.3).

5.1 Model formulation

As described in the previous section, we consider a static ridge of nematic (N), resting on an ideal solid substrate (S), in an atmosphere of passive gas (G), as shown in Figure 5.1, which also indicates the Cartesian coordinates x, y and z that we use. The nematic ridge is bounded by the gas–nematic interface at $z = h(x)$ and the nematic–substrate interface at $z = 0$, and has two nematic–

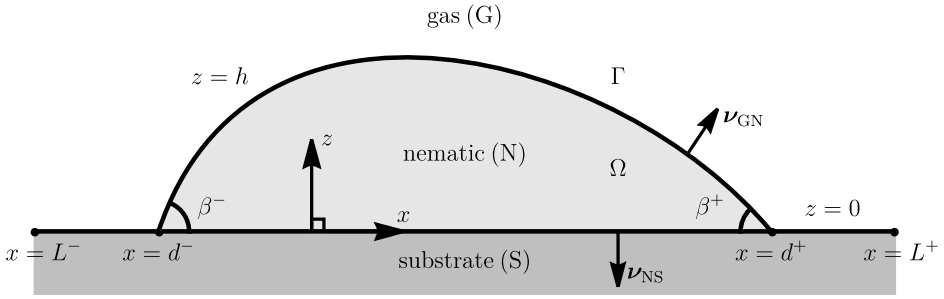

Figure 5.1: A schematic of a static ridge of nematic (N), resting on an ideal solid substrate (S) at $z = 0$, $L^- \leq x \leq L^+$, in an atmosphere of passive gas (G), with gas–nematic interface at $z = h$ and contact lines at $x = d^{\pm}$. The Cartesian coordinates x, y and z (where the y-direction is into the page), the boundary of the nematic ridge Γ, the outward unit normals $\boldsymbol{\nu}$, the contact angles $\beta^{\pm}$, and the region of nematic in the (x, z)-plane Ω are also indicated.

substrate–gas three-phase contact lines at $x = d^-$ and $x = d^+$. We assume that the ridge height h and the position of the contact lines do not vary in the y-direction, so that the contact lines form two infinitely-long parallel lines in the y-direction and the ridge height h is subject to two Dirichlet boundary conditions given by $h(d^-) = 0 = h(d^+)$. We also assume that the director $\boldsymbol{n}$ is confined to the (x, z)-plane, and hence takes the form

$$\boldsymbol{n} = (\cos\theta, 0, \sin\theta), \tag{5.1}$$

and $\theta = \theta(x, z)$ is the director angle, which does not vary in the y-direction.

The boundary of the nematic ridge, denoted by Γ, consists of the gas–nematic interface, denoted by Γ_{GN}, and the nematic–substrate interface, denoted by Γ_{NS}. The corresponding outward unit normals of Γ_{NS} and Γ_{GN}, which we denote by $\boldsymbol{\nu}_{\mathrm{NS}}$ and $\boldsymbol{\nu}_{\mathrm{GN}}$, are given by

$$\boldsymbol{\nu}_{\mathrm{GN}} = -\frac{h_x}{\sqrt{1 + h_x^2}}\hat{\boldsymbol{x}} + \frac{1}{\sqrt{1 + h_x^2}}\hat{\boldsymbol{z}}, \tag{5.2}$$

$$\boldsymbol{\nu}_{\mathrm{NS}} = -\hat{\boldsymbol{z}}, \tag{5.3}$$

respectively. These two interfaces meet the gas–substrate interface, denoted by Γ_{GS}, at the two contact lines $x = d^{\pm}$. The left-hand and right-hand edges of the substrate are denoted by $x = L^{-}$ and $x = L^{+}$, respectively, as shown in Figure 5.1. The contact angles formed between Γ_{GN} and Γ_{NS} at $x = d^{\pm}$ are denoted by β^{-} and β^{+}, respectively, and satisfy

$$\tan \beta^{\pm} = \mp h_x \quad \text{at} \quad x = d^{\pm}, \tag{5.4}$$

where the subscript x denotes differentiation with respect to x. We note that there is no requirement for h to be symmetric about its midpoint and, in particular, no requirement for the contact angles to be the same.

In general, we do not fix either the contact line positions or the contact angles, and allow $d^{\pm}$, and $\beta^{\pm}$ to be unknowns. However, if the substrate has been treated in such a way as to pin the contact lines or fix the contact angles, then $d^{\pm}$ or $\beta^{\pm}$, respectively, are prescribed and the nematic Young equations, which will be derived shortly, are not relevant. The ridge has a prescribed constant cross-sectional area A in the (x, z)-plane, so that

$$\iint \mathrm{d}\Omega = A, \tag{5.5}$$

where Ω is the region of nematic in the (x, z)-plane bounded by Γ, as shown in Figure 5.1.

We also include the effects of gravity. We assume the gravity acts in the (x, z)-plane but, in order to keep the setup as general as possible, do not specify its direction.

In Section 5.2 we derive the governing equations for a nematic ridge using the calculus of variations assuming that the ridge height h is a single-valued function of x. A necessary, but not sufficient, condition for the ridge height to

be single-valued is that the contact angles are acute (i.e. $0 \leq \beta^{\pm} \leq \pi/2$). We have performed the corresponding derivation when the ridge height h is a double-valued function of x, the details of which are provided in Appendix A.

5.2 Constrained minimisation of the free energy

Using the calculus of variations we minimise the free energy of the system E subject to the area constraint (5.5) and the two boundary conditions $h(d^{\pm}) = 0$, and in doing so derive the governing equations for the dependent variables θ, h, $d^{\pm}$, $\beta^{\pm}$ and a Lagrange multiplier associated with the area constraint (5.5), which we denote by p_0. The free energy of the system E is the sum of the bulk elastic energy of the nematic, denoted by E_{bulk}, and the interface energies, denoted by E_{GN}, E_{NS} and E_{GS}, for the interfaces Γ_{GN}, Γ_{NS} and Γ_{GS}, respectively, where

$$E_{\text{bulk}} = \int_{d^-}^{d^+} \int_0^h \Big(W(\theta, \theta_x, \theta_z) + \psi_{\text{g}} \Big) \, \mathrm{d}z \, \mathrm{d}x, \tag{5.6}$$

$$E_{\text{GN}} = \int_{d^-}^{d^+} \sqrt{1 + h_x^2} \left[\omega_{\text{GN}}(\theta, h_x) \right]^{z=h} \mathrm{d}x, \tag{5.7}$$

$$E_{\text{NS}} = \int_{d^-}^{d^+} \left[\omega_{\text{NS}}(\theta) \right]^{z=0} \mathrm{d}x, \tag{5.8}$$

$$E_{\text{GS}} = \int_{L^-}^{d^-} \left[\omega_{\text{GS}} \right]^{z=0} \mathrm{d}x + \int_{d^+}^{L^+} \left[\omega_{\text{GS}} \right]^{z=0} \mathrm{d}x. \tag{5.9}$$

In (5.6) the bulk elastic energy density $W(\theta, \theta_x, \theta_z)$ is assumed to be of the form of the Oseen–Frank bulk elastic energy density [201], which depends on the director angle θ and on elastic distortions of the director via its derivatives with respect to x and z [201]. Also in (5.6), the gravitational potential energy density $\psi_{\text{g}}(x, z)$ is allowed to depend on one or both of the Cartesian coordinates x and z. In (5.7) and (5.8) the interface energy densities $\omega_{\text{GN}}(\theta, h_x)$ and $\omega_{\text{NS}}(\theta)$ are assumed to be of the form of the Rapini–Papoular energy density [172], which depends on the

difference between the director and the orientation of the interfaces via the director angle θ and the slopes of those interfaces, namely h_x and zero, respectively. In (5.9) the interface energy density ω_{GS} takes a constant value.

We define the functional $F = F(\theta, \theta_x, \theta_z, h, h_x, d^-, d^+) = E + \mathcal{C}_{\mathrm{area}}$ as the sum of the free energy (per unit length in the y-direction) of the system E and an appropriate area constraint term $\mathcal{C}_{\mathrm{area}}$ corresponding to the area constraint, given by

$$\mathcal{C}_{\mathrm{area}} = p_0 \times \left(A - \int_{d^-}^{d^+} \int_0^h \mathrm{d}z \, \mathrm{d}x \right), \tag{5.10}$$

so that the functional F is given by

$$F = E_{\mathrm{bulk}} + E_{\mathrm{GN}} + E_{\mathrm{NS}} + E_{\mathrm{GS}} + \mathcal{C}_{\mathrm{area}}. \tag{5.11}$$

We now consider the variation of the functional F, given by (5.11) with (5.6)–(5.10), with respect to small variations of the variables θ, h, d^- and d^+ of the form

$$\theta \to \theta + \delta_\theta, \quad h \to h + \delta_h, \quad d^+ \to d^+ + \delta_{d^+}, \quad d^- \to d^- + \delta_{d^-}. \tag{5.12}$$

There are no constraints on the director angle θ and therefore there are no constraints on the variation of the director angle δ_θ. There is, however, a constraint on the ridge height h because of the two boundary conditions $h(d^\pm) = 0$ so that the variation of the ridge height δ_h at the contact lines satisfies

$$\delta_h = -h_x \delta_{d^-} = -\tan\beta^- \, \delta_{d^-} \quad \text{at} \quad x = d^-, \tag{5.13}$$

$$\delta_h = -h_x \delta_{d^+} = \tan\beta^+ \, \delta_{d^+} \quad \text{at} \quad x = d^+. \tag{5.14}$$

The variation of the functional F, denoted by δF, is given by

$$\delta F = F(\theta+\delta_\theta,(\theta+\delta_\theta)_x,(\theta+\delta_\theta)_z,h+\delta_h,(h+\delta_h)_x,d^-+\delta_{d^-},d^++\delta_{d^+}) - F(\theta,\theta_x,\theta_z,h,h_x,d^-,d^+). \tag{5.15}$$

We now proceed by considering the variation of each term in (5.11) in turn, and neglect terms in (5.15) that are $O(\delta_\theta^2)$, $O(\delta_h^2)$, $O(\delta_{d^-}^2)$ and $O(\delta_{d^+}^2)$.

For the bulk elastic energy $E_{\rm bulk}$, given by (5.6), using the variations (5.12) shows that $\delta E_{\rm bulk}$ is given by

$$\delta E_{\rm bulk} = \int_{d^-}^{d^+}\int_0^h \delta_\theta\frac{\partial W}{\partial\theta}+\delta_{\theta x}\frac{\partial W}{\partial\theta_x}+\delta_{\theta z}\frac{\partial W}{\partial\theta_z}\,\mathrm{d}z\,\mathrm{d}x+\int_{d^-}^{d^+}\delta_h\left[W+\psi_{\rm g}\right]^{z=h}\,\mathrm{d}x + \delta_{d^+}\left[\int_0^h (W+\psi_{\rm g})\,\mathrm{d}z\right]^{x=d^+} - \delta_{d^-}\left[\int_0^h (W+\psi_{\rm g})\,\mathrm{d}z\right]^{x=d^-}. \tag{5.16}$$

Since $h(d^\pm)=0$, the last two terms in (5.16) are identically zero. The terms in (5.16) containing derivatives of δ_θ, namely $\delta_{\theta x}$ and $\delta_{\theta z}$, are transformed into terms involving δ_θ by using the divergence theorem, namely

$$\int\int \delta_{\theta\alpha}\frac{\partial W}{\partial\theta_\alpha}\,\mathrm{d}\Omega = \oint_\Gamma \delta_\theta\frac{\partial W}{\partial\theta_\alpha}\hat{\boldsymbol{\alpha}}\cdot\boldsymbol{\nu}\,\mathrm{d}\Gamma - \int\int \delta_\theta\frac{\partial}{\partial\alpha}\left(\frac{\partial W}{\partial\theta_\alpha}\right)\,\mathrm{d}\Omega, \tag{5.17}$$

where $\alpha = x$ or $\alpha = z$. The line integral along Γ in (5.17) is composed of a component along $\Gamma_{\rm NS}$ at $z=0$ from $x=d^-$ to $x=d^+$ with $\mathrm{d}\Gamma=\mathrm{d}x$ and outward unit normal (5.2), and a component along $\Gamma_{\rm GN}$ from $x=d^+$ to $x=d^-$ on $z=h$ with $\mathrm{d}\Gamma=-\sqrt{1+h_x^2}\,\mathrm{d}x$ and outward unit normal (5.3), and is given explicitly

by

$$\oint_\Gamma \delta_\theta \frac{\partial W}{\partial \theta_\alpha} \hat{\boldsymbol{\alpha}} \cdot \boldsymbol{\nu} \, \mathrm{d}\Gamma = -\int_{d^-}^{d^+} \left[\delta_\theta \frac{\partial W}{\partial \theta_\alpha} \right]^{z=0} \hat{\boldsymbol{\alpha}} \cdot \hat{\boldsymbol{z}} \, \mathrm{d}x + \int_{d^+}^{d^-} \left[\delta_\theta \frac{\partial W}{\partial \theta_\alpha} \right]^{z=h} \hat{\boldsymbol{\alpha}} \cdot (h_x \hat{\boldsymbol{z}} - \hat{\boldsymbol{z}}) \, \mathrm{d}x. \tag{5.18}$$

Equations (5.16)–(5.18) can be combined and rearranged to express the variation of the bulk elastic energy δE_{bulk} as

$$\begin{aligned} \delta E_{\mathrm{bulk}} = {} & \int_{d^-}^{d^+} \int_0^h \delta_\theta \left(\frac{\partial W}{\partial \theta} - \frac{\partial}{\partial x} \left(\frac{\partial W}{\partial \theta_x} \right) - \frac{\partial}{\partial z} \left(\frac{\partial W}{\partial \theta_z} \right) \right) \mathrm{d}z \, \mathrm{d}x \\ & + \int_{d^-}^{d^+} \delta_h \left[W + \psi_{\mathrm{g}} \right]^{z=h} \mathrm{d}x - \int_{d^-}^{d^+} \left[\delta_\theta h_x \frac{\partial W}{\partial \theta_x} \right]^{z=h} \mathrm{d}x \\ & + \int_{d^-}^{d^+} \left[\delta_\theta \frac{\partial W}{\partial \theta_z} \right]^{z=h} \mathrm{d}x - \int_{d^-}^{d^+} \left[\delta_\theta \frac{\partial W}{\partial \theta_z} \right]^{z=0} \mathrm{d}x. \end{aligned} \tag{5.19}$$

For the gas–nematic interface energy E_{GN}, given by (5.7), using the variations (5.12) and carrying out integration by parts on the terms involving δ_{hx} shows that δE_{GN} is given by

$$\begin{aligned} \delta E_{\mathrm{GN}} = {} & \int_{d^-}^{d^+} \Bigg[\delta_\theta \sqrt{1+h_x^2} \frac{\partial \omega_{\mathrm{GN}}}{\partial \theta} \\ & \qquad + \delta_h \left(\sqrt{1+h_x^2} \frac{\partial \omega_{\mathrm{GN}}}{\partial \theta} \frac{\partial \theta}{\partial z} - \frac{\partial}{\partial x} \Big(\frac{\partial}{\partial h_x} \big(\sqrt{1+h_x^2} \, \omega_{\mathrm{GN}} \big) \Big) \right) \Bigg]^{z=h} \mathrm{d}x \\ & + \delta_{d^+} \left[\sqrt{1+h_x^2} \, \omega_{\mathrm{GN}} \right]^{x=d^+} - \delta_{d^-} \left[\sqrt{1+h_x^2} \, \omega_{\mathrm{GN}} \right]^{x=d^-} \qquad (5.20) \\ & + \left[\delta_h \frac{\partial}{\partial h_x} \left(\sqrt{1+h_x^2} \, \omega_{\mathrm{GN}} \right) \right]_{d^-}^{x=d^+} - \left[\delta_h \frac{\partial}{\partial h_x} \left(\sqrt{1+h_x^2} \, \omega_{\mathrm{GN}} \right) \right]^{x=d^-}. \end{aligned} \tag{5.21}$$

Substituting for the variation of the ridge height δ_h at the contact lines, given by

(5.13) and (5.14), then yields

$$\begin{aligned}\delta E_{\mathrm{GN}} = \int_{d^-}^{d^+} \Bigg[& \delta_\theta \sqrt{1+h_x^2}\frac{\partial \omega_{\mathrm{GN}}}{\partial \theta} \\ & + \delta_h \left(\sqrt{1+h_x^2}\frac{\partial \omega_{\mathrm{GN}}}{\partial \theta}\frac{\partial \theta}{\partial z} - \frac{\partial}{\partial x}\Big(\frac{\partial}{\partial h_x}\big(\sqrt{1+h_x^2}\,\omega_{\mathrm{GN}}\big)\Big)\right)\Bigg]^{z=h} \mathrm{d}x \\ & + \delta_{d^+}\left[\sqrt{1+h_x^2}\,\omega_{\mathrm{GN}} - h_x\frac{\partial}{\partial h_x}\left(\sqrt{1+h_x^2}\,\omega_{\mathrm{GN}}\right)\right]^{x=d^+} \\ & - \delta_{d^-}\left[\sqrt{1+h_x^2}\,\omega_{\mathrm{GN}} - h_x\frac{\partial}{\partial h_x}\left(\sqrt{1+h_x^2}\,\omega_{\mathrm{GN}}\right)\right]^{x=d^-} .\end{aligned} \tag{5.22}$$

For the nematic–substrate interface energy E_{NS}, given by (5.8), using the variations (5.12) shows that δE_{NS} is given by

$$\delta E_{\mathrm{NS}} = \int_{d^-}^{d^+} \left[\delta_\theta \frac{\partial \omega_{\mathrm{NS}}}{\partial \theta}\right]^{z=0} \mathrm{d}x + \delta_{d^+}\left[\omega_{\mathrm{NS}}\right]^{x=d^+} - \delta_{d^-}\left[\omega_{\mathrm{NS}}\right]^{x=d^-} . \tag{5.23}$$

For the gas–substrate interface energy E_{GS}, given by (5.9), using the variations (5.12) shows that δE_{GS} is given by

$$\delta E_{\mathrm{GS}} = \delta_{d^-}\left[\omega_{\mathrm{GS}}\right]^{x=d^-} - \delta_{d^+}\left[\omega_{\mathrm{GS}}\right]^{x=d^+} . \tag{5.24}$$

Finally, for the area constraint $\mathcal{C}_{\mathrm{area}}$, given by (5.10), using the variations (5.12) and the two boundary conditions $h(d^\pm) = 0$, shows that $\delta\mathcal{C}_{\mathrm{area}}$ is given by

$$\delta\mathcal{C}_{\mathrm{area}} = -\int_{d^-}^{d^+} p_0\,\delta_h \,\mathrm{d}x. \tag{5.25}$$

The variation of the functional F is obtained by adding the terms from each of the individual variations, given by (5.19) and (5.22)–(5.25), so that

$$\delta F = \delta E_{\mathrm{bulk}} + \delta E_{\mathrm{GN}} + \delta E_{\mathrm{NS}} + \delta E_{\mathrm{GS}} + \delta\mathcal{C}_{\mathrm{area}}. \tag{5.26}$$

Since we seek extrema of the free energy E for which $\delta F = 0$, and the variations δ_θ, $[\delta_\theta]^{z=0}$, $[\delta_\theta]^{z=h}$, δ_h, δ_{d^+} and δ_{d^-} are independent and arbitrary, their coefficients in δF, given by (5.26), must be zero. Together with the area constraint (5.5) and the two boundary conditions $h(d^\pm) = 0$, the coefficients of each variation yield the governing equations for a nematic ridge, as described in the next section.

5.3 Governing equations for a nematic ridge

Each of the six governing equations derived from setting the coefficients of δ_θ, $[\delta_\theta]^{z=h}$, $[\delta_\theta]^{z=0}$, δ_h, δ_{d^+} and δ_{d^-} in (5.26) to zero has a specific physical meaning, namely the balance of elastic torque within the bulk of the nematic, the balance-of-couple conditions on the gas–nematic and nematic–substrate interfaces, the balance-of-stress condition on the gas–nematic interface, and the balance-of-stress conditions at the contact lines, respectively. These equations, together with the area constraint, are summarised below.

The balance of elastic torque within the bulk of the nematic, i.e. the Euler–Lagrange equation, for the elastic free energy density $W(\theta, \theta_x, \theta_z)$, is

$$\frac{\partial W}{\partial \theta} - \frac{\partial}{\partial x}\left(\frac{\partial W}{\partial \theta_x}\right) - \frac{\partial}{\partial z}\left(\frac{\partial W}{\partial \theta_z}\right) = 0. \tag{5.27}$$

The balance-of-couple conditions on the gas–nematic interface and the nematic–substrate interface, namely the weak anchoring conditions [151,201], are given by

$$\frac{\partial W}{\partial \theta_z} - h_x \frac{\partial W}{\partial \theta_x} + \sqrt{1 + h_x^2}\, \frac{\partial \omega_{\mathrm{GN}}}{\partial \theta} = 0 \tag{5.28}$$

on $z = h$ and

$$-\frac{\partial W}{\partial \theta_z} + \frac{\partial \omega_{\mathrm{NS}}}{\partial \theta} = 0 \tag{5.29}$$

on $z = 0$, respectively.

The balance-of-stress condition on the gas–nematic interface, which is usually referred to as the Young–Laplace equation [48], is given by

$$W + \psi_{\mathrm{g}} - p_0 + \sqrt{1 + h_x^2}\,\frac{\partial \omega_{\mathrm{GN}}}{\partial \theta}\frac{\partial \theta}{\partial z} - \frac{\partial}{\partial x}\left(\frac{\partial}{\partial h_x}\left(\sqrt{1 + h_x^2}\;\omega_{\mathrm{GN}}\right)\right) = 0 \tag{5.30}$$

on $z = h$. To distinguish between the classical isotropic Young–Laplace equation and (5.30) we henceforth refer to (5.30) as the *nematic Young–Laplace equation*.

The balance-of-stress conditions at the contact lines, which are usually referred to as Young equations [48], are given by

$$\omega_{\mathrm{NS}} - \omega_{\mathrm{GS}} + \sqrt{1 + h_x^2}\,\omega_{\mathrm{GN}} - h_x \frac{\partial}{\partial h_x}\left(\sqrt{1 + h_x^2}\,\omega_{\mathrm{GN}}\right) = 0 \tag{5.31}$$

at $x = d^{\pm}$. To distinguish between the classical isotropic Young equations and (5.31) we henceforth refer to (5.31) as the *nematic Young equations*.

As mentioned previously, the theoretical description of a volume of nematic bounded by a gas-nematic and nematic-substrate interface has previously been considered by Jenkins and Barratt [102], who obtained general forms of the interfacial conditions, which correspond to equations (5.28)–(5.30), and the force per length on a contact line, and Rey [181, 182], who obtained the general forms of the nematic Young–Laplace equation and the nematic Young equations, which correspond to equations (5.30) and (5.31), respectively.

Once explicit forms of the energy densities W, ψ_{g}, ω_{GN}, ω_{NS} and ω_{GS} have been prescribed, the balance of elastic torque within the bulk of the nematic (5.27), the

three interface conditions (5.28)–(5.30), the two nematic Young equations (5.31), the area constraint (5.5), and the two boundary conditions $h(d^{\pm}) = 0$ specify the full problem for the five unknowns $\theta(x, z)$, $h(x)$, d^{-}, d^{+} and p_0. The unknown contact angles $\beta^{\pm}$ are obtained from the slope of the ridge height h_x and (5.4).

5.3.1 The Oseen–Frank bulk elastic energy density and Rapini–Papoular interface energy densities

As mentioned above, for the bulk elastic energy density W we use the standard Oseen–Frank bulk elastic energy density, defined by (1.11) and discussed in Section 1.7.1. Substituting (5.1) into (1.11) yields

$$W(\theta, \theta_x, \theta_z) = \frac{K_1}{2} \left(\theta_z \cos\theta - \theta_x \sin\theta\right)^2 + \frac{K_3}{2} \left(\theta_x \cos\theta + \theta_z \sin\theta\right)^2, \qquad (5.32)$$

which only depends on splay and bend elastic deformations. Although we proceed using the full Oseen–Frank energy density (5.32), we note that the commonly used one-constant approximation of the elastic constants [201] can be implemented in (5.32) by setting $K = K_1 = K_3$, in which case $W(\theta_x, \theta_z) = K\left(\theta_x^2 + \theta_z^2\right)/2$. The one-constant approximation will be used in Chapter 6.

As also mentioned above, for the interface energy densities involving the nematic, namely ω_{GN} and ω_{NS}, we use the standard Rapini–Papoular form, defined by (1.17) and discussed in Section 1.7.3. The appropriate form of the Rapini–Papoular energy densities for the gas–nematic interface and nematic–substrate interface is given by

$$\omega_{\mathrm{GN}} = \sigma_{\mathrm{GN}} + \frac{C_{\mathrm{GN}}}{4} \left(1 - 2(\boldsymbol{\nu}_{\mathrm{GN}} \cdot \mathbf{n})^{\mathbf{2}}\right), \qquad (5.33)$$

$$\omega_{\mathrm{NS}} = \sigma_{\mathrm{NS}} + \frac{C_{\mathrm{NS}}}{4} \left(1 - 2(\boldsymbol{\nu}_{\mathrm{NS}} \cdot \mathbf{n})^{\mathbf{2}}\right), \qquad (5.34)$$

where $\boldsymbol{\nu}_{\mathrm{GN}}$, C_{GN} and σ_{GN} are the outward unit normal (given by (5.2)), anchoring strength and isotropic interfacial tension for the gas–nematic (GN) interface, respectively, $\boldsymbol{\nu}_{\mathrm{NS}}$, C_{NS} and σ_{NS} are the outward unit normal (given by (5.3)), anchoring strength and isotropic interfacial tension for the nematic–substrate (NS) interface, respectively. Substituting (5.2) and (5.3) into (5.33) and (5.34) yields

$$\omega_{\mathrm{GN}}(\theta, h_x) = \sigma_{\mathrm{GN}} + \frac{C_{\mathrm{GN}}}{4}\left[\frac{1-h_x^2}{1+h_x^2}\cos 2\theta + \frac{2h_x}{1+h_x^2}\sin 2\theta\right], \tag{5.35}$$

$$\omega_{\mathrm{NS}}(\theta) = \sigma_{\mathrm{NS}} + \frac{C_{\mathrm{NS}}}{4}\cos 2\theta. \tag{5.36}$$

The gas–substrate interface has constant energy density

$$\omega_{\mathrm{GS}} = \sigma_{\mathrm{GS}}, \tag{5.37}$$

where σ_{GS} is the isotropic interfacial tension of the gas–substrate interface.

5.3.2 Governing equations for the Oseen–Frank bulk elastic energy density and Rapini–Papoular interface energy densities

Using (5.32) in (5.27) yields the balance of elastic torque within the bulk of the nematic,

$$\begin{aligned}&\big(K_1\sin^2\theta + K_3\cos^2\theta\big)\theta_{xx} + \big(K_1\cos^2\theta + K_3\sin^2\theta\big)\theta_{zz} \\ &\quad + (K_3 - K_1)\big[\,(\theta_z\cos\theta - \theta_x\sin\theta)\,(\theta_x\cos\theta + \theta_z\sin\theta) + \theta_{xz}\sin 2\theta\big] = 0.\end{aligned} \tag{5.38}$$

Using (5.32) and (5.35) in (5.28) yields the balance-of-couple condition on the gas–nematic interface,

$$\begin{aligned}\big(K_1\cos^2\theta + K_3\sin^2\theta\big)\theta_z + \frac{1}{2}(K_3 - K_1)(\theta_x - h_x\theta_z)\sin 2\theta \\ - \big(K_1\sin^2\theta + K_3\cos^2\theta\big)h_x\theta_x \\ + \frac{C_{\mathrm{GN}}}{2\sqrt{1+h_x^2}}\left[(h_x^2-1)\sin 2\theta + 2h_x\cos 2\theta\right] = 0\end{aligned} \tag{5.39}$$

on $z = h$. Using (5.36) in (5.29) yields the balance-of-couple condition on the nematic–substrate interface,

$$-\big(K_1\cos^2\theta + K_3\sin^2\theta\big)\theta_z - \frac{1}{2}(K_3 - K_1)\theta_x\sin 2\theta - \frac{C_{\mathrm{NS}}}{2}\sin 2\theta = 0 \tag{5.40}$$

on $z = 0$. Using (5.32) and (5.35) in (5.30) yields the nematic Young–Laplace equation,

$$\begin{aligned}p_0 - W - \psi_{\mathrm{g}} + \sigma_{\mathrm{GN}}\frac{h_{xx}}{(1+h_x^2)^{3/2}} + \frac{C_{\mathrm{GN}}}{4\,(1+h_x^2)^{5/2}}\Bigg[3h_{xx}\Big[(h_x^2-1)\cos 2\theta - 2h_x\sin 2\theta\Big] \\ + (1+h_x^2)\Bigg(4\cos 2\theta\Big[\theta_x - h_x(1+h_x^2)\theta_z\Big] \\ + 2\sin 2\theta\Big[(1-h_x^4)\theta_z + h_x(3+h_x^2)\theta_x\Big]\Bigg)\Bigg] = 0\end{aligned} \tag{5.41}$$

on $z = h$. In order to express the nematic Young equations (5.31) in terms of the contact angles β^- and β^+, we use the relations (5.4). Then, using (5.35)–(5.37)

in (5.31) yields

$$\frac{C_{\mathrm{NS}}}{4}\cos 2\theta + \frac{C_{\mathrm{GN}}}{4}\left[\cos 2(\theta-\beta^-)\cos\beta^- - 2\sin 2(\theta-\beta^-)\sin\beta^-\right] = \sigma_{\mathrm{GS}} - \sigma_{\mathrm{NS}} - \sigma_{\mathrm{GN}}\cos\beta^-, \tag{5.42}$$

$$\frac{C_{\mathrm{NS}}}{4}\cos 2\theta + \frac{C_{\mathrm{GN}}}{4}\left[\cos 2(\theta+\beta^+)\cos\beta^+ - 2\sin 2(\theta+\beta^+)\sin\beta^+\right] = \sigma_{\mathrm{GS}} - \sigma_{\mathrm{NS}} - \sigma_{\mathrm{GN}}\cos\beta^+ \tag{5.43}$$

at $x = d^-$ and $x = d^+$, respectively. The terms on the right-hand sides of (5.42) and (5.43) appear in the classical isotropic Young equations, while the terms on the left-hand sides are due to the anisotropic nature of the nematic arising from the weak anchoring on the nematic–substrate interface and on the gas–nematic interface. We note that the classical isotropic Young equations (1.39) are recovered from the nematic Young equations (5.42) and (5.43) by setting $C_{\mathrm{NS}} = C_{\mathrm{GN}} = 0$.

In summary, the balance of elastic torque within the bulk of the nematic (5.38), the three interface conditions (5.39)–(5.41), the two nematic Young equations (5.42) and (5.43), the area constraint (5.5), and the two boundary conditions $h(d^{\pm}) = 0$ specify the problem for the five unknowns $\theta(x,z)$, $h(x)$, d^-, d^+ and p_0. We note that, as previously mentioned, while the nematic Young equations (5.42) and (5.43) were derived assuming the ridge height h is a single-valued function of x, they also hold when the ridge height h is a double-valued function of x (as shown in Appendix A), and therefore the nematic Young equations (5.42) and (5.43) are valid for both scenarios.

5.4 Conclusions

In this chapter we have derived the governing equations and boundary conditions for a two-dimensional static ridge of nematic resting on an ideal solid substrate in an atmosphere of passive gas. Specifically, in Sections 5.1 and 5.2, we derived the governing equations by minimising the free energy, which is given by the sum of the bulk elastic energy, gravitational potential energy, and the interface energies, subject to a prescribed constant cross-sectional area. We then, in Section 5.3, chose explicit forms of the bulk elastic energy density and the interface energy densities, namely the standard Oseen–Frank bulk elastic energy density and the Rapini–Papoular interface energy densities, and obtained the governing equations (5.38)–(5.43). Specifically, (5.38)–(5.43) determine the director angle $\theta(x, z)$, the ridge height $h(x)$, the contact line positions $x = d^{\pm}$, and the Lagrange multiplier p_0, in terms of the physical parameters, namely the splay and bend elastic constants K_1 and K_3, the isotropic interfacial tensions σ_{GN}, σ_{NS}, and σ_{GS}, and the anchoring strengths C_{GN} and C_{NS}. The governing equations can readily be adapted to include other effects, such as to include electromagnetic forces, additional contact line effects, non-ideal substrates, or more detailed models for the nematic molecular order, such as Q-tensor theory [152]. The governing equations derived in this chapter will now be applied in Chapter 6 to the scenario of a thin ridge of nematic with pinned contact lines where we can make significant progress in solving these equations.

The governing equations derived in this chapter represent the most common experimental situation, in which the nematic partially coats the substrate (i.e. the partial wetting state). These equations can also be used to describe the equilibrium states of complete dewetting, which we denote by $\mathbb{D}$, and of complete wetting, which we denote by $\mathbb{W}$. In the complete dewetting state, in which the gas–nematic interface forms a cylinder, the nematic Young equations (5.42)

and (5.43), the two boundary conditions $h(d^{\pm}) = 0$, and the balance-of-couple condition on the nematic–solid interface (5.40) are not relevant. For the case that the gas–nematic interface is a perfectly circular cylinder, the possible director configurations have been extensively studied (see, for example, Kleman [115]). Similarly, in the complete wetting state, in which the nematic forms a film that completely coats the substrate, the nematic Young equations (5.42) and (5.43) and the two boundary conditions $h(d^{\pm}) = 0$ are not relevant. The behaviour of the director and gas–nematic interface for nematic films has been studied previously (see, for example, Sonin [197] and Manyuhina [139]). In Chapter 7, we will discuss further how the governing equations relate to the complete dewetting and complete wetting states.

Chapter 6

A thin pinned static ridge of nematic

In this chapter we consider the application of the governing equations derived in Chapter 5 to a pinned static ridge of nematic (N) of prescribed cross-sectional area A resting on an ideal solid substrate (S) in an atmosphere of passive gas (G) as shown in Figure 6.1. Much like in Chapter 5, the ridge has a gas–nematic interface (the nematic free surface) at $z = h(x)$ and a nematic–substrate interface at $z = 0$. However, unlike Chapter 5, we now assume the nematic–substrate–gas three-phase contact lines at $x = d^-$ and $x = d^+$ are pinned (i.e. fixed). Experimentally, pinned contact lines can be achieved by treatment of the substrate to create either surface roughness [105] or hydrophobic and hydrophilic areas [159]. In terms of governing equations derived in Chapter 5, as the two contact lines are pinned, the nematic Young equations (5.42) and (5.43) are no longer relevant and the positions of the contact lines are now prescribed. Without loss of generality, the positions of the pinned contact lines are given by $d^+ = d$ and $d^- = -d$, where d is the prescribed constant semi-width of the ridge, and therefore the Dirichlet

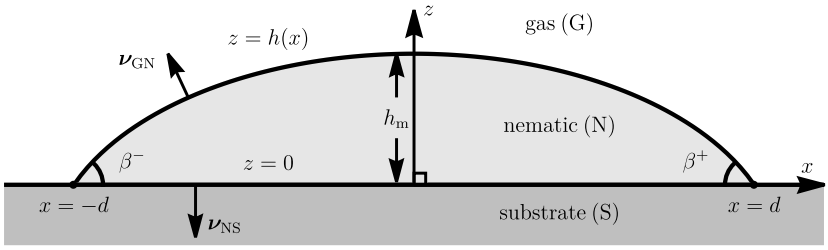

Figure 6.1: A schematic of a pinned static ridge of nematic (N) resting on an ideal solid substrate (S) in an atmosphere of passive gas (G), bounded by a gas–nematic interface at $z = h(x)$ and a nematic–substrate interface at $z = 0$, with pinned contact lines at $x = \pm d$. The Cartesian coordinates x and z (where the y-direction is into the page), the contact angles β^- and β^+, outward normals of the nematic–substrate interface and gas–nematic interface $\boldsymbol{\nu}_{\mathrm{NS}}$ and $\boldsymbol{\nu}_{\mathrm{GN}}$, respectively, and the height at the middle of the ridge h_{m} are also indicated.

condition on the height of the ridge is now given by

$$h = 0 \quad \text{at} \quad x = \pm d. \tag{6.1}$$

We proceed in Section 6.1 and formulate the governing equations and boundary conditions for a thin ridge of nematic with pinned contact lines. We then obtain analytical solutions for situations with a uniform director field in Section 6.2 before describing situations with a distorted director field in Section 6.3. We then obtain numerical solutions for various values of anchoring strength in Section 6.4 and subsequently numerically investigate when either a uniform or a distorted director field is energetically preferred in Section 6.5. In Section 6.6, we describe the behaviour of the director in different regions of the nematic–substrate and gas–nematic anchoring-strength parameter plane, and investigate the behaviour of the height of the ridge in Section 6.7.

The pinned ridge of nematic we consider in this chapter has many features relevant to recent research into the self-organisation of columnar discotic liquid crystal (discotic) phases into ridges [21, 237], which has applications to the controlled printing of semiconductors. Another area of recent research in which

pinned ridges of liquid crystal occur is diffraction gratings [17, 23].

6.1 Model formulation

From Section 6.1.2 onwards we will consider the situation in which the ridge is thin, and so it is appropriate in this chapter to assume that the height of the ridge h is a single-valued function of x. We remind the reader that the (unknown) contact angles formed between the nematic–substrate and gas–nematic interfaces are given by (5.4), the height of the ridge h is subject to the prescribed cross-sectional area constraint (5.5), and the director $\boldsymbol{n} = \boldsymbol{n}(x, z)$ is expressed in terms of the director angle $\theta = \theta(x, z)$, which is given by (5.1).

6.1.1 Governing equations for a pinned nematic ridge

In this chapter, unlike Chapter 5, we take the one-constant approximation of the Frank–Oseen bulk elastic energy density (for more detail, see Section 1.7.1), so that W is given by (1.14). The Rapini–Papoular interface energy densities ω_{NS} and ω_{GN} remain the same as in Chapter 5, namely (5.35) and (5.36), respectively. In order to simplify the present problem we also neglect the effects of gravity. Gravitational effects can be compared with surface-tension effects by considering the relative size of the capillary length l and the semi-width d. Specifically, when $l \gg d$ gravitational effects can be neglected when compared to surface-tension effects and when $l \ll d$ surface tension can be neglected compared to gravitational effects. The capillary length for a gas–nematic interface between air and 5CB is given by $l = \sqrt{\sigma_{\mathrm{GN}}/(\rho g)} \simeq 2 \times 10^{-3}\,\mathrm{m}$, where $\rho = 1020\,\mathrm{kg\,m^{-3}}$ is the density of 5CB [201] and g is the magnitude of acceleration due to gravity. We assume that $d \ll 2 \times 10^{-3}\,\mathrm{m}$, and therefore neglect gravitational effects and set $\psi_{\mathrm{g}} = 0$ in (5.41). This assumption is certainly appropriate for many applications, including

nematic diffraction gratings where $d \simeq 5 \times 10^{-8}\,\mathrm{m}$ [17], discotic ridges used for new semiconductor applications where $d \simeq 3.7 \times 10^{-6}\,\mathrm{m}$ [21], and possibly for nematic droplets used in the ODF method where $d \simeq 10^{-4}$–$10^{-2}\,\mathrm{m}$ as stated in Table 1.1.

With the one-constant approximation of the Frank–Oseen bulk elastic energy density, $\psi_{\mathrm{g}} = 0$ and pinned contact lines, the balance of elastic torque within the bulk of the nematic (5.38) is given by

$$0 = \theta_{xx} + \theta_{zz}, \tag{6.2}$$

and the three interfacial equations (5.39)–(5.41) are given by

$$0 = -K\theta_z - \frac{C_{\mathrm{NS}}}{2}\sin 2\theta, \tag{6.3}$$

$$0 = K\big(\theta_z - h_x\theta_x\big) + \frac{C_{\mathrm{GN}}}{2\sqrt{1+h_x^2}}\Big[(h_x^2-1)\sin 2\theta + 2h_x\cos 2\theta\Big], \tag{6.4}$$

$$\begin{aligned} 0 = p_0 - \frac{K}{2}\left(\theta_x^2+\theta_z^2\right) + \sigma_{\mathrm{GN}}\frac{h_{xx}}{\left(1+h_x^2\right)^{3/2}} \\ + \frac{C_{\mathrm{GN}}}{4\left(1+h_x^2\right)^{5/2}}\Big[3h_{xx}\Big((h_x^2-1)\cos 2\theta - 2h_x\sin 2\theta\Big) \\ + (1+h_x^2)\Big(4\cos 2\theta\Big[\theta_x - h_x(1+h_x^2)\theta_z\Big] \\ + 2\sin 2\theta\Big[(1-h_x^4)\theta_z + h_x(3+h_x^2)\theta_x\Big]\Big)\Big], \end{aligned} \tag{6.5}$$

on $z = 0$, $z = h$, and $z = h$, respectively. For future reference, we note that the total energy of the pinned ridge E_{tot} is given by

$$E_{\mathrm{tot}} = \int_{-d}^{d}\int_{0}^{h} W\,\mathrm{d}z\,\mathrm{d}x + \int_{-d}^{d}\omega_{\mathrm{NS}}\,\mathrm{d}x + \int_{-d}^{d}\omega_{\mathrm{GN}}\sqrt{1+h_x^2}\,\mathrm{d}x. \tag{6.6}$$

6.1.2 A thin pinned nematic ridge

To allow for greater analytical progress and because many of the practical applications described in Section 1.10.2 the nematic ridges and droplets are thin, such that the height of the ridge or droplet is much smaller than its width, we now focus on the case that the ridge is thin. We define an appropriate small nondimensional aspect ratio ϵ in terms of the semi-width d and the cross-sectional area A as

$$\epsilon = \frac{A}{d^2} \ll 1. \tag{6.7}$$

For a thin ridge with $\epsilon \ll 1$ we nondimensionalise and scale the variables according to

$$\begin{gathered}
x = d\,x^*, \qquad z = \epsilon d\,z^*, \qquad h = \epsilon d\,h^*, \\
h_{\mathrm{m}} = \epsilon d\,{h_{\mathrm{m}}}^*, \qquad \beta^- = \epsilon\,{\beta^-}^*, \qquad \beta^+ = \epsilon\,{\beta^+}^*, \\
p_0 = \epsilon\frac{\sigma_{\mathrm{GN}}}{d}\,p_0^*, \qquad E_{\mathrm{tot}} = d\sigma_{\mathrm{GN}}\,E_{\mathrm{tot}}^*, \qquad K = \epsilon^3 d\sigma_{\mathrm{GN}}\,K^*, \\
\sigma_{\mathrm{NS}} = \sigma_{\mathrm{GN}}\,\sigma_{\mathrm{NS}}^*, \qquad C_{\mathrm{NS}} = \epsilon^2\sigma_{\mathrm{GN}}\,C_{\mathrm{NS}}^*, \qquad C_{\mathrm{GN}} = \epsilon^2\sigma_{\mathrm{GN}}\,C_{\mathrm{GN}}^*,
\end{gathered} \tag{6.8}$$

where the stars (*) denote nondimensional variables. Note that we have nondimensionalised lengths in the x-direction with d and lengths in the z-direction with ϵd, and hence the contact angles are scaled with ϵ. The interfacial tension σ_{NS} and anchoring strengths C_{NS} and C_{GN} are nondimensionalised with the interfacial tension σ_{GN}. In order to study the most interesting regime, in which surface tension, anchoring and elasticity are comparable, we have scaled the elastic constant K and anchoring strengths C_{NS} and C_{GN} such that contributions of surface tension, anchoring and elasticity appear at leading order in the governing equations. Less interesting regimes for which elastic effects are much stronger or much weaker than anchoring effects will be discussed shortly.

With the stars dropped for clarity, at leading order in ϵ the bulk elastic equation (6.2) reduces to

$$\theta_{zz} = 0, \tag{6.9}$$

and hence θ is given by

$$\theta = \theta_{\mathrm{NS}} + \big(\theta_{\mathrm{GN}} - \theta_{\mathrm{NS}}\big)\frac{z}{h}, \tag{6.10}$$

where $\theta_{\mathrm{NS}} = \theta_{\mathrm{NS}}(x) = \theta(x,0)$ and $\theta_{\mathrm{GN}} = \theta_{\mathrm{GN}}(x) = \theta(x,h(x))$ denote the (unknown) values of θ on the nematic–substrate interface $z = 0$ and on the gas–nematic interface $z = h$, respectively. At leading order in ϵ, equations (6.3)–(6.5) reduce to

$$K\big(\theta_{\mathrm{GN}} - \theta_{\mathrm{NS}}\big) + C_{\mathrm{NS}} h \sin\theta_{\mathrm{NS}} \cos\theta_{\mathrm{NS}} = 0, \tag{6.11}$$

$$K\big(\theta_{\mathrm{GN}} - \theta_{\mathrm{NS}}\big) - C_{\mathrm{GN}} h \sin\theta_{\mathrm{GN}} \cos\theta_{\mathrm{GN}} = 0, \tag{6.12}$$

$$p_0 + h_{xx} + \frac{K}{2}\left(\frac{\theta_{\mathrm{GN}} - \theta_{\mathrm{NS}}}{h}\right)^2 = 0, \tag{6.13}$$

respectively. Unlike the full balance-of-couple condition on the gas–nematic interface (6.4), the leading-order balance-of-couple condition on the gas–nematic interface (6.12) depends only on the local height of the ridge h but not its derivatives. In particular, in the thin-film limit (6.12) is identical to a balance-of-couple condition on a flat gas–nematic interface (i.e. when h is constant); therefore, θ_{GN} behaves as if the gas–nematic interface were locally flat. In the leading-order nematic Young–Laplace equation (6.13), the leading-order curvature of the gas–nematic interface (i.e. h_{xx}) is coupled to a term which depends on both elastic effects and anchoring effects, namely $K\left(\theta_{\mathrm{GN}} - \theta_{\mathrm{NS}}\right)^2/(2h^2)$.

At leading order in ϵ, the contact-line conditions (6.1) are given by

$$h = 0 \quad \text{at} \quad x = \pm 1, \tag{6.14}$$

and hence it follows from the balance-of-couple conditions (6.11) and (6.12) that $\theta = \theta_{\mathrm{NS}} = \theta_{\mathrm{GN}}$ at $x = \pm 1$. Also at leading order in ϵ, the prescribed cross-sectional area constraint is given by

$$1 = \int_{-1}^{1} h \, \mathrm{d}x, \tag{6.15}$$

and the leading-order contact angles are given by $\beta^{-} = h_x$ at $x = -1$ and $\beta^{+} = -h_x$ at $x = 1$.

For a thin pinned ridge the total energy given by (6.6) reduces to

$$E_{\mathrm{tot}} = 2\,(1 + \sigma_{\mathrm{NS}}) + \frac{1}{2}\epsilon^2 \Delta E + O(\epsilon^3), \tag{6.16}$$

showing that E_{tot} takes the constant value of $2(1 + \sigma_{\mathrm{NS}})$ at leading order in ϵ, and that variations in E_{tot} appear at second order in ϵ via the term $\Delta E = \Delta E(h, \theta_{\mathrm{NS}}, \theta_{\mathrm{GN}})$, which can be decomposed as

$$\Delta E = E_{\mathrm{iso}} + E_{\mathrm{elast}} + E_{\mathrm{NS}} + E_{\mathrm{GN}}, \tag{6.17}$$

where

$$\begin{aligned} E_{\mathrm{iso}} &= \int_{-1}^{1} h_x^2 \, \mathrm{d}x, \qquad E_{\mathrm{elast}} = K \int_{-1}^{1} \frac{(\theta_{\mathrm{GN}} - \theta_{\mathrm{NS}})^2}{h} \, \mathrm{d}x, \\ E_{\mathrm{NS}} &= \frac{C_{\mathrm{NS}}}{2} \int_{-1}^{1} \cos 2\theta_{\mathrm{NS}} \, \mathrm{d}x, \qquad E_{\mathrm{GN}} = \frac{C_{\mathrm{GN}}}{2} \int_{-1}^{1} \cos 2\theta_{\mathrm{GN}} \, \mathrm{d}x, \end{aligned} \tag{6.18}$$

are the second-order isotropic energy E_{iso}, elastic energy E_{elast}, nematic–substrate interface anchoring energy E_{NS}, and gas–nematic interface anchoring energy E_{GN},

respectively. The special case of an isotropic fluid is recovered by setting $K = C_{\rm NS} = C_{\rm GN} = 0$, so that the second-order energy reduces to $\Delta E = E_{\rm iso}$. The second-order isotropic energy $E_{\rm iso}$ is minimised subject to the contact-line conditions (6.14) and the area constraint (6.26) by the solution for the height of the ridge and the Lagrange multiplier for a static pinned isotropic ridge in the absence of gravity, denoted $h_{\rm iso} = h_{\rm iso}(x)$ and $p_{\rm I}$, respectively, namely

$$h_{\rm iso} = \frac{3}{4}(1 - x^2) \quad \text{and} \quad p_{\rm I} = \frac{3}{2}. \tag{6.19}$$

For future reference, we note from inspection of (6.18) and (6.19) that $E_{\rm iso} \geq 3/4$, $E_{\rm elast} \geq 0$, $-|C_{\rm NS}|/2 \leq E_{\rm NS} \leq |C_{\rm NS}|/2$, and $-|C_{\rm GN}|/2 \leq E_{\rm GN} \leq |C_{\rm GN}|/2$.

In summary, the equations and boundary conditions for a thin pinned ridge given by the system (6.11)–(6.15) involve the unknowns $\theta_{\rm NS}(x)$, $\theta_{\rm GN}(x)$, $h(x)$ and p_0 and the parameters K, $C_{\rm NS}$ and $C_{\rm GN}$. Once the solutions for $\theta_{\rm NS}$, $\theta_{\rm GN}$, h, and p_0 have been determined, the contact angles $\beta^+ = -h_x(1)$ and $\beta^- = h_x(-1)$, the director angle $\theta = \theta_{\rm NS} + (\theta_{\rm GN} - \theta_{\rm NS})z/h$, and the second-order energy ΔE (given by (6.17)) can be readily determined.

For future reference, we note that if h, p_0, $\theta_{\rm NS}$ and $\theta_{\rm GN}$ are solutions of the system (6.11)–(6.13) and (6.24)–(6.26) for anchoring strengths $C_{\rm NS}$ and $C_{\rm GN}$, then there are three solutions denoted by $\tilde{h}$, $\tilde{p}_0$, $\tilde{\theta}_{\rm NS}$ and $\tilde{\theta}_{\rm GN}$ for anchoring strengths $\tilde{C}_{\rm NS}$ and $\tilde{C}_{\rm GN}$ with $\tilde{h} = h$, $\tilde{p}_0 = p_0$ and

$$\tilde{\theta}_{\rm NS} = \theta_{\rm GN}, \qquad \tilde{\theta}_{\rm GN} = \theta_{\rm NS}, \qquad \tilde{C}_{\rm NS} = C_{\rm GN}, \qquad \tilde{C}_{\rm GN} = C_{\rm NS}, \tag{6.20}$$

$$\tilde{\theta}_{\rm NS} = \frac{\pi}{2} - \theta_{\rm NS}, \quad \tilde{\theta}_{\rm GN} = \frac{\pi}{2} - \theta_{\rm GN}, \quad \tilde{C}_{\rm NS} = -C_{\rm NS}, \quad \tilde{C}_{\rm GN} = -C_{\rm GN}, \tag{6.21}$$

$$\tilde{\theta}_{\rm NS} = \frac{\pi}{2} - \theta_{\rm GN}, \quad \tilde{\theta}_{\rm GN} = \frac{\pi}{2} - \theta_{\rm NS}, \quad \tilde{C}_{\rm NS} = -C_{\rm GN}, \quad \tilde{C}_{\rm GN} = -C_{\rm NS}. \tag{6.22}$$

In (6.20), exchanging $C_{\rm NS}$ and $C_{\rm GN}$ leads to an exchange of the $\theta_{\rm NS}$ and $\theta_{\rm GN}$ solutions. In (6.21), changing $C_{\rm NS}$ and $C_{\rm GN}$ from planar to homeotropic preferred, or

vice versa, leads to a rotation of the director angles by $\pi/2$. In (6.22), exchanging C_{NS} and C_{GN} (as in (6.20)) and changing them from planar to homeotropic preferred, or vice versa (as in (6.21)), leads to an exchange of the θ_{NS} and θ_{GN} solutions and a rotation of the director angles by $\pi/2$. As a consequence of (6.20)–(6.22), any particular solution for a given pair of anchoring strengths also provides solutions for three other pairs of anchoring strengths, which are obtained using (6.20)–(6.22).

The leading-order problem given by the system (6.11)–(6.15) yields multiple solutions which can be trivially related. Specifically, if h, p_0, and θ are solutions of the system (6.11)–(6.15), then $\bar{h}$, $\bar{p}_0$, and $\bar{\theta}$ are also solutions of the system (6.11)–(6.15) where

$$\bar{h} = h, \quad \bar{p}_0 = p_0, \quad \text{and} \quad \bar{\theta} = m\pi \pm \theta, \tag{6.23}$$

where m is any integer value. Provided θ is non-constant it is useful to denote solutions that can be expressed as $m\pi + \theta$ "positive" θ solutions, and solutions that can be expressed as $m\pi - \theta$ "negative" θ solutions. We note that the terms "positive" and "negative" θ solutions refer to the sign of θ compared to the closest integer multiple of π rather than the numerical value of the θ solution. Furthermore, for the thin ridge considered in this chapter, since there are no x-derivatives of θ in the system (6.11)–(6.15), any solution for θ as a function of x can contain any number of discontinuities, provided (6.11)–(6.13) are satisfied through the discontinuity and, in particular, that $(\theta_{\mathrm{GN}} - \theta_{\mathrm{NS}})^2$ is continuous. Specifically, any solution for θ can contain a discontinuous jump to $m\pi \pm \theta$ at any position x. Any such discontinuities in the leading-order solution are associated with disclination lines. Although the present thin-film limit allows for the existence of disclination lines, in the absence of the present thin-film limit, disclination lines are, in general, energetically unfavourable compared to solutions without disclination lines

because they have an increased elastic energy associated with large x-derivatives of θ [132, 205, 219]. The exception is for situations where the symmetry of the system may necessitate the presence of a disclination line at the centre of the ridge. Indeed, previous work on nematic microwrinkle grooves by Ohzono and Fukuda [158], nematic microfluidic channels by Sungupta et al. [193], and nematic droplets by Kleman [115] shows that disclination lines are often found experimentally at the centre of grooves, channels, and droplets, respectively. We therefore only allow a disclination line at the centre of the ridge (i.e. at $x = 0$).

6.1.3 The symmetry of the height of the ridge and the director angle

For the remainder of this chapter, we assume that the height of the ridge h is symmetric about its midpoint, i.e. that h is an even function of x, and that h has a single maximum at $x = 0$, denoted by $h_{\mathrm{m}} = h(0)$. As we assume h is an even function of x, the two contact angles β^- and β^+ are equal, i.e. $\beta = \beta^- = \beta^+$. Although we have been unable to formally prove the validity of these assumptions, we note that extensive numerical investigations of the system (6.11)–(6.15), including using asymmetric initial conditions for θ_{NS}, θ_{GN} and h (for more details, see Appendix B), have only ever found continuous even symmetry solutions for h. These extensive numerical investigations have also only found continuous solutions for θ_{NS} and θ_{GN} that have even symmetry, i.e. no solutions for θ_{NS} and θ_{GN} that are continuous have been found with odd symmetry or asymmetry. Discontinuous solutions for θ_{NS} and θ_{GN}, i.e. those that contain disclination lines, can be obtained by using asymmetric initial conditions for θ_{NS} and θ_{GN} (for more details, see Appendix B).

Given the symmetry of continuous solutions for the director angles θ_{NS} and θ_{GN} and the height of the ridge h, we can now focus on solutions for θ_{NS}, θ_{GN} and

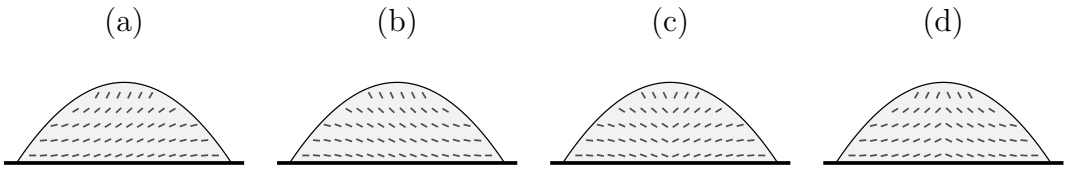

Figure 6.2: Schematic diagram showing the director $\boldsymbol{n}$ (indicated by the solid grey rods) with planar anchoring preferred on the nematic–substrate interface and homeotropic anchoring preferred the gas–nematic interface for (a) a positive θ solution with even symmetry, (b) a negative θ solution with even symmetry, (c) a positive θ solution in the right-hand half with odd symmetry, and (d) a negative θ solution in the right-hand half with odd symmetry.

h in the right-hand half of the ridge $0 \leq x \leq 1$. We construct the solution for θ_{NS} and θ_{GN} in the left-hand half of the ridge $-1 \leq x < 0$ using either odd symmetry about $x = 0$, so that $\theta_i(x) = -\theta_i(-x)$, or even symmetry about $x = 0$, so that $\theta_i(x) = \theta_i(-x)$, where $i = \mathrm{NS}$ or $i = \mathrm{GN}$. We construct the solution for h in the left-hand half of the ridge $-1 \leq x < 0$ using even symmetry. The θ_{NS} and θ_{GN} solutions with odd symmetry have a disclination line at $x = 0$, which corresponds to a jump in θ from $m\pi \pm \theta$ to $m\pi \mp \theta$ at the centre of the ridge, and the θ_{NS} and θ_{GN} solutions with even symmetry do not have a disclination line at the centre of the ridge. In the present thin-film limit, there are therefore four different, but energetically equivalent, solutions for θ that may be constructed from a single solution for θ in the right-hand half of the ridge, namely either a positive θ solution or a negative θ solution in the right-hand half of the ridge with either even or odd symmetry in the left-hand half of the ridge. To illustrate these four different θ solutions, Figure 6.2 shows the director $\boldsymbol{n}$ with planar anchoring preferred on the nematic–substrate interface and with homeotropic anchoring preferred the gas–nematic interface. Figure 6.2(a) and (b) show the positive and negative θ solutions with even symmetry, respectively, where the homeotropic weak anchoring on the gas–nematic interface fails to align the director normally to the gas–nematic interface in the left-hand half and right-hand half, respectively, but no disclination

line present at the centre of the ridge. Figure 6.2(c) shows the positive θ solution in the right-hand half with odd symmetry, where the homeotropic weak anchoring on the gas–nematic interface aligns the director normally to the gas–nematic interface, but there is a disclination line at the centre of the ridge. Figure 6.2(d) shows the negative θ solution in the right-hand half with odd symmetry, where the homeotropic weak anchoring on the gas–nematic interface fails to align the director normally to the gas–nematic interface in both the left-hand half and right-hand half and there is a disclination line at the centre of the ridge. A consideration of higher-order energy terms that describe the increased elastic energy associated with the disclination line or the increased anchoring energy associated with the director not aligning normally to the homeotropic gas–nematic interface would be required in order to determine which solution has the lowest energy, and is therefore energetically preferred. Although we will not consider higher-order energy terms and can therefore not determine which of these solutions has the lowest energy, the previous works mentioned in Section 6.1.2, which show that disclination lines have been found at the centre of grooves, channels, and droplets, may indicate that the lowest energy of these solutions will be the positive θ solution in the right-hand half with odd symmetry (Figure 6.2(c)). However, further theoretical and experimental work is required to confirm this.

As we now consider solutions in the right-hand half of the ridge, the two contact-line conditions (6.14) may be replaced by a single contact-line condition, namely

$$h = 0 \quad \text{at} \quad x = d, \tag{6.24}$$

and a symmetry and regularity condition, namely

$$h_x = 0 \quad \text{at} \quad x = 0. \tag{6.25}$$

Also, the area constraint (6.15) may be expressed as

$$2\int_0^1 h\,\mathrm{d}x = 1, \tag{6.26}$$

and the two contact angles β^- and β^+ are now equal, i.e. $\beta = \beta^- = \beta^+$.

6.1.4 The limits of strong and weak elasticity

Although in what follows we focus on the most interesting regime in which surface-tension, anchoring and elasticity effects are all comparable, namely $K \simeq |C_{\mathrm{NS}}|, |C_{\mathrm{GN}}|$, it is useful to discuss briefly the director angle behaviour in the limit when elastic effects are much stronger than anchoring effects, namely $K \gg |C_{\mathrm{NS}}|, |C_{\mathrm{GN}}|$, and in the limit when elastic effects are much weaker than anchoring effects, namely $K \ll |C_{\mathrm{NS}}|, |C_{\mathrm{GN}}|$. When $K \gg |C_{\mathrm{NS}}|, |C_{\mathrm{GN}}|$, elastic effects dominate and the system (6.11)–(6.13) and (6.24)–(6.26) has director angle solutions which are uniform everywhere with $\theta \equiv \theta_{\mathrm{NS}} = \theta_{\mathrm{GN}}$, which will be discussed in Section 6.2. When $K \ll |C_{\mathrm{NS}}|, |C_{\mathrm{GN}}|$, anchoring effects dominate and θ_{NS} and θ_{GN} are constants given by their preferred orientation on the nematic–substrate interface and gas–nematic interface, respectively. For non-antagonistic anchoring, this leads to director angle solutions that are uniform everywhere with $\theta \equiv \theta_{\mathrm{NS}} = \theta_{\mathrm{GN}}$. However, for antagonistic anchoring, this will lead to distorted director solutions with $\theta_{\mathrm{NS}} \neq \theta_{\mathrm{GN}}$, except for close to the contact lines (i.e. near to $x = \pm 1$), where there are boundary layers, namely a narrow reorientational boundary layer in which elastic effects become significant and $\theta_{\mathrm{NS}} \to \theta_{\mathrm{GN}}$, and a second narrow uniform boundary layer in which $\theta \equiv \theta_{\mathrm{NS}} = \theta_{\mathrm{GN}}$. In the present thin-film limit, dimensional values introduced in Section 6.1.1 indicate that the most physically realistic limits to consider are $K \simeq |C_{\mathrm{NS}}|, |C_{\mathrm{GN}}|$ and $K \gg |C_{\mathrm{NS}}|, |C_{\mathrm{GN}}|$.

6.2 Uniform director solutions

The system (6.11)–(6.13) and (6.24)–(6.26) has uniform director solutions for all values of C_{NS}, C_{GN} and K, given by

$$\theta_{\mathrm{NS}} = \theta_{\mathrm{GN}} \equiv \frac{m\pi}{2}, \quad h = h_{\mathrm{iso}}(x), \quad \text{and} \quad p_0 = p_{\mathrm{I}}, \tag{6.27}$$

so that $\theta \equiv m\pi/2$, where m is any integer, and h_{iso} and p_{I} are the solutions for the height and for the Lagrange multiplier for an isotropic ridge given by (6.19), respectively. In particular, the height at the middle of the ridge and contact angle are $h_{\mathrm{m}} = h(0) = 3/4$ and $\beta = -h_x(1) = 3/2$, respectively. We note that these solutions are independent of C_{NS}, C_{GN}, and K; however, the second-order energy (6.17) of these solutions depends on C_{NS} and C_{GN} and is given by

$$\Delta E = \frac{3}{4} + \frac{1}{2}\left(C_{\mathrm{NS}} + C_{\mathrm{GN}}\right)\cos m\pi. \tag{6.28}$$

Inspection of (6.28) shows that a uniform homeotropic solution, which we call "the H solution", with $\theta \equiv \theta_{\mathrm{NS}} = \theta_{\mathrm{GN}} \equiv \pi/2$ (i.e. odd values of m) and hence $\boldsymbol{n} = \hat{\boldsymbol{z}}$, is energetically preferred when $C_{\mathrm{NS}} + C_{\mathrm{GN}} > 0$, and a uniform planar solution, which we call "the P solution", with $\theta \equiv \theta_{\mathrm{NS}} = \theta_{\mathrm{GN}} \equiv 0$ (i.e. even values of m) and hence $\boldsymbol{n} = \hat{\boldsymbol{x}}$, is energetically preferred when $C_{\mathrm{NS}} + C_{\mathrm{GN}} < 0$. When $C_{\mathrm{NS}} + C_{\mathrm{GN}} > 0$, either the anchoring is non-antagonistic with homeotropic anchoring, or the anchoring is antagonistic with the homeotropic anchoring being the strongest, and when $C_{\mathrm{NS}} + C_{\mathrm{GN}} < 0$, either the anchoring is non-antagonistic with planar anchoring, or the anchoring is antagonistic with the planar anchoring being the strongest.

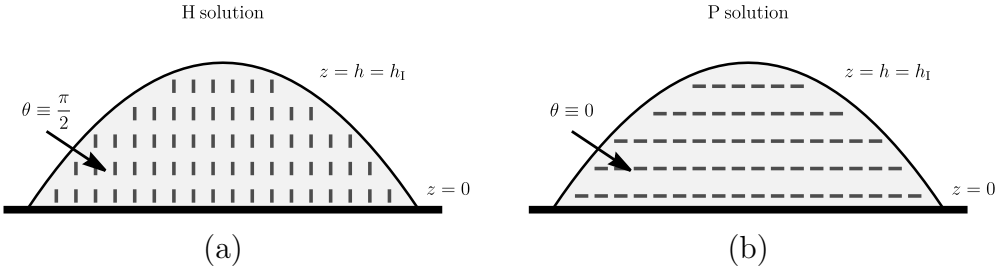

Figure 6.3: Sketches of (a) the H solution and (b) the P solution. The director field $\boldsymbol{n}$ is indicated by the solid grey rods with $\boldsymbol{n} = \hat{\boldsymbol{z}}$ in (a) and $\boldsymbol{n} = \hat{\boldsymbol{x}}$ in (b).

From (6.28) the second-order energies of the H and P solutions are given by

$$\Delta E_{\mathrm{H}} = \frac{3}{4} - \frac{1}{2}\left(C_{\mathrm{NS}} + C_{\mathrm{GN}}\right) \quad \text{and} \quad \Delta E_{\mathrm{P}} = \frac{3}{4} + \frac{1}{2}\left(C_{\mathrm{NS}} + C_{\mathrm{GN}}\right), \tag{6.29}$$

respectively. Figure 6.3(a) and (b) show sketches of the H solution and P solution, respectively. As the director is uniform everywhere for these solutions, the director angle in the vicinity of the contact lines is determined by the interface with the strongest anchoring, namely $\theta = \pi/2$ when $C_{\mathrm{NS}} + C_{\mathrm{GN}} > 0$ and $\theta = 0$ when $C_{\mathrm{NS}} + C_{\mathrm{GN}} < 0$.

6.3 Distorted director solutions

In addition to the H and P solutions, which are solutions for all values of C_{NS}, C_{GN} and K, for certain values of C_{NS}, C_{GN} and K there can also be solutions of the system (6.11)–(6.13) and (6.24)–(6.26) with $\theta_{\mathrm{NS}} \neq \theta_{\mathrm{GN}}$ in which the director is distorted, and therefore the system has non-unique solutions. For these distorted director solutions, the balance-of-couple conditions (6.11) and (6.12) can be combined and rearranged into the form

$$\frac{h_{\mathrm{c}}}{h} = f(\theta_{\mathrm{NS}}, \theta_{\mathrm{GN}}) \quad \text{for} \quad \theta_{\mathrm{NS}} \neq \theta_{\mathrm{GN}}. \tag{6.30}$$

In (6.30), h_c is the Jenkins–Barratt–Barbero–Barberi critical thickness [9, 102] discussed in Section 1.7.4, hereafter simply referred to as "the critical thickness" for brevity, given by

$$h_c = K\left(\frac{1}{C_{NS}} + \frac{1}{C_{GN}}\right), \tag{6.31}$$

and the function $f(\theta_{NS}, \theta_{GN})$ is given by

$$f(\theta_{NS}, \theta_{GN}) = \frac{\sin 2\theta_{NS} - \sin 2\theta_{GN}}{2\left(\theta_{NS} - \theta_{GN}\right)}, \tag{6.32}$$

which, using the mean value theorem, lies in the range $|f(\theta_{NS}, \theta_{GN})| < 1$ for $\theta_{NS} \neq \theta_{GN}$. We note that although h_c is referred to as a thickness it can be positive, negative or zero. In particular, inspection of (6.31) shows that for antagonistic anchoring, if homeotropic alignment is stronger (i.e. $C_{NS} > |C_{GN}| > 0$ or $C_{GN} > |C_{NS}| > 0$) then $h_c < 0$, if planar alignment is stronger (i.e. $C_{NS} < -|C_{GN}| < 0$ or $C_{GN} < -|C_{NS}| < 0$) then $h_c > 0$, and if homeotropic and planar alignment are of equal strength (i.e. $C_{NS} = -C_{GN}$) then $h_c = 0$. Similarly, for non-antagonistic anchoring, if the preferred director alignments are homeotropic (i.e. $C_{NS} > 0$ and $C_{GN} > 0$) then $h_c > 0$, and if the preferred director alignments are planar (i.e. $C_{NS} < 0$ and $C_{GN} < 0$) then $h_c < 0$.

Equation (6.30) determines the values of the critical thickness h_c, and therefore values of C_{NS}, C_{GN} and K, for which distorted director solutions are possible. In particular, since $|f(\theta_{NS}, \theta_{GN})| < 1$ then by (6.30), $h > |h_c|$ provided that $\theta_{NS} \neq \theta_{GN}$. Therefore, the director can only be distorted in the z-direction, i.e. have a solution with $\theta_{NS} \neq \theta_{GN}$, at positions x for which $h > |h_c|$. Conversely, at positions x for which $h \leq |h_c|$ the director can only be uniform in the z-direction, i.e. with $\theta \equiv \theta_{NS} = \theta_{GN} = m\pi/2$. Consequently, when $h \leq |h_c|$ for all $0 \leq x \leq 1$, the director is uniform everywhere and the solution is either the H solution or

the P solution, given by (6.27). When $h > |h_c|$ at $x = 0$, either the solution for the director is uniform in an edge region $x_c \leq x \leq 1$, where $x = x_c$ is the critical position at which $h(x_c) = |h_c|$, and distorted in a central region $0 \leq x < x_c$ in which $h > |h_c|$ and $\theta = (\theta_{GN} - \theta_{NS})z/h + \theta_{NS}$ or the solution for the is uniform everywhere, i.e. the H solution or the P solution. We call distorted director solutions with a homeotropic edge region "D_H solutions" and distorted director solutions with a planar edge region "D_P solutions". In summary, D_H and D_P solutions are given by

$$\theta = \begin{cases} (\theta_{GN} - \theta_{NS})\,\dfrac{z}{h} + \theta_{NS} & \text{for} \quad 0 \leq x < x_c, \\ \dfrac{m\pi}{2} & \text{for} \quad x_c \leq x \leq 1, \end{cases} \tag{6.33}$$

where m is an odd integer for D_H solutions and m is an even integer for D_P solutions.

In the edge region, the nematic Young–Laplace equation (6.13) reduces to $h_{xx} = -p_0$, which may be integrated with respect to x using the contact line condition (6.24) and $h(x_c) = |h_c|$ to yield the height of the ridge h in terms of two as-yet-unknown quantities p_0 and x_c, namely

$$h = (1 - x)\left[\frac{p_0}{2}(x - x_c) + \frac{|h_c|}{1 - x_c}\right] \quad \text{for} \quad x_c \leq x \leq 1, \tag{6.34}$$

i.e. in the edge region h is a quadratic function of x. In the limit $x_c \to 0^+$, the solution (6.34) must satisfy the symmetry and regularity condition (6.25) and the area constraint (6.26), which yield $|h_c| = p_0/2$ and $p_0 = p_I = 3/2$, respectively, and hence as $x_c \to 0^+$ then $h \to h_{iso}$ and $|h_c| \to 3/4$, where h_{iso} is given by (6.19). In particular, in the limit $x_c \to 0^+$ the edge region occupies the entire ridge and D_H and D_P solutions transition to the H and P solutions, respectively.

The second-order energy ΔE for D_H and D_P solutions can be expressed using

(6.17), (6.18), (6.33) and (6.34), as

$$\Delta E = \int_0^{x_c} \left[K\frac{(\theta_{GN}-\theta_{NS})^2}{h} + h_x^2 + \frac{C_{NS}}{2}\cos 2\theta_{NS} + \frac{C_{GN}}{2}\cos 2\theta_{GN} \right] \mathrm{d}x + \frac{C_{NS}+C_{GN}}{2}(1-x_c)\cos m\pi + \frac{h_c^2}{1-x_c} + \frac{p_0^2}{12}(1-x_c)^3. \quad (6.35)$$

Since the director angle in the edge region enters (6.35) only through the term involving $C_{NS}+C_{GN}$, D_H solutions (i.e. odd m) are energetically preferred to D_P solutions (i.e. even m) when $C_{NS}+C_{GN}>0$ and hence when $h_c<0$, and D_P solutions are energetically preferred to D_H solutions when $C_{NS}+C_{GN}<0$ and hence when $h_c>0$. Therefore, similar to the H and P solutions discussed in Section 6.2, for D_H and D_P solutions, the director angle in the vicinity of the contact lines is determined by the interface with the strongest anchoring, namely $\theta=\pi/2$ at $x=1$ when $C_{NS}+C_{GN}>0$ and $\theta=0$ at $x=1$ when $C_{NS}+C_{GN}<0$.

In general, in the central region, the director angles θ_{NS} and θ_{GN}, and the height of the ridge h must be determined numerically. We note that a parametric solution to the system (6.11)–(6.13) and (6.24)–(6.26) is available; however, the practical value of this solution is severely limited as it relies on also obtaining a numerical solution of the problem in order to determine if there is a turning point in either θ_{NS} or θ_{GN}. The details of this parametric solution are provided in Appendix C.

A special case of completely distorted director solutions, which we call "D solutions", occur when the anchoring strengths of the nematic–substrate interface and the gas–nematic interface are exactly equal and opposite, i.e. when $C_{GN}=-C_{NS}$, and hence the critical thickness is zero, i.e. $h_c=0$. In this special case the central region occupies the entire ridge and the director is distorted everywhere, i.e. $\theta_{NS}\neq\theta_{GN}$ for $0\leq x<1$. We note that further analytical progress can be made asymptotically for D solutions in the distinguished limits $C_{GN}=-C_{NS}\to 0$

and $C_{\mathrm{GN}} = -C_{\mathrm{NS}} \to \infty$ (see Appendix D for more details).

6.4 Solutions for the director angles and height of the ridge

We now proceed to solve the system (6.11)–(6.13) and (6.24)–(6.26) numerically and determine the regions of parameter space in which the possible solutions discussed above are energetically preferred. The numerical procedure used to solve the system (6.11)–(6.13) and (6.24)–(6.26) used MATLAB's stiff differential-algebraic equation solver *ode15s* [142] (for more detail see Appendix B). Representative numerical solutions for θ_{NS} and θ_{GN} (Figure 6.4) and for the height of the ridge h and the director field $\boldsymbol{n}$ (Figure 6.5) are plotted in Figures 6.4 and 6.5, respectively, for $K = 1$, with homeotropic anchoring on the gas–nematic interface for various values of $C_{\mathrm{GN}} > 0$ and planar anchoring on the nematic–substrate interface for various values of $C_{\mathrm{NS}} < 0$. Figure 6.4(a) and Figure 6.5(a) illustrate that when the planar anchoring strength of the nematic–substrate interface is stronger than the homeotropic anchoring strength of the gas–nematic interface (specifically in the case when $C_{\mathrm{NS}} = -4.75$ and $C_{\mathrm{GN}} = 0.75$), the P solution is obtained. Figure 6.4(b)–(d) and Figure 6.5(b)–(d) show that when the anchoring strengths are closer in magnitude with the planar anchoring being the stronger of the two (specifically in the cases when $C_{\mathrm{NS}} = -4.25$ and $C_{\mathrm{GN}} = 1.25$, $C_{\mathrm{NS}} = -3.5$ and $C_{\mathrm{GN}} = 2$, and $C_{\mathrm{NS}} = -3$ and $C_{\mathrm{GN}} = 2.5$), $\mathrm{D_P}$ solutions are obtained. We note that for the $\mathrm{D_P}$ solution shown in Figure 6.4(b) in the central region both θ_{NS} and θ_{GN} are monotonic functions of x; whereas, for the $\mathrm{D_P}$ solutions shown in Figure 6.4(c) and (d) θ_{NS} is monotonic but θ_{GN} is non-monotonic. In Figure 6.4(e) and Figure 6.5(e), when the anchoring strength of the nematic–substrate interface and gas–nematic interface are equal and opposite

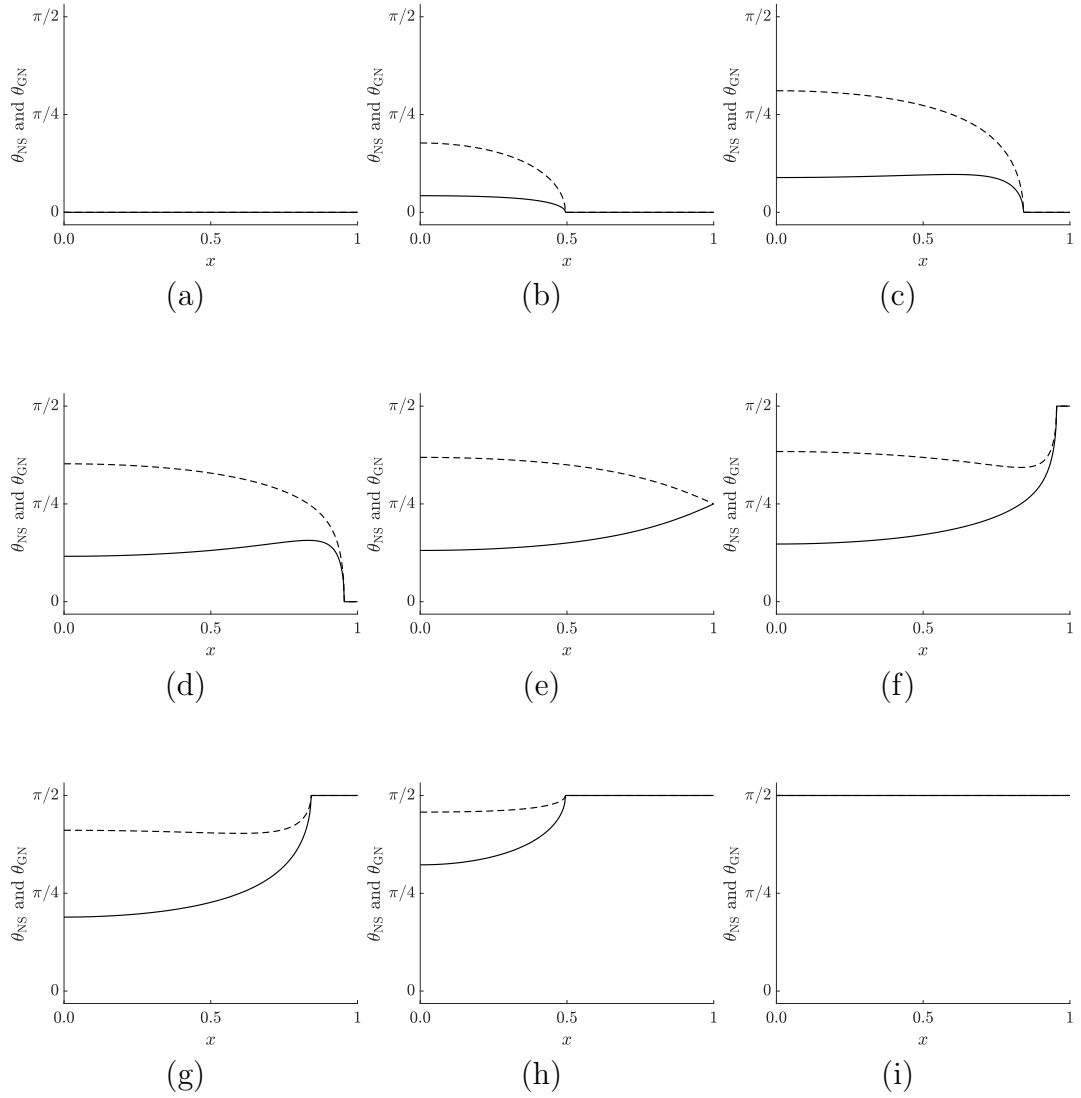

Figure 6.4: Representative numerical solutions for the director angle on the nematic–substrate interface θ_{NS} (solid line) and the gas–nematic interface θ_{GN} (dashed line) for $K = 1$, with homeotropic anchoring on the gas–nematic interface for $C_{\mathrm{GN}} = C_{\mathrm{NS}} + 5.5 > 0$, and planar anchoring on the nematic–substrate interface for (a) $C_{\mathrm{NS}} = -4.75$, (b) $C_{\mathrm{NS}} = -4.25$, (c) $C_{\mathrm{NS}} = -3.5$, (d) $C_{\mathrm{NS}} = -3$, (e) $C_{\mathrm{NS}} = -2.75$, (f) $C_{\mathrm{NS}} = -2.5$, (g) $C_{\mathrm{NS}} = -2$, (h) $C_{\mathrm{NS}} = -1.25$, and (i) $C_{\mathrm{NS}} = -0.75$.

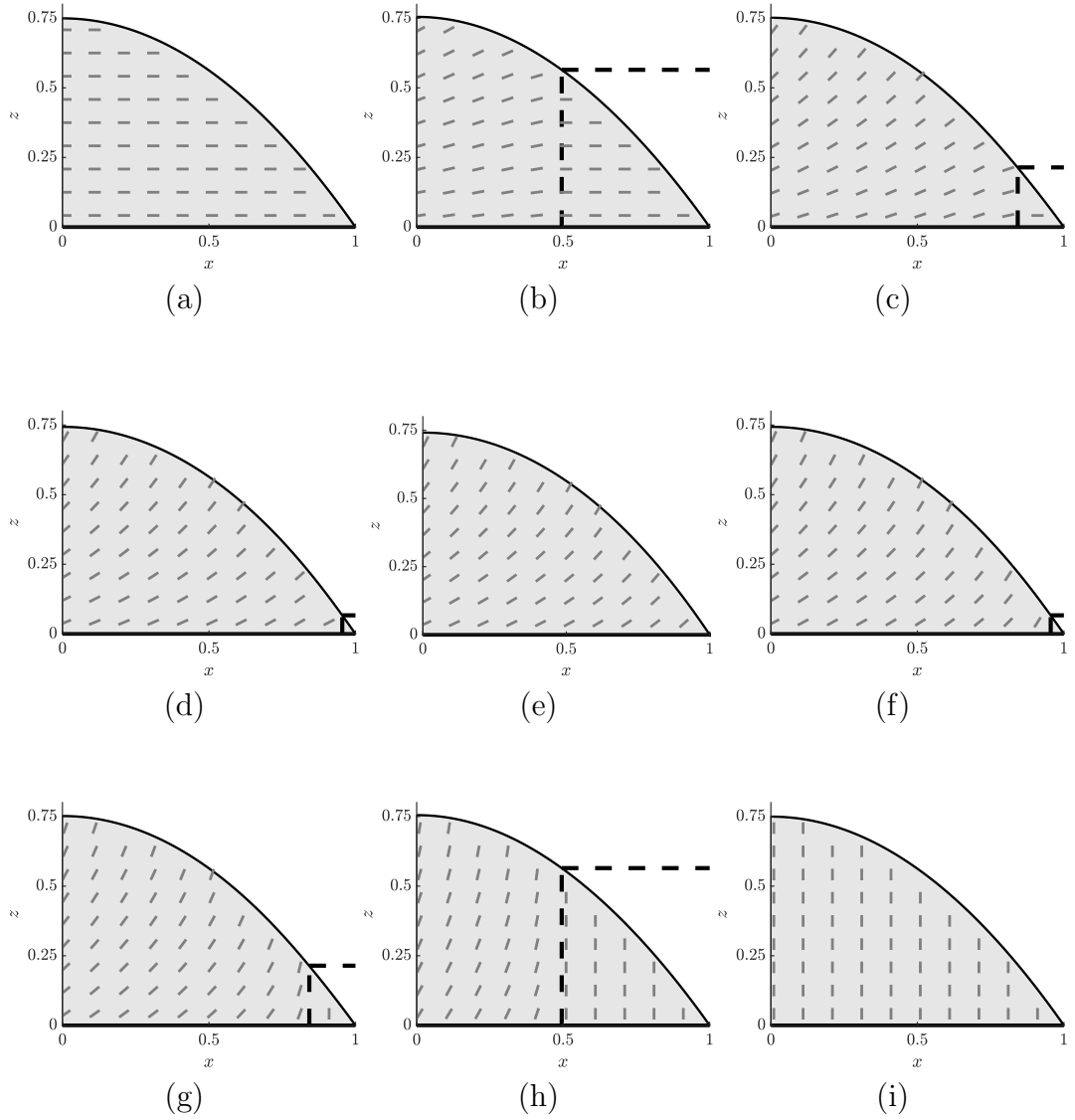

Figure 6.5: Representative numerical solutions for the height of the ridge h (solid line bounding the grey region) and the director field $\boldsymbol{n}$ (grey rods) for $K = 1$, with homeotropic anchoring on the gas–nematic interface for $C_{\mathrm{GN}} = C_{\mathrm{NS}} + 5.5 > 0$, and planar anchoring on the nematic–substrate interface for (a) $C_{\mathrm{NS}} = -4.75$, (b) $C_{\mathrm{NS}} = -4.25$, (c) $C_{\mathrm{NS}} = -3.5$, (d) $C_{\mathrm{NS}} = -3$, (e) $C_{\mathrm{NS}} = -2.75$, (f) $C_{\mathrm{NS}} = -2.5$, (g) $C_{\mathrm{NS}} = -2$, (h) $C_{\mathrm{NS}} = -1.25$, and (i) $C_{\mathrm{NS}} = -0.75$. The critical thickness $z = h(x_{\mathrm{c}}) = |h_{\mathrm{c}}|$ and the critical position $x = x_{\mathrm{c}}$ are shown by dashed lines.

(specifically $C_{\mathrm{GN}} = -C_{\mathrm{NS}} = 2.75$), a D solution is obtained, in which θ_{NS} and θ_{GN} are symmetric about $\pi/4$. Figure 6.4(f)–(h) and Figure 6.5(f)–(h) show that when the anchoring strengths are closer in magnitude with the homeotropic anchoring being the stronger of the two (specifically in the cases when $C_{\mathrm{NS}} = -2.5$ and $C_{\mathrm{GN}} = 3$, $C_{\mathrm{NS}} = -2$ and $C_{\mathrm{GN}} = 3.5$, and $C_{\mathrm{NS}} = -1.25$ and $C_{\mathrm{GN}} = 4.25$), $\mathrm{D_H}$ solutions are obtained. Much like the $\mathrm{D_P}$ solutions discussed above, for the $\mathrm{D_H}$ solution shown in Figure 6.4(f), both θ_{NS} and θ_{GN} are monotonic functions of x; whereas, for the $\mathrm{D_H}$ solutions shown in Figure 6.4(g) and (h), θ_{NS} is non-monotonic but θ_{GN} is monotonic. Figure 6.4(i) and Figure 6.5(i) illustrate that when the homeotropic anchoring strength of the gas–nematic interface is stronger than the planar anchoring strength of the nematic–substrate (specifically in the case when $C_{\mathrm{NS}} = -0.75$ and $C_{\mathrm{GN}} = 4.75$), the H solution is obtained.

Although there is some variation in the height of the ridge h evident in Figure 6.5, we note that for the anchoring strengths shown in Figures 6.4 and 6.5, h does not vary greatly from $h = h_{\mathrm{iso}}$. In particular, the maximum difference in the magnitude of h and $h = h_{\mathrm{iso}}$ for the solutions shown in Figures 6.4 and 6.5 is $\max|h - h_{\mathrm{iso}}| \simeq 0.009$ for the D solution shown in Figure 6.4(e) and Figure 6.5(e). We note that for larger anchoring strengths than those used in Figures 6.4 and 6.5 there is a greater variation of h from $h = h_{\mathrm{iso}}$, which we will discuss in Section 6.7.

Some of the solutions presented in Figures 6.4 and 6.5 are related to other solutions presented in Figures 6.4 and 6.5 by (6.20)–(6.22). In particular, using (6.22) on the solutions shown in Figure 6.4(i), (h), (g), and (f), we obtain the solutions shown in Figure 6.4(a), (b), (c), and (d).

6.5 Energetically preferred solutions

6.5.1 Antagonistic anchoring

For antagonistic anchoring, both distorted director solutions (i.e. $\mathrm{D_H}$, $\mathrm{D_P}$ and D solutions) and the uniform director solutions (i.e. the H and P solutions) are possible solutions to the system (6.11)–(6.13) and (6.24)–(6.26). To determine which solutions have the lowest second-order energy and are therefore the energetically preferred solutions, we now compare the second-order energy ΔE, given by (6.17) and (6.18), of the solutions shown in Figures 6.4 and 6.5 with the second-order energy of the H and P solutions, namely ΔE_{H} and ΔE_{P}. The $\mathrm{D_H}$ and $\mathrm{D_P}$ solutions shown in Figure 6.4(b) and (h), (c) and (g), and (d) and (f) have equal second-order energy given by $\Delta E \simeq -0.760$, $\Delta E \simeq -0.248$, and $\Delta E \simeq -0.077$, respectively. For each of these $\mathrm{D_H}$ and $\mathrm{D_P}$ solutions, ΔE is less than ΔE_{H} and ΔE_{P} for the same parameter values. Therefore the $\mathrm{D_H}$ and $\mathrm{D_P}$ solutions shown in Figure 6.4(b)–(d) and Figure 6.4(f)–(h), respectively, are energetically preferred to the H and P solutions. The D solution shown in Figure 6.4(e) has second-order energy given by $\Delta E \simeq -0.050$, which is less than ΔE_{H} and ΔE_{P}. Therefore the D solution shown in Figure 6.4(e) is energetically preferred to the H and P solutions.

As previously mentioned, further analytical progress can be made asymptotically for D solutions in the distinguished limit $C_{\mathrm{GN}} = -C_{\mathrm{NS}} \to 0$. In particular, in the limit $C_{\mathrm{GN}} = -C_{\mathrm{NS}} \to 0$, the second-order energy of D solutions is given by $\Delta E \simeq 3/4 - C_{\mathrm{GN}}^2/8K$ (see Appendix D for more details), which is always less than the second-order energy of the H and P solutions (6.29) with $C_{\mathrm{GN}} = -C_{\mathrm{NS}}$, namely $\Delta E_{\mathrm{H}} = \Delta E_{\mathrm{P}} = 3/4$, and therefore in this limit D solutions are energetically preferred to the H and P solutions. In fact, extensive numerical investigations, covering a range of parameters values including $10^{-1} \leq K \leq 10^2$, $|C_{\mathrm{NS}}| \leq 10^2$, $|C_{\mathrm{GN}}| \leq 10^2$, strongly suggest that for antagonistic anchoring, dis-

torted director solutions (i.e. D_H, D_P and D solutions) are of lower energy than the uniform director solutions (i.e. the H and P solutions) when $|h_c| < 3/4$. As a consequence, the energetically preferred solutions for antagonistic anchoring can be expressed in terms of the critical thickness h_c as follows: H, D_H, D, D_P and P solutions are energetically preferred for $h_c \leq -3/4$, $-3/4 < h_c < 0$, $h_c = 0$, $0 < h_c < 3/4$, and $h_c \geq 3/4$, respectively. Figure 6.6 shows a schematic summary of the energetically preferred solutions for antagonistic anchoring in terms of the critical thickness h_c.

6.5.2 Non-antagonistic anchoring

For non-antagonistic anchoring, distorted director solutions are possible when $|h_c| < 3/4$; however, inspection of the second-order energy ΔE, given by (6.17) and (6.18), for distorted director solutions with non-antagonistic anchoring show that $E_{iso} \geq 3/4$, $E_{elast} > 0$, $E_{NS} > -|C_{NS}|/2$, and $E_{GN} > -|C_{GN}|/2$, and therefore either $\Delta E > \Delta E_H$ or $\Delta E > \Delta E_P$ for these solutions. Hence these distorted director solutions are never energetically preferred, and so we will not discuss them further here; however, we note that similar high-energy distorted director solutions in a static layer of nematic of uniform thickness bounded between two parallel substrates with non-antagonistic anchoring has been studied previously (for more details, see Davidson [44]).

6.6 Anchoring-strength parameter plane

The energetically preferred solutions summarised in Figure 6.6 can be presented in a single anchoring-strength parameter plane (i.e. a C_{NS}–C_{GN} parameter plane) as shown in Figure 6.7 in the particular case of $K = 1$. As we will discuss below, this figure would be qualitatively similar for other values of K. The parame-

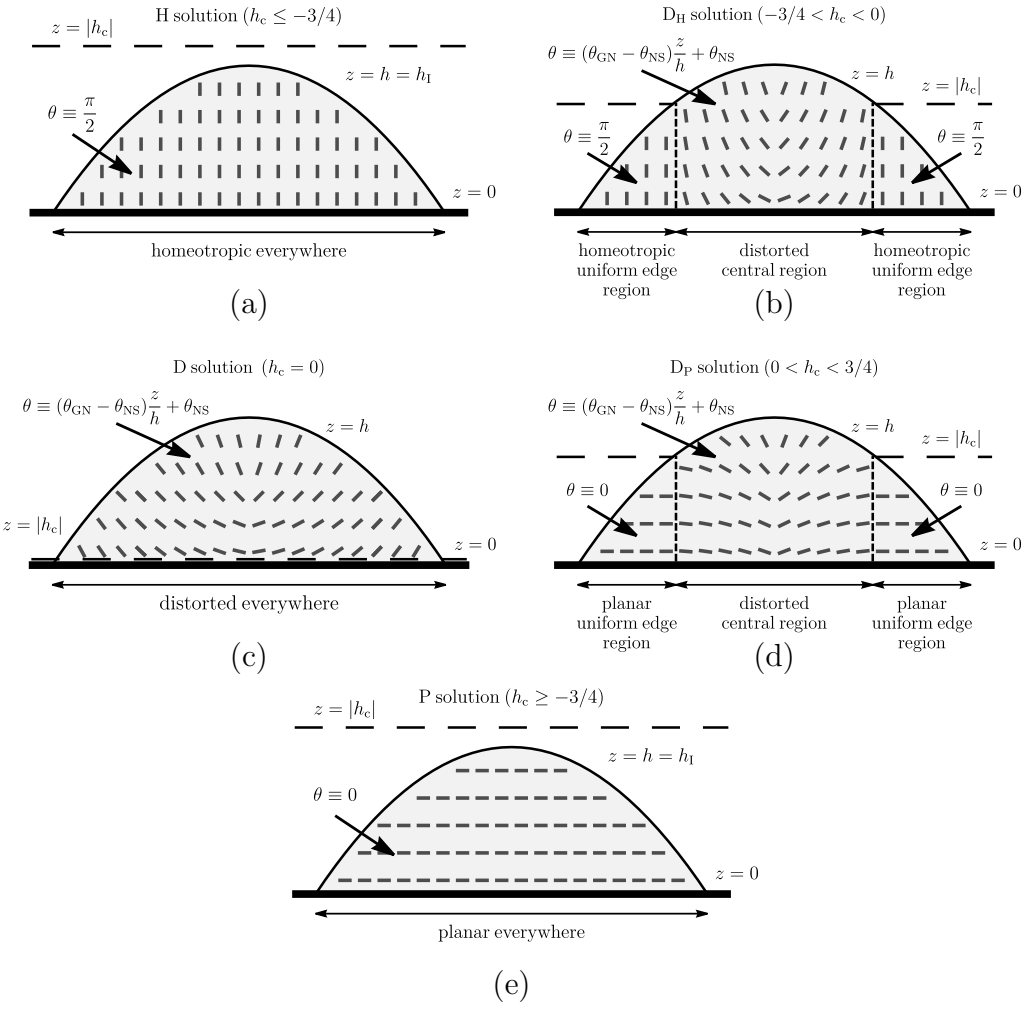

Figure 6.6: Schematic summary of the energetically preferred solutions for antagonistic anchoring in terms of the critical thickness h_c. Sketches of (a) the H solution ($h_c \leq -3/4$), (b) a D_H solution ($-3/4 < h_c < 0$), (c) a D solution ($h_c = 0$), (d) a D_P solution ($0 < h_c < 3/4$), and (e) the P solution ($h_c \geq 3/4$) are shown, where the director field $\boldsymbol{n}$ is indicated by the solid grey rods. The magnitude of the critical thickness $|h_c|$ and the critical position x_c are shown by the horizontal and vertical dashed lines at $z = |h_c|$ and $x = x_c$, respectively.

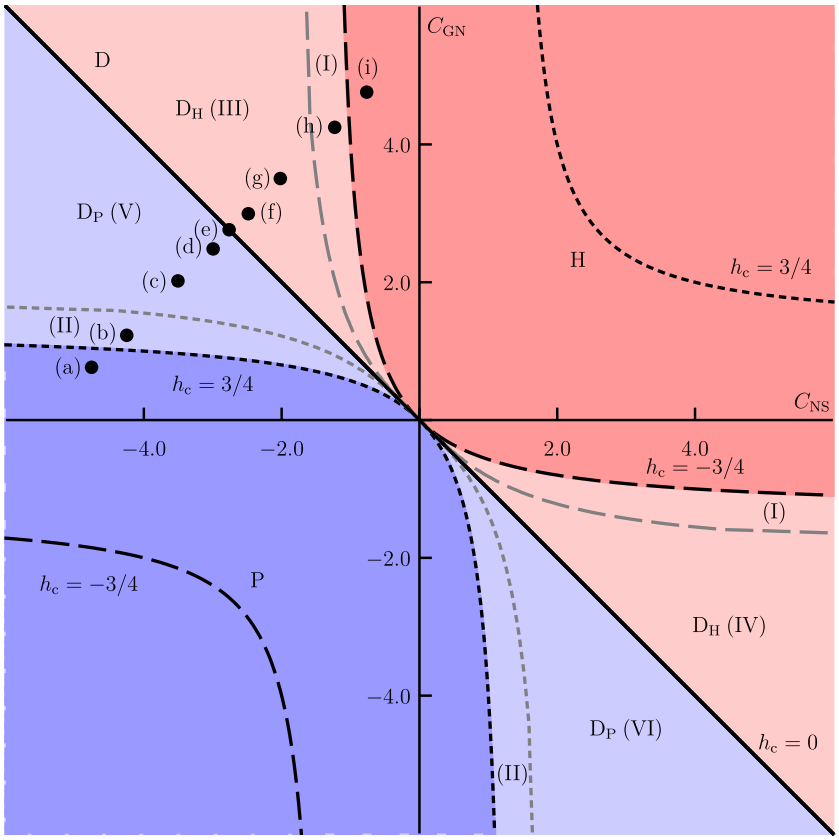

Figure 6.7: The C_{NS}–C_{GN} parameter plane for $K = 1$. Regions of the parameter plane where the H solution (shown in dark red), the P solution (shown in dark blue), $\mathrm{D_P}$ solutions (shown in light blue), and $\mathrm{D_H}$ solutions (shown in light red) are energetically preferred are labelled. D solutions are energetically preferred along the solid black line corresponding to $h_c = 0$, the black dashed line corresponds to $h_c = -3/4$, the black dotted line corresponds to $h_c = 3/4$, and the solutions shown in Figures 6.4 and 6.5 are labelled (a)–(i) and indicated by solid points (•). The dashed grey, dotted grey, and solid black lines separate the regions (I) and (II) in which both θ_{NS} and θ_{GN} are monotonic functions of x, and the regions (III)–(VI) in which one of θ_{NS} and θ_{GN} is a monotonic function of x and the other is a non-monotonic function of x, as described in the text.

ter plane contains three curves separating the regions of energetically preferred solutions: the solid black line on which $h_c = 0$ corresponds to D solutions, the dashed line on which $h_c = -3/4$ separates the region in which the H solution is energetically preferred from the region in which D_H solutions are energetically preferred, and the dotted line on which $h_c = 3/4$ separates the region in which the P solution is energetically preferred from the region in which D_P solutions are energetically preferred. The solutions shown Figures 6.4 and 6.5 are labelled (a)–(i) and indicated by solid points on the parameter plane. Using (6.31), the curves on which $h_c = 3/4$ and $h_c = -3/4$ are given in terms of the parameters C_{NS}, C_{GN} and K by

$$C_{GN} = \frac{4KC_{NS}}{3C_{NS} - 4K} \tag{6.36}$$

and

$$C_{GN} = -\frac{4KC_{NS}}{3C_{NS} + 4K}, \tag{6.37}$$

respectively. In the limit of $C_{NS} \to \infty$ the curves (6.36) and (6.37) approach $C_{GN} = 4K/3$ and $C_{GN} = -4K/3$ from above, respectively, and in the limit of $C_{NS} \to -\infty$ they approach $C_{GN} = 4K/3$ and $C_{GN} = -4K/3$ from below, respectively. In particular, Figure 6.7 shows that for $C_{NS} > 4K/3$ or $C_{GN} > 4K/3$ the planar P solution is never energetically preferred and, similarly, for $C_{NS} < -4K/3$ or $C_{GN} < -4K/3$ the homeotropic H solution is never energetically preferred. This result may be important for industrial applications involving pinned nematic ridges, where uniform homeotropic or planar director alignment (i.e. the H or P solutions) could be eliminated by selecting the anchoring of the nematic–substrate ($i = NS$) and/or the gas–nematic ($i = GN$) interfaces to be $|C_i| > 4K/3$.

As K is varied, the curves on which $h_c = -3/4$ and $h_c = 3/4$, given by (6.36) and (6.37), vary; however, the qualitative behaviour shown in Figure 6.7 remains the same. In particular, for weak elastic effects $K \ll 1$, the curves on which $h_c = \pm 3/4$ approach the axes $C_{NS} = 0$ and $C_{GN} = 0$, showing that D_H and D_P solutions are energetically preferred for all situations with antagonistic anchoring when elastic effects are weak. For strong elastic effects $K \gg 1$, the curves on which $h_c = \pm 3/4$ approach the straight line $C_{GN} = -C_{NS}$, showing that the H and P solutions are energetically preferred for all situations with antagonistic anchoring when elastic effects are strong.

In the top right and bottom left quadrants of Figure 6.7 which correspond to non-antagonistic anchoring, i.e. where $C_{NS}C_{GN} > 0$, the P solution and the H solution are energetically preferred for all values K, respectively. In these quadrants we have indicated the two regions in which $|h_c| < 3/4$, i.e. above the dotted line in the top right quadrant and below the dashed line in bottom left quadrant, in which the distorted director solutions are possible. However, as previously stated, the P solution is always the energetically preferred solution in the bottom left quadrant, and the H solution is always the energetically preferred solution in the top right quadrant.

Figure 6.7 shows six regions, labelled (I)–(VI), which correspond to regions of the parameter plane where either both θ_{NS} and θ_{GN} are monotonic functions of x, or one of θ_{NS} and θ_{GN} is a monotonic function of x and the other is a non-monotonic function of x. In particular, in the regions (I) and (II) shown in Figure 6.7, which are between the dashed black and grey lines and the dotted black and grey lines, respectively, both θ_{NS} and θ_{GN} are monotonic functions of x (as shown in Figure 6.4(b) and (h)). In the regions (III) and (VI) shown in Figure 6.7, which are in the top left quadrant between the solid black and dashed grey lines, and the bottom right quadrant between the dotted grey and solid black

lines, respectively, θ_{NS} is a monotonic function of x and θ_{GN} is a non-monotonic function of x (as shown in Figure 6.4(f) and (g)). In the regions (IV) and (V) shown in Figure 6.7, which are in the bottom right quadrant between the solid black and dashed grey lines and the top left quadrant between the dotted grey and solid black lines, respectively, θ_{NS} is a non-monotonic function of x and θ_{GN} is a monotonic function of x (as shown in Figure 6.4(c) and (d)). These six regions of the anchoring-strength parameter plane are used as part of the parametric solution discussed in Appendix C.

6.7 Behaviour of the height of the ridge h

As discussed previously, for the H and P solutions, the height of the ridge is given by $h = h_{\mathrm{iso}}$, whereas, for $\mathrm{D_H}$, $\mathrm{D_P}$, and D solutions, h must be obtained numerically. In Figure 6.8, we plot contours of the height at the middle of the ridge h_{m}, the contact angle β, and the critical position x_{c} on the C_{NS}–C_{GN} parameter plane for $K = 1$. In particular, Figure 6.8 shows that h_{m}, β, and x_{c} take the constant values $h_{\mathrm{m}} = 3/4$, $\beta = 3/2$, and $x_{\mathrm{c}} = 0$, respectively, for the H and P solutions.

Figure 6.8(a) and (b) show that for $\mathrm{D_H}$, $\mathrm{D_P}$, and D solutions, h_{m} and β can vary non-monotonically as a function of C_{NS} or C_{GN}. For example, for any D solution in Figure 6.8(a) and (b) which are energetically preferred along the line $C_{\mathrm{GN}} = -C_{\mathrm{NS}}$, upon reducing the magnitude of either C_{NS} or C_{GN}, the D solution transitions to a $\mathrm{D_H}$ or $\mathrm{D_P}$ solution, and there is an initial increase and then a subsequent decrease in h_{m}, accompanied by an initial decrease and then a subsequent increase in β. Continued reductions in the magnitude of either C_{NS} or C_{GN} result in $h_{\mathrm{c}} \geq 3/4$, where a $\mathrm{D_H}$ or $\mathrm{D_P}$ solution transitions to the H solution or the P solution, respectively, with $h_{\mathrm{m}} = 3/4$ and $\beta = 3/2$. Figure 6.8(c) shows that for $\mathrm{D_H}$, $\mathrm{D_P}$ and D solutions, x_{c} varies monotonically as a function of C_{NS} or C_{GN}.

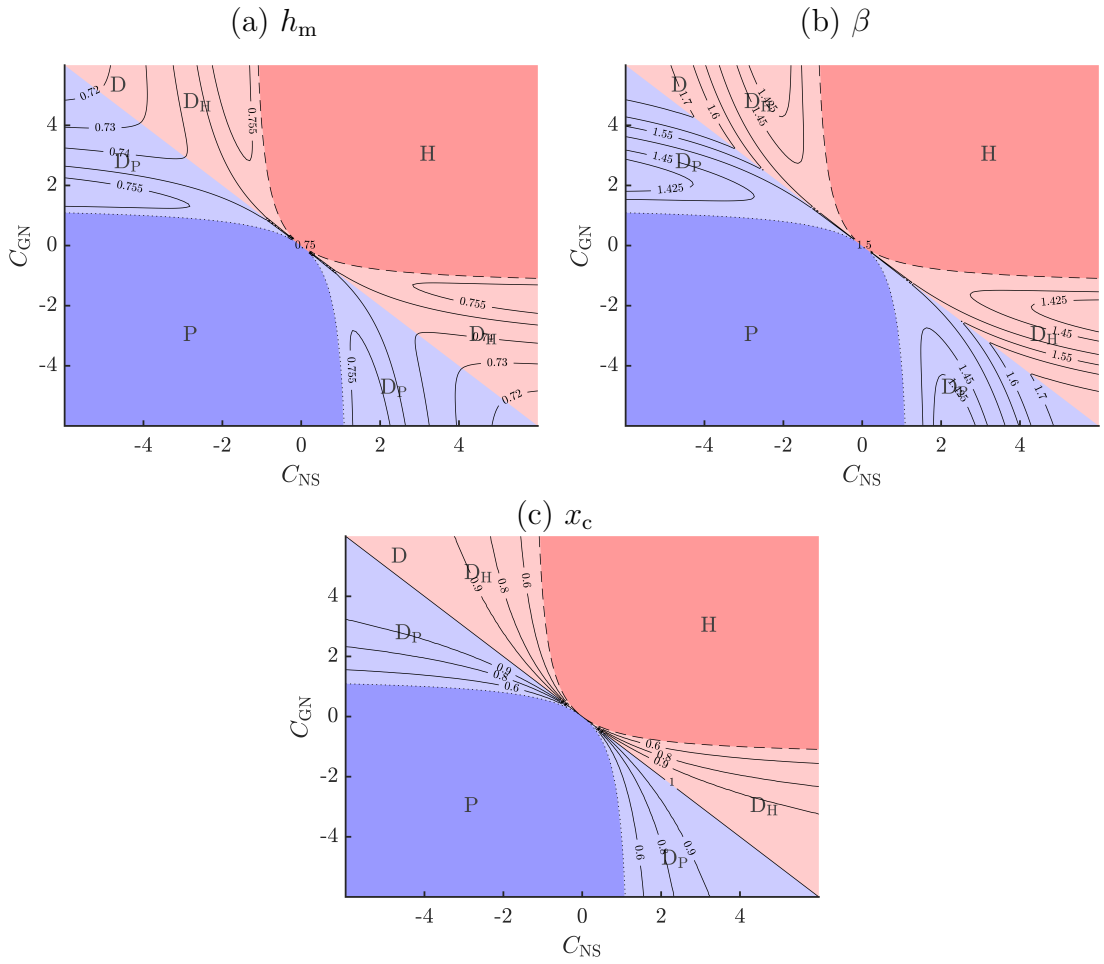

Figure 6.8: Contours of (a) the height at the middle of the ridge h_{m}, (b) the contact angle β, and (c) the critical position x_{c} obtained from numerical solutions of the system (6.11)–(6.13) and (6.24)–(6.26) plotted on the C_{NS}–C_{GN} parameter plane for $K = 1$. The dotted and dashed curves correspond to the contours $h_{\mathrm{m}} = 3/4$, $\beta = 3/2$, and $x_{\mathrm{c}} = 0$ on which $h_{\mathrm{c}} = 3/4$ and $h_{\mathrm{c}} = -3/4$, respectively. Regions of the C_{NS}–C_{GN} parameter plane are coloured and labelled as described in Figure 6.7.

For example, for any D solution in Figure 6.8(c), upon reducing the magnitude of either C_{NS} or C_{GN}, the D solution transitions to a $\mathrm{D_H}$ or $\mathrm{D_P}$ solution and x_{c} decreases. Continued reductions in the magnitude of either C_{NS} or C_{GN} result in a monotonic decrease in x_{c} from $x_{\mathrm{c}} = 1$ to $x_{\mathrm{c}} = 0$, where a $\mathrm{D_H}$ or $\mathrm{D_P}$ solution transitions to the H solution or the P solution, respectively.

Some of the non-monotonic behaviour of h_{m} and β shown in Figure 6.8(a) and (b) can be explained by considering how the height of the ridge adjusts through changes in h_{m} and β to reduce the elastic energy, which is given in (6.18). Clearly, for $\mathrm{D_H}$ and $\mathrm{D_P}$ solutions, the contribution to the elastic energy from the edge region, where $\theta \equiv \theta_{\mathrm{NS}} = \theta_{\mathrm{GN}}$, is zero, but the contribution to the elastic energy in the central region, where $\theta_{\mathrm{NS}} \neq \theta_{\mathrm{GN}}$, is nonzero. For D solutions, the central region occupies the whole ridge, and close to the contact lines where $h \to 0$, the contribution to the elastic energy is large. In order to reduce this large contribution to the elastic energy, h adjusts accordingly. In particular, h_{m} decreases and β increases, i.e. increasing h close to the contact lines. To illustrate this clearly, an example D solution is plotted in Figure 6.9(a) for $K = 1$ and $C_{\mathrm{NS}} = -C_{\mathrm{GN}} = -100$. As discussed above, upon reducing the magnitude of either C_{NS} or C_{GN} from $C_{\mathrm{NS}} = -C_{\mathrm{GN}}$, a D solution will transition to a $\mathrm{D_H}$ or $\mathrm{D_P}$ solution, and there is an initial increase in h_{m} and an initial decrease in β. This initial adjustment of h can be explained as h adjusting to increase h_{m} to reduce the contribution to the elastic energy in the central region. Because h must obey the area constraint (6.26), the increase in h_{m} is associated with a decrease in β. To illustrate this clearly, an example $\mathrm{D_P}$ solution is plotted in Figure 6.9(b) for $K = 1$, $C_{\mathrm{NS}} = -100$ and $C_{\mathrm{GN}} = 2$. As discussed above, after further reducing the magnitude of either C_{NS} or C_{GN}, there is a subsequent decrease in h_{m} and an increase in β until $h_{\mathrm{m}} = 3/4$ and $\beta = 3/2$, where a $\mathrm{D_H}$ or $\mathrm{D_P}$ solution transitions to the H solution or the P solution, respectively. Explaining these subsequent adjustments of h in terms of just the elastic energy is not possible. Finally,

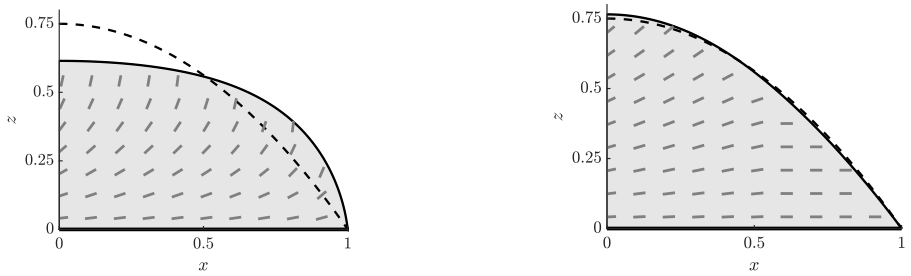

Figure 6.9: Numerical solutions for the height of the ridge h (solid line bounding the grey region) and the director field $\boldsymbol{n}$ (grey rods) are plotted for $K = 1$, with homeotropic anchoring on the gas–nematic interface (a) $C_{\mathrm{GN}} = 100$ and (b) $C_{\mathrm{GN}} = 2$, and with planar anchoring on the nematic–substrate interface $C_{\mathrm{NS}} = -100$. The height for an isotropic ridge $h = h_{\mathrm{iso}} = 3(1 - x^2)/4$ is also shown by the thick dashed line.

we note that the values of the anchoring strengths at which the minimum and maximum values of h_{m} and β occur must be determined numerically.

6.8 Conclusions

Motivated by the recent interest in situations that involve droplets and ridges of nematic, we have analysed the behaviour of a pinned static ridge of nematic resting on an ideal solid substrate in an atmosphere of passive gas. In Section 6.1, we used the general system of governing equations and boundary conditions derived in Chapter 5 in the limit of a small aspect ratio $\epsilon = A/d^2 \ll 1$ to obtain the governing equations for a thin ridge of nematic. When the contact lines of the ridge are pinned the system is given by (6.11)–(6.13) and (6.24)–(6.26) and involves four unknowns: the director angle on the nematic–substrate interface θ_{NS}, the director angle on the gas–nematic interface θ_{GN}, the height of the ridge h, and the Lagrange multiplier p_0 as well as three non-dimensional parameters: the one-constant elastic constant K, the anchoring strength of the nematic–substrate

interface C_{NS}, and anchoring strength of the gas–nematic interface C_{GN}.

In Section 6.2, we described the uniform director solutions of the system (6.11)–(6.13) and (6.24)–(6.26), namely the homeotropic H solution and the planar P solution. In Section 6.3, we described the distorted director solutions of the system (6.11)–(6.13) and (6.24)–(6.26), namely $\mathrm{D_H}$ solutions, which are distorted in a central region and homeotropic in an edge region, $\mathrm{D_P}$ solutions, which are distorted in a central region and planar in an edge region, and D solutions, which are distorted throughout the ridge. These solutions are obtained numerically in Section 6.4. Further extensive numerical investigations, which were discussed in Section 6.5 show that the energetically preferred solutions can be expressed in terms of the critical thickness h_{c}. In particular, as shown in Figures 6.6 and 6.7 for antagonistic anchoring, the H, $\mathrm{D_H}$, D, $\mathrm{D_P}$ and P solutions are energetically preferred for $h_{\mathrm{c}} \leq -3/4$, $-3/4 < h_{\mathrm{c}} < 0$, $h_{\mathrm{c}} = 0$, $0 < h_{\mathrm{c}} < 3/4$ and $h_{\mathrm{c}} \geq 3/4$, respectively. For non-antagonistic anchoring, the H solution is energetically preferred for $C_{\mathrm{NS}} + C_{\mathrm{GN}} > 0$, and the P solution is energetically preferred for $C_{\mathrm{NS}} + C_{\mathrm{GN}} < 0$. In Section 6.7, the behaviour of the height of the ridge h was investigated numerically. In particular, we found that $\mathrm{D_H}$, $\mathrm{D_P}$, and D solutions can have a non-monotonic behaviour as a function of C_{NS} and C_{GN}.

Rather intriguingly, the results obtained in this chapter may provide two alternative means of measuring the anchoring strength of the gas–nematic interface C_{GN}, which, as mentioned in Section 1.7.3 has rarely been measured. Firstly, experimental observation of a planar or homeotropic edge region could allow for a direct measurement of the critical thickness $h(x_{\mathrm{c}}) = |h_{\mathrm{c}}|$, and thus using (6.31) and experimentally determined values of C_{NS} and K, C_{GN} could be estimated. This experiment could be repeated for various values $\epsilon = A/d^2 \ll 1$ to allow repeated measurement of h_{c}. Secondly, experimental measurement of the height at the middle of the ridge h_{m}, the contact angle β, and experimentally determined

values of C_{NS} and K, may provide a method to estimate C_{GN} by using C_{GN} as a fitting parameter between the numerical solutions of the system (6.11)–(6.13) and (6.24)–(6.26) and the experimental measurements of h_{m} and β.

In principle, the results described in this chapter can be used to measure C_{GN} for any ridge of nematic that is thin and has pinned contact lines. One of the only examples in the literature for which both C_{GN} and C_{NS} have been measured is for a ridge of the nematic MBBA surrounded by air on a glass substrate rubbed with paper. For this situation the material parameters can be approximated using $K \simeq 6.75 \times 10^{-12}\,\mathrm{N}$ (obtained from an average of the MBBA splay and bend elastic constants) [201], $C_{\mathrm{GN}} > 4 \times 10^{-4}\,\mathrm{N\,m^{-1}}$ [30,197], and $C_{\mathrm{NS}} \simeq -10^{-7}\,\mathrm{N\,m^{-1}}$ [141, 197], and hence the dimensional critical thickness is given by $h_{\mathrm{c}} = K/C_{\mathrm{NS}} + K/C_{\mathrm{GN}} \simeq -6.75 \times 10^{-4}\,\mathrm{m}$. Specifically, this means that this MBBA ridge the H solution is energetically preferred provided $h \leq |h_{\mathrm{c}}| \simeq 6.75 \times 10^{-4}\,\mathrm{m}$ and a $\mathrm{D_H}$ solution is energetically preferred provided $h > |h_{\mathrm{c}}| \simeq 6.75 \times 10^{-4}\,\mathrm{m}$. Eliminating unwanted distortion within the centre of a nematic ridge may be particularly useful in some practical applications where distortion within the centre of a nematic ridge is unwanted, and a uniform homeotropic orientation is desired, for example, for diffraction gratings [17,23] or perhaps for droplets in the ODF method. Chapter 3 showed that flow-driven reorientation of the nematic molecules during squeezing depended on the anchoring case considered within the droplet. The work presented in this chapter may indicate that controlling the initial director field within the droplets in the ODF method may be possible by selecting thin droplets (with $H \leq |h_{\mathrm{c}}|$) or altering the anchoring of the nematic–substrate interface. However, the degree to which the present results for a nematic ridge apply to nematic droplets is still unclear.

Finally, we note that the present analysis shows that the director alignment in the vicinity of the contact lines is dictated by the interface with the largest mag-

nitude anchoring strength, and in the special case that the anchoring strength of the interfaces are equal and opposite, the director adopts an average orientation between planar and homeotropic at the contact lines, i.e. $\theta = \pi/4$. For example, for the MBBA ridge mentioned above, for which $C_{\mathrm{GN}} > |C_{\mathrm{NS}}| > 0$, the present analysis predicts that the director in the vicinity of the contact lines has homeotropic orientation.

Chapter 7

The equilibrium states and transitions of a ridge of nematic

Motivated by the results of Chapter 6, which predicts that anchoring breaking occurs in the vicinity of the two contact lines for a thin pinned ridge, we now consider a final application of the governing equations derived in Chapter 5. In particular, using just the nematic Young equations (5.42) and (5.43) under the assumption that anchoring breaking occurs in the vicinity of the contact lines, we determine the regions of parameter space for which the equilibrium state is that of partial wetting $\mathbb{P}$, complete wetting $\mathbb{W}$ or complete dewetting $\mathbb{D}$, and the parameter curves on which transitions between these equilibrium states occur.

For an isotropic system, described in Section 1.10.1, the classification of each equilibrium state and the transitions that can occur between them are well known [48,153] and can be obtained by analytically solving the classical isotropic Young–Laplace equation and determining the free energy of each equilibrium state. For a nematic ridge, unlike an isotropic ridge, the free energy of each equilibrium state cannot be determined analytically; however, by comparison with the well-known results for the isotropic ridge, the classification of each equilibrium

state and the transitions that can occur between them are obtained. In particular, in Sections 7.1 and 7.3, we use the nematic Young equations derived in Chapter 5 to determine the continuous and discontinuous transitions between the equilibrium states of complete wetting, partial wetting, and complete dewetting which can occur. Previously, Rey [182] found that discontinuous transitions between partial wetting and complete wetting, and between partial wetting and complete dewetting occur because of weak anchoring forces at the contact lines [182]. However, without the assumption that anchoring breaking occurs in the vicinity of the contact lines, an explicit description of these transitions was not possible. Under this assumption, in Sections 7.1 and 7.3, we find continuous transitions analogous to those that occur in the classical case of an isotropic liquid, a variety of discontinuous transitions, contact-angle hysteresis, and regions of parameter space in which multiple partial wetting states that do not occur in the case of an isotropic liquid exist.

7.1 The nematic Young equations

Analogously to the isotropic system discussed in Section 1.10.1, for the nematic ridge, we can determine the regions of parameter space in which the different equilibrium states exist and the parameter curves at which transitions between these states occur, from just the nematic Young equations (5.42) and (5.43). At first sight, determining these regions of parameter space and parameter curves would appear to involve solving the governing equations for θ in the bulk of the nematic ridge, which would, in turn, involve solving for the ridge height h, the contact line positions $x = d^{\pm}$, and the Lagrange multiplier p_0. However, under the assumption that anchoring breaking occurs in the vicinity of the contact lines, we can make significant progress with just the nematic Young equations (5.42) and (5.43).

7.1.1 The director orientation at the contact lines

At the contact lines the preferred director orientations on the gas–nematic and the nematic–substrate interfaces are, in general, different. Even when the anchoring is non-antagonistic (i.e. either planar or homeotropic anchoring preferred on both interfaces), since the preferred director orientation of both interfaces is measured *relative* to that interface, and the two interfaces meet at the non-zero contact angles $\beta^{\pm}$, the orientations are, in general, not the same. Hence the director cannot, in general, align with the preferred orientations of both interfaces. There are three potential remedies for this: (i) the contact angles are such that the preferred orientations on both interfaces coincide exactly; (ii) there may be defects (disclination lines in this two-dimensional case) at one or both of the contact lines; (iii) the weak anchoring on both interfaces allows anchoring breaking to occur in the vicinity of the contact lines and the director(s) on one or both of the interfaces deviates from the preferred alignment(s) and attains the same orientation on both interfaces.

7.1.1.1 Case (i): The preferred director orientations coincide

Case (i) is a very special case in which the contact angles are such that the preferred director orientations on the two interfaces coincide exactly at the contact lines. When the preferred orientations on the two interfaces are antagonistic, the contact angles must be exactly $\beta^{\pm} = \pi/2$ to allow the director to be tangent to one interface and perpendicular to the other. In particular, if $C_{\mathrm{NS}} < 0$ and $C_{\mathrm{GN}} > 0$ then $\theta = 0$ and $\beta^{\pm} = \pi/2$, and if $C_{\mathrm{NS}} > 0$ and $C_{\mathrm{GN}} < 0$ then $\theta = \pi/2$ and $\beta^{\pm} = \pi/2$. In both of these situations, the nematic Young equations (5.42) and (5.43) both reduce to $\sigma_{\mathrm{GS}} - \sigma_{\mathrm{NS}} = -|C_{\mathrm{NS}}|/4$. When the preferred orientations on the two interfaces are non-antagonistic, the contact angles must be exactly $\beta^{\pm} = 0$ to allow the director to be tangent or perpendicular to both interfaces.

In particular, for planar anchoring on both interfaces $\theta = 0$ and $\beta^{\pm} = 0$, and for homeotropic anchoring on both interfaces $\theta = \pi/2$ and $\beta^{\pm} = 0$, and the nematic Young equations (5.42) and (5.43) reduce to $\sigma_{\mathrm{GS}} - \sigma_{\mathrm{NS}} - \sigma_{\mathrm{GN}} = -(|C_{\mathrm{NS}}| + |C_{\mathrm{GN}}|)/4$. Since this special case is highly unlikely to occur in practice, we do not consider this case any further.

7.1.1.2 Case (ii): Disinclination lines at one or both of the contact lines

As discussed in Section 1.10.2, Rey [183] considered the occurrence of a disclination line at a contact line with infinite planar anchoring on the gas–nematic and nematic–substrate interfaces. Since infinitely-strong anchoring cannot be broken, the director must adopt a splayed configuration (for a full account of splayed director configurations, see Stewart [201]) in the vicinity of the contact line, with a disinclination line located at the contact line [183]. Even for finite anchoring strengths there is still the possibility of disinclination lines forming at one or both of the contact lines; however, in the remainder of this chapter, we assume that the energy associated with anchoring breaking is lower than the energy associated with the formation of a disclination line, and so do not consider this case any further.

7.1.1.3 Case (iii): Anchoring breaking in the vicinity of the contact lines

Having ruled out cases (i) and (ii), we are left with case (iii). In this case the weak anchoring on the interfaces allows anchoring breaking to occur in the vicinity of the contact lines so that the director(s) on one or both of the interfaces deviates from the preferred alignment(s) and attains the same orientation on the two interfaces. In Chapter 5, we found that for a thin pinned ridge, because the

height of the ridge is, by definition, zero at the contact lines, but may exceed the critical thickness elsewhere, the energetically preferred director in the vicinity of the contact line is dictated by the interface with the largest anchoring strength. For an unpinned and non-thin nematic ridge, we also expect that, close to the contact lines, where the ridge height approaches zero and hence the separation between the nematic–substrate and gas–nematic interfaces is always less than the critical thickness, anchoring breaking occurs and the director is dictated by the interface with the largest anchoring strength. Specifically, if the nematic–substrate interface has the stronger anchoring (i.e. if $|C_{\mathrm{NS}}| > |C_{\mathrm{GN}}|$) then the director at the contact lines aligns parallel to the nematic–substrate interface with $\theta = 0$ at $x = d^{\pm}$ in the case of planar anchoring corresponding to $C_{\mathrm{NS}} < 0$ or perpendicular to the nematic–substrate interface with $\theta = \pi/2$ at $x = d^{\pm}$ in the case of homeotropic anchoring corresponding to $C_{\mathrm{NS}} > 0$; we call both of these scenarios "nematic–substrate (NS) dominant anchoring". Correspondingly, if the gas–nematic interface has the stronger anchoring (i.e. if $|C_{\mathrm{GN}}| > |C_{\mathrm{NS}}|$) then the director at the contact lines aligns parallel to the gas–nematic interface with $\theta = \beta^{\pm}$ at $x = d^{\pm}$ in the case of planar anchoring corresponding to $C_{\mathrm{GN}} < 0$ or perpendicular to the gas–nematic interface with $\theta = \beta^{\pm} + \pi/2$ at $x = d^{\pm}$ in the case of homeotropic anchoring corresponding to $C_{\mathrm{GN}} > 0$; we call both of these situations "gas–nematic (GN) dominant anchoring".

There are two special situations in which anchoring breaking cannot occur as described above because the interfaces have either equal anchoring strengths ($C_{\mathrm{NS}} = C_{\mathrm{GN}}$) or equal and opposite anchoring strengths ($C_{\mathrm{NS}} = -C_{\mathrm{GN}}$), which is considered for a thin pinned ridge in Appendix D. In both of these situations, anchoring breaking occurs on both interfaces and the director orientation adopts the average of the preferred orientations [183]. A local energy minimisation in the vicinity of the contact lines, ignoring the contribution of the bulk energy (corresponding to $\partial(\omega_{\mathrm{GN}} + \omega_{\mathrm{NS}})/\partial\theta = 0$ at $x = d^{\pm}$) is used to obtain the director

angle. In particular, when the anchoring strengths of the interfaces are equal and planar anchoring is preferred, the director angles are $\theta = \beta^{\pm}/2$ at $x = d^{\pm}$, in agreement with Rey [183], and when the anchoring strengths of the interfaces are equal and homeotropic anchoring is preferred, the director angles are $\theta = \beta^{\pm}/2 + \pi/2$ at $x = d^{\pm}$. When the anchoring strengths of the interfaces are equal and opposite, the director angles are $\theta = \beta^{\pm}/2 + \pi/4$ or $\theta = \beta^{\pm}/2 - \pi/4$ at $x = d^{\pm}$. This result is in agreement with that obtained for a thin pinned ridge in Appendix D.

Since for an ideal substrate the material properties are the same at the contact lines, anchoring breaking must occur in the same way in the vicinity of the contact lines, and hence the director angles at the two contact lines must be the same. However, as we will show below, in some situations the nematic Young equations (5.42) and (5.43) allow for more than one possible contact angles for the same parameter values, and so $\beta^{\pm}$ do not, in general, have to be the same and so the ridge can be asymmetric. Moreover, the contact angles $\beta^{\pm}$ will necessarily be different if the substrate is non-ideal and the material properties at the two contact lines are different (for example, if the substrate was manufactured so that the values of C_{NS} at $x = d^{\pm}$ were different, or if gradients in the temperature of the gas or adsorption of a surfactant from the gas lead to different values of C_{GN} at $x = d^{\pm}$ [144]). Without loss of generality, we consider only the left-hand contact line, which is described by the nematic Young equation (5.42), and write $\beta^{-} = \beta$ for simplicity. The corresponding results for the right-hand contact line can be obtained in the same way.

7.2 Nematic spreading parameters

For NS-dominant anchoring (for which either $\theta = 0$ or $\theta = \pi/2$) the nematic Young equation (5.42) reduces to a cubic equation for $\cos\beta$, namely either

$$\sigma_{\mathrm{GS}} - \left(\sigma_{\mathrm{NS}} + \tfrac{1}{4}C_{\mathrm{NS}}\right) - \left(\sigma_{\mathrm{GN}} + \tfrac{1}{4}C_{\mathrm{GN}}\right)\cos\beta = -\tfrac{1}{2}C_{\mathrm{GN}}\cos\beta\left(\cos^2\beta - 1\right) \quad (7.1)$$

when $\theta = 0$ or

$$\sigma_{\mathrm{GS}} - \left(\sigma_{\mathrm{NS}} - \tfrac{1}{4}C_{\mathrm{NS}}\right) - \left(\sigma_{\mathrm{GN}} - \tfrac{1}{4}C_{\mathrm{GN}}\right)\cos\beta = \tfrac{1}{2}C_{\mathrm{GN}}\cos\beta\left(\cos^2\beta - 1\right) \quad (7.2)$$

when $\theta = \pi/2$. On the other hand, for GN-dominant anchoring (for which either $\theta = \beta$ or $\theta = \beta + \pi/2$) the nematic Young equation (5.42) reduces to a quadratic equation for $\cos\beta$, namely either

$$\sigma_{\mathrm{GS}} - \left(\sigma_{\mathrm{NS}} + \tfrac{1}{4}C_{\mathrm{NS}}\right) - \left(\sigma_{\mathrm{GN}} + \tfrac{1}{4}C_{\mathrm{GN}}\right)\cos\beta = \tfrac{1}{2}C_{\mathrm{NS}}\left(\cos^2\beta - 1\right) \quad (7.3)$$

when $\theta = \beta$ or

$$\sigma_{\mathrm{GS}} - \left(\sigma_{\mathrm{NS}} - \tfrac{1}{4}C_{\mathrm{NS}}\right) - \left(\sigma_{\mathrm{GN}} - \tfrac{1}{4}C_{\mathrm{GN}}\right)\cos\beta = -\tfrac{1}{2}C_{\mathrm{NS}}\left(\cos^2\beta - 1\right) \quad (7.4)$$

when $\theta = \beta + \pi/2$. Equations (7.1)–(7.4) may each be written in terms of just two parameters as follows. Specifically, (7.1) and (7.2) may be written as

$$S_{\mathrm{N}} + 1 - \cos\beta = -\Delta_{\mathrm{GN}}\cos\beta\left(\cos^2\beta - 1\right), \quad (7.5)$$

while (7.3) and (7.4) may be written as

$$S_{\mathrm{N}} + 1 - \cos\beta = \Delta_{\mathrm{NS}}\left(\cos^2\beta - 1\right), \quad (7.6)$$

where S_{N}, Δ_{NS} and Δ_{GN} are defined by

$$S_{\mathrm{N}} = \frac{4\sigma_{\mathrm{GS}} - (4\sigma_{\mathrm{NS}} - |C_{\mathrm{NS}}|)}{4\sigma_{\mathrm{GN}} - |C_{\mathrm{GN}}|} - 1, \tag{7.7}$$

$$\Delta_{\mathrm{NS}} = \frac{2C_{\mathrm{NS}}}{4\sigma_{\mathrm{GN}} - |C_{\mathrm{GN}}|}, \tag{7.8}$$

$$\Delta_{\mathrm{GN}} = \frac{2C_{\mathrm{GN}}}{4\sigma_{\mathrm{GN}} - |C_{\mathrm{GN}}|}, \tag{7.9}$$

respectively. Note that while the *nematic spreading parameter* S_{N} is the appropriate generalisation of the isotropic spreading parameter S_{I} defined in (1.40), the scaled anchoring coefficients Δ_{NS} and Δ_{GN} have no isotropic counterparts. We also note that when $\Delta_{\mathrm{NS}} = \Delta_{\mathrm{GN}} = 0$ (i.e. when $C_{\mathrm{GN}} = C_{\mathrm{NS}} = 0$) then $S_{\mathrm{N}} = S_{\mathrm{I}} = (\sigma_{\mathrm{GS}} - \sigma_{\mathrm{NS}})/\sigma_{\mathrm{GN}} - 1$, and the nematic Young equations (7.5) and (7.6) both reduce to the classical isotropic Young equation (1.39).

The right-hand sides of the nematic Young equations (7.5) and (7.6) each involve only one parameter, namely the scaled anchoring coefficients Δ_{NS} and Δ_{GN}, respectively. At first sight, it may seem counter-intuitive that Δ_{NS} appears in the case of GN-dominant anchoring and Δ_{GN} appears in the case of NS-dominant anchoring. However, for GN–dominant anchoring the director is aligned with the preferred director orientation of the gas–nematic interface, and so the corresponding anchoring energy, and therefore the couple on the director, is zero. The non-zero contribution to the anchoring energy therefore derives from the breaking of the nematic–substrate interface anchoring. The corresponding explanation applies to the NS-dominant case. The right-hand sides of equations (7.5) and (7.6) may therefore be interpreted physically as the contribution to the balance of stress at the contact line associated with the breaking of the anchoring on the interface with the weaker anchoring.

Figure 7.1 shows surface plots of the contact angle β given by (7.5) and (7.6) as a function of S_{N} and Δ_{GN} for NS-dominant anchoring and as a function of

S_{N} and Δ_{NS} for GN-dominant anchoring. In particular, Figure 7.1 shows there are parameter curves in both scenarios for which the number of solutions for β change. On these parameter curves the contact angle is multi-valued and therefore a variety of continuous and discontinuous transitions can occur.

7.3 The equilibrium states and transitions of a nematic ridge

With the director angle determined by anchoring breaking in the vicinity of the contact lines we can now obtain the equilibrium states and transitions of a nematic ridge from the nematic Young equations (7.5) and (7.6). Specifically, we consider solutions for the contact angle β to the nematic Young equations (7.5) and (7.6). As (7.5) and (7.6) are cubic and quadratic equations for $\cos\beta$, respectively, they can have between zero and three real solutions for β and between zero and two real solutions for β, respectively. Each of these solutions for β corresponds to a different partial wetting state, and therefore, unlike for the isotropic system described in Section 1.10.1, a nematic ridge can have multiple partial wetting states.

Following the same approach as for the isotropic system in Section 1.10.1, the S_{N} and Δ_{NS} (for GN-dominant anchoring) or the S_{N} and Δ_{GN} (for NS-dominant anchoring) values at which there is a change in the number of possible equilibrium states are *transition points*. Specifically, a transition occurs when an increase or decrease in S_{N}, Δ_{NS} or Δ_{GN} leads to an prior equilibrium state no longer existing or a new equilibrium state coming into existence. In an analogous manner to the isotropic case, at $S_{\mathrm{N}} = -2$ and $S_{\mathrm{N}} = 0$ the number of equilibrium states changes, which leads to transitions to a new equilibrium state as S_{N} increases or decreases through $S_{\mathrm{N}} = -2$ and $S_{\mathrm{N}} = 0$. However, unlike in the isotropic case in which only

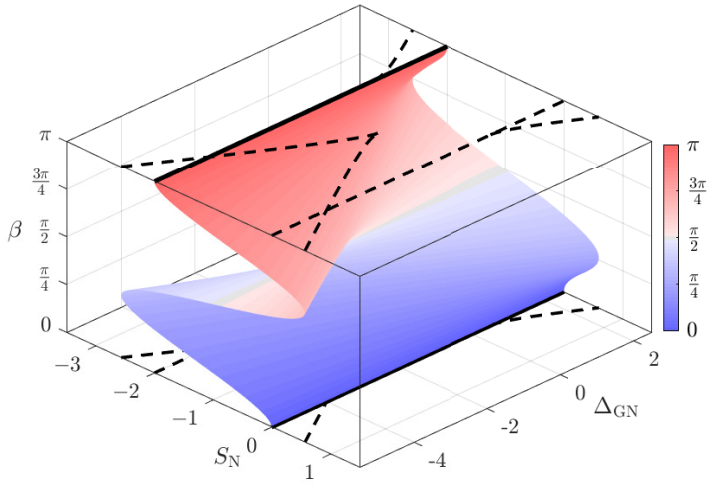

(a) NS-dominant anchoring

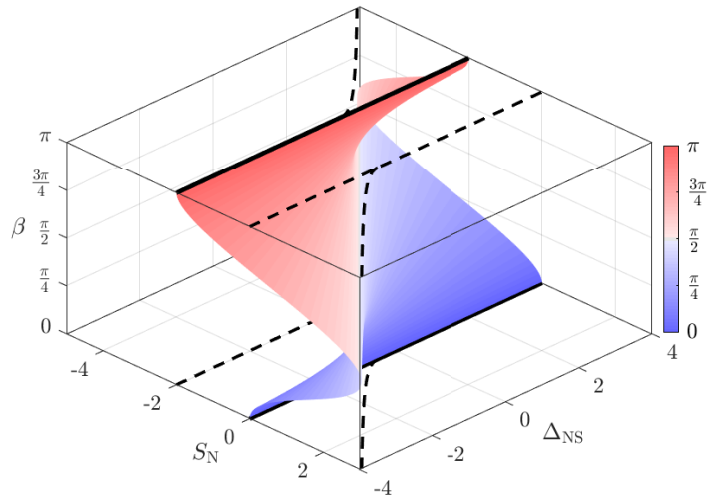

(b) GN-dominant anchoring

Figure 7.1: Surface plots of the contact angle β for (a) the NS-dominant anchoring Young equation (7.5) as a function of S_N and Δ_{GN}, and (b) the GN-dominant anchoring Young equation (7.6) as a function of S_N and Δ_{NS}. The parameter curves of S_N and Δ_{GN} or of S_N and Δ_{NS} for which the number of solutions for β change are indicated on the planes $\beta = 0$ and $\beta = \pi$. In particular, $S_N = 0$ and $S_N = -2$ are shown by solid lines and $S_N = -1 \pm \sqrt{4(1+\Delta_{GN})^3/(27\Delta_{GN})}$ and $S_N = -1 - \Delta_{NS} - 1/(4\Delta_{NS})$ are shown by dashed lines.

continuous transitions occur, in the nematic case discontinuous transitions can also occur, i.e. the contact angle can change discontinuously. Previously, Rey [182] found that discontinuous transitions between the partial wetting and complete wetting states, and between the partial wetting and complete dewetting states are possible (his equation (19) and (20), respectively) [182]. However, without making the additional assumption that anchoring breaking occurs in the vicinity of the contact lines, he was not able to obtain and explicit description of these transitions.

In both NS- and GN-dominant anchoring, the nature of the different transitions, the contact angle transitions, and the transition points can be obtained from just the nematic Young equations (7.5) and (7.6). In NS-dominant anchoring the transition behaviour depends on whether $\Delta_{\mathrm{GN}} < -4$, $-4 \leq \Delta_{\mathrm{GN}} < -1$, $-1 \leq \Delta_{\mathrm{GN}} \leq 1/2$, or $\Delta_{\mathrm{GN}} > 1/2$, whereas in GN-dominant anchoring the transition behaviour depends on whether $\Delta_{\mathrm{NS}} < -1/2$, $-1/2 \leq \Delta_{\mathrm{NS}} \leq 1/2$, or $\Delta_{\mathrm{NS}} > 1/2$. Figures 7.2 and 7.3 show sketches of the solutions for the contact angle β as a function of the nematic spreading parameter S_{N} for these four ranges of Δ_{GN} for NS-dominant anchoring and for these three ranges of Δ_{NS} for GN-dominant anchoring, respectively. In Figures 7.2 and 7.3 and what follows, a rightward arrow ($\Rightarrow$) denotes a discontinuous transition for increasing S_{N}, and a leftward arrow ($\Leftarrow$) denotes a discontinuous transition for decreasing S_{N}. Thus, for example, a discontinuous transition from complete wetting to partial wetting for increasing S_{N} is denoted by $\mathbb{W} \Rightarrow \mathbb{P}$, and a discontinuous transition from partial wetting to complete wetting for decreasing S_{N} is denoted by $\mathbb{W} \Leftarrow \mathbb{P}$. In addition, we denote the transition in the contact angle that is associated with a discontinuous transition using the same notation, so that, for example, the contact angle transition for a $\mathbb{W} \Rightarrow \mathbb{P}$ transition, for which the contact angle transitions discontinuously from $\beta = 0$ to $\beta = \beta^*$, is denoted by $0 \Rightarrow \beta^*$. We also remind the reader of the notation introduced in Section 1.10.1. In particular, a

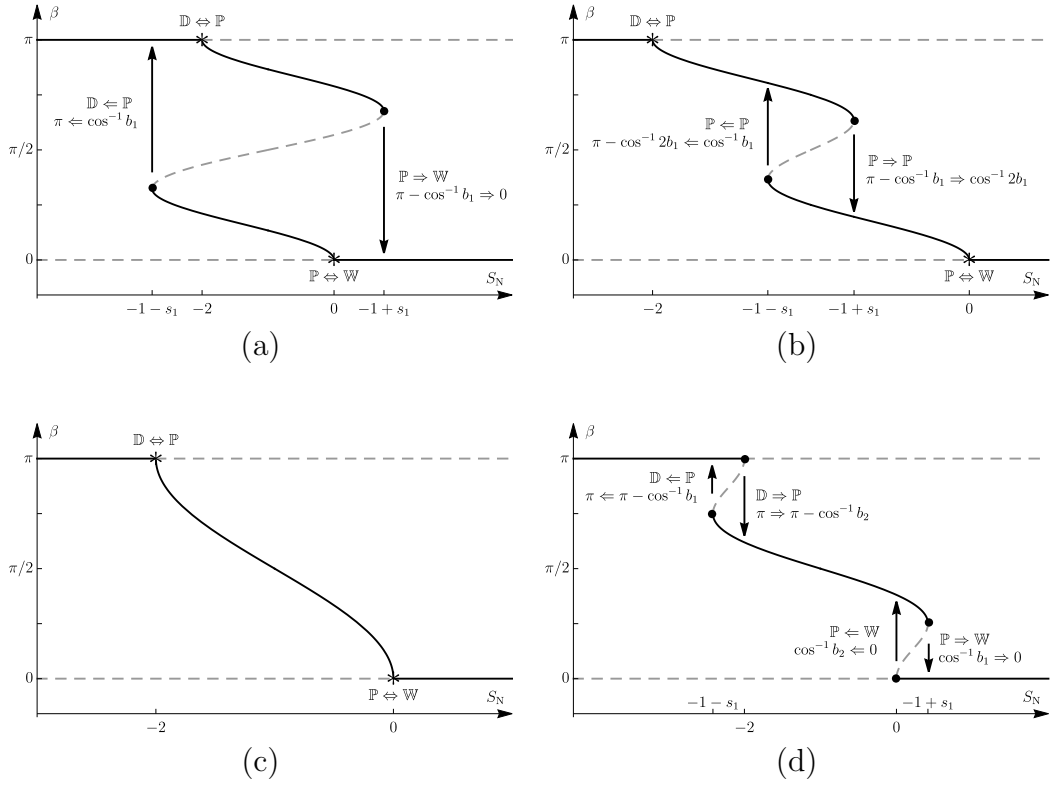

Figure 7.2: Sketches of the solutions for the contact angle β as a function of the nematic spreading parameter S_N for NS-dominant anchoring according to (7.5) for the four ranges of Δ_GN: (a) $\Delta_\mathrm{GN} < -4$, (b) $-4 \leq \Delta_\mathrm{GN} \leq -1$, (c) $-1 \leq \Delta_\mathrm{GN} \leq 1/2$, and (d) $\Delta_\mathrm{GN} > 1/2$. The transition points are labelled and shown by stars ($*$) for a continuous transition and by solid points ($\bullet$) for a discontinuous transition, where $s_1 = \sqrt{4(1+\Delta_\mathrm{GN})^3/(27\Delta_\mathrm{GN})}$, $b_1 = \sqrt{(1+\Delta_\mathrm{GN})/(3\Delta_\mathrm{GN})}$ and $b_2 = -1/2 + \sqrt{\Delta_\mathrm{GN}(\Delta_\mathrm{GN}+4)}/(2\Delta_\mathrm{GN})$. The direction of the arrows shows the direction of each discontinuous transition and the associated jump in β. The solid black lines denote the hypothesised local minimum energy states and the dashed grey lines denote the hypothesised local maximum energy states.

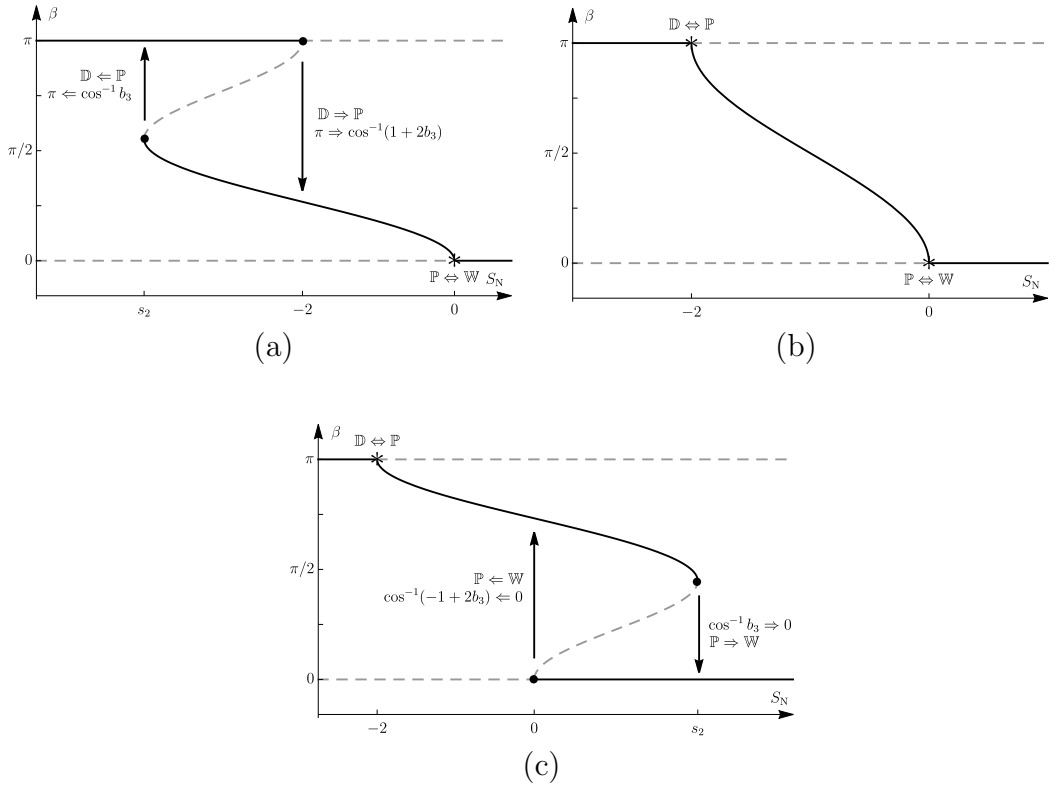

Figure 7.3: Sketches of the solutions for the contact angle β as a function of the nematic spreading parameter S_N for GN-dominant anchoring according to (7.6) for the three ranges of Δ_{NS}: (a) $\Delta_{NS} < -1/2$, (b) $-1/2 \leq \Delta_{NS} \leq 1/2$, and (c) $\Delta_{NS} > 1/2$. The transition points are labelled and shown by stars ($*$) for a continuous transition and by solid points ($\bullet$) for a discontinuous transition, where $s_1 = \sqrt{4(1+\Delta_{GN})^3/(27\Delta_{GN})}$, $b_1 = \sqrt{(1+\Delta_{GN})/(3\Delta_{GN})}$ and $b_2 = -1/2 + \sqrt{\Delta_{GN}(\Delta_{GN}+4)}/(2\Delta_{GN})$. The direction of the arrows shows the direction of each discontinuous transition and the associated jump in β. The solid black lines denote the hypothesised local minimum energy states and the dashed grey lines denote the hypothesised local maximum energy states.

continuous transition between two equilibrium states for both increasing and decreasing S_{N} is denoted with a double arrow ($\Leftrightarrow$). Summaries of all of the possible transitions shown in Figures 7.2 and 7.3 are given in Tables 7.1 and 7.2 for NS- and GN-dominant anchoring, respectively.

Although for a nematic ridge, unlike an isotropic ridge, the free energy of each equilibrium state cannot be determined analytically and therefore we cannot determine the energy of the equilibrium states, we can hypothesise the local minimum energy states for the nematic ridge by comparison with the isotropic system described in Section 1.10.1. In particular, the complete dewetting state is a local minimum energy state for $S_{\mathrm{N}} < -2$, and a local maximum energy state for $S_{\mathrm{N}} \geq -2$. Similarly, the complete wetting state is a local minimum energy state for $S_{\mathrm{N}} > 0$, and a local maximum energy state for $S_{\mathrm{N}} \leq 0$. We also expect that there will always be at least one local minimum energy state, and so for $-2 \leq S_{\mathrm{N}} \leq 0$, for which complete wetting and complete dewetting are local maximum energy states, the local minimum energy state is one of partial wetting. The local minimum and maximum energy states are shown in Figures 7.2 and 7.3 by black solid lines and grey dashed lines, respectively. In the absence of a full dynamical theory, we also hypothesise that the continuous and discontinuous transitions shown in Figures 7.2 and 7.3 each correspond to classical pitchfork or fold bifurcations [87]. In particular, the transitions at $S_{\mathrm{N}} = -2$ and $S_{\mathrm{N}} = 0$ are pitchfork bifurcations which, where a change in S_{N}, Δ_{GN}, or Δ_{NS} leads to a local minimum energy state becoming a local maximum energy state, forcing the system to transition continuously (through a super-critical pitchfork bifurcation) or discontinuously (through a sub-critical pitchfork bifurcation) to a new local minimum energy state. Furthermore, the discontinuous transitions at $S_{\mathrm{N}} = -1 \pm s_1$ and $S_{\mathrm{N}} = s_2$, where $s_1 = \sqrt{4(1+\Delta_{\mathrm{GN}})^3/(27\Delta_{\mathrm{GN}})}$ and $s_2 = -1 - \Delta_{\mathrm{NS}} - 1/(2\Delta_{\mathrm{NS}})$, are associated with fold bifurcations, where a change in S_{N}, Δ_{GN}, or Δ_{NS} leads to a local minimum energy state combining with a local maximum

Range of Δ_{GN}	S_{N} value at transition	Nature of transition	Contact angle transition
$\Delta_{\mathrm{GN}} < -4$	$-1 - s_1\,(< -2)$	$\mathbb{D} \Leftarrow \mathbb{P}$	$\pi \Leftarrow \cos^{-1} b_1$
	-2	$\mathbb{D} \Leftrightarrow \mathbb{P}$	Continuous ($\beta = \pi$)
	0	$\mathbb{P} \Leftrightarrow \mathbb{W}$	Continuous ($\beta = 0$)
	$(0 <)\ -1 + s_1$	$\mathbb{P} \Rightarrow \mathbb{W}$	$\pi - \cos^{-1} b_1 \Rightarrow 0$
$-4 \leq \Delta_{\mathrm{GN}} < -1$	-2	$\mathbb{D} \Leftrightarrow \mathbb{P}$	Continuous ($\beta = \pi$)
	$(-2 \leq)\ -1 - s_1\,(< -1)$	$\mathbb{P} \Leftarrow \mathbb{P}$	$\pi - \cos^{-1} 2b_1 \Leftarrow \cos^{-1} b_1$
	$(-1 <)\ -1 + s_1\,(\leq 0)$	$\mathbb{P} \Rightarrow \mathbb{P}$	$\pi - \cos^{-1} b_1 \Rightarrow \cos^{-1} 2b_1$
	0	$\mathbb{P} \Leftrightarrow \mathbb{W}$	Continuous ($\beta = 0$)
$-1 \leq \Delta_{\mathrm{GN}} \leq 1/2$	-2	$\mathbb{D} \Leftrightarrow \mathbb{P}$	Continuous ($\beta = \pi$)
	0	$\mathbb{P} \Leftrightarrow \mathbb{W}$	Continuous ($\beta = 0$)
$\Delta_{\mathrm{GN}} > 1/2$	$-1 - s_1\,(< -2)$	$\mathbb{D} \Leftarrow \mathbb{P}$	$\pi \Leftarrow \pi - \cos^{-1} b_1$
	-2	$\mathbb{D} \Rightarrow \mathbb{P}$	$\pi \Rightarrow \pi - \cos^{-1} b_2$
	0	$\mathbb{P} \Leftarrow \mathbb{W}$	$\cos^{-1} b_2 \Leftarrow 0$
	$(0 <)\ -1 + s_1$	$\mathbb{P} \Rightarrow \mathbb{W}$	$\cos^{-1} b_1 \Rightarrow 0$

Table 7.1: Summary of the transitions for NS-dominant anchoring obtained from (7.5). The four ranges of values of Δ_{GN}, the S_{N} value at which transitions occur, where $s_1 = \sqrt{4(1+\Delta_{\mathrm{GN}})^3/(27\Delta_{\mathrm{GN}})}$, the nature of the different transitions and the contact angle transitions, where $b_1 = \sqrt{(1+\Delta_{\mathrm{GN}})/(3\Delta_{\mathrm{GN}})}$ and $b_2 = -1/2 + \sqrt{\Delta_{\mathrm{GN}}(\Delta_{\mathrm{GN}}+4)}/(2\Delta_{\mathrm{GN}})$, are shown.

Range of Δ_{GN}	S_{N} value at transition	Nature of transition	Contact angle transition
$\Delta_{\mathrm{NS}} < -1/2$	-2	$\mathbb{D} \Leftrightarrow \mathbb{P}$	Continuous ($\beta = \pi$)
	0	$\mathbb{P} \Leftarrow \mathbb{W}$	$\cos^{-1}(-1 + 2b_3) \Leftarrow 0$
	$(0 <)\, s_2$	$\mathbb{P} \Rightarrow \mathbb{W}$	$\cos^{-1} b_3 \Rightarrow 0$
$-1/2 \leq \Delta_{\mathrm{NS}} \leq 1/2$	-2	$\mathbb{D} \Leftrightarrow \mathbb{P}$	Continuous ($\beta = \pi$)
	0	$\mathbb{P} \Leftrightarrow \mathbb{W}$	Continuous ($\beta = 0$)
$\Delta_{\mathrm{NS}} > 1/2$	$s_2\,(< -2)$	$\mathbb{D} \Leftarrow \mathbb{P}$	$\pi \Leftarrow \cos^{-1} b_3$
	-2	$\mathbb{D} \Rightarrow \mathbb{P}$	$\pi \Rightarrow \cos^{-1}(1 + 2b_3)$
	0	$\mathbb{P} \Leftrightarrow \mathbb{W}$	Continuous ($\beta = 0$)

Table 7.2: Summary of the transitions for GN-dominant anchoring obtained from (7.6). The three ranges of values of Δ_{GN}, the S_{N} value at which transitions occur, where $s_2 = -1 - \Delta_{\mathrm{NS}} - 1/(4\Delta_{\mathrm{NS}})$, the nature of the different transitions and the contact angle transitions, where $b_3 = -1/(2\Delta_{\mathrm{NS}})$, are shown.

energy state, forcing the system to transition discontinuously to an alternative local minimum energy state.

Figure 7.2(a) and (b) and Figure 7.3(a) and (c) also show that there are ranges of S_{N} values for which there are two local minimum energy states (shown by solid black lines). Perhaps most interestingly, we see from Figure 7.2(a) that when $-2 \leq S_{\mathrm{N}} \leq 0$ and from Figure 7.2(b) that when $-1 - s_1 \leq S_{\mathrm{N}} \leq -2$ there are two local minimum energy partial wetting states. This implies that the effects of anchoring breaking in the vicinity of the contact lines can give rise to the possibility of two local minimum energy partial wetting states, a situation that does not occur in the analogous isotropic case.

7.3.1 Behaviour for large scaled anchoring coefficients

From the results summarised in Tables 7.1 and 7.2 the asymptotic behaviour of the transitions in the limits of large scaled anchoring coefficients $\Delta_{\mathrm{GN}} \to \pm\infty$ and $\Delta_{\mathrm{NS}} \to \pm\infty$ may be determined. For example, for NS-dominant anchoring, as $\Delta_{\mathrm{GN}} \to \infty$ the contact angle transition for the $\mathbb{P} \Leftarrow \mathbb{W}$ transition approaches $\pi/2 \Leftarrow 0$ and the contact angle transition for the $\mathbb{D} \Rightarrow \mathbb{P}$ transition approaches $\pi \Rightarrow \pi/2$. Perhaps most interestingly, this limiting behaviour shows that for GN-dominant anchoring, in the limit $\Delta_{\mathrm{NS}} \to \infty$ the contact angle transition for the $\mathbb{D} \Rightarrow \mathbb{P}$ transition approaches $\pi \Rightarrow 0$, i.e. a discontinuous transition from complete dewetting directly to complete wetting, which bypasses the partial wetting state. Similarly, in the limit $\Delta_{\mathrm{NS}} \to -\infty$ the contact angle transition for the $\mathbb{P} \Leftarrow \mathbb{W}$ transition approaches $\pi \Leftarrow 0$, i.e. a discontinuous transition from complete wetting directly to complete dewetting.

7.3.2 Contact-angle hysteresis

The discontinuous transitions shown in Figure 7.2(a), (b), and (d) and Figure 7.3(a) and (c) show that the behaviour of the contact angle is hysteretic. This nematic contact-angle hysteresis, which occurs for an ideal substrate, is fundamentally different from the well-known phenomenon of isotropic contact-angle hysteresis which only occurs for a non-ideal substrate. However, we note that when $-1 \leq \Delta_{\mathrm{GN}} \leq 1/2$ for NS-dominant anchoring, as shown in Figure 7.2(c), and when $-1/2 \leq \Delta_{\mathrm{NS}} \leq 1/2$ for GN-dominant anchoring, as shown in Figure 7.3(b), the behaviour is similar to the isotropic case and no contact-angle hysteresis occurs.

7.4 Conclusion

Motivated by the results of Chapter 6, which predicts that anchoring breaking occurs in the vicinity of the two contact lines for a thin pinned ridge, after discussing the nematic Young equations (5.42) and (5.43) in Section 7.1, in Section 7.3, under the assumption that anchoring breaking occurs in the vicinity of the contact lines, we used the nematic Young equations (5.42) and (5.43) to determine regions of parameter space for which the equilibrium state is one of partial wetting, complete wetting or complete dewetting, and the parameter curves at which transitions between these equilibrium states occur. In particular, it was shown that the nematic Young equations in the case of NS-dominant anchoring and GN-dominant anchoring, which are given by (7.5) and (7.6), can each be written in terms of two parameters, namely the nematic spreading parameter S_{N}, and the scaled anchoring coefficients Δ_{GN} and Δ_{NS}. In both situations, we found continuous transitions, which correspond to those that occur in the isotropic case, a variety of discontinuous transitions, contact-angle hysteresis, and multiple partial

wetting states that do not occur in the case of an isotropic liquid exist. Summaries of all the transitions for GN-dominant and NS-dominant anchoring are sketched in Figures 7.2 and 7.3 and shown in Tables 7.1 and 7.2, respectively.

For simplicity we considered only the left-hand contact line, which is described by the nematic Young equation (5.42). Corresponding results are obtained for the right-hand contact line to those detailed in Section 7.3, which also allow for more than one possible contact angle value for the same parameter values, and so $\beta^{\pm}$ do not, in general, have to be the same and the ridge can be asymmetric. This is in agreement with observations by Vanzo et al. [210], who found that anisotropic effects can lead to varying contact angle values around elongated sessile nematic droplets.

The anisotropic wetting and dewetting phenomena predicted are interesting from a technological perspective. For instance, many authors have investigated tailored dewetting of liquid films to produce patterned films [21, 82, 237] in applications that involve the structured deposition of a material, e.g. to create a diffraction grating [17, 23]. The variety of possible transitions between two-dimensional equilibrium states will have similar forms in three dimensions, which may be relevant to the ODF method and adaptive-lens technologies [3, 112].

Concerning potential future comparisons with the results of physical experiments of the situation considered in this chapter, we have shown that discontinuous transitions and contact-angle hysteresis will occur if the parameters are such that $\Delta_{\mathrm{GN}} > 1/2$ or $\Delta_{\mathrm{GN}} < -1$, or $|\Delta_{\mathrm{NS}}| > 1/2$. Inspection of (7.8) and (7.9) shows that this is certainly the case when $\sigma_{\mathrm{GN}} \simeq C_{\mathrm{GN}}$. For standard low-molecular-mass nematics, for which the isotropic interfacial tension is typically larger than the anchoring strength [197], this may be difficult to achieve. For example, for the typical parameter values stated in Section 1.7.3, $|\Delta_{\mathrm{GN}}| \ll 1$ and $|\Delta_{\mathrm{NS}}| \ll 1$, and so the present analysis indicates that, in general, the clas-

sical isotropic Young equations (1.39) are a good approximation for the nematic Young equations (5.42) and (5.43). However, for high-molecular-mass nematics, e.g. nematic polymers, or particularly strong anchoring, the anchoring strengths would be considerably higher, and the transitions could potentially be observed experimentally. For example, the use of polymeric compounds to produce tailored anchoring [207] produces a strong preference for polymers to align at interfaces [133, 232] and may result in large anchoring strengths, which could lead to $|\Delta_{\mathrm{GN}}| = O(1)$ and $|\Delta_{\mathrm{NS}}| = O(1)$ and hence the transitions predicted could potentially be observed. Alternatively, the situation in which the surrounding fluid is the isotropic melt of the nematic could lower the isotropic interfacial tension σ_{GN}. In this situation, the isotropic interfacial tension for the isotropic–nematic interface σ_{IN} would be much smaller than the gas–nematic interfacial tension σ_{GN} and may become comparable with the anchoring strength C_{GN}. For instance, σ_{IN} was measured for the nematic MBBA as $\sigma_{\mathrm{IN}} = 10^{-5}\,\mathrm{Nm}^{-1}$ [123], which is three orders of magnitude smaller than typical isotropic interfacial tension for a gas–nematic interface σ_{GN} [61]. Such a situation could be realised experimentally by using controlled heating and cooling of regions of a substrate coated in a nematic film [60, 207].

The range of anisotropic wetting and dewetting phenomena occurring in this nematic system allows the control of nematic ridges beyond that which is possible for isotropic ridges. Further theoretical investigations, particularly into the dynamics of transitions, and experimental realisations of this model, would be beneficial to explore the possible applications of these results.

Chapter 8

Conclusions and further work

8.1 Conclusions

This thesis has considered the mathematical modelling and analysis of the widely used ODF method for the industrial manufacturing of liquid crystal displays. Firstly, in Chapters 2 to 4, we considered three problems relating to the fluid dynamics of nematics in the ODF method. Secondly, in Chapters 5 to 7 we considered we considered a static ridge of nematic resting on an ideal solid substrate surrounded by passive fluid, which gives insight into the initial stage of the ODF method and more general situations involving nematic free surfaces and three-phase contact lines. The main results and key conclusions of each chapter are detailed below.

In the first half of Chapter 2 (Sections 2.1 to 2.2), we considered a simple model for the squeezed coalescence of several nematic droplets as occurs in the ODF method. Although this simple model neglects many effects, including surface tension, elasticity, anchoring, and contact line dynamics, we found that the radial boundary speed of droplets predicted by this simple model shows a strik-

ing qualitative similarity to ODF mura, which is often observed in the ODF method [36, 125, 167]. Using the results of this model, we suggested methods to reduce the radial boundary speed of the droplets, including dispensing the nematic into a higher number of low volume droplets and reducing the downward speed of the top substrate, which could potentially reduce the formation of ODF mura. In the second half of Chapter 2 (Sections 2.3 to 2.4), we considered two limiting regimes of Ericksen–Leslie theory, namely the flow dominated-regime and the elasticity-dominated regime, which allow us to make qualitative comparisons between experimental photographs of a two-droplet ODF test setup (shown in Figure 1.9) and numerical calculations of the transmission of light in these regimes. We found striking qualitative agreement between these experimental photographs and the flow dominated regime, suggesting that flow effects could play an essential role in forming ODF mura.

In Chapter 3, motivated by the need for a better fundamental understanding of director reorientation due to the flow of nematic during the ODF method, we formulated and analysed a squeeze-film model for the ODF method. Specifically, we considered a nematic squeeze film in the asymptotic regime in which the drop is thin, inertial effects are weak, and elasticity effects are strong for four cases of infinite anchoring at the downward moving top substrate and the stationary bottom substrate, and for two different scenarios for the motion of the top substrate (namely, prescribed speed and prescribed force). We obtained asymptotic solutions for the director orientation, radial flow, vertical flow, shear stress, couple stress, and force on the top substrate, which help to improve our understanding of the ODF method.

In Chapter 4, we formulated and analysed a model for pressure-driven channel flow of nematic using a dissipative weak anchoring condition on the substrates to investigate the transient flow-driven distortion of the nematic molecules on

the substrates from their required orientation in the ODF method. We obtained quasi-steady asymptotic solutions for the director angle and the velocity in the limit of small Leslie angle and found that solutions depend on two key non-dimensional parameters, namely the Ericksen number and an anchoring strength parameter. Our findings indicate that there is sufficient time for transient flow-driven distortion of the nematic director on the substrates from their required orientation to occur, which could potentially lead to the formation of ODF mura.

In Chapter 5, we derived the governing equations for a static ridge of nematic resting on an ideal solid substrate surrounded by passive fluid. We derived the governing equations using the constrained energy minimisation of the free energy of the nematic ridge, which consists of energy contributions from the bulk of the nematic, which depend on the Oseen–Frank bulk elastic energy density, and from the nematic–solid and gas–nematic interfaces, which each depend on the Rapini–Papoular surface energy density. The governing equations include nematic Young equations, which describe the behaviour of the nematic three-phase contact lines.

The governing equations derived in Chapter 5 were applied to two related problems involving a ridge of a nematic in Chapters 6 and 7. In Chapter 6, we obtained an anchoring-strength parameter plane in terms of the nematic–solid and gas–nematic anchoring strengths, which summarises the energetically preferred solutions for the situation in which the ridge is thin and has pinned contact lines. In particular, we found that the energetically preferred solutions can be related to the Jenkins–Barratt–Barbero–Barberi critical thickness [9, 102]. The analysis presented in Chapter 6 predicts that in the vicinity of each nematic three-phase contact line, anchoring breaking occurs, and the interface with the strongest anchoring determines the director orientation. In Chapter 7, motivated by the results in Chapter 6, we considered analysis of the nematic Young equations under the assumption that anchoring breaking occurs in the vicinity of each contact line.

In particular, we analysed continuous and discontinuous transitions between the equilibrium states of complete wetting, partial wetting, and complete dewetting that occur. We found continuous transitions analogous to those that occur in the classical well-studied case of an isotropic liquid, and a variety of discontinuous transitions, contact-angle hysteresis, and regions of parameter space in which multiple partial wetting states exist that do not occur in the case of an isotropic liquid.

8.2 Further work

The work presented in this thesis could be extended in several directions. In general, throughout this thesis, we have used continuum models for nematics which only consider the average orientation of the nematic molecules and neglect variations in the orientational order of the nematic. In Chapters 2 to 4, various approximations of Ericksen–Leslie theory were used to examine aspects of the fluid dynamics of the ODF method and in Chapters 5 to 7, we used the Oseen–Frank bulk elastic energy density, which all neglect variations in the nematic orientational order. Future work should undoubtedly consider how nematic orientational order evolves in the ODF method, for example, using Berris–Edwards theory [13], and how defects can occur in nematic ridges, for example, using Q-tensor theory [152].

The simple model considered in Chapter 2 could be extended and improved in several ways. In particular, the model for the evolution of the droplet boundary only considers the conservation of volume, and so many effects could be included in future studies, including anchoring, surface tension, and elasticity. We also considered two limiting regimes of Ericksen–Leslie theory, and therefore an obvious extension of this work would be to consider the full Ericksen–Leslie theory

within the squeezed coalescing droplets, which would likely require a numerical approach.

The asymptotic solutions obtained in Chapter 3 neglect many physical effects, which may be important in the ODF method. For example, the values shown in Table 3.1 indicate that the Ericksen number is typically large in the ODF method, and an asymptotic solution in the limit of a large Ericksen number may be more appropriate. However, we note that seeking a solution in the limit of a large Ericksen number leads to a non-linear boundary layer problem that will probably need to be solved numerically. An extension of the squeeze film problem undertaken in Chapter 3 should therefore consider numerical solutions to the full Ericksen–Leslie equations to account for a full range of Ericksen numbers. We also note that for the planar anchoring case considered in Chapter 3, it would be relatively straightforward to use the asymptotic approach used in Chapter 4 for the squeeze film problem, in which we assumed that the ratio of viscosities ϵ is small and obtained the large Ericksen number behaviour asymptotically. However, we note that this approach would not be relevant to the other anchoring conditions considered in Chapter 3 where flow alignment towards the (typically small) Leslie angle would require rotations of the director angle that are not asymptotically small, and therefore would be invalid for the asymptotic approach used in Chapter 4.

In Chapter 4, we used a dissipative weak anchoring condition to examine flow-driven distortion of the nematic director on the substrates to give insights into the ODF method and the formation of ODF mura. Although this approach describes how the nematic director on the substrates may respond to flow, it does not include a model of elastic or inelastic deformation to the alignment layer caused by the flow. In future work, a model that allows for the preferred director orientation of the substrate to change due to high flow rates may be more realistic

in considering flow-driven distortion of nematic and alignment layer molecules. We also note that the results of Chapter 4 are relevant for devices with planar anchoring, such as IPS devices, and are not directly relevant to devices with homeotropic anchoring, such as VAN devices, or to devices in which the director does not remain in-plane, such as TN or STN devices. In the future, dissipative homeotropic weak anchoring could be considered to give insight into VAN devices where flow alignment towards the (typically small) Leslie angle involves a much larger rotation of the director than that described in Chapter 4, and so we suspect that such devices are even more susceptible to flow-driven misalignment of the director on the substrates during filling than those studied in Chapter 4. We note that the approach used in Chapter 4 would have to be adapted considerably to handle dissipative homeotropic weak anchoring as the asymptotic expansions, which assume the director angle is small, would no longer be valid, and perhaps a numerical approach would be required.

The governing equations derived in Chapter 5 for a static ridge of nematic provide the basis for several relatively straightforward extensions. In particular, the approach could easily be adapted to include electromagnetic forces, a non-uniform substrate, including prescribed surface grooves or varied substrate anchoring behaviour, or more detailed models for the nematic order, such as Q-tensor theory [152]. We note that the governing equations were derived on the assumption that the director remains in-plane, which could undoubtedly be relaxed in future studies to allow director alignment in three dimensions, such as twist deformations [201]. Finally, we note that the more common situation of a nematic droplet, rather than a two-dimensional ridge, could be considered using the same energy minimisation framework and is certainly worthy of future research.

In Chapters 6 and 7, we considered two applications of the governing equations

derived in Chapter 5. The thin-film limit considered in Chapter 6 decouples the slope of the gas–nematic interface and the gas–nematic interface anchoring terms in the governing equations, and so, the director angle on the interface behaves as if it were locally flat. In future work, the thin-film limit should be relaxed so that the behaviour of the free surface anchoring can account for the variation of the free surface slope; however, we note that a numerical approach will probably then be required. Another valuable direction for future work would be to include the effects of electric fields to study how the application of electric fields may be used to control the equilibrium states of partial wetting, complete wetting and complete dewetting. The results obtained in Chapter 7 could also be extended to consider the dynamics of wetting or dewetting, which may help with comparisons to equivalent experimental investigations, and would be an exciting area of future study. However, it may then be necessary to allow for flow within the ridge and include a model of contact line movement, which would require significant adaptions of the governing equations derived in Chapter 5.

Perhaps the most obvious direction for future work on ridges of nematic would be to use the approach presented in Chapter 6 to consider a thin unpinned nematic ridge. The key difference between this future consideration and Chapter 6 would be that the semi-width d would now be unknown, and the Young equations (5.42) and (5.43) would be required to complete the governing equations. Preliminary results for this situation indicate that the solutions obtained in Chapter 6 for a thin pinned ridge are relevant for a thin unpinned ridge. In particular, the uniform homeotropic and planar solutions (i.e. the H and P solutions), distorted solutions (i.e. $\mathrm{D_H}$, $\mathrm{D_P}$, and D solutions), and an additional solution for which the nematic completely wets the substrate (denoted the wetting W solution) are obtained. Similarly to Figure 8.1 in Chapter 6, the energetically preferred solutions for a thin unpinned ridge of nematic can be presented in a C_{NS}–C_{GN} parameter plane, as shown in Figure 8.1. Whilst the behaviour of the director in this unpinned

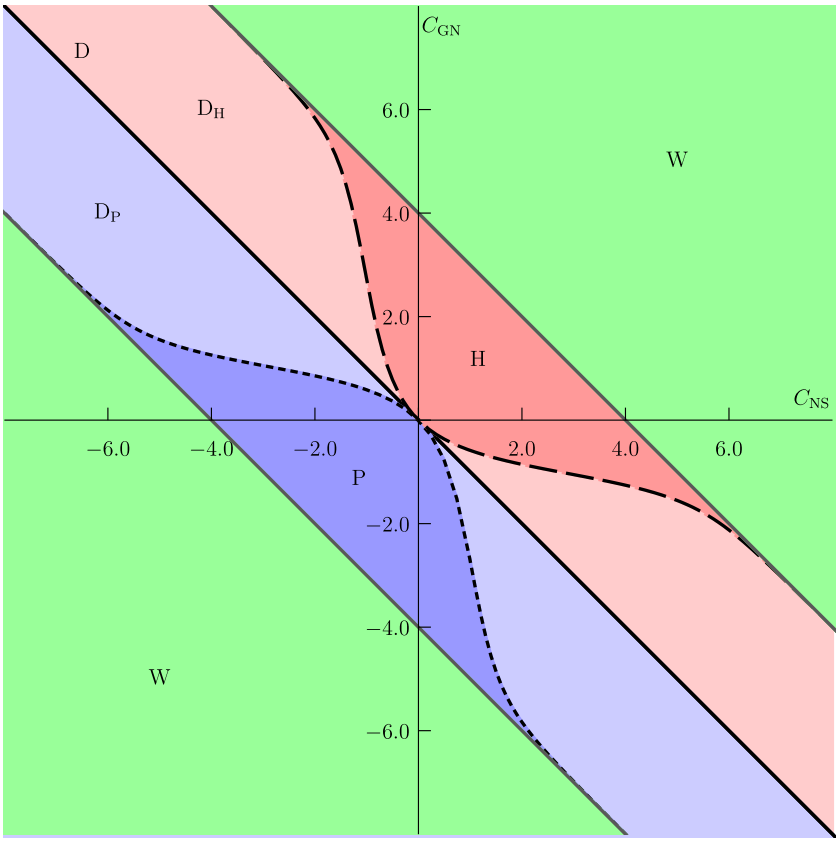

Figure 8.1: The C_{NS}–C_{GN} parameter plane for $K = 1$ for a thin unpinned ridge of nematic. Regions of the parameter plane where the H solution (shown in dark red), the P solution (shown in dark blue), $\mathrm{D_P}$ solutions (shown in light blue), $\mathrm{D_H}$ solutions (shown in light red) and the W solution are energetically preferred are labelled. D solutions are energetically preferred along the solid black line corresponding to $h_{\mathrm{c}} = 0$, the black dashed line corresponds to $h_{\mathrm{c}} = -3/4$, the black dotted line corresponds to $h_{\mathrm{c}} = 3/4$.

system is similar to the pinned ridge, initial numerical results indicate that the behaviour of the height of the ridge can be significantly different.

In summary, the work undertaken in this thesis has gone a long way to analyse problems relating to LCD manufacturing and systems with a nematic free surface and three-phase contact line, but there are still many interesting aspects which future work should seek to uncover.

Appendix A

Derivation of the governing equations for a static ridge of nematic when the ridge height h is a double-valued function of x.

In this Appendix the derivation of the governing equations for a nematic ridge when h is a double-valued function of x is presented. For simplicity of the expressions derived in this Appendix, we take the one-constant approximation and neglect gravitational effects. This derivation involves splitting the gas–nematic interface into three parts in each of which h is a single-valued function of x. In particular, we divide the gas-nematic interface into three single-valued functions of x, namely the lower left ("L"), upper ("U"), and lower right ("R") components

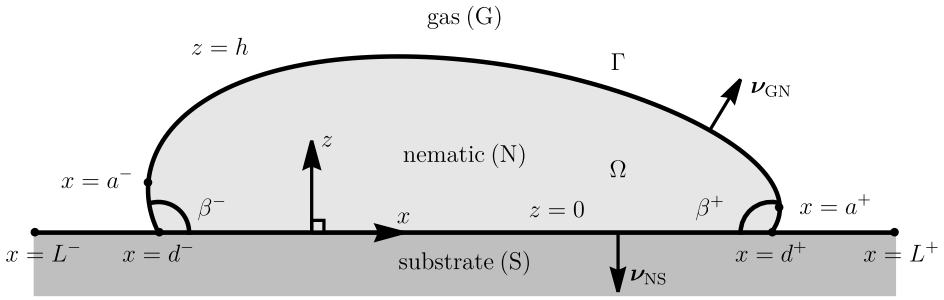

Figure A.1: A schematic of a static ridge of nematic when h is a double-valued function of x. The Cartesian coordinates x, y and z (where the y-direction is into the page), the points $x = a^+$ and $x = a^-$, the components of the gas-nematic interface $h_L(x)$, $h_U(x)$ and $h_R(x)$, boundary of the nematic ridge Γ, the outward unit normals $\boldsymbol{\nu}$, the contact angles $\beta^{\pm}$, and the region of nematic in the (x, z)-plane Ω are also indicated.

$z = h_L(x)$, $z = h_U(x)$ and $z = h_R(x)$, such that

$$h_L = h_U \quad \text{at} \quad x = a^-, \tag{A.1}$$

$$h_U = h_R \quad \text{at} \quad x = a^+, \tag{A.2}$$

where $h_U > h_L$ and $h_U > h_R$, and $x = a^-$ and $x = a^+$ are the locations for which $\mathrm{d}h_L/\mathrm{d}x \to -\infty$ and $\mathrm{d}h_U/\mathrm{d}x \to \infty$, and $\mathrm{d}h_R/\mathrm{d}x \to \infty$ and $\mathrm{d}h_U/\mathrm{d}x \to -\infty$, respectively, as shown in Figure A.1. In this formulation the boundary conditions are subject to the two Dirichlet boundary conditions $h_L(d^-) = 0 = h_R(d^+)$ and the definitions of the contact angles (5.4) are given by

$$h_{Lx} = \tan\beta^- \quad \text{at} \quad x = d^-, \tag{A.3}$$

$$-h_{Rx} = \tan\beta^+ \quad \text{at} \quad x = d^+, \tag{A.4}$$

and the unit outward normals (5.2) are given by

$$\boldsymbol{\nu}_{\mathrm{NS}} = -\hat{\mathbf{z}} \quad \text{on} \quad z = 0, \tag{A.5}$$

$$\boldsymbol{\nu}_{\mathrm{GN}} = \frac{h_{Lx}}{\sqrt{1+h_{Lx}^2}}\hat{\mathbf{x}} - \frac{1}{\sqrt{1+h_{Lx}^2}}\hat{\mathbf{z}} \quad \text{on} \quad z = h_L, , \tag{A.6}$$

$$\boldsymbol{\nu}_{\mathrm{GN}} = -\frac{h_{Ux}}{\sqrt{1+h_{Ux}^2}}\hat{\mathbf{x}} + \frac{1}{\sqrt{1+h_{Ux}^2}}\hat{\mathbf{z}} \quad \text{on} \quad z = h_U, , \tag{A.7}$$

$$\boldsymbol{\nu}_{\mathrm{GN}} = \frac{h_{Rx}}{\sqrt{1+h_{Rx}^2}}\hat{\mathbf{x}} - \frac{1}{\sqrt{1+h_{Rx}^2}}\hat{\mathbf{z}} \quad \text{on} \quad z = h_R, . \tag{A.8}$$

The free energy components (5.6)–(5.9) in this formulation can then be expressed as

$$\begin{aligned} E_{\mathrm{bulk}} = &\int_{a^-}^{d^-}\int_{h_L}^{h_U(a^-)} W \,\mathrm{d}z\mathrm{d}x + \int_{a^-}^{d^-}\int_{h_U(a^-)}^{h_U} W \,\mathrm{d}z\mathrm{d}x \\ &+ \int_{d^-}^{d^+}\int_{0}^{h_U} W \,\mathrm{d}z\mathrm{d}x + \int_{d^+}^{a^+}\int_{h_R}^{h_U(a^+)} W \,\mathrm{d}z\mathrm{d}x \\ &+ \int_{d^+}^{a^+}\int_{h_U(a^+)}^{h_U} W \,\mathrm{d}z\mathrm{d}x, \end{aligned} \tag{A.9}$$

$$\begin{aligned} E_{\mathrm{GN}} = &-\int_{d^-}^{a^-} [\omega_{\mathrm{GN}}(\theta, h_{Lx})]^{z=h_L} \sqrt{1+h_{Lx}^2}\,\mathrm{d}x \\ &+ \int_{a^-}^{a^+} [\omega_{\mathrm{GN}}(\theta, h_{Ux})]^{z=h_U} \sqrt{1+h_{Ux}^2}\,\mathrm{d}x \\ &- \int_{a^+}^{d^+} [\omega_{\mathrm{GN}}(\theta, h_{Rx})]^{z=h_R} \sqrt{1+h_{Rx}^2}\,\mathrm{d}x, \end{aligned} \tag{A.10}$$

$$E_{\mathrm{NS}} = \int_{d^-}^{d^+} [\omega_{\mathrm{NS}}(\theta)]^{z=0}\,\mathrm{d}x, \tag{A.11}$$

$$E_{\mathrm{GS}} = \int_{d^+}^{L^+} [\omega_{\mathrm{GS}}]^{z=0}\,\mathrm{d}x + \int_{L^-}^{d^-} [\omega_{\mathrm{GS}}]^{z=0}\,\mathrm{d}x, \tag{A.12}$$

and the area constraint term $\mathcal{C}_{\mathrm{area}}$, is given by

$$\mathcal{C}_{\mathrm{area}} = p_0 \left(A - \int_{d^-}^{d^+} h_U \,\mathrm{d}x - \int_{a^-}^{d^-} (h_U - h_L)\,\mathrm{d}x - \int_{d^+}^{a^+} (h_U - h_R)\,\mathrm{d}x \right). \tag{A.13}$$

We now proceed using the same method described Section 5.2. Specifically, we take the variation of the functional F, given by (A.9)–(A.13) and (5.11), with respect to small variations of the variables θ, h_L, h_U, h_R, d^- and d^+ of the form

$$\begin{aligned} &\theta \to \theta + \delta_\theta, \quad h_R \to h_R + \delta_{h_R}, \quad h_U \to h_U + \delta_{h_U}, \\ &h_L \to h_L + \delta_{h_L}, \quad d^+ \to d^+ + \delta_{d^+}, \quad d^- \to d^- + \delta_{d^-}. \end{aligned} \tag{A.14}$$

The variation of the functional F, denoted by δF, is given by

$$\begin{aligned} \delta F = F\big(&\theta + \delta_\theta, (\theta + \delta_\theta)_x, (\theta + \delta_\theta)_z, h_L + \delta_{h_L}, (h_L + \delta_{h_L})_x, \\ &h_U + \delta_{h_U}, (h_U + \delta_{h_U})_x, h_R + \delta_{h_R}, (h_R + \delta_{h_R})_x, d^- + \delta_{d^-}, d^+ + \delta_{d^+}\big) \\ &- F(\theta, \theta_x, \theta_z, h_L, h_{Lx}, h_U, h_{Ux}, h_R, h_{Rx}, d^-, d^+). \end{aligned} \tag{A.15}$$

The variation of each term in (A.9)–(A.13) and (5.11) is considered in turn, and we neglect terms in (A.15) that are $O(\delta_\theta^2)$, $O(\delta_{h_L}^2)$, $O(\delta_{h_U}^2)$, $O(\delta_{h_R}^2)$, $O(\delta_{d^-}^2)$ and $O(\delta_{d^+}^2)$.

For the bulk elastic energy E_{bulk}, given by (A.9), using the variations (A.14) and after some manipulation we arrive at the variation of the bulk energy δE_{bulk}, which can be expressed as

$$\begin{aligned} \delta E_{\text{bulk}} = &\int\int \left(\delta_\theta \frac{\partial W}{\partial \theta} + \delta_{\theta x} \frac{\partial W}{\partial \theta_x} + \delta_{\theta z} \frac{\partial W}{\partial \theta_z}\right) \, \mathrm{d}\Omega \\ &+ \delta_{d^-} \left[\int_{h_L}^{h_U(a^-)} W \, \mathrm{d}z + \int_{h_U(a^-)}^{h_U} W \, \mathrm{d}z - \int_0^{h_U} W \, \mathrm{d}z\right]^{x=d^-} \\ &+ \delta_{d^+} \left[\int_0^{h_U} W \, \mathrm{d}z - \int_{h_U(a^+)}^{h_U} W \, \mathrm{d}z - \int_{h_R}^{h_U(a^+)} W \, \mathrm{d}z\right]^{x=d^+} \\ &- \int_{a^-}^{d^-} \delta_{h_L} \left[W\right]^{z=h_L} \, \mathrm{d}x + \int_{a^-}^{a^+} \delta_{h_U} \left[W\right]^{z=h_U} \, \mathrm{d}x \\ &- \int_{d^+}^{a^+} \delta_{h_R} \left[W\right]^{z=h_R} \, \mathrm{d}x. \end{aligned} \tag{A.16}$$

Similarly to Section 5.2, h_R and h_L that are evaluated at $x = d^-$ and $x = d^+$ are removed using the two Dirichlet boundary conditions $h_L(d^-) = 0 = h_R(d^+)$ and the terms that contain derivatives of a variation, namely $\delta_{\theta x}$ and $\delta_{\theta z}$, are simplified using (5.17). Some care should be taken as the line integral along Γ in (5.17) is now composed of many components. In particular, namely a component along Γ_{NS} which remains the same as Section 5.2 and components along Γ_{GN} for $z = h_L$, $z = h_U$, and $z = h_R$. Specifically, the components are; a component along Γ_{NS} at $z = 0$ from $x = d^-$ to $x = d^+$ with $\mathrm{d}\Gamma = \mathrm{d}x$ and outward unit normal (A.5), a component along Γ_{GN} at $z = h_R$ from $x = d^+$ to $x = a^+$ with $\mathrm{d}\Gamma = \sqrt{1 + h_{Rx}^2}\,\mathrm{d}x$ and outward unit normal (A.6), a component along Γ_{GN} at $z = h_U$ from $x = a^+$ to $x = a^-$ with $\mathrm{d}\Gamma = -\sqrt{1 + h_{Rx}^2}\,\mathrm{d}x$ and outward unit normal (A.7), and a component along Γ_{GN} at $z = h_L$ from $x = a^-$ to $x = d^+$ with $\mathrm{d}\Gamma = \sqrt{1 + h_{Rx}^2}\,\mathrm{d}x$ and outward unit normal (A.8). The line integral along Γ in (5.17) is given by

$$\begin{aligned}\oint_\Gamma \delta_\theta \frac{\partial W}{\partial \theta_\alpha}\left(\hat{\boldsymbol{\alpha}}\cdot\hat{\boldsymbol{\nu}}\right)\mathrm{d}\Gamma = &-\int_{d^-}^{d^+}\left[\delta_\theta\frac{\partial W}{\partial\theta_\alpha}\right]^{z=0}\left(\hat{\boldsymbol{\alpha}}\cdot\hat{\boldsymbol{z}}\right)\mathrm{d}x\\ &+\int_{d^+}^{a^+}\left[\delta_\theta\frac{\partial W}{\partial\theta_\alpha}\right]^{z=h_R}\left(\hat{\boldsymbol{\alpha}}\cdot\left(h_{Rx}\hat{\boldsymbol{x}}-\hat{\boldsymbol{z}}\right)\right)\mathrm{d}x\\ &+\int_{a^+}^{a^-}\left[\delta_\theta\frac{\partial W}{\partial\theta_\alpha}\right]^{z=h_U}\left(\hat{\boldsymbol{\alpha}}\cdot\left(h_{Ux}\hat{\boldsymbol{x}}-\hat{\boldsymbol{z}}\right)\right)\mathrm{d}x\\ &+\int_{a^-}^{d^-}\left[\delta_\theta\frac{\partial W}{\partial\theta_\alpha}\right]^{z=h_L}\left(\hat{\boldsymbol{\alpha}}\cdot\left(h_{Lx}\hat{\boldsymbol{x}}-\hat{\boldsymbol{z}}\right)\right)\mathrm{d}x. \qquad \text{(A.17)}\end{aligned}$$

The combining (A.16), (5.17), and (A.17) yields variation of the bulk energy

δE_{bulk}, namely

$$\begin{aligned}\delta E_{\text{bulk}} = \int\int \delta_\theta \left(\frac{\partial W}{\partial \theta} - \frac{\partial}{\partial x}\left(\frac{\partial W}{\partial \theta_x}\right) - \frac{\partial}{\partial z}\left(\frac{\partial W}{\partial \theta_z}\right)\right) \, \mathrm{d}\Omega - \int_{a^-}^{d^-} \delta_{h_L} \left[W\right]^{z=h_L} \, \mathrm{d}x \\ + \int_{a^-}^{a^+} \delta_{h_U} \left[W\right]^{z=h_U} \, \mathrm{d}x - \int_{d^+}^{a^+} \delta_{h_R} \left[W\right]^{z=h_R} \, \mathrm{d}x \\ + \int_{d^+}^{a^+} h_{Rx} \left[\delta_\theta \frac{\partial W}{\partial \theta_x}\right]^{z=h_R} \, \mathrm{d}x + \int_{a^+}^{a^-} h_{Ux} \left[\delta_\theta \frac{\partial W}{\partial \theta_x}\right]^{z=h_U} \, \mathrm{d}x \\ + \int_{a^-}^{d^-} h_{Lx} \left[\delta_\theta \frac{\partial W}{\partial \theta_x}\right]^{z=h_L} \, \mathrm{d}x - \int_{d^-}^{d^+} \left[\delta_\theta \frac{\partial W}{\partial \theta_z}\right]^{z=0} \, \mathrm{d}x \\ - \int_{d^+}^{a^+} \left[\delta_\theta \frac{\partial W}{\partial \theta_z}\right]^{z=h_R} \, \mathrm{d}x - \int_{a^+}^{a^-} \left[\delta_\theta \frac{\partial W}{\partial \theta_z}\right]^{z=h_U} \, \mathrm{d}x \\ - \int_{a^-}^{d^-} \left[\delta_\theta \frac{\partial W}{\partial \theta_z}\right]^{z=h_L} \, \mathrm{d}x. \end{aligned} \tag{A.18}$$

For the gas–nematic interface energy E_{GN}, given by (A.10), substituting the variations (A.14) into (A.10) and carrying out integration by parts on any terms involving $\delta_{h_L x}$, $\delta_{h_U x}$, or $\delta_{h_R x}$ and simplifying, yields the variation of the gas–

nematic interface energy δE_{GN}:

$$\begin{aligned}
\delta E_{\mathrm{GL}} = &- \int_{d^-}^{a^-} \left[\delta_\theta \sqrt{1+{h_{Lx}}^2} \frac{\partial \omega_{\mathrm{GN}}}{\partial \theta} + \delta_{h_L} \left(\sqrt{1+{h_{Lx}}^2} \frac{\partial \omega_{\mathrm{GN}}}{\partial \theta} \frac{\partial \theta}{\partial z} \right.\right. \\
&\qquad \left.\left. - \frac{\partial}{\partial x} \left[\frac{\partial}{\partial h_{Lx}} \left(\sqrt{1+{h_{Lx}}^2}\, \omega_{\mathrm{GN}} \right) \right] \right) \right]^{z=h_L} \mathrm{d}x \\
&+ \int_{a^-}^{a^+} \left[\delta_\theta \sqrt{1+{h_{Ux}}^2} \frac{\partial \omega_{\mathrm{GN}}}{\partial \theta} + \delta_{h_U} \left(\sqrt{1+{h_{Ux}}^2} \frac{\partial \omega_{\mathrm{GN}}}{\partial \theta} \frac{\partial \theta}{\partial z} \right.\right. \\
&\qquad \left.\left. - \frac{\partial}{\partial x} \left[\frac{\partial}{\partial h_{Ux}} \left(\sqrt{1+{h_{Ux}}^2}\, \omega_{\mathrm{GN}} \right) \right] \right) \right]^{z=h_U} \mathrm{d}x \\
&- \int_{a^+}^{d^+} \left[\delta_\theta \sqrt{1+{h_{Rx}}^2} \frac{\partial \omega_{\mathrm{GN}}}{\partial \theta} + \delta_{h_R} \left(\sqrt{1+{h_{Rx}}^2} \frac{\partial \omega_{\mathrm{GN}}}{\partial \theta} \frac{\partial \theta}{\partial z} \right.\right. \\
&\qquad \left.\left. - \frac{\partial}{\partial x} \left[\frac{\partial}{\partial h_{Rx}} \left(\sqrt{1+{h_{Rx}}^2}\, \omega_{\mathrm{GN}} \right) \right] \right) \right]^{z=h_R} \mathrm{d}x \\
&- \delta_{d^+} \left[\sqrt{1+{h_{Rx}}^2}\, \omega_{\mathrm{GN}} - h_{Rx} \frac{\partial}{\partial h_{Rx}} \left(\sqrt{1+{h_{Rx}}^2}\, \omega_{\mathrm{GN}} \right) \right]^{x=d^+} \\
&+ \delta_{d^-} \left[\sqrt{1+{h_{Lx}}^2}\, \omega_{\mathrm{GN}} - h_{Lx} \frac{\partial}{\partial h_{Lx}} \left(\sqrt{1+{h_{Lx}}^2}\, \omega_{\mathrm{GN}} \right) \right]^{x=d^-} . \qquad \text{(A.19)}
\end{aligned}$$

For the nematic–solid interface energy E_{NS}, given by (A.11), the variations (A.14) in (A.11) yields the variation δE_{NS}:

$$\delta E_{\mathrm{NS}} = \int_{d^-}^{d^+} \left[\delta_\theta \frac{\partial \omega_{\mathrm{NS}}}{\partial \theta} \right]_{z=0} \mathrm{d}x + \delta_{d^+} \left[\omega_{\mathrm{NS}} \right]_{x=d^+} - \delta_{d^-} \left[\omega_{\mathrm{NS}} \right]_{x=d^-} , \qquad \text{(A.20)}$$

which is identical to result obtained in Section 5.2, namely (5.23).

For the gas–solid interface energy E_{GS}, given by (A.12), the variation δE_{GS} is found by combining the gas–solid interface energy (A.12), and the variations (A.14), yielding

$$\delta E_{\mathrm{GS}} = \delta_{d^-} \left[\omega_{\mathrm{GS}} \right]_{x=d^-} - \delta_{d^+} \left[\omega_{\mathrm{GS}} \right]_{x=d^+} , \qquad \text{(A.21)}$$

which is identical to result obtained in Section 5.2, namely (5.24).

Finally, the variation of the area constraint $\mathcal{C}_{\text{area}}$, given by (A.13), is found by combining (A.13), the variations (A.14), and the two Dirichlet boundary conditions $h_L(d^-) = 0 = h_R(d^+)$ to give

$$\delta\mathcal{C}_{\text{area}} = -\int_{a^-}^{a^+} p_0\,\delta_{h_U}\,\mathrm{d}x + \int_{a^-}^{d^-} p_0\,\delta_{h_L}\,\mathrm{d}x + \int_{d^+}^{a^+} p_0\,\delta_{h_R}\,\mathrm{d}x. \tag{A.22}$$

Again we proceed identically to Section 5.2 and seek extrema of the free energy E for which $\delta F = 0$, and the variations δ_θ, $[\delta_\theta]^{z=0}$, $[\delta_\theta]^{z=h_L}$, $[\delta_\theta]^{z=h_U}$, $[\delta_\theta]^{z=h_R}$, δ_{h_L}, δ_{h_U}, δ_{h_R}, δ_{d^+} and δ_{d^-} are independent and arbitrary, their coefficients in δF, given by (5.15), must be zero. Together with the area constraint (5.5) and the two boundary conditions $h_L(d^-) = 0$ and $h_R(d^+) = 0$, the coefficients of each variation yield the governing equations for a nematic ridge, as described in the next section.

The meaning of each of the coefficients δ_θ, $[\delta_\theta]_{z=0}$, $[\delta_\theta]_{z=h_L}$, $[\delta_\theta]_{z=h_U}$, $[\delta_\theta]_{z=h_R}$, δ_{h_L}, δ_{h_U}, δ_{h_R}, δ_{d^+} and δ_{d^-} correspond to meaning of the coefficients discussed in 5.3. However, there are now three coefficients representing the balance-couple-condition on the gas–nematic interface, namely $[\delta_\theta]_{z=h_L}$, $[\delta_\theta]_{z=h_U}$, $[\delta_\theta]_{z=h_R}$, and the nematic Young–Laplace equation, namely δ_{h_L}, δ_{h_U}, δ_{h_R}. These equations, together with the area constraint, are summarised below.

The the balance of elastic torque within the bulk of the nematic and the balance-of-couple on the nematic–solid interface when the ridge height h is a double-valued function of x are identical to the the balance of elastic torque within the bulk of the nematic and the balance-of-couple on the nematic–solid interface stated in Section 5.3 when the ridge height h is a single-valued function of x , namely (5.27) and (5.29). The balance-of-couple condition on the three

components of the gas–nematic interface, are given by

$$\frac{\partial W}{\partial \theta_z} - h_{Lx}\frac{\partial W}{\partial \theta_x} - \sqrt{1+h_{Lx}^2}\,\frac{\partial \omega_{\mathrm{GN}}}{\partial \theta} = 0, \tag{A.23}$$

$$\frac{\partial W}{\partial \theta_z} - h_{Ux}\frac{\partial W}{\partial \theta_x} + \sqrt{1+h_{Ux}^2}\,\frac{\partial \omega_{\mathrm{GN}}}{\partial \theta} = 0, \tag{A.24}$$

$$\frac{\partial W}{\partial \theta_z} - h_{Rx}\frac{\partial W}{\partial \theta_x} - \sqrt{1+h_{Rx}^2}\,\frac{\partial \omega_{\mathrm{GN}}}{\partial \theta} = 0, \tag{A.25}$$

on $z = h_L$, $z = h_U$, and $z = h_R$, respectively. The nematic Young–Laplace equation on the three components of the gas–nematic interface, are given by

$$\begin{aligned} W - p_0 - \sqrt{1+h_{Lx}^2}\,\frac{\partial \omega_{\mathrm{GN}}}{\partial \theta}\frac{\partial \theta}{\partial z} \\ + \frac{\partial}{\partial x}\left(\sqrt{1+h_{Lx}^2}\,\frac{\partial \omega_{\mathrm{GN}}}{\partial h_{Lx}} + \frac{h_{Lx}}{\sqrt{1+h_{Lx}^2}}\,\omega_{\mathrm{GN}}\right) = 0, \end{aligned} \tag{A.26}$$

$$\begin{aligned} W - p_0 + \sqrt{1+h_{Ux}^2}\,\frac{\partial \omega_{\mathrm{GN}}}{\partial \theta}\frac{\partial \theta}{\partial z} \\ - \frac{\partial}{\partial x}\left(\sqrt{1+h_{Ux}^2}\,\frac{\partial \omega_{\mathrm{GN}}}{\partial h_{Ux}} + \frac{h_{Ux}}{\sqrt{1+h_{Ux}^2}}\,\omega_{\mathrm{GN}}\right) = 0, \end{aligned} \tag{A.27}$$

$$\begin{aligned} W - p_0 - \sqrt{1+h_{Rx}^2}\,\frac{\partial \omega_{\mathrm{GN}}}{\partial \theta}\frac{\partial \theta}{\partial z} \\ + \frac{\partial}{\partial x}\left(\sqrt{1+h_{Rx}^2}\,\frac{\partial \omega_{\mathrm{GN}}}{\partial h_{Rx}} + \frac{h_{Rx}}{\sqrt{1+h_{Rx}^2}}\,\omega_{\mathrm{GN}}\right) = 0, \end{aligned} \tag{A.28}$$

on $z = h_L$, $z = h_U$, and $z = h_R$, respectively, and the nematic Young equations [47] at the contact lines are given by

$$\omega_{\mathrm{NS}} - \omega_{\mathrm{GS}} - \sqrt{1+h_{Lx}^2}\,\omega_{\mathrm{GN}} + h_{Lx}\frac{\partial}{\partial h_x}\left(\sqrt{1+h_{Lx}^2}\,\omega_{\mathrm{GN}}\right) = 0, \tag{A.29}$$

$$\omega_{\mathrm{NS}} - \omega_{\mathrm{GS}} - \sqrt{1+h_{Rx}^2}\,\omega_{\mathrm{GN}} + h_{Rx}\frac{\partial}{\partial h_x}\left(\sqrt{1+h_{Rx}^2}\,\omega_{\mathrm{GN}}\right) = 0, \tag{A.30}$$

at $x = d^-$ and $x = d^+$, respectively. We note that the nematic Young equations (A.29) and (A.30) are different to (5.31); however, as we will see shortly, when the Young equations are expressed in terms of the contact angles with (A.3) and

(A.4) the Young equations are identical.

The full set of governing equations (5.27), (5.29), and (A.23)–(A.30) is then completed by the area constraint (5.5), the two Dirichlet boundary conditions $h_L(d^-) = 0 = h_R(d^+)$, and the continuity conditions (A.1) and (A.2). Once explicit forms of the energy densities W, ω_{GN}, ω_{NS} and ω_{GS} have been prescribed, the solutions for θ, h_L, h_U, h_R, d^-, d^+ and p_0 can be determined.

A.1 Governing equations for the Oseen–Frank bulk elastic energy density and Rapini–Papoular interface energy densities

Similarly to Section (5.2), the Rapini–Papoular energy densities ω_{GN} and ω_{NS}, the constant gas–solid interface energy density, and Oseen–Frank elastic energy density W, given by (5.33), (5.34), (5.37) and (5.32), respectively, are now used with the unit outward normals (A.5)–(A.8), to specify the governing equations. In particular, we recover the the balance of elastic torque within the bulk of the nematic (5.38) and the balance of couple on the nematic–solid interface equation (5.40), and the balance of couple on the gas–nematic interface equation (5.39) is now given by

$$K\left(\theta_z - h_{Lx}\theta_x\right) - \frac{C_{\mathrm{GN}}}{2\sqrt{1+h_{Lx}^2}}\left(\left(h_{Lx}^2-1\right)\sin 2\theta + 2h_{Lx}\cos 2\theta\right) = 0, \tag{A.31}$$

$$K\left(\theta_z - h_{Ux}\theta_x\right) + \frac{C_{\mathrm{GN}}}{2\sqrt{1+h_{Ux}^2}}\left(\left(h_{Ux}^2-1\right)\sin 2\theta + 2h_{Ux}\cos 2\theta\right) = 0, \tag{A.32}$$

$$K\left(\theta_z - h_{Rx}\theta_x\right) - \frac{C_{\mathrm{GN}}}{2\sqrt{1+h_{Rx}^2}}\left(\left(h_{Rx}^2-1\right)\sin 2\theta + 2h_{Rx}\cos 2\theta\right) = 0, \tag{A.33}$$

on $z = h_L$, $z = h_U$, and $z = h_R$, respectively, the nematic Young–Laplace equation (5.41) is now given by

$$p_0 - W - \sigma_{\mathrm{GN}} \frac{h_{Lxx}}{\left(1 + h_{Lx}^2\right)^{3/2}} - \frac{C_{\mathrm{GN}}}{4\left(1 + h_{Lx}^2\right)^{5/2}} \Bigg[3h_{Lxx} \Big((h_{Lx}^2 - 1)\cos 2\theta - 2h_{Lx} \sin 2\theta \Big) + (1 + h_{Lx}^2) \Bigg(4\cos 2\theta \Big[\theta_x - h_{Lx}(1 + h_{Lx}^2)\theta_z \Big] + 2\sin 2\theta \Big[(1 - h_{Lx}^4)\theta_z + h_{Lx}(3 + h_{Lx}^2)\theta_x \Big] \Bigg) \Bigg] = 0, \quad \text{(A.34)}$$

$$p_0 - W - \sigma_{\mathrm{GN}} \frac{h_{Uxx}}{\left(1 + h_{Ux}^2\right)^{3/2}} - \frac{C_{\mathrm{GN}}}{4\left(1 + h_{Ux}^2\right)^{5/2}} \Bigg[3h_{Uxx} \Big((h_{Ux}^2 - 1)\cos 2\theta - 2h_{Ux} \sin 2\theta \Big) + (1 + h_{Ux}^2) \Bigg(4\cos 2\theta \Big[\theta_x - h_{Ux}(1 + h_{Ux}^2)\theta_z \Big] + 2\sin 2\theta \Big[(1 - h_{Ux}^4)\theta_z + h_{Ux}(3 + h_{Ux}^2)\theta_x \Big] \Bigg) \Bigg] = 0, \quad \text{(A.35)}$$

$$p_0 - W - \sigma_{\mathrm{GN}} \frac{h_{Rxx}}{\left(1 + h_{Rx}^2\right)^{3/2}} - \frac{C_{\mathrm{GN}}}{4\left(1 + h_{Rx}^2\right)^{5/2}} \Bigg[3h_{Rxx} \Big((h_{Rx}^2 - 1)\cos 2\theta - 2h_{Rx} \sin 2\theta \Big) + (1 + h_{Rx}^2) \Bigg(4\cos 2\theta \Big[\theta_x - h_{Rx}(1 + h_{Rx}^2)\theta_z \Big] + 2\sin 2\theta \Big[(1 - h_{Rx}^4)\theta_z + h_{Rx}(3 + h_{Rx}^2)\theta_x \Big] \Bigg) \Bigg] = 0, \quad \text{(A.36)}$$

on $z = h_L$, $z = h_U$, and $z = h_R$, respectively, and we recover the nematic Young equations (5.42) and (5.43).

In summary, when the ridge height h is a double-valued function of x the balance of elastic torque within the bulk of the nematic (5.38), the interface equations (5.40) and (A.31)–(A.36), Young equations (5.42) and (5.43), the two Dirichlet boundary conditions $h_L(d^-) = 0 = h_R(d^+)$, the area constraint (5.5) and continuity conditions (A.1) and (A.2) completely describe the nematic ridge.

Appendix B

Numerical procedure for solving the system (6.11)–(6.13) and (6.24)–(6.26)

The solutions presented in Chapter 5 were obtained with the programming and numerical computing platform MATLAB [142]. Specifically, MATLAB's stiff differential-algebraic equation solver *ode15s* was used to be obtain numerical solutions to the system (6.11)–(6.13) and (6.24)–(6.26). We included pseudo-time derivatives and pseudo-time coefficients, denoted by ξ_1, ξ_2, ξ_3, and ξ_4 to the system (6.11)–(6.13) and (6.24)–(6.26) so that the balance-of-couple condition on the nematic–substrate interface (6.11), the balance-of-couple condition on the gas–nematic interface (6.12), and the Young–Laplace equation (6.13), take the

forms

$$\xi_1 \frac{\mathrm{d}\theta_{\mathrm{NS}}}{\mathrm{d}t} = K\big(\theta_{\mathrm{GN}} - \theta_{\mathrm{NS}}\big) + C_{\mathrm{NS}} h \sin\theta_{\mathrm{NS}} \cos\theta_{\mathrm{NS}}, \tag{B.1}$$

$$\xi_2 \frac{\mathrm{d}\theta_{\mathrm{GN}}}{\mathrm{d}t} = K\big(\theta_{\mathrm{GN}} - \theta_{\mathrm{NS}}\big) - C_{\mathrm{GN}} h \sin\theta_{\mathrm{GN}} \cos\theta_{\mathrm{GN}}, \tag{B.2}$$

$$\xi_3 \frac{\mathrm{d}h}{\mathrm{d}t} = p_0 + h_{xx} + \frac{K}{2}\left(\frac{\theta_{\mathrm{GN}} - \theta_{\mathrm{NS}}}{h}\right)^2, \tag{B.3}$$

respectively, and the area constraint (6.26) takes the form

$$\xi_4 \frac{\mathrm{d}p_0}{\mathrm{d}t} = \frac{1}{2} - \int_0^1 h \,\mathrm{d}x. \tag{B.4}$$

The contact-line condition (6.24) and the symmetry and regularity condition (6.25) are unchanged. We numerically solved the pseudo-time-dependent equations (B.1)–(B.4), (6.24) and (6.25), and then allowed the pseudo-time-dependent numerical solutions to approach a steady state, at which point the solution of (B.1)–(B.4), (6.24) and (6.25) approaches the solution of the system (6.11)–(6.13) and (6.24)–(6.26).

All of the numerical solutions presented in the current work used the initial condition $\theta_{\mathrm{NS}} = \theta_{\mathrm{GN}} = \pi(\sin(2\pi x) + 1)/4$, $h = h_{\mathrm{iso}} = 3(1 - x^2)/4$ and $p_0 = p_{\mathrm{I}} = 3/4$ and pseudo-time coefficient values of $\xi_1 = 0.01$, $\xi_2 = 0.01$, $\xi_3 = 1$, and $\xi_4 = 0.01$. As mentioned in Section 6.1.3, during numerical testing asymmetric initial conditions for θ_{NS}, θ_{GN} and h were used, which led to symmetric solutions for h and symmetric continuous θ solutions. The asymmetric discontinuous θ solutions mentioned in Section 6.1.2 were generated by numerically solving the system (6.11)–(6.15) with asymmetric initial conditions. In particular, the asymmetric initial condition $\theta_{\mathrm{NS}} = \theta_{\mathrm{GN}} = \pi(\tanh(4(x - \bar{x})))/2$, where $x = \bar{x}$ $(0 < |\bar{x}| < 1)$, $h = h_{\mathrm{iso}} = 3(1 - x^2)/4$ and $p_0 = p_{\mathrm{I}} = 3/4$ was used to obtain asymmetric discontinuous θ solutions with a discontinuity at $x = \bar{x}$.

Appendix C

Parametric solution for the system (6.11)–(6.13) and (6.24)–(6.26)

In this Appendix we provide a parametric solution of equations (6.11)–(6.13) and (6.24)–(6.26). First we introduce a parameter $\kappa = \kappa(x)$ defined by

$$\kappa = \frac{2K}{C_{\rm NS}C_{\rm GN}}\frac{\theta_{\rm GN} - \theta_{\rm NS}}{h}, \tag{C.1}$$

in terms of which (6.11) and (6.12) give

$$\sin 2\theta_{\rm NS} = -C_{\rm GN}\kappa, \quad \sin 2\theta_{\rm GN} = C_{\rm NS}\kappa. \tag{C.2}$$

Therefore $\theta_{\rm NS}$, $\theta_{\rm GN}$ and h may be written in terms of κ as

$$\theta_{\rm NS} = \frac{m_{\rm NS}\pi}{2} - \frac{(-1)^{m_{\rm NS}}}{2}\sin^{-1}(C_{\rm GN}\kappa), \tag{C.3}$$

$$\theta_{\rm GN} = \frac{m_{\rm GN}\pi}{2} + \frac{(-1)^{m_{\rm GN}}}{2}\sin^{-1}(C_{\rm NS}\kappa), \tag{C.4}$$

$$h = \frac{K}{C_{\rm NS}C_{\rm GN}}f(\kappa), \tag{C.5}$$

where $m_{\rm NS}$ and $m_{\rm GN}$ are integers, and $f(\kappa)$ is defined by $f(\kappa) = 2(\theta_{\rm GN} - \theta_{\rm NS})/\kappa$, that is,

$$f(\kappa) = \frac{(m_{\rm GN} - m_{\rm NS})\pi}{\kappa} + \frac{(-1)^{m_{\rm GN}}\sin^{-1}(C_{\rm NS}\kappa) + (-1)^{m_{\rm NS}}\sin^{-1}(C_{\rm GN}\kappa)}{\kappa}. \tag{C.6}$$

Clearly the representation of $\theta_{\rm NS}$, $\theta_{\rm GN}$ and h, given by (C.3)–(C.5), respectively, requires that $-1 \leq C_{\rm NS}\kappa \leq 1$ and $-1 \leq C_{\rm GN}\kappa \leq 1$. Since $\theta_{\rm NS}$, $\theta_{\rm GN}$, h, h_x and h_{xx} are continuous, and since $\theta_{\rm NS} = \theta_{\rm GN} \equiv m\pi/2$ for $x \geq x_{\rm c}$ (where again $x_{\rm c}$ denotes the position $x = x_{\rm c}$ where $h(x_{\rm c}) = |h_{\rm c}|$), equation (C.1) shows that $\kappa = 0$ at $x = x_{\rm c}$, and so (C.3) and (C.4) require that $m_{\rm NS} = m_{\rm GN} = m$ on the branch of solutions that contains $x = x_{\rm c}$. Without loss of generality we may take $m_{\rm NS}$ and $m_{\rm GN}$ to be either $m_{\rm NS} = m_{\rm GN} = 0$ corresponding to a $\rm D_P$ solution or $m_{\rm NS} = m_{\rm GN} = 1$ corresponding to a $\rm D_H$ solution on the branch of solutions that contains $x = x_{\rm c}$. We remind the reader that inspection of (6.35) shows that $\rm D_P$ solutions (i.e. $m_{\rm NS} = m_{\rm GN} = 0$ on the branch of solutions that contains $x = x_{\rm c}$) are energetically preferred to $\rm D_H$ solutions for $h_{\rm c} > 0$ and $\rm D_P$ solutions (i.e. $m_{\rm NS} = m_{\rm GN} = 1$ on the branch of solutions that contains $x = x_{\rm c}$) are energetically preferred to $\rm D_H$ solutions for $h_{\rm c} > 0$.

Inspection of the solutions of the system (6.11)–(6.13) and (6.24)–(6.26) shows that for certain values of $C_{\rm NS}$ and $C_{\rm GN}$ (see those shown in Figures 6.4 and 6.5), either both $\theta_{\rm NS}$ and $\theta_{\rm GN}$ are monotonic functions of x or one of $\theta_{\rm NS}$ and $\theta_{\rm GN}$ is a monotonic function of x and the other is non-monotonic. In the case that both

$\theta_{\rm NS}$ and $\theta_{\rm GN}$ are monotonic functions of x, the branch of solutions that contains $x = x_{\rm c}$ is valid for the entire central region $0 \leq x \leq x_{\rm c}$. However, when one of $\theta_{\rm NS}$ and $\theta_{\rm GN}$ is a monotonic function of x and the other is non-monotonic, the branch of solutions that contains $x = x_{\rm c}$ is valid only in an interval $x_{\rm s} \leq x \leq x_{\rm c}$, where $x = x_{\rm s}$ is the position of a stationary point of $\kappa(x)$, at which κ takes the stationary value $\kappa = \kappa_{\rm s}$ where

$$\kappa_{\rm s} = \frac{\mathrm{sgn}(C_{\rm NS})}{\max(|C_{\rm NS}|, |C_{\rm GN}|)}. \tag{C.7}$$

At $x = x_{\rm s}$ the angle $\theta_{\rm NS}$ (if $|C_{\rm NS}| < |C_{\rm GN}|$) or $\theta_{\rm GN}$ (if $|C_{\rm NS}| > |C_{\rm GN}|$) takes the value $\pi/4$, and the other angle, $\theta_{\rm GN}$ or $\theta_{\rm NS}$ respectively, has a stationary point as a function of x. To the left of $x_{\rm s}$, that is, in the interval $0 \leq x \leq x_{\rm s}$, the angle that takes the value $\pi/4$ at $x = x_{\rm s}$ must change to a different branch, corresponding to a different value of either $m_{\rm NS}$ or $m_{\rm GN}$ in the representation (C.3)–(C.5). Inspection of solutions of the system (6.11)–(6.13) and (6.24)–(6.26) allow us to assign regions (I)–(VI) of the $C_{\rm NS}$–$C_{\rm GN}$ parameter plane, shown in Figure 6.7, where either both $\theta_{\rm NS}$ and $\theta_{\rm GN}$ are monotonic functions of x or one of $\theta_{\rm NS}$ and $\theta_{\rm GN}$ is a monotonic function of x and the other is non-monotonic, and therefore we can assign regions of the $C_{\rm NS}$–$C_{\rm GN}$ parameter plane where a change in the solution branch is required. Table C.1 provides the relevant values of $m_{\rm NS}$ and $m_{\rm GN}$ on the different branches, as indicated by numerical solutions of the system (6.11)–(6.13) and (6.24)–(6.26), which depend on the regions (I)–(VI) of the $C_{\rm NS}$–$C_{\rm GN}$ parameter plane shown in Figure 6.7.

To complete the solution we need to relate κ to x. Substitution from (C.1) and (C.5) into (6.13) gives a differential equation for κ, namely

$$p_0 + \frac{C_{\rm NS}^2 C_{\rm GN}^2}{8K}\kappa^2 = -\frac{K}{C_{\rm NS}C_{\rm GN}}[f(\kappa)]_{xx} \tag{C.8}$$

Region of Figure 6.7	$m_{\rm NS}$	$m_{\rm GN}$	x
(I)	1	1	$0 \le x \le x_{\rm c}$
(II)	0	0	$0 \le x \le x_{\rm c}$
(III)	$\begin{cases} 0 \\ 1 \end{cases}$	1	$\begin{cases} 0 \le x \le x_{\rm s} \\ x_{\rm s} \le x \le x_{\rm c} \end{cases}$
(IV)	1	$\begin{cases} 0 \\ 1 \end{cases}$	$\begin{cases} 0 \le x \le x_{\rm s} \\ x_{\rm s} \le x \le x_{\rm c} \end{cases}$
(V)	0	$\begin{cases} 1 \\ 0 \end{cases}$	$\begin{cases} 0 \le x \le x_{\rm s} \\ x_{\rm s} \le x \le x_{\rm c} \end{cases}$
(VI)	$\begin{cases} 1 \\ 0 \end{cases}$	0	$\begin{cases} 0 \le x \le x_{\rm s} \\ x_{\rm s} \le x \le x_{\rm c} \end{cases}$

Table C.1: The values of $m_{\rm NS}$ and $m_{\rm GN}$ in the intervals $0 \le x \le x_{\rm s}$ and $x_{\rm s} \le x \le x_{\rm c}$ in the parametric representation of $\theta_{\rm NS}$, $\theta_{\rm GN}$ and h given by (C.3)–(C.5), respectively, for the six regions (I)–(VI) of the $C_{\rm NS}$–$C_{\rm GN}$ parameter plane shown Figure 6.7.

(which, we note, does not involve the independent variable x explicitly). Defining $q = q(x)$ by

$$q = h_x = \frac{K}{C_{\rm NS}C_{\rm GN}} f'(\kappa)\kappa_x, \tag{C.9}$$

so that

$$\kappa_x = \frac{C_{\rm NS}C_{\rm GN}}{K}\frac{q}{f'(\kappa)}, \tag{C.10}$$

we thus have

$$p_0 + \frac{C_{\rm NS}^2 C_{\rm GN}^2}{8K}\kappa^2 = -q_x = -q_\kappa \kappa_x = -\frac{C_{\rm NS}C_{\rm GN}}{K}\frac{qq_\kappa}{f'(\kappa)}. \tag{C.11}$$

Therefore

$$qq_\kappa = -\frac{K}{C_{\rm NS}C_{\rm GN}}\left(p_0 + \frac{C_{\rm NS}^2 C_{\rm GN}^2}{8K}\kappa^2\right) f'(\kappa), \tag{C.12}$$

and so, on the assumption that $h_x \le 0$ in $0 \le x \le x_{\rm c}$, we have

$$q = -\sqrt{I(\kappa)}, \tag{C.13}$$

where $I = I(\kappa)$ is defined by

$$I(\kappa) = \frac{2K}{C_{\rm NS}C_{\rm GN}}\int_\kappa^{\kappa_{\rm m}} \left(p_0 + \frac{C_{\rm NS}^2 C_{\rm GN}^2}{8K}\tilde\kappa^2\right) f'(\tilde\kappa)\,{\rm d}\tilde\kappa, \tag{C.14}$$

that is,

$$I(\kappa) = \frac{C_{\rm NS}C_{\rm GN}}{2}\left[\frac{4Kp_0 f(\tilde\kappa)}{C_{\rm NS}^2 C_{\rm GN}^2} - \frac{\tilde\kappa^2 f(\tilde\kappa)}{2} - (-1)^{m_{\rm NS}}\frac{\sqrt{1 - C_{\rm GN}^2\tilde\kappa^2}}{C_{\rm GN}} - (-1)^{m_{\rm GN}}\frac{\sqrt{1 - C_{\rm NS}^2\tilde\kappa^2}}{C_{\rm NS}}\right]_\kappa^{\kappa_{\rm m}}, \tag{C.15}$$

with $\kappa_{\rm m}$ denoting the (as yet unknown) value of κ at $x = 0$. With (C.9), equation (C.13) is

$$\frac{K}{C_{\rm NS}C_{\rm GN}} f'(\kappa)\kappa_x = -\sqrt{I(\kappa)}, \tag{C.16}$$

which may be integrated to give x in terms of κ:

$$x = J(\kappa), \tag{C.17}$$

where $J = J(\kappa)$ is defined by

$$J(\kappa) = \frac{K}{C_{\rm NS}C_{\rm GN}} \int_{\kappa}^{\kappa_{\rm m}} \frac{f'(\tilde{\kappa})}{\sqrt{I(\tilde{\kappa})}}\, {\rm d}\tilde{\kappa}. \tag{C.18}$$

The positions $x = x_{\rm c}$ and $x = x_{\rm s}$ correspond to $\kappa = 0$ and $\kappa = \kappa_{\rm s}$, respectively, and so

$$x_{\rm c} = J(0), \tag{C.19}$$

$$x_{\rm s} = J(\kappa_{\rm s}). \tag{C.20}$$

At $x = x_{\rm c}$ the parametric solution must match with the solution in the edge region, i.e. where $x_{\rm c} \le x \le 1$, in which either $\theta_{\rm NS} = \theta_{\rm GN} \equiv 0$ or $\theta_{\rm NS} = \theta_{\rm GN} \equiv \pi/2$ and the free surface height is a quadratic function of x with unknown coefficients given by (6.34). Continuity of h and h_{xx} at $x = x_{\rm c}$ are trivially satisfied, and continuity of h_x at $x = x_{\rm c}$ leads to the condition

$$\frac{|h_{\rm c}|}{1 - x_{\rm c}} - \frac{1}{2} p_0 (1 - x_{\rm c}) = \sqrt{I(0)}. \tag{C.21}$$

In addition using (C.5), (C.17) and (6.34) the area constraint (6.26) reduces to

$$1 = |h_{\rm c}|(1 - x_{\rm c}) + \frac{p_0}{6}(1 - x_{\rm c})^3 + \frac{2K^2}{C_{\rm NS}^2 C_{\rm GN}^2} \int_0^{\kappa_{\rm m}} \frac{f(\kappa) f'(\kappa)}{\sqrt{I(\kappa)}}\, {\rm d}\kappa. \tag{C.22}$$

In summary, when $h > |h_{\rm c}|$ the solution for $\theta_{\rm NS}$, $\theta_{\rm GN}$ and h in $0 \le x < x_{\rm c}$ is given parametrically (with parameter κ) by (C.3)–(C.5) and (C.17), with the values of $m_{\rm NS}$ and $m_{\rm GN}$ and the κ intervals as specified in Table C.1, and when $h \le |h_{\rm c}|$ the solution for $\theta_{\rm NS}$, $\theta_{\rm GN}$ and h in $x_{\rm c} \le x \le 1$ is given explicitly by $\theta_{\rm NS} = \theta_{\rm GN} \equiv 0$ or $\theta_{\rm NS} = \theta_{\rm GN} \equiv \pi/2$ and (6.34), in which, the four unknown constants $x_{\rm c}$, $x_{\rm s}$, p_0, and $\kappa_{\rm m}$ must be determined numerically from the four algebraic relations (C.19)–(C.22). The height of the free surface in the middle of the ridge and the

contact angle β may then be determined by

$$h_{\rm m} = \frac{K}{C_{\rm NS}C_{\rm GN}} f(\kappa_{\rm m}) \quad \text{and} \quad \beta = -\frac{1}{2}p_0(1-x_{\rm c}) - \frac{|h_{\rm c}|}{1-x_{\rm c}}, \tag{C.23}$$

respectively.

C.1 Applying the parametric solution to the solution shown in Figure 6.4(d) and Figure 6.5(d)

We now consider a particular example to demonstrate use of this parametric solution. Consider the solution shown in Figure 6.4(d) and Figure 6.5(d) where $K = 1$, $C_{\rm NS} = -3$, and $C_{\rm GN} = 2.5$ which is within region (V) of the $C_{\rm NS}$–$C_{\rm GN}$ parameter plane. As stated in Table C.1, for region (V) of the $C_{\rm NS}$–$C_{\rm GN}$ parameter plane $m_{\rm NS} = 0$ and $m_{\rm GN} = 1$ for $0 \le x \le x_{\rm s}$, and $m_{\rm NS} = m_{\rm GN} = 0$ for $x_{\rm s} \le x \le x_{\rm c}$, and hence (C.3)–(C.5) take the forms given by

$$\theta_{\rm NS} = -\frac{1}{2}\sin^{-1}(C_{\rm GN}\kappa) \quad \text{for} \quad 0 \le x \le x_{\rm c}, \tag{C.24}$$

$$\theta_{\rm GN} = \begin{cases} \dfrac{\pi}{2} - \dfrac{1}{2}\sin^{-1}(C_{\rm NS}\kappa) & \text{for} \quad 0 \le x \le x_{\rm s}, \\ \dfrac{1}{2}\sin^{-1}(C_{\rm NS}\kappa) & \text{for} \quad x_{\rm s} \le x \le x_{\rm c}, \end{cases} \tag{C.25}$$

$$h = \begin{cases} \dfrac{K\left[\pi - \sin^{-1}(C_{\rm NS}\kappa) + \sin^{-1}(C_{\rm GN}\kappa)\right]}{C_{\rm NS}C_{\rm GN}\kappa} & \text{for} \quad 0 \le x \le x_{\rm s}, \\ \dfrac{K\left[\sin^{-1}(C_{\rm NS}\kappa) + \sin^{-1}(C_{\rm GN}\kappa)\right]}{C_{\rm NS}C_{\rm GN}\kappa} & \text{for} \quad x_{\rm s} \le x \le x_{\rm c}, \end{cases} \tag{C.26}$$

respectively, where κ is obtained from (C.17) with the algebraic conditions (C.19)–(C.22). In this case $\theta_{\rm NS}$ increases from $-(1/2)\sin^{-1}(C_{\rm GN}\kappa_{\rm m})$ at $x = 0$ to a maximum value $-(1/2)\sin^{-1}(C_{\rm GN}/C_{\rm NS})$ at $x = x_{\rm s}$, and then decreases to 0 at $x = x_{\rm c}$,

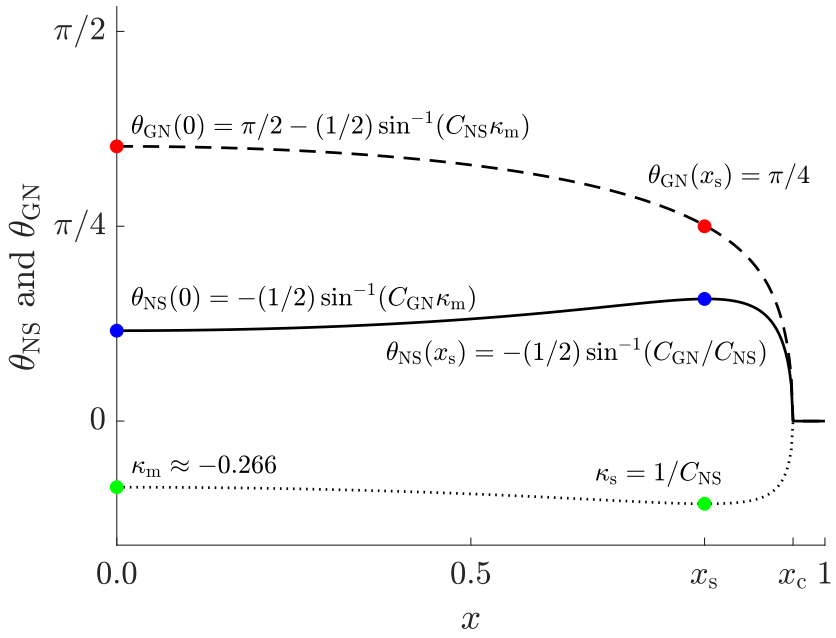

Figure C.1: Solutions for the director angle on the nematic–substrate interface θ_{NS} (solid line) and the gas–nematic interface θ_{GN} (dashed line) obtained using the parametric solution given in this Appendix for $K = 1$, $C_{\mathrm{NS}} = -3$ and $C_{\mathrm{GN}} = 2.5$. The parameter κ (dotted line) is also plotted and the values of θ_{NS} (blue dots), θ_{GN} (red dots), κ (green dots) at $x = 0$ and $x = x_{\mathrm{s}}$ are labelled.

whereas θ_{GN} decreases monotonically from $\pi/2 - (1/2)\sin^{-1}(C_{\mathrm{NS}}\kappa_{\mathrm{m}})$ at $x = 0$ to 0 at $x = x_{\mathrm{c}}$, passing through the value $\theta_{\mathrm{GN}} = \pi/4$ at $x = x_{\mathrm{s}}$, as shown in Figure C.1.

Corresponding descriptions for other values of C_{NS} and C_{GN} are similar, but are omitted here for brevity.

Appendix D

Asymptotic analysis of completely distorted D solutions

Unlike $\mathrm{D_H}$ and $\mathrm{D_P}$ solutions, significant progress can be made asymptotically for D solutions in the limits of small $C_{\mathrm{NS}} = -C_{\mathrm{GN}}$ and large $C_{\mathrm{NS}} = -C_{\mathrm{GN}}$. In order to make analytical progress in this case we set $C = C_{\mathrm{NS}} = -C_{\mathrm{GN}}$, and note that the system (6.11)–(6.13) and (6.24)–(6.26) has solutions for θ_{NS} and θ_{GN} of the form

$$\theta_{\mathrm{NS}} = \psi + \delta \quad \text{and} \quad \theta_{\mathrm{GN}} = \psi - \delta, \tag{D.1}$$

where ψ is a constant and $\delta = \delta(x)$. Without loss of generality we consider only $C > 0$ for which $C_{\mathrm{NS}} > 0$ and $C_{\mathrm{GN}} < 0$, and note that solutions for $C < 0$ can simply be obtained from the solutions for $C > 0$ using (6.22). From (D.1) and (6.10) the solution for the director angle is given by

$$\theta = \psi + \left(1 - \frac{2z}{h}\right)\delta, \tag{D.2}$$

and therefore θ takes the constant value $\theta(x, z = h/2) \equiv \psi$ on $z = h/2$.

Using (D.1) the governing equations (6.11)–(6.13) can be expressed in terms of the unknowns δ, ψ, and h and the parameters C and K as

$$0 = -4K\delta + Ch\left(\sin 2\psi \cos 2\delta + \cos 2\psi \sin 2\delta\right), \tag{D.3}$$

$$0 = -4K\delta + Ch\left(\sin 2\psi \cos 2\delta - \cos 2\psi \sin 2\delta\right), \tag{D.4}$$

$$0 = p_0 + 2K\left(\frac{\delta}{h}\right)^2 + h_{xx}. \tag{D.5}$$

Subtracting (D.4) from (D.3) yields

$$\psi = \frac{\pi}{4} + \frac{p\pi}{2}, \tag{D.6}$$

where p is any integer. We note that because of the equivalence of the director angles θ and $\theta + m\pi$ mentioned earlier, all solutions with odd p are identical, and all solutions with even p are identical. Without loss of generality we set $p = 0$ so that $\psi = \pi/4$ and note that solutions with even p can be obtained by adding $p\pi$, and solutions with odd p can be obtained by adding $(p-1)\pi$ and using (6.22).

Combining (D.3) or (D.4) and (D.6) and rearranging yields an expression for h in terms of δ, namely

$$h = \frac{4K}{C}\frac{\delta}{\cos 2\delta}, \tag{D.7}$$

where the equation satisfied by δ is given by combining (D.5) and (D.7) to yield

$$0 = p_0 + \frac{C^2}{8K}\cos^2 2\delta + \frac{4K}{C}\frac{\mathrm{d}^2}{\mathrm{d}x^2}\left(\frac{\delta}{\cos 2\delta}\right), \tag{D.8}$$

which must, in general, be solved numerically. The appropriate conditions on δ

are

$$\delta = 0 \quad \text{at} \quad x = \pm 1, \tag{D.9}$$

$$\delta_x = 0 \quad \text{at} \quad x = 0, \tag{D.10}$$

$$\frac{C}{8K} = \int_0^1 \frac{\delta}{\cos 2\delta}\, \mathrm{d}x, \tag{D.11}$$

which are obtained from the contact-line condition (6.24), the symmetry and regularity condition (6.25) and the area constraint (6.26) with (D.7), respectively. From (D.2) and (D.9), for D solutions the director at the contact line is given by $\boldsymbol{n} = (1/\sqrt{2})(1, \pm 1)$.

We now consider the solutions of (D.7)–(D.11) in two useful, albeit specialised, asymptotic limits for which asymptotic solutions indicate the dependence of anchoring effects on both the director angle and the height of the ridge. In particular, we consider the limit of small C, where antagonistic anchoring effects are much weaker than elastic, namely $C \ll K$, and in the limit of large C, where antagonistic anchoring effects are much stronger than elastic, namely $C \gg K$.

D.1 Asymptotic solution in the limit of small C

In the limit $C \to 0$ we seek asymptotic solutions for δ and p_0 in powers of C in the forms

$$\delta = \delta_0 + C\delta_1 + C^2\delta_2 + C^3\delta_3 + C^4\delta_4 + O(C^5), \tag{D.12}$$

$$p_0 = p_{0,0} + Cp_{0,1} + C^2p_{0,2} + C^3p_{0,3} + C^4p_{0,4} + O(C^5), \tag{D.13}$$

and note that the asymptotic solution for h in powers of C can be obtained form (D.7) and (D.12). Substituting the expansions (D.12) and (D.13) into (D.7)–

(D.11), we obtain the asymptotic solutions for h, δ and p_0, given by

$$h = \frac{3}{4}\left(1-x^2\right) - C^4\frac{3}{35840\,K^3}\left(1-x^2\right)\left(5-28x^2+7x^4\right) + O(C^5), \tag{D.14}$$

$$\delta = C\frac{3}{16\,K}\left(1-x^2\right) - C^3\frac{27}{2048\,K^3}\left(1-x^2\right)^3 + O(C^5), \tag{D.15}$$

$$p_0 = \frac{3}{2} - C^2\frac{1}{8K} + C^4\frac{27}{2240\,K^3} + O(C^5). \tag{D.16}$$

Combining (D.1), (D.6), (D.15) and (6.10) yields the solution for the director angle θ given by

$$\theta = \frac{\pi}{4} + \frac{3C}{16\,K}\left(1-x^2\right)\left(1-\frac{2z}{h}\right) + O(C^3). \tag{D.17}$$

At leading order in C, θ is uniform everywhere with $\theta \equiv \psi = \pi/4$ (i.e. the average of planar and homeotropic orientation), and $p_0 = p_{\mathrm{I}}$ and $h = h_{\mathrm{iso}}$. At first order in C, θ is quadratic function of x.

Using (D.14), (D.15), (6.17) and (6.18) the second-order energy ΔE is given by

$$\Delta E = \frac{3}{4} - \frac{C^2}{8K} + O(C^3), \tag{D.18}$$

which is always less than the second-order energy for the H solution and P solution with $C = C_{\mathrm{NS}} = -C_{\mathrm{GN}}$, which is given by $\Delta E_{\mathrm{P}} = \Delta E_{\mathrm{H}} = 3/4$. Therefore in the limit of small $C = C_{\mathrm{NS}} = -C_{\mathrm{GN}}$, the completely distorted solutions given by (D.14)–(D.15) are energetically preferred to uniform solutions given by (6.27).

D.2 Asymptotic solution in the limit of large C

In the limit $C \to \infty$, (D.8) is a singular differential equation for δ. Inspection of (D.8) yields the appropriate outer solution $\delta = \delta_0 + O(C^{-1})$ where

$$\delta_0 = \frac{\pi}{4} + \frac{q\pi}{2}, \tag{D.19}$$

and q is any integer. The outer solution for the director angle is therefore given by

$$\theta = \frac{\pi}{2}\left[q + 1 - (2q+1)\frac{z}{h}\right] + O(C^{-1}). \tag{D.20}$$

Consideration of the second-order energy, given by (6.17) and (6.18), yields that the outer solution (D.19) with $q = 0$, i.e. $\delta_0 = \pi/4$, is the energetically preferred outer solution. We can therefore write the outer solution δ, given by (D.19), as

$$\delta = \frac{\pi}{4} + O(C^{-1}), \tag{D.21}$$

which leads to the outer solution for the director angle, given by (D.20), namely

$$\theta = \frac{\pi}{2}\left(1 - \frac{2z}{h}\right) + O(C^{-1}). \tag{D.22}$$

Inspection of the boundary condition (D.9), the outer solution (D.22), and the Young–Laplace equation (D.8) shows that there is a boundary layer in δ near $x = 1$ of thickness $O(C^{-3/2})$. The inner solution is then given by $\delta = \bar{\delta} + O(C^{-3/2})$, where the leading-order inner solution $\bar{\delta} = \bar{\delta}(\bar{x})$ satisfies (D.8) with the rescaling $\bar{x} = \sqrt{C^3/(32K)}(1 - x)$, namely

$$\frac{\mathrm{d}^2}{\mathrm{d}\bar{x}^2}\left(\frac{\bar{\delta}}{\cos 2\bar{\delta}}\right) + \cos^2 2\bar{\delta} = 0. \tag{D.23}$$

The solution $\bar{\delta}$ is obtained by solving (D.23) numerically subject to the boundary condition $\bar{\delta} = 0$ at $\bar{x} = 0$ (obtained from (D.9)) and the matching condition $\bar{\delta} \to \pi/4$ in the limit $\bar{x} \to \infty$. A composite solution can then be formed using the outer solution and inner solution, namely

$$\delta = \frac{\pi}{4} + \bar{\delta}\left(\sqrt{\frac{C^3}{32K}}(1-x)\right) + O(C^{-1}). \tag{D.24}$$

The height of the ridge h can then be obtained by combining (D.7) and (D.24).

The composite solution (D.24) has to be obtained numerically from (D.23), and hence the solution for the height of the ridge h, given by combining (D.7) and (D.24), is unknown. Instead of proceeding numerically to obtain the height of the ridge h we approximate the solution for δ using only the outer solution δ_0, i.e. $\delta \approx \delta_0 = \pi/4$, ignoring the contribution from the boundary layer. Combining $\delta \approx \delta_0 = \pi/4$, $h \approx h_0$, (D.7) and (D.8) yields

$$p_0 + \frac{\pi^2 K}{8h_0^2} \approx -h_{0xx}, \tag{D.25}$$

which has the implicit solution for h_0, given by

$$\frac{b\pi\sqrt{K}}{4h_{m0}^{3/2}}(1-x) \approx F(a,b) - E(a,b), \tag{D.26}$$

where $F(a,b)$ and $E(a,b)$ are the incomplete elliptic integrals of the first and second kind, respectively,

$$a = \arcsin\sqrt{\frac{h_0}{h_{m0}}}, \quad \text{and} \quad b = -\frac{8p_0 h_{m0}^{\,2}}{\pi^2 K}. \tag{D.27}$$

Substituting (D.26) into the symmetry condition (6.25) and the area constraint

(6.26) leads to

$$h_{m0} = \frac{\pi^{2/3} K^{1/3} b^{2/3}}{2^{4/3}\Big(E(b)^2 - 2E(b)F(b) + F(b)^2\Big)^{2/3}} \tag{D.28}$$

and

$$\frac{1}{2} = h_{m0} + \frac{4{h_{m0}}^{5/2}\big(2(1-b)F(b) - (2-b)E(b)\big)}{3K^{1/2}b^2\pi}, \tag{D.29}$$

respectively, where $F(b)$ and $E(b)$ are the complete elliptic integrals of the first and second kind. Equations (D.28) and (D.29) can be combined to obtain an algebraic equation for m which can be solved numerically, and subsequently h_{m0} can be obtained from (D.28) or (D.29), and finally p_0 can be obtained from $p_0 = -b\pi^2 K/(8{h_{m0}}^2)$.

In the limit $x \to 1$, the approximate implicit solution for h_0, given by (D.26), satisfies

$$h_0 \simeq \frac{1}{2}\left(\frac{3\pi\sqrt{K}}{2}\right)^{2/3}(1-x)^{2/3} \quad \text{as} \quad x \to 1. \tag{D.30}$$

Differentiating (D.30) yields the approximate gradient of the height of the ridge in the limit $C \to \pm\infty$, given by

$$h_{0x} \simeq -\frac{1}{3}\left(\frac{3\pi\sqrt{K}}{2}\right)^{2/3}(1-x)^{-1/3} \quad \text{as} \quad x \to 1, \tag{D.31}$$

and so, in particular, the (scaled) contact angle approaches infinity ($\beta \approx -h_{0x} \to \infty$) as $C \to \pm\infty$.

In summary, in the limit of large C the outer solution for the director angle is given by (D.22) and approximate solution for the height of the ridge is given by (D.26).

D.3 Comparison of asymptotic solutions and numerical solutions

Figure D.1 shows the director angle on the nematic–substrate interface θ_{NS} and the gas–nematic interface θ_{GN}, and the height of the ridge h plotted as functions of x for the numerical solution of (6.11)–(6.13) and (6.24)–(6.26) (shown in Figure D.1(a) and Figure D.1(b)), small C asymptotic solutions given by (D.17) with $z = 0$, (D.17) with $z = h$ and (D.14) (shown in Figure D.1(a)) and the large C asymptotic solutions (D.22) with $z = 0$, (D.22) with $z = h$ and (D.26) (shown in Figure D.1(b)) for $K = 1$ and (a) $C = 1$ and (b) $C = 1000$. In Figure D.1(a) when $C = 1$, the height of the ridge h shows good agreement between the numerical and small C asymptotic solution, namely h is approximately isotropic, i.e. $h \approx h_{\mathrm{iso}}$, as predicted by (D.14). Figure D.1(a) also shows θ_{NS} and θ_{GN} are small perturbations around $\pi/4$, as predicted by (D.15). In Figure D.1(b) when $C = 1000$, the numerical and large C approximate asymptotic solution which is given by $\delta = \pm\pi/4$ and (D.25), show good agreement for the free surface height h for $0 \leq x \leq 1$, and for the director angles θ_{NS} and θ_{GN} except in the boundary layer near $x = 1$. We note that the numerical solution shown in Figure D.1(a) has $\Delta E \simeq 0.629$ and the numerical solution shown in Figure D.1(b) has $\Delta E \simeq -991.335$, i.e. the second-order energy for completely distorted solutions is lower than the uniform director solutions with $C = C_{\mathrm{NS}} = -C_{\mathrm{GN}}$, which is given by $\Delta E_{\mathrm{H}} = \Delta E_{\mathrm{P}} = 3/4$, and therefore completely distorted solutions are energetically preferred for $C = 1$ and $C = 1000$.

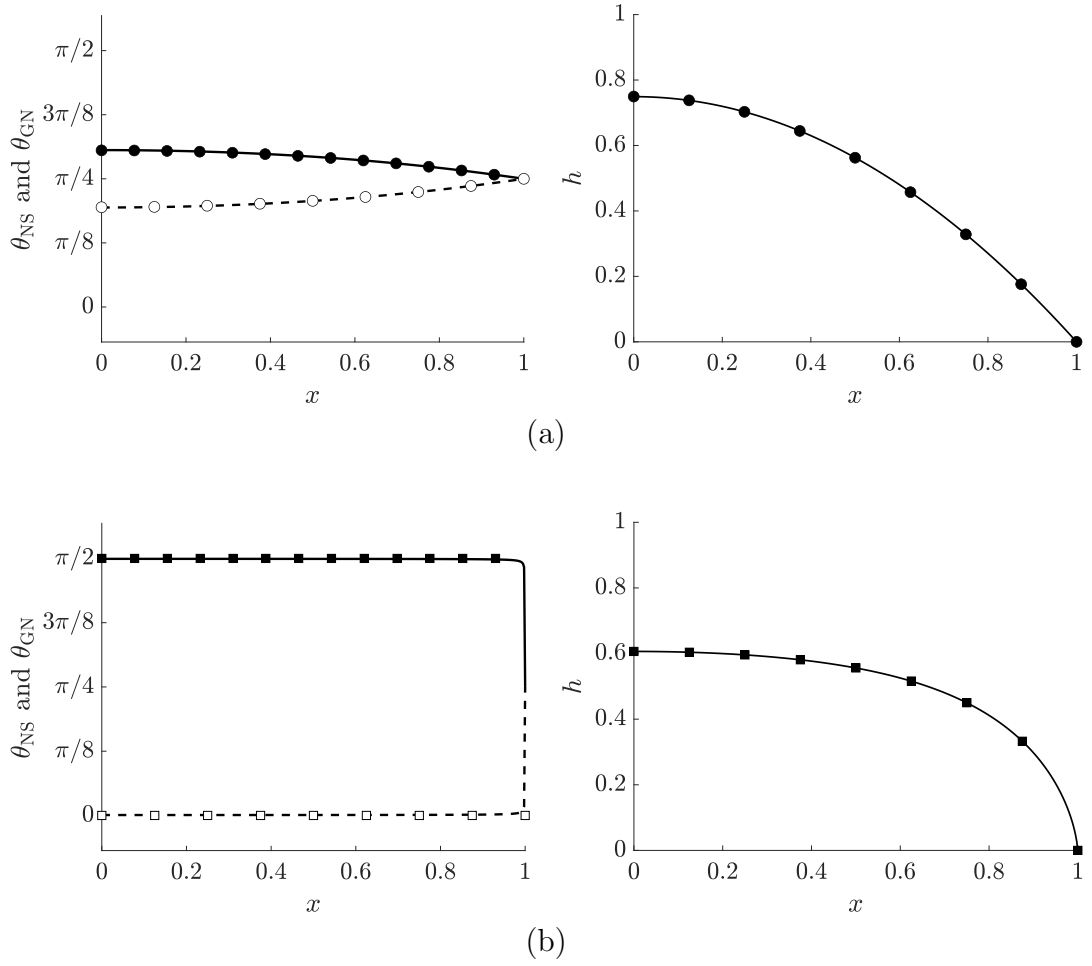

Figure D.1: The director angle on the nematic–substrate interface $\theta_{\rm NS}$ and the gas–nematic interface $\theta_{\rm GN}$, and the height of the ridge h from the numerical solution of (6.11)–(6.13) and (6.24)–(6.26) (shown in (a) and (b) by solid lines for h and $\theta_{\rm NS}$, and dashed lines for $\theta_{\rm GN}$), small-C asymptotic solutions given by (D.17) with $z = 0$, (D.17) with $z = h$, and (D.14) (shown in (a) by solid circles for $\theta_{\rm NS}$ and h and open circles for $\theta_{\rm GN}$), respectively, and the large-C asymptotic solutions (D.22) with $z = 0$, (D.22) with $z = h$, and (D.26) (shown in (b) by solid squares for h and $\theta_{\rm NS}$ and open squares for $\theta_{\rm GN}$), respectively, are plotted as functions of x for $K = 1$ for (a) $C = 1$ and (b) $C = 1000$.

Bibliography

[1] D. J. Acheson. *Elementary Fluid Dynamics*. Oxford University Press, 1990.

[2] J. Alamán, R. Alicante, J. I. Peña, and C. Sánchez-Somonlinos. Inkjet printing of functional materials for optical and photonic applications. *Materials*, 9(11):910, 2016.

[3] J. F. Algorri, D. C. Zografopoulos, V. Urruchi, and J. M. Sánchez-Pena. Recent advances in adaptive liquid crystal lenses. *Crystals*, 9(5):272, 2019.

[4] M. P. Allen. Molecular simulation of liquid crystals. *Molecular Physics*, 117(18):2391–2417, 2019.

[5] T. G. Anderson, E. Mema, L. Kondic, and L. J. Cummings. Transitions in Poiseuille flow of nematic liquid crystal. *International Journal of Non-Linear Mechanics*, 75:15–21, 2015.

[6] D. Armitage, I. Underwood, and S.-T. Wu. Transmissive liquid crystal microdisplays. In *Introduction to Microdisplays*, chapter 5, pages 149–172. John Wiley & Sons, Ltd, 2006.

[7] R. J. Atkin. Poiseuille flow of liquid crystals of the nematic type. *Archive for Rational Mechanics and Analysis*, 38(3):224–240, 1970.

[8] R. J. Atkin and T. J. Sluckin. Frank Matthews Leslie 8 March 1935–15 June 2000. *Biographical Memoirs of Fellows of the Royal Society*, 49:315–333, 2003.

[9] G. Barbero and R. Barberi. Critical thickness of a hybrid aligned nematic liquid crystal cell. *Journal de Physique*, 44(5):609–616, 1983.

[10] G. Barbero and E. K. Lenzi. Importance of the surface viscosity on the relaxation of an imposed deformation in a nematic liquid crystal cell. *Physics Letters A*, 374(13–14):1565–1569, 2010.

[11] V. M. O. Batista, M. L. Blow, and M. M. Telo da Gama. The effect of anchoring on the nematic flow in channels. *Soft Matter*, 11(23):4674–4685, 2015.

[12] P. W. Benzie and S. J. Elston. Optics of liquid crystals and liquid crystal displays. In J. Chen, W. Cranton, and M. Fihn, editors, *Handbook of Visual Display Technology*, chapter 7.2.1, pages 1365–1385. Springer, 2012.

[13] A. N. Beris and B. J. Edwards. *Thermodynamics of Flowing Systems: With Internal Microstructure*. Oxford University Press, 1994.

[14] A. S. Bhadwal, N. J. Mottram, A. Saxena, I. C. Sage, and C. V. Brown. Electrically controlled topological micro cargo transportation. *Soft Matter*, 16(12):2961–2970, 2020.

[15] P. Biscari. Curvature effects on the surface viscosity of nematic liquid crystals. *European Journal of Mechanics - B/Fluids*, 21(6):739–750, 2002.

[16] Y. Björnståhl. Untersuchungen über anisotrope flüssigkeiten. *Annalen der Physik*, 361(11):161–207, 1918.

[17] M. L. Blow and M. M. Telo da Gama. Interfacial motion in flexo- and order-electric switching between nematic filled states. *Journal of Physics: Condensed Matter*, 25(24):245103, 2013.

[18] E. Bose. Für und wider die emulsionsnatur der kristallinischen flüssigkeiten. *Zeitschrift für Chemie und Industrie der Kolloide*, 2:248, 1908.

[19] G. Boyd. LCD backlights. In J. Chen, W. Cranton, and M. Fihn, editors, *Handbook of Visual Display Technology*, chapter 7.5.1, pages 1609–1623. Springer, 2012.

[20] G. Boyd. Optical enhancement films. In J. Chen, W. Cranton, and M. Fihn, editors, *Handbook of Visual Display Technology*, chapter 7.5.2, pages 1625–1646. Springer, 2012.

[21] J. P. Bramble, D. J. Tate, D. J. Revill, K. H. Sheikh, J. R. Henderson, F. Liu, X. Zeng, G. Ungar, R. J. Bushby, and S. D. Evans. Planar alignment of columnar discotic liquid crystals by isotropic phase dewetting on chemically patterned surfaces. *Advanced Functional Materials*, 20(6):914–920, 2010.

[22] T. P. Brody, J. A. Asars, and G. D. Dixon. A 6 × 6 inch 20 lines-per-inch liquid-crystal display panel. *IEEE Transactions on Electron Devices*, 20(11):995–1001, 1973.

[23] C. V. Brown, G. G. Wells, M. I. Newton, and G. McHale. Voltage-programmable liquid optical interface. *Nature Photonics*, 3(7):403–405, 2009.

[24] W. R. Burghardt and G. G. Fuller. Transient shear flow of nematic liquid crystals: manifestations of director tumbling. *Journal of Rheology*, 34(6):959–992, 1990.

[25] C. M. Care and D. J. Cleaver. Computer simulation of liquid crystals. *Reports on Progress in Physics*, 68(11):2665–2700, 2005.

[26] T. Carlsson and F. M. Leslie. The development of theory for flow and dynamic effects for nematic liquid crystals. *Liquid Crystals*, 26(9):1267–1280, 1999.

[27] M. Cavallaro, Jr., L. Botto, E. P. Lewandowski, M. Wang, and K. J. Stebe. Curvature-driven capillary migration and assembly of rod-like particles. *Proceedings of the National Academy of Sciences*, 108(52):20923–20928, 2011.

[28] C.-T. Chen. Inkjet printing of microcomponents: theory, design, characteristics and applications. In N. Kamanina, editor, *Features of Liquid Crystal Display Materials and Processes*, chapter 3, pages 43–60. IntechOpen, 2011.

[29] H.-W. Chen, J.-H. Lee, B.-Y. Lin, S. Chen, and S.-T. Wu. Liquid crystal display and organic light-emitting diode display: present status and future perspectives. *Light: Science & Applications*, 7:17168, 2018.

[30] R. Chiarelli, S. Faetti, and L. Fronzoni. Determination of the molecular orientation at the free surface of liquid crystals from Brewster angle measurements. *Optics Communications*, 46(1):9–13, 1983.

[31] A. G. Chimielewski. Viscosity coefficients of some nematic liquid crystals. *Molecular Crystals and Liquid Crystals*, 132(3–4):339–352, 1986.

[32] P. J. Collings and M. Hird. *Introduction to Liquid Crystals.* Taylor & Francis, 1997.

[33] J. R. L. Cousins. TakeAIM 2019: [1 New Notification]. *Mathematics Today*, 56(5):206, October, 2020.

[34] J. R. L. Cousins, S. K. Wilson, N. J. Mottram, D. Wilkes, and L. Weegels. Squeezing a drop of nematic liquid crystal with strong elasticity effects. *Physics of Fluids*, 31(8):083107, 2019.

[35] J. R. L. Cousins, S. K. Wilson, N. J. Mottram, D. Wilkes, and L. Weegels. Transient flow-driven distortion of a nematic liquid crystal in channel flow with dissipative weak planar anchoring. *Physical Review E*, 102(6):062703, 2020.

[36] J. R. L. Cousins, S. K. Wilson, N. J. Mottram, D. Wilkes, L. Weegels, and K. Lin. LCT8-4: A model for the formation of mura during the One-Drop-Filling process. In *Proceedings of the 25th International Display Workshops (IDW 2018)*, volume 1, pages 125–127. Society for Information Display, 2018.

[37] M. Crespo, A. Majumdar, A. M. Ramos, and I. M. Griffiths. Solution landscapes in nematic microfluidics. *Physica D: Nonlinear Phenomena*, 351–352:1–13, 2017.

[38] D. Crowdy and H. Kang. Squeeze flow of multiply-connected fluid domains in a Hele-Shaw cell. *Journal of Nonlinear Science*, 11(4):279–304, 2001.

[39] P. K. Currie. Couette flow of a nematic liquid crystal in the presence of a magnetic field. *Archive for Rational Mechanics and Analysis*, 37(3):222–242, 1970.

[40] P. K. Currie. Parodi's relation as a stability condition for nematics. *Molecular Crystals and Liquid Crystals*, 28(3–4):335–338, 1974.

[41] P. K. Currie. Viscometric flows of anisotropic fluids. *Rheologica Acta*, 16(2):205–212, 1977.

[42] P. K. Currie. Apparent viscosity during viscometric flow of nematic liquid crystals. *Journal de Physique*, 40(5):501–505, 1979.

[43] P. K. Currie and G. P. MacSithigh. The stability and dissipation of solutions for shearing flow of nematic liquid crystals. *The Quarterly Journal of Mechanics and Applied Mathematics*, 32(4):499–511, 1979.

[44] A. J. Davidson. *Flexoelectric switching in a bistable nematic device*. PhD thesis, University of Strathclyde, 2004.

[45] A. J. Davidson and N. J. Mottram. Flexoelectric switching in a bistable nematic device. *Physical Review E*, 65(5):051710, 2002.

[46] L. R. P. de Andrade Lima and A. D. Rey. Assessing flow alignment of nematic liquid crystals through linear viscoelasticity. *Physical Review E*, 70(1):011701, 2004.

[47] P. G. de Gennes. Wetting: statics and dynamics. *Reviews of Modern Physics*, 57(3):827–863, 1985.

[48] P. G. de Gennes, F. Brochard-Wyart, and D. Quéré. *Capillarity and Wetting Phenomena*. Springer, 2004.

[49] P. G. de Gennes and J. Prost. *The Physics of Liquid Crystals*. Oxford University Press, 1993.

[50] R. F. de Souza, E. K. Lenzi, R. T. de Souza, L. R. Evangelista, Q. Li, and R. S. Zola. Surface induced twist in nematic and chiral nematic liquid crystals: stick-slip-like and constrained motion. *Soft Matter*, 14(11):2084–2093, 2018.

[51] R. F. de Souza, D.-K. Yang, E. K. Lenzi, L. R. Evangelista, and R. S. Zola. Effect of surface viscosity, anchoring energy, and cell gap on the response time of nematic liquid crystals. *Annals of Physics*, 346:14–21, 2014.

[52] R. T. de Souza, E. K. Lenzi, and L. R. Evangelista. Surface viscosity and reorientation process in an asymmetric nematic cell. *Liquid Crystals*, 37(12):1559–1568, 2010.

[53] R. D. Deegan, O. Bakajin, T. F. Dupont, G. Huber, S. R. Nagel, and T. A. Witten. Capillary flow as the cause of ring stains from dried liquid drops. *Nature*, 389:827–829, 1997.

[54] A. L. Demirel and B. Jérôme. Restructuring-induced dewetting and re-entrant wetting of thin glassy films. *Europhysics Letters*, 45(1):58–64, 1999.

[55] C. Denniston, D. Marenduzzo, E. Orlandini, and J. M. Yeomans. Lattice boltzmann algorithm for three-dimensional liquid-crystal hydrodynamics. *Philosophical Transactions of the Royal Society of London A*, 362:1745–1754, 2004.

[56] C. Denniston, E. Orlandini, and J. M. Yeomans. Simulations of liquid crystals in poiseuille flow. *Computational and Theoretical Polymer Science*, 11(5):389–395, 2001.

[57] G. Derfel. Development of the shear flow induced deformation in nematic layers. *Molecular Crystals and Liquid Crystals Incorporating Nonlinear Optics*, 191(1):377–381, 1990.

[58] G. Derfel and B. Radomska. Modelling of the simple shear flow of a flow-aligning nematic. *Liquid Crystals*, 23(5):741–748, 1997.

[59] J. Dhar and S. Chakraborty. Electrically modulated capillary filling imbibition of nematic liquid crystals. *Physical Review E*, 97(4):043107, 2018.

[60] P. Dhara and R. Mukherjee. Phase transition and dewetting of a 5CB liquid crystal thin film on a topographically patterned substrate. *Royal Society of Chemistry Advances*, 9(38):21685–21694, 2019.

[61] P. Dhara and R. Mukherjee. Influence of substrate surface properties on spin dewetting, texture and phase transition of 5CB liquid crystal thin film. *Journal of Physical Chemistry B*, 124(7):1293–1300, 2020.

[62] M. Doi. Molecular dynamics and rheological properties of concentrated solutions of rodlike polymers in isotropic and liquid crystalline phases. *Journal of Polymer Science: Polymer Physics Edition*, 19(2):229–243, 1981.

[63] D. A. Dunmur, A. Fukuda, and G. R. Luckhurst, editors. *Physical Properties of Liquid Crystals: Nematics*. The Institution of Electrical Engineers, 2001.

[64] G. E. Durand and E. G. Virga. Hydrodynamic model for surface nematic viscosity. *Physical Review E*, 59(4):4137–4142, 1999.

[65] T. Elze and T. G. Tanner. Temporal properties of liquid crystal displays: Implications for vision science experiments. *PLOS ONE*, 7(9):1–20, 09 2012.

[66] J. L. Ericksen. Anisotropic fluids. *Archive for Rational Mechanics and Analysis*, 4:231–237, 1959.

[67] J. L. Ericksen. Conservation laws for liquid crystals. *Transactions of the Society of Rheology*, 5:23–34, 1961.

[68] J. L. Ericksen. Inequalities in liquid crystal theory. *Physics of Fluids*, 9(6):1205–1207, 1966.

[69] J. L. Ericksen. Liquid crystals with variable degree of orientation. *Archive for Rational Mechanics and Analysis*, 113:97–120, 1991.

[70] C. W. Extrand. Origins of wetting. *Langmuir*, 32(31):7697–7706, 2016.

[71] K.-C. Fan, J.-Y. Chen, C.-H. Wang, and W.-C. Pan. Development of a drop-on-demand droplet generator for one-drop-fill technology. *Sensors and Actuators A: Physical*, 147(2):649–655, 2008.

[72] J. Feng and L. G. Leal. Pressure-driven channel flows of a model liquid-crystalline polymer. *Physics of Fluids*, 11(10):2821–2835, 1999.

[73] J. L. Fergason. Display devices utilizing liquid crystal light modulation, US Patent 3 731 986, filed April 1971, issued May 1973.

[74] J. Fisher and A. G. Fredrickson. Interfacial effects on the viscosity of a nematic mesophase. *Molecular Crystals*, 8(1):267–284, 1969.

[75] F. C. Frank. I. Liquid crystals. On the theory of liquid crystals. *Discussions of the Faraday Society*, 25:19–28, 1958.

[76] V. Freedericksz and V. Zolina. Forces causing the orientation of an anisotropic liquid. *Transactions of the Faraday Society*, 29:919–930, 1933.

[77] G. Friedel. Les étas mésomorphes de la matière. *Annales de Physique*, 9(18):273–474, 1922.

[78] Ch. Gähwiller. Temperature dependence of flow alignment in nematic liquid crystals. *Physical Review Letters*, 28(24):1554–1556, 1972.

[79] Ch. Gähwiller. Direct determination of the five independent viscosity coefficients of nematic liquid crystals. *Molecular Crystals and Liquid Crystals*, 20(3–4):301–318, 1973.

[80] G. Gassler. Cathode ray tubes (CRTs). In J. Chen, W. Cranton, and M. Fihn, editors, *Handbook of Visual Display Technology*, chapter 6.2.1, pages 1043–1054. Springer, 2012.

[81] L. Gattermann and A. Ritschke. Über azoxyphenoläther. *Berichte der Deutschen Chemischen Gesellschaft*, 23(1):1738–1750, 1890.

[82] D. Gentili, G. Foschi, F. Valle, M. Cavallini, and F. Biscarini. Applications of dewetting in micro and nanotechnology. *Chemical Society Reviews*, 41(12):4430–4443, 2012.

[83] A. Gharbi, F. R. Fekih, and G. Durand. Dynamics of surface anchoring breaking in a nematic liquid crystal. *Liquid Crystals*, 12(3):515–520, 1992.

[84] W. M. Gibbons, P. J. Shannon, S.-T. Sun, and B. J. Swetlin. Surface-mediated alignment of nematic liquid crystals with polarized laser light. *Nature*, 351:49–50, 1991.

[85] G. W. Gray, K. J. Harrison, and J. A. Nash. New family of nematic liquid crystals for displays. *Electronics Letters*, 9(6):130–131, 1973.

[86] H. Gruler. Williams domains and dielectric alignment in a nematic liquid crystal. *Molecular Crystals and Liquid Crystals*, 27(1–2):31–41, 1974.

[87] J. Guckenheimer and P. J. Holmes. *Nonlinear Oscillations, Dynamical Systems, and Bifurcations of Vector Fields*. Springer, 1983.

[88] D. Halliday, R. Resnick, and J. Walker. *Principles of Physics*. John Wiley & Sons, 2010.

[89] W. H. Han and A. D. Rey. Supercritical bifurcations in simple shear flow of a non-aligning nematic: reactive parameter and director anchoring effects. *Journal of Non-Newtonian Fluid Mechanics*, 48(1–2):181–210, 1993.

[90] K. Hanaoka, Y. Nakanishi, Y. Inoue, S. Tanuma, Y. Koike, and K. Okamoto. 40.1: A new MVA-LCD by polymer sustained alignment technology. *Society for Information Display International Symposium Digest of Technical Papers*, 35(1):1200–1203, 2004.

[91] Y. Hatwalne, S. Ramaswamy, M. Rao, and R. A. Simha. Rheology of active-particle suspensions. *Physical Review Letters*, 92(11):118101, 2004.

[92] G. H. Heilmeier and L. A. Zanoni. Electro-optical device, US Patent 3 499 112, filed March 1967, issued March 1970.

[93] G. H. Heilmeier, L. A. Zanoni, and L. A. Barton. Dynamic scattering: a new electrooptic effect in certain classes of nematic liquid crystals. *Proceedings of the IEEE*, 56(7):1162–1171, 1968.

[94] W. Helfrich and M. Schadt. Optical device, Swiss Patent 532 261, filed December 1970, issued December 1972.

[95] D. Helmer, A. Voigt, S. Wagner, N. Keller, K. Sachsenheimer, F. Kotz, T. M. Nargang, and B. E. Rapp. Suspended liquid subtractive lithography: One-step generation of 3D channel geometries in viscous curable polymer matrices. *Scientific Reports*, 7(7387):1–5, 2017.

[96] S. Herminghaus, K. Jacobs, K. Mecke, J. Bischof, A. Fery, M. Ibn-Elhaj, and S. Schlagowski. Spinodal dewetting in liquid crystal and liquid metal films. *Science*, 282(5390):916–919, 1998.

[97] J. P. Hernández-Ortiz, B. T. Gettelfinger, J. Moreno-Razo, and J. J. de Pablo. Modeling flows of confined nematic liquid crystals. *The Journal of Chemical Physics*, 134(13):134905, 2011.

[98] A. Hochbaum and M. M. Labes. Alignment and texture of thin liquid crystal films on solid substrates. *Journal of Applied Physics*, 53(4):2998–3002, 1982.

[99] H. Hong. In-Plane Switching (IPS) technology. In J. Chen, W. Cranton, and M. Fihn, editors, *Handbook of Visual Display Technology*, chapter 7.3.3, pages 1469–1483. Springer, 2012.

[100] Y. Hori. *Hydrodynamic Lubrication*. Springer, 2006.

[101] S. D. Hunnisett and J. C. A. van der Sluijs. Ultrasonic shear and capillary viscosity study of 4-cyano-4'-n-hepylbiphenyl in the nematic and the isotropic state. *Journal de Physique – Lettres*, 44(2):L–59–L–63, 1983.

[102] J. T. Jenkins and P. J. Barratt. Interfacial effects in the static theory of nematic liquid crystals. *The Quarterly Journal of Mechanics and Applied Mathematics*, 27(1):111–127, 1974.

[103] J. C. Jones. The fiftieth anniversary of the liquid crystal display. *Liquid Crystals Today*, 27(3):44–70, 2018.

[104] L. P. Jones. Alignment properties of liquid crystals. In J. Chen, W. Cranton, and M. Fihn, editors, *Handbook of Visual Display Technology*, chapter 7.2.2, pages 1387–1402. Springer, 2012.

[105] Y. V. Kalinin, V. Berejnov, and R. E. Thorne. Contact line pinning by microfabricated patterns: effects of microscale topography. *Langmuir*, 25(9):5391–5397, 2009.

[106] H. Kamiya, K. Tajima, K. Toriumi, K. Terada, H. Inoue, T. Yokoue, N. Shimizu, T. Kobayashi, S. Odahara, G. Hougham, C. Cai, J. H. Glownia, R. J. von Gutfeld, R. John, and S.-C. A. Lien. 56.3: Development of One Drop Fill technology for AM-LCDs. *Society for Information Display International Symposium Digest of Technical Papers*, 32(1):1354–1357, 2001.

[107] H. P. Kavehpour. Coalescence of drops. *Annual Review of Fluid Mechanics*, 47:245–268, 2015.

[108] H. Kawamoto. The history of liquid-crystal display and its industry. In *2012 Third IEEE HISTory of ELectro-technology CONference (HISTELCON)*, pages 1–6, 2012.

[109] P. J. Kedney and F. M. Lesle. Switching in a simple bistable nematic cell. *Liquid Crystals*, 24(4):613–618, 1998.

[110] H. Kelker. History of liquid crystals. *Molecular Crystals and Liquid Crystals*, 21(1–2):1–48, 1973.

[111] K. J. Kim and S. S. Sundar. Does panel type matter for LCD monitors? A study examining the effects of S-IPS, S-PVA, and TN panels in video gaming and movie viewing. In *Human-Computer Interaction – INTERACT 2011*, pages 281–288. Springer, 2011.

[112] S.-U. Kim, J.-H. Na, C. Kim, and S.-D. Lee. Design and fabrication of liquid crystal-based lenses. *Liquid Crystals*, 44(12–13):2121–2132, 2017.

[113] N. Kimura, T. Ishihara, H. Miyata, T. Kumakura, K. Tomizawa, A. Inoure, S. Horino, and Y. Inaba. 60.2: Invited paper: New technologies for large-sized high-quality LCD TV. *Society for Information Display International Symposium Digest of Technical Papers*, 36(1):1734–1737, 2005.

[114] M. Klasen-Memmer and H. Hirschmann. Liquid crystal materials for devices. In J. Chen, W. Cranton, and M. Fihn, editors, *Handbook of Visual Display Technology*, chapter 7.1.3, pages 1315–1342. Springer, 2012.

[115] M. Kléman. *Points, Lines and Walls in Liquid Crystals, Magnetic Systems and Various Ordered Media*. John & Wiley Sons, 1983.

[116] M. Kléman and S. A. Pikin. A new kind of orientation instability in Couette flow nematics with finite anchoring energy. *Journal de Mécanique*, 18(4):661–672, 1979.

[117] H. Kneppe, F. Schneider, and N. K. Sharma. Rotational viscosity γ_1 of nematic liquid crystals. *The Journal of Chemical Physics*, 77(6):3203–3208, 1982.

[118] A. P. Krekhov, L. Kramer, A. Buka, and A. N. Chuvirov. Flow alignment of nematics under oscillatory shear. *Journal de Physique II*, 3(9):1387–1396, 1993.

[119] Y. R. Kwon, Y. E. Choi, P. Wen, B. H. Lee, J. C. Kim, M.-H. Lee, K.-U. Jeong, and S. H. Lee. Polymer stabilized vertical alignment liquid crystal display: effect of monomer structures and their stabilizing characteristics. *Journal of Physics D: Applied Physics*, 49(16):165501, 2016.

[120] M.-A. Y.-H. Lam, L. J. Cummings, and L. Kondic. Stability of thin fluid films characterised by a complex form of effective disjoining pressure. *Journal of Fluid Mechanics*, 841:925–961, 2018.

[121] M.-A. Y.-H. Lam, L. J. Cummings, and L. Kondic. Computing dynamics of thin films via large scale GPU-based simulations. *Journal of Computational Physics: X*, 2:100001, 2019.

[122] M.-A. Y.-H. Lam, L. Kondic, and L. J. Cummings. Effects of spatially-varying substrate anchoring on instabilities and dewetting of thin nematic liquid crystal films. *Soft Matter*, 16(44):10187–10197, 2020.

[123] D. Langevin and M. A. Bouchiat. Molecular order and surface tension for the nematic-isotropic interface of MBBA, deduced from light reflectivity and light scattering measurements. *Molecular Crystals and Liquid Crystals*, 22(3–4):317–331, 1973.

[124] O. D. Lavrentovich. Transport of particles in liquid crystals. *Soft Matter*, 10(9):1264–1283, 2014.

[125] H. Lee, S. Song, J. Lee, A. Xiao, T. Min, and S. Su. 9.3: Analysis of liquid crystal drop mura in high resolution mobile thin film transistor liquid crystal displays. *Society for Information Display International Symposium Digest of Technical Papers*, 45(1):97–99, 2014.

[126] O. Lehmann. Über fliessende krystalle. *Zeitschrift für Physikalische Chemie*, 4U(1):462–472, 1889.

[127] F. M. Leslie. Some constitutive equations for anisotropic fluids. *The Quarterly Journal of Mechanics and Applied Mathematics*, 19(3):357–370, 1966.

[128] F. M. Leslie. Some constitutive equations for liquid crystals. *Archive for Rational Mechanics and Analysis*, 28:265–283, 1968.

[129] F. M. Leslie. Distortion of twisted orientation patterns in liquid crystals by magnetic fields. *Molecular Crystals and Liquid Crystals*, 12(1):57–72, 1970.

[130] F. M. Leslie. Theory of flow phenomena in nematic liquid crystals. In J. L. Ericksen and D. Kinderlehrer, editors, *Theory and Applications of Liquid Crystals*, chapter 12, pages 235–254. Springer, 1987.

[131] F. M. Leslie, J. S. Laverty, and T. Carlsson. Continuum theory for biaxial nematic liquid crystals. *The Quarterly Journal of Mechanics and Applied Mathematics*, 45(4):595–606, 1992.

[132] A. H. Lewis, I. Garlea, J. Alvarado, O. J. Dammone, P. D. Howell, A. Majumdar, B. M. Mulder, M. P. Lettinga, G. H. Koenderink, and D. G. A. L. Aarts. Colloidal liquid crystals in rectangular confinement: theory and experiment. *Soft Matter*, 10(39):7865–7873, 2014.

[133] X. Li, T. Yanagimachi, C. Bishop, C. Smith, M. Dolejsi, H. Xie, K. Kurihara, and P. F. Nealey. Engineering the anchoring behavior of nematic

liquid crystals on a solid surface by varying the density of liquid crystalline polymer brushes. *Soft Matter*, 14(37):7569–7577, 2018.

[134] F.-H. Lin and C. Liu. Static and dynamic theories of liquid crystals. *Journal of Partial Differential Equations*, 14(4):289–330, 2001.

[135] T.-S. Lin, L. J. Cummings, A. J. Archer, L. Kondic, and U. Thiele. Note on the hydrodynamic description of thin nematic films: strong anchoring model. *Physics of Fluids*, 25(8):082102, 2013.

[136] T.-S. Lin, L. Kondic, U. Thiele, and L. J. Cummings. Modelling spreading dynamics of nematic liquid crystals in three spatial dimensions. *Journal of Fluid Mechanics*, 729:214–230, 2013.

[137] Y. Luo, G. A. Braggin, G. T. Olson, A. R. Stevenson, W. L. Ruan, and S. Zhang. Nematic order drives macroscopic patterns of graphene oxide in drying drops. *Langmuir*, 30(48):14631–14637, 2014.

[138] R. Ma. Organic light emitting diodes (OLEDS). In J. Chen, W. Cranton, and M. Fihn, editors, *Handbook of Visual Display Technology*, chapter 6.6.1, pages 1209–1222. Springer, 2012.

[139] O. V. Manyuhina. Shaping thin nematic films with competing boundary conditions. *European Physical Journal E*, 37(6):48–52, 2014.

[140] Expert Market Research. Global TFT-LCD display panel market outlook, accessed 30-11-2020, available at: https://www.expertmarketresearch.com/reports/tft-lcd-market.

[141] T. Marusiy, Yu. Reznikov, V. Reshetnyak, M. Soskin, and A. Khighnyak. Effect of surface-induced anchoring on NLC light scattering characteristics. *Molecular Crystals and Liquid Crystals Incorporating Nonlinear Optics*, 152(1):495–502, 1987.

[142] MATLAB. *version 9.6.0.1114505 (R2019a)*. MathWorks, 2019.

[143] M. Ch. Mauguin. Sur les cristaux liquides de M. Lehmann. *Bulletin de la Sociót française de Minéralogie*, 34(3):71–117, 1911.

[144] M. K. McCamley, M. Ravnik, A. W. Artenstein, S. M. Opal, S. Žumer, and G. P. Crawford. Detection of alignment changes at the open surface of a confined nematic liquid crystal sensor. *Journal of Applied Physics*, 105(12):123504, 2009.

[145] J. G. McIntosh and F. M. Leslie. Flow induced surface switching in a bistable nematic device. *Journal of Engineering Mathematics*, 37:129–142, 2000.

[146] J. G. McIntosh, F. M. Leslie, and D. M. Sloan. Stability for shearing flow of nematic liquid crystals. *Continuum Mechanics and Thermodynamics*, 9(5):293–308, 1997.

[147] X.-D. Mi and D.-K. Yang. Capillary filling of nematic liquid crystals. *Physical Review E*, 58(2):1992–2000, 1998.

[148] M. Miesowicz. The three coefficients of viscosity of anisotropic liquids. *Nature*, 158:27, 1946.

[149] M. Miesowicz. Liquid crystals in my memories and now—the role of anisotropic viscosity in liquid crystals research. *Molecular Crystals and Liquid Crystals*, 97(1):1–11, 1983.

[150] S. Mondal, I. M. Griffiths, F. Charlet, and A. Majumdar. Flow and nematic director profiles in a microfluidic channel: the interplay of nematic material constants and backflow. *Fluids*, 3(2):39, 2018.

[151] N. J. Mottram and C. J. P. Newton. Liquid crystal theory and modelling. In J. Chen, W. Cranton, and M. Fihn, editors, *Handbook of Visual Display Technology*, chapter 7.2.3, pages 1403–1429. Springer, 2012.

[152] N. J. Mottram and C. J. P. Newton. Introduction to Q-tensor theory. *arXiv:1409.3542*, 2014.

[153] F. Mugele and J. Heikenfeld. *Electrowetting: Fundamental Principles and Practical Applications*. John Wiley & Sons, 2019.

[154] I. Müller. *Thermodynamics*. Pitman, 1985.

[155] COMSOL Multiphysics. *COMSOL Multiphysics Reference Manual*. COMSOL Multiphysics.

[156] COMSOL Multiphysics. *Version 5.5. http://www.comsol.com*. COMSOL, Inc., Burlington MA, 2019.

[157] Yu. A. Nastishin, R. D. Polak, S. V. Shiyanovskii, V. H. Bodnar, and O. D. Lavrentovich. Nematic polar anchoring strength measured by electric field techniques. *Journal of Applied Physics*, 86(8):4199–4213, 1999.

[158] T. Ohzono and J. Fukuda. Zigzag line defects and manipulation of colloids in a nematic liquid crystal in microwrinkle grooves. *Nature Communications*, 3:701, 2012.

[159] D. Orejon, K. Sefiane, and M. E. R. Shanahan. Stick–slip of evaporating droplets: substrate hydrophobicity and nanoparticle concentration. *Langmuir*, 27(21):12834–12843, 2011.

[160] C. W. Oseen. Beiträge zur theorie der anisotropen flüssigkeiten. *Arkiv för Matematik, Astronomi och Fysik*, 19A(9):1–19, 1925.

[161] C. W. Oseen. The theory of liquid crystals. *Transactions of the Faraday Society*, 29:883–899, 1933.

[162] P. Oswald. Measurement with a rotating magnetic field of the surface viscosity of a nematic liquid crystal. *Europhysics Letters*, 100(2):26001, 2012.

[163] P. Oswald, G. Poy, F. Vittoz, and V. Popa-Nita. Experimental relationship between surface and bulk rotational viscosities in nematic liquid crystals. *Liquid Crystals*, 40(6):734–744, 2013.

[164] O. Parodi. Stress tensor for a nematic liquid crystal. *Journal de Physique*, 31(7):581–584, 1970.

[165] P. Pieranski and E. Guyon. Shear-flow-induced transition in nematics. *Solid State Communications*, 13(4):435–437, 1973.

[166] S. Pikin, G. Ryschenkow, and W. Urbach. On new type of electrohydrodynamics instability in tilted nematic layers. *Journal de Physique*, 37(3):241–244, 1976.

[167] W. K. Pratt, S. S. Sawkar, and K. O'Reilly. Automatic blemish detection in liquid crystal flat panel displays. *Proceedings of SPIE*, 3306:1–12, 1998.

[168] J. Quintans Carou. *Thin-Film Flow of Liquid Crystals*. PhD thesis, University of Strathclyde, 2007.

[169] J. Quintans Carou, B. R. Duffy, N. J. Mottram, and S. K. Wilson. Steady flow of a nematic liquid crystal in a slowly varying channel. *Molecular Crystals and Liquid Crystals*, 438(1):237/[1801]–249/[1813], 2005.

[170] J. Quintans Carou, B. R. Duffy, N. J. Mottram, and S. K. Wilson. Shear-driven and pressure-driven flow of a nematic liquid crystal in a slowly varying channel. *Physics of Fluids*, 18(2):027105, 2006.

[171] J. Quintans Carou, N. J. Mottram, S. K. Wilson, and B. R. Duffy. A mathematical model for blade coating of a nematic liquid crystal. *Liquid Crystals*, 34(5):621–631, 2007.

[172] A. Rapini and M. Papoular. Distorsion d'une lamelle nématique sous champ magnétique conditions d'ancrage aux parois. *Journal de Physique Colloque*, 30(C4):C4–54–C4–56, 1969.

[173] E. P. Raynes and I. C. Sage. Chemicals to calculators: the early exploitation of cyanobiphenyl liquid crystals. *Liquid Crystals*, 42(5–6):722–731, 2015.

[174] E. P. Raynes and C. M. Waters. Supertwisted nematic liquid crystal displays. *Displays*, 8(2):59–63, 1987.

[175] P. Raynes. Twisted Nematic and Supertwisted Nematic LCDs. In J. Chen, W. Cranton, and M. Fihn, editors, *Handbook of Visual Display Technology*, chapter 7.3.1, pages 1433–1444. Springer, 2012.

[176] F. Reinitzer. Beiträge zur kenntniss des cholesterins. *Monatshefte für Chemie - Chemical Monthly*, 9:421–441, 1888.

[177] F. Reinitzer. Contributions to the knowledge of cholesterol. *Liquid Crystals*, 5(1):7–18, 1989.

[178] G. Reiter. Dewetting of thin polymer films. *Physical Review Letters*, 68(1):75–78, 1992.

[179] A. D. Rey. Orientational transition in radial flow of a nematic liquid. *Journal of Non-Newtonian Fluid Mechanics*, 40(2):177–200, 1991.

[180] A. D. Rey. Periodic textures of nematic polymers and orientational slip. *Macromolecules*, 24(15):4450–4456, 1991.

[181] A. D. Rey. The Neumann and Young equations for nematic contact lines. *Liquid Crystals*, 27(2):195–200, 2000.

[182] A. D. Rey. Young–Laplace equation for liquid crystal interfaces. *The Journal of Chemical Physics*, 113(23):10820–10822, 2000.

[183] A. D. Rey. Nematostatics of triple lines. *Physical Review E*, 67(1):011706, 2003.

[184] A. D. Rey. Capillary models for liquid crystal fibers, membranes, films, and drops. *Soft Matter*, 3(11):1349—1368, 2007.

[185] A. D. Rey and M. M. Denn. Jeffrey–Hamel flow of Leslie–Ericksen nematic liquids. *Journal of Non-Newtonian Fluid Mechanics*, 27(3):375–401, 1988.

[186] A. D. Rey and M. M. Denn. Dynamical phenomena in liquid-crystalline materials. *Annual Review of Fluid Mechanics*, 34:233–266, 2002.

[187] A. D. Rey and T. Tsuji. Recent advances in theoretical liquid crystal rheology. *Macromolecular Theory and Simulations*, 7(6):623–639, 1998.

[188] W. Rickert, E. N. Vilchevskaya, and W. H. Müller. A note on Couette flow of nematic crystals according to the Ericksen–Leslie theory. *ZAMM - Zeitschrift für Angewandte Mathematik und Mechanik*, 100(1):e201900035, 2020.

[189] Ó. A. Rojas-Gómez, M. M. Telo da Gama, and J. M. Romero-Enrique. Wetting of nematic liquid crystals on crenellated substrates: A Frank–Oseen approach. *Crystals*, 9(8):430, 2019.

[190] L. F. Rull and J. M. Romero-Enrique. Computer simulation study of the nematic–vapour interface in the Gay–Berne model. *Molecular Physics*, 115(9–12):1214–1224, 2017.

[191] M. Schadt and W. Helfrich. Voltage-dependent optical activity of a twisted nematic liquid crystal. *Applied Physics Letters*, 18(4):127–128, 1971.

[192] S. Schlagowski, K. Jacobs, and S. Herminghaus. Nucleation-induced undulative instability in thin films of nCB liquid crystals. *Europhysics Letters*, 57(4):519–525, 2002.

[193] A. Sengupta, U. Tkalec, and C. Bahr. Nematic textures in microfluidic environment. *Soft Matter*, 7(14):6542–6549, 2011.

[194] A. Sengupta, U. Tkalec, M. Ravnik, J. M. Yeomans, C. Bahr, and S. Herminghaus. Liquid crystal microfluidics for tunable flow shaping. *Physical Review Letters*, 110(4):048303, 2013.

[195] M. J. Shelley, F.-R. Tian, and K. Wlodarski. Hele–Shaw flow and pattern formation in a time-dependent gap. *Nonlinearity*, 10(6):1471–1495, 1997.

[196] M. Slavinec, G. D. Crawford, S. Kralj, and S. Žumer. Determination of the nematic alignment and anchoring strength at the curved nematic–air interface. *Journal of Applied Physics*, 81(5):2153–2156, 1997.

[197] A. A. Sonin. *The Surface Physics of Liquid Crystals*. Gordon & Breach Science Publishers, 1995.

[198] A. M. Sonnet and E. G. Virga. *Dissipative Ordered Fluids*. Springer, 2012.

[199] J. Stelzer, R. Hirning, and H.-R. Trebin. Influence of surface anchoring and viscosity upon the switching behavior of twisted nematic cells. *Journal of Applied Physics*, 74(10):6046–6052, 1993.

[200] M. J. Stephen and J. P. Straley. Physics of liquid crystals. *Reviews of Modern Physics*, 46(4):617–704, 1974.

[201] I. W. Stewart. *The Static and Dynamic Continuum Theory of Liquid Crystals*. Taylor & Francis, 2004.

[202] S. Terashita, K. Watanabe, and F. Shimoshikiryoh. 6-2: Novel liquid crystal display mode "UV^{2}A II" with photo alignment technology for a large-screen 8K display. *Society for Information Display International Symposium Digest of Technical Papers*, 50(1):62–65, 2019.

[203] D. J. Ternet, R. G. Larson, and L. G. Leal. Flow-aligning and tumbling in small-molecule liquid crystals: pure components and mixtures. *Rheologica Acta*, 38:183–197, 1999.

[204] C. Tilford. Pressure and vacuum measurements. In B. W. Rossiter and R. C. Baetzold, editors, *Physical Methods of Chemistry, Volume 6, Determination of Thermodynamic Properties*, chapter 2, pages 101–173. Wiley, 1992.

[205] C. Tsakonas, A. J. Davidson, C. V. Brown, and N. J. Mottram. Multistable alignment states in nematic liquid crystal filled wells. *Applied Physics Letters*, 90(11):111913, 2007.

[206] H. M. van der Kooij, S. A. Semerdzhiev, J. Buijs, D. J. Broer, and D. Liu. Morphing of liquid crystal surfaces by emergent collectivity. *Nature Communications*, 10:3501, 2019.

[207] M. W. J. van der Wielen, E. P. I. Baars, M. Giesbers, M. A. Cohen Stuart, and G. J. Fleer. The effect of substrate modification on the ordering and dewetting behavior of thin liquid-crystalline polymer films. *Langmuir*, 16(26):10137–10143, 2000.

[208] D. van Effenterre and M. P. Valignat. Stability of thin nematic films. *The European Physical Journal E*, 12(3):362–372, 2003.

[209] F. Vandenbrouck, M. P. Valignat, and A. M. Cazabat. Thin nematic films: metastability and spinodal dewetting. *Physical Review Letters*, 82(13):2693–2696, 1999.

[210] D. Vanzo, M. Ricci, R. Berardi, and C. Zannoni. Wetting behaviour and contact angles anisotropy of nematic nanodroplets on flat surfaces. *Soft Matter*, 12(5):1610–1620, 2016.

[211] M. T. Viciosa, A. M. Nunes, A. Fernandes, P. L. Almeida, M. H. Godinho, and M. D. Dionísio. Dielectric studies of the nematic mixture E7 on a hydroxypropylcellulose substrate. *Liquid Crystals*, 29(3):429–441, 2002.

[212] E. Virga. *Variational Theories for Liquid Crystals*. Chapman & Hall, 1994.

[213] A. B. E. Vix, P Müller-Buschbaum, W. Stocker, M. Stamm, and J. P. Rabe. Crossover between dewetting and stabilization of ultrathin liquid crystalline polymer films. *Langmuir*, 16(26):10456–10462, 2000.

[214] R. Voituriez, J. Joanny, and J. Prost. Spontaneous flow transition in active polar gels. *Europhysics Letters*, 70(3):404–410, 2005.

[215] D. Vorländer. Einfluß der molekularen gestalt auf den krystallinisch-flüssigen zustand. *Berichte der Deutschen Chemischen Gesellschaft*, 40(2):1970–1972, 1970.

[216] J. Wahl and F. Fischer. Elastic and viscosity constants of nematic liquid crystals from a new optical method. *Molecular Crystals and Liquid Crystals*, 22(3–4):359–373, 1973.

[217] J. Walton. *Mathematical Modelling of Active Nematic Liquid Crystals in Confined Regions*. PhD thesis, University of Strathclyde, 2020.

[218] J. Walton, G. McKay, M. Grinfeld, and N. J. Mottram. Pressure-driven changes to spontaneous flow in active nematic liquid crystals. *The European Physical Journal E*, 43:51, 2020.

[219] J. Walton, N. J. Mottram, and G. McKay. Nematic liquid crystal director structures in rectangular regions. *Physical Review E*, 97(2):022702, 2018.

[220] P. K. Weimer. The TFT a new thin-film transistor. *Proceedings of the IRE*, 50(6):1462–1469, 1962.

[221] L. Weng, P.-C. Liao, C.-C. Lin, T.-L. Ting, W.-H. Hsu, J.-J. Su, and L.-C. Chien. Anchoring energy enhancement and pretilt angle control of liquid crystal alignment on polymerized surfaces. *AIP Advances*, 5(9):097218, 2015.

[222] R. Williams. Domains in liquid crystals. *The Journal of Chemical Physics*, 39(2):384–388, 1963.

[223] V. Williams. Liquid crystal microscopy: gallery of LC images, accessed 03-02-2021, available at: http://lcmicroscopy.weebly.com/lc-photogallery.html.

[224] M. R. Wilson. Molecular simulation of liquid crystals: progress towards a better understanding of bulk structure and the prediction of material properties. *Chemical Society Reviews*, 36(12):1881–1888, 2007.

[225] Y. Yamamoto. LCD processing and testing. In J. Chen, W. Cranton, and M. Fihn, editors, *Handbook of Visual Display Technology*, chapter 7.6.1, pages 1649–1671. Springer, 2012.

[226] H. Yokoyama. Surface anchoring of nematic liquid crystals. *Molecular Crystals and Liquid Crystals Incorporating Nonlinear Optics*, 165(1):265–316, 1988.

[227] H. Yokoyama and H. A. van Sprang. A novel method for determining the anchoring energy function at a nematic liquid crystal-wall interface from director distortions at high fields. *Journal of Applied Physics*, 57(10):4520–4526, 1985.

[228] H. Yoshida. Vertically Aligned Nematic (VAN) LCD technology. In J. Chen, W. Cranton, and M. Fihn, editors, *Handbook of Visual Display Technology*, chapter 7.3.4, pages 1485–1505. Springer, 2012.

[229] M. A. Zaki Ewiss, G. Nabil, S. Schlagowski, and S. Herminghaus. Wetting behaviour of 5CB and 8CB and their binary mixtures above the isotropic transition. *Liquid Crystals*, 31(4):557–566, 2004.

[230] C. Zannoni. Computer simulation and molecular design of model liquid crystals. In Fabbrizzi L. and Poggi A., editors, *Chemistry at the Beginning of the Third Millennium*, pages 329–342. Springer, 2000.

[231] J. Zheng, H. Shi, G. Chen, Y. Huang, H. Wei, S. Wang, and W. Wen. Relaxation of liquid bridge after droplets coalescence. *AIP Advances*, 6(11):115115, 2016.

[232] J. Zhou, D. M. Collard, J. O. Park, and M. Srinivasarao. Control of anchoring of nematic fluids at polymer surfaces created by in situ photopolymerization. *The Journal of Physical Chemistry B*, 109(18):8838–8844, 2005.

[233] P. Ziherl and I. Muševič. A note on observability of fluctuation-induced structural interaction in a nematic mesophase. *Liquid Crystals*, 28(7):1057–1062, 2001.

[234] P. Ziherl, R. Podgornik, and S. Žumer. Pseudo-Casimir structural force drives spinodal dewetting in nematic liquid crystals. *Physical Review Letters*, 84(6–7):1228–1231, 2000.

[235] H. Zocher. Über die einwirkung elektrischer, magnetischer und mechanischer kräfte auf mesophasen. *Physikalische Zeitschrift*, 28:790–796, 1927.

[236] H. Zocher. The effect of a magnetic field on the nematic state. *Transactions of the Faraday Society*, 29(140):945–957, 1933.

[237] C. Zou, J. Wang, M. Wang, Y. Wu, K. Gu, Z. Shen, G. Xiong, H. Yang, L. Jiang, and T. Ikeda. Patterning of discotic liquid crystals with tunable molecular orientation for electronic applications. *Small*, 14(21):1800557, 2018.

[238] I. Zúñiga and F. M. Leslie. Shear-flow instabilities in non-flow-aligning nematic liquid crystals. *Liquid Crystals*, 5(2):725–734, 1989.